Diffusion Studies in Toughenable Low-E Coatings

Justyna Kulczyk-Malecka

A thesis submitted in partial fulfilment of the requirements of Manchester Metropolitan University for the degree of Doctor of Philosophy

School of Engineering

Manchester Metropolitan University

In collaboration with

Pilkington Technology Management Ltd.

August 2012

Declaration

This is to certify that the material contained in this thesis has been produced by the author and has not been accepted in substance for any other degree and is not currently submitted in candidature for any other academic award.

Justyna Kulczyk-Malecka

Abstract

Low emissivity (Low-E) coatings are applied to large area architectural glazing to reduce heat losses from buildings. They combine high visible transparency with high reflectance in the far-infrared region. To achieve this combination of properties, Low-E coatings generally consist of dielectric-silver-dielectric multi-layer systems or stacks, where the thin (~10 nm) silver layer reflects long wavelength IR back into the building and the dielectric layers both protect the silver and act as anti-reflectance layers. The dielectric layers are commonly TiO_2, SnO_2 or ZnO, and all the layers are usually deposited by magnetron sputtering. The market for Low-E coatings has grown considerably in recent years due to environmental legislation and increased energy costs. To further expand the market, the next generation of Low-E coatings are increasingly being deposited onto toughenable glass, which is post-deposition annealed at temperatures of up to 650^{o}C. However, under these conditions, silver atoms are highly mobile and can rapidly diffuse through the other constituent layers of the coating stack, which can have a detrimental impact on the performance of the coating.

Diffusion in polycrystalline films occurs much faster than in bulk samples and by different mechanisms. This is caused by the physical properties of thin films, which may contain a high density of defects such as dislocations, vacancies and grain boundaries that can act as pathways for diffusion processes. The aim of this project therefore is to carry out a detailed study of diffusion processes in dielectric-silver coating systems deposited under industrially relevant conditions (i.e. using commercially available magnetron designs and power deliver modes).

TiO_2 coatings have been deposited onto float glass substrates by reactive pulsed magnetron sputtering and characterised using Raman spectroscopy, scanning electron microscopy, energy-dispersive X-ray spectroscopy, atomic force microscopy and X-ray diffraction. The coatings have been annealed at temperatures in the range of 100^{o}C to 800^{o}C and re-analysed to determine the effect of annealing on the film structures. An interesting transition from a weakly crystalline rutile-like structure with very small grain sizes to a strongly crystalline anatase structure or mixed-phase structure with much larger grains was observed as annealing temperature was increased. Selected coatings were over coated with silver and annealed for a second time. These coatings were analysed by X-ray photoelectron spectroscopy and secondary ion mass spectrometry to determine the diffusion profiles of silver through the titania layer and the reverse diffusion of sodium from the glass substrates. Little difference in the diffusion rate of silver was observed with annealing temperature, but sodium was observed to diffuse significantly faster through samples annealed at higher temperature range.

Similar studies have been performed for Al-doped ZnO, Zn_2SnO_4 and Si_3N_4 coatings. These films have been post-deposition annealed at 650^{o}C then over coated with silver and re-annealed at 250^{o}C. Diffusion profiles for both Ag and Na atoms were measured using secondary ion mass spectrometry.

Finally dielectric/Ag/dielectric layers were deposited to investigate the behaviour of silver and sodium after annealing at 250^{o}C. The basic models of diffusion mechanisms in thin films have been developed using Fick’s second diffusion law. Analytical modelling was used to fit the experimental data into a concentration dependent curve that represents the solution to Fick’s second law. Moreover selected dielectric/Ag/dielectric stacks were subjected to temperature dependency of silver diffusion studies using Arrhenius diffusion principle. Samples were post-deposition annealed at the temperature range of 200-650^{o}C for 5 minutes to investigate silver diffusion at different heat treatment conditions and diffusivity values were used to find activation energies and frequency factors from Arrhenius plot.

Overall findings from the diffusion studies are that from dielectric materials investigated in this work Al-doped ZnO coatings have the best barrier properties for silver atoms diffusion and show relatively low values for sodium diffusion, when not annealed at relatively high temperatures. Zinc stannate, on the other hand, was found to be the material through which atoms investigated here diffuse fairly easily. Both silver and sodium atoms were found to have the highest diffusion rates through zinc stannate films relative to the other coatings investigated in this work.

Acknowledgments

During the past four years of my PhD I have worked with many fantastic people to whom I am very grateful for their help and support. Foremost, I would like to thank my supervisor Professor Peter Kelly for his scientific guidance, support, encouragement and enthusiasm. I am also very gratefully for unforgettable days out and opportunities to present my work at conferences.

Within the University I would like to thank all of the members of Surface Engineering group, who I was working with throughout the past four years, for their support and always being willing to help out. Especially I would like to thank Dr. Glen West for his supervision, patience and enthusiasm. Without those guys the experience of my PhD would not have been so amazing.

I am grateful for the support from Dr. Vlad Vishnyakov and providing invaluable analytical results for the past four years.

I owe deep gratitude to Pilkington Technology Management Ltd. for funding this project. I would like to thank for endless support from the members of research team at Lathom, especially Dr. Greg Clarke, Dr. John Ridealgh and Dr. Monica Hughes for their support, interesting project meetings, thoughts provoking discussions and providing extra data for this thesis; Dr. Mark Farnworth, Dr. Chris Welsby and Dr. Alex Abbott for providing endless analysis and support throughout this project.

I would like to thank Professor Lindsay Greer and Dr. Zoe Barber from University of Cambridge for invaluable help in understanding the diffusion processes in solids and pointing the right direction in research development. Moreover I am very grateful for the AFM analysis provided by Dr. Nadia Stelmashenko from Wolfson College in Cambridge.

I especially want to thank my family, my Mum and Dad for their love and care, and for believing in me, and my sisters for their encouragement, support and enthusiasm.

And last but definitely not least to my husband Krzysztof, without whose support this thesis could not been written. This thesis is dedicated to you.

I. List of Figures

II. List of Tables

III. List of Equations

IV. Table of Content

1. Introduction

The deposition of functional coatings on large-area float glass has been the subject of substantial research and development in the glass industry in recent years. Solar control and low emissivity (Low-E) coatings are the most popular products for large area glazing. [1] Low emissivity coatings are applied to large area architectural glazing to reduce heat losses from buildings. They combine high visible transparency with high reflectance in the far-infrared region. To achieve this combination of properties, Low-E coatings generally consist of dielectric-silver-dielectric multi-layer systems or stacks, where the thin (~10nm) silver layer reflects long wavelength IR back into the building and the dielectric layers both protect the silver and act as anti-reflectance layers. The dielectric layers are commonly TiO_2, SnO_2 or ZnO [2], and all the layers are usually deposited by magnetron sputtering, which is considered to be one of the most important large-area coating technologies. [1, 3] The market for Low-E coatings has grown considerably in recent years due to environmental legislation and increased energy costs. To further expand the market, the next generation of Low-E coatings are increasingly being deposited onto toughenable glass, which is post-deposition annealed at temperatures of up to 650^{o}C. However, under these conditions, silver atoms are highly mobile and can rapidly diffuse through the other constituent layers of the coating stack, which can have a detrimental impact on the performance of the coating.

As diffusion in thin films occurs much faster and with different mechanisms than in bulk samples the importance of studying this process rises dramatically. Thin films are very sensitive to the smallest changes in their impurity concentration; diffusion may, therefore, entail large differences in electrical conductivity, corrosion resistance or the optical proprieties of a film. The main technique used to analyse diffusion in this study is secondary ion mass spectrometry (SIMS), but some coatings have also been analysed by X-ray photoelectron spectroscopy (XPS).

1.1 Research Directions

In this work the main focus was on diffusion measurements of silver and sodium atoms through dielectric layers. In the literature many papers can be found, which describe diffusion in thin films [4-15] and Low-E coatings. [16-19] However in all cases the approach differs from the one taken in this study.

In this work coatings were deposited by reactive pulsed DC magnetron sputtering. The experimental procedure mostly took place in the Surface Engineering Group at Manchester Metropolitan University; however some coatings were deposited at Pilkington Technology Management Ltd. in Lathom. Dielectric coatings have been deposited under a range of different conditions, which are relevant to industrial applications. The main reason for this approach was to find the best parameters to deposit Low-E coatings, which are still possible to perform on an industrial scale and which have not been used before.

Diffusion measurements were performed mostly by using time-of-flight secondary ion mass spectrometry (TOF-SIMS). However other analytical techniques, such as XPS or SIMS with magnetic sector analyser, were used to describe diffusion in some of the deposited coatings.

1.2 Thesis Layout

In this thesis the background information is provided in Chapters 1-8, and the project plan and methodology described in Chapter 9. The results from various experimental procedures and analysis are discussed in Chapters 10-14.

In the next chapter the properties of low emissivity glass are described in general. Also the structure and properties of deposited materials and substrates are illustrated here. Chapter 3 characterises the basics of plasma and its properties in general. Chapter 4 moves into the area of physical vapour deposition processes, where basics of various deposition techniques are mentioned, before focusing on magnetron sputtering. The possible effects onto thin films growth and proprieties resulting from using different deposition techniques and operating parameters are explained in Chapter 5. Chapter 6 describes diffusion, its mechanisms and a thin film mathematical approach. Information about the experimental equipment used to produce films and analytical techniques performed to describe coating proprieties, are given in Chapter 7 and Chapter 8 respectively. The project plan and methodology are described in Chapter 9.

The properties of deposited titania coatings, its structural changes after annealing at a variety of temperatures, and finally silver and sodium diffusion studies through TiO_2 are presented in Chapter 10. Chapter 11 describes Al-doped ZnO (AZO) coatings, which have been divided into two sections. The first section investigates the structure of AZO films with relatively high thickness before and after annealing at 650^oC. Section 2 investigates the structure and proprieties of AZO coatings of an average thickness of 80 nm. The diffusion of silver and sodium atoms has been studied here. In Chapter 12 zinc stannate coatings deposited at the Pilkington Technology Management Ltd. laboratory are summarised. Films were deposited under a large range of conditions, post deposition annealed and characterised by various analytical techniques to compare structures and morphologies. Coatings were then over coated with silver and the diffusion of Ag and Na was investigated. Chapter 13 describes the structure and morphology of silicon nitride coatings. Coatings were over coated with silver and the diffusion was measured, after annealing at 250^oC. Moreover the temperature dependence on diffusion was investigated using the Arrhenius equation. Selected samples were additionally annealed at temperatures in the range of $100\text{-}600^oC$ and the diffusion of silver was measured. From the Arrhenius plot activation energies and frequency factors were calculated.

Dielectric/Ag/dielectric stacks were deposited onto float glass and the diffusion of silver was investigated after annealing over the temperature range of $100\text{-}600^oC$. Chapter 14 investigates temperature dependent diffusion in titania-Ag-titania, AZO-Ag-AZO and silicon nitride-Ag-silicon nitride stacks.

Chapter 15 concludes the findings from this work and finally, Chapter 16 gives suggestions for the future work.

2. Low Emissivity Glass

This chapter describes low emissivity coatings and their applications. Also it contains a description of the substrate material and materials used for thin film deposition. Throughout this study thin films were deposited by reactive magnetron sputtering from metallic targets such as titanium, zinc, zinc-tin, silicon and silver.

2.1 Low-E Coatings

Sputtered silver-based coatings with multi-layer systems of dielectric/Ag/dielectric/glass and a double silver layer structure of dielectric/Ag/dielectric/Ag/dielectric/glass have excellent properties of heat insulation, solar energy reflection and low sheet resistance. At present, they are widely used as solar control coatings for automotive windshields and electromagnetic wave shielding coatings for plasma display panels and low emissivity coatings. Among these applications, Low-E coatings have the largest market mainly in insulating glazing units (IGU) because of their high performance for thermal insulation. [20] Low emissivity glass coatings were developed initially for reducing energy consumption in cold climate areas. [21] Modern insulating glass units with Low-E coatings effectively reduce heat loss by a factor of four in comparison with conventional insulating glass units. Also the energy used for heating the building can be up to 30% less than for conventional construction materials in most climate areas.

Low-E coatings transmits short wavelength (1.4-3 µm) infrared and reflect 85-95 % of the long (8-15 µm) wavelength IR back into the building, whilst still providing a high visible transparency of 60-65 %. As mentioned, Low-E coatings generally consist of dielectric-silver-dielectric multi-layer stacks. The thin silver layer (~10 nm) sandwiched between the dielectric layers is transparent to visible light and improves reflection in the infrared region. The dielectric layers act as anti-reflectance layers and also protect the silver layer as silver is not resistant to corrosion and if exposed to air would quickly oxidize and lose its conductivity and transparency. The dielectric layers are commonly titanium dioxide, silicon dioxide, zinc oxide, tin oxide, zinc stannate, bismuth oxide and silicon nitride [1], and all the layers are usually deposited by magnetron sputtering, which is considered to be one of the most important large-area coating technologies. [1, 3] A typical basic Low-E coating stack is presented below; however commercial products will include proprietary variations, such as blocker layers to further protect the silver, mainly between the metal layer and upper dielectric film.

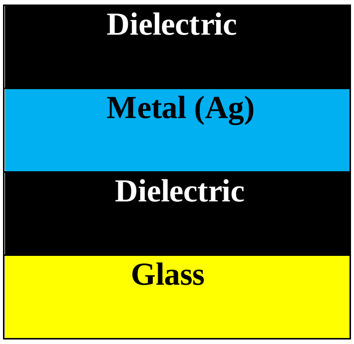

Figure 2.1: Typical design of Low-E stack.

Low-E glass is only used in insulated glass units and the coating must be positioned at the inside of the IGU filled with argon gas, at a surface facing the space between panels. Figure 2.2 represents a schematic design of a Low-E IGU, where the optimal position for Low-E glass is surface 3 as in this design the highest energy is gained from solar radiation.

The silver-based Low-E coating is not durable against mechanical abrasion, chemical agents, and high temperature treatment. [22] Moisture attack causes the appearance of many white dots on the coatings after exposure to a humid atmosphere. These dots are caused by increased silver migration in a moist atmosphere. This results in silver agglomerations and delamination of the upper layer of the coatings which leads to the film peeling off and the occurrence of the white dots effect. In order to avoid this degradation, the stock size glass products with the coating are generally packed with desiccants in plastic films during transport and storage. [20]

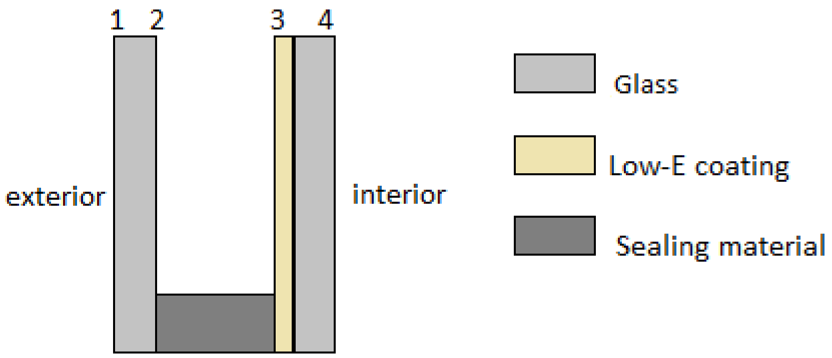

Figure 2.2: Schematic representation of low emissivity glass in an insulated glass unit.

As mentioned earlier, the next generation of Low-E coatings are being deposited onto glass, which is post-deposition annealed at temperatures up to 650°C. In this work the temperature selected for annealing studies was 250°C. Silver atoms are still mobile in these conditions; however the rate of penetration into adjacent layers is much less. The chosen temperature was selected from the preliminary studies carried out by the project sponsors Pilkington Technology Management Ltd.

2.2 Substrates

In this work thin films were grown onto 4 mm thick soda-lime float glass supplied by Pilkington Technology Management Ltd. The substrate size was 10 cm x 10 cm and each slide was cleaned by the supplier in a large industrial washer in hot steamed distilled water. Samples were vacuum packed to avoid any further contamination of the glass surface during transport. Small particles such as dust were removed from the glass surface by a compressed air duster prior to loading the sample into the vacuum chamber.

Soda-lime glass is the most common form of glass produced. It is composed of natural materials such as silica sand, limestone, soda ash, dolomite and other minor ingredients. Table 2.1 presents the chemical composition of soda-lime glass. The soda serves as a flux to lower the temperature at which the silica melts, and the lime acts as a stabilizer for the silica. Soda-lime glass is inexpensive, chemically stable, reasonably hard, and extremely workable, because it is capable of being re-softened a number of times if necessary. These qualities make it suitable for manufacturing a wide array of glass products, including light bulbs, windowpanes, bottles, and art objects. [23]

Float glass shows high transmittance of solar radiation, has low optical dispersion and refractive index (n=1.52 at 550 nm). It absorbs light of wavelengths greater than 4 µm with its highest radiation occurring for a black body. It is also partially transparent to UV light in the range of 315-380 nm wavelengths, but it is opaque for wavelengths below 300 nm.

Float glass has a smooth surface, although it contains tin oxide on the surface of one side. Tin oxide diffuses into the glass during float glass production, as it rests on a molten tin float bath. The tin layer can be identified using UV light (254 nm wavelength), as the tin oxide fluoresces.

Table 2.1: Chemical composition of float glass (source: Pilkington Technology Management Ltd.)

Chemical formula	**Source**	**Mass proportion (wt %)**
SiO_2	Silica sand	72.6
Na_2O	Soda ash	13
CaO	Limestone	8.4
MgO	Dolomite	4.0
Al_2O_3	-	1.0
Minor ingredients	-	1.0

2.3 Titanium Dioxide

Titanium dioxide is an important material in optical applications due to its high refractive index, high hardness and chemical resistance. TiO_2 typically occurs in amorphous, anatase or rutile structure, whereas brookite and β-TiO_2 phases are rather rare, particularly for thin films. The refractive index (n) and crystallinity increases from amorphous (n<2.3) to rutile phase (n>2.6, at wavelength of 550 nm), thus increasing temperature, ion flux or energy tend to change the crystalline structure and physical proprieties of the film. [24] Rutile has been identified as a stable form of titania, whereas the other forms are metastable. At annealing temperatures below $600^{o}C$ anatase grows faster than rutile, whereas the transition temperature depends on grain size, impurities and the deposition process of anatase. It is known that the decrease in the average particle size in anatase from coarse crystals to fine nanocrystals can shift the onset of transition temperature during annealing to much lower values. [25] Rutile structures are formed by higher energy processes and in the presence of Ti in the vapour phase. Amorphous films, on the other hand occur due to differences in the packing density of the involved phases. [26] As anatase and rutile have different proprieties when used under the same conditions in a given applications the issue of relative stability of anatase and rutile phases is of major interest in nanocrystalline titania systems.

Many different techniques can be used to deposit TiO_2 such as sol-gel processes [27-29], chemical vapour deposition [30-34], ion beam depositions [35] and magnetron sputtering. [26, 36-39] It plays important role in solar control [40] anti-reflective and finally Low-E coatings.

The figure below represents three main crystalline structures of titanium dioxide.

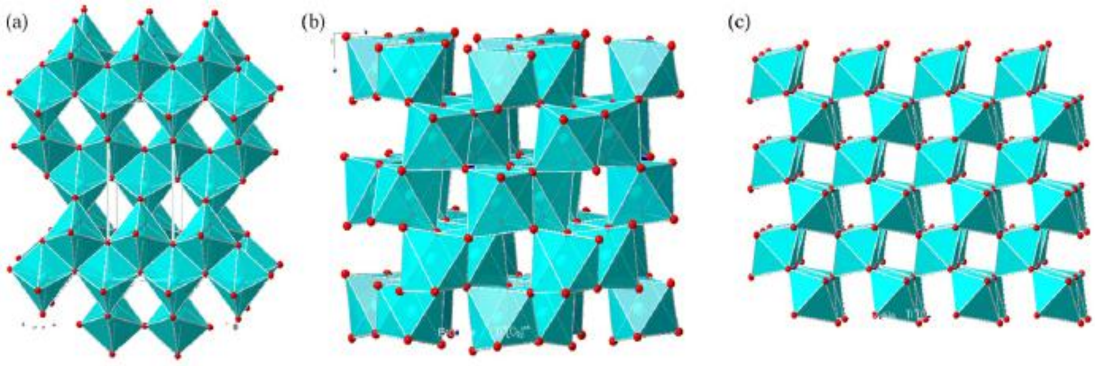

Figure 2.3: Phases of titanium dioxide: (a) anatase, (b) brookite and (c) rutile. [41]

2.4 Aluminium Doped Zinc Oxide

Zinc oxide is a well known semiconductor with a wide band gap (3.3 eV) [42] large exciton binding energy (60 meV) and a hexagonal wurtzite structure. [43] Non-stoichiometric un-doped ZnO thin films usually show n-type conductivity due to oxygen vacancies and zinc interstitials. Large amounts of oxygen vacancies makes it unstable in corrosive, humid ambient, as it can absorb O_2 and H_2O quite easily. Pure ZnO has low thermal stability and high resistivity, therefore ZnO is usually doped with metals such as Al, In, Ga, B and F. [44-47] Doping such metals into ZnO enables the production of highly conductive thin films with a high refractive index in the IR region and high transmittance in the visible optical region (85%). [46-48] Moreover doping aluminium into zinc oxide can reduce the stress in the ZnO/Ag/ZnO stack and therefore moisture degradation in Low-E coatings. Ando *et.al* reported that the high compressive internal stress caused peeling of the top ZnO layer, which can be reduced by depositing AZO instead of ZnO in the triple sandwich stack. He found that the moisture enhanced the silver migration in the silver layer that resulted in decreasing the interface adhesion force between the top ZnO layer and the silver layer, followed by the peeling. [1, 20, 22, 49]

Aluminium doped zinc oxide (AZO) films have become well known transparent conductive oxides (TCO) successfully replacing ITOs due to their similar electrical and optical proprieties but with much lower costs. [44] These coatings have high optical transparency and low electrical resistivity, which makes them very desirable for many thin film devices. Depending on their transmittance, conductivity and structure they are widely used in energy efficient flat panel displays, energy efficient smart coatings on architectural glasses, or piezoelectric cantilevers. [47] On an industrial scale Al-doped ZnO are mainly produced by magnetron sputtering. This technique enables the deposition of films with high transparency and low resistance and good film uniformity at low substrate temperature. [44] The properties of ZnO coatings strongly depend on various deposition parameters such as power, working gas pressure, substrate temperature and target specification, i.e. doping ratio, target purity, etc. and it is very important to find an optimal conditions. That is why the most successful method seems to be mid-frequency magnetron sputtering and RF sputtering. [42]

2.5 Zinc Stannate

Zn-Sn-O (ZTO) systems have attracted much attention as new TCO coatings, due to their high visible transmittance and n-type electrical conductivity with wide band gap energy of 3.6 eV and by being composed of abundant and inexpensive materials. [50-53] ZTO films have not been studied extensively but films are known to be resistant to chemical etching, especially at high Sn concentrations. [51] The ZTO films have a good thermal stability; the crystallisation temperature is relatively high, which is why ZTO tends to be amorphous in thin film form. [54]

ZTO as a transparent high resistivity semiconductor is used in gas sensors, moisture detectors, electronic materials and plating additives. Zinc stannate shows a lack of inversion symmetry which indicates ferro-electricity, piezoelectric effect, photo-elasticity and non-linear optical polarizability. Moreover, Zn-Sn-O groups are transparent conductive oxides, making ZTO a promising material for multifunctional applications. [55-57]

2.6 Silicon Nitride

Silicon nitride (Si_3N_4) is a covalent material which has high oxidation and corrosion resistance, low mass density, high dielectric constant and a wide range of hardnesses. Its properties, such as high thermal stability, chemical inertness, hardness and good dielectric behaviour makes it very desirable in many fields, such as cutting tools, engine moving parts, fabrication of the microelectronic devices, by providing isolation between devices and serving as a mask against impurities. It is widely used as an insulator between conductors and as a diffusion barrier for metals, water and oxygen, even at very high temperatures. [58-60] The transparency of silicon nitride over a wide spectral range from near-ultraviolet (UV) to infrared (IR) region, along with its passivating properties makes it suitable for many optical applications. [59] It is widely used in the semiconductor industry for surface passivation and protection to prevent contamination and damage, as a mask for local oxidation, antireflective coating etc.

The hardness and optical properties of these films are influenced by the N/Si ratio in the film, the total hydrogen content and the bonding between silicon, nitrogen, and hydrogen. The conventional technique to deposit silicon nitride is high temperature (700-800^{o}C) CVD, which enables the deposition of stoichiometric Si_3N_4, but results in hydrogen contamination, due to the choice of precursors. [60] Such a high temperature is undesirable and one of the advantages of depositing silicon nitride by reactive sputtering is much lower deposition temperature and the higher purity of the resulting coating, especially the lack of hydrogen contamination of the film surface. [61]

2.7 Silver

Silver is widely used in optical coating design as an infrared reflective component. In Low-E systems Ag is a metal of choice due to its high reflectance and comparatively low absorption in the visible region (400-700 nm approximately). These properties of Low-E coatings are achieved by the high quality of the thin silver layer (~10 nm) sandwiched between transparent dielectric layers, which act as anti-reflectance layers. Silver based Low-E coatings display a lack of mechanical and environmental durability, therefore dielectric layers protect the thin silver coating from oxidation during deposition and from degradation during annealing. In addition, Ag becomes very mobile in the presence of moisture, causing local agglomerations and therefore poor adhesion and delamination of the coating. As mentioned before this effect is known as white dots. Moreover the compressive stress within the coating can also lead to poor adhesion and film delamination.

Another important aspect in silver deposition is the surface morphology of the base layer. As Ag tends to create islands during film growth it is highly important that the dielectric film onto which Ag will be deposited has a smooth surface to promote the formation of a continuous layer of silver at the interface. Furthermore Ag films are more durable in their crystalline form and, therefore zinc oxide is often chosen as a base material of a multi-layer stack as ZnO promotes the formation of crystalline Ag layers. The durability of silver-based Low-E coatings has been studied by Nadel [19] and Kusano *et al.*, who tried to obtain thermal stability of silver in ITO/Ag/ITO and ZnO/Ag/ZnO stacks. [62]

3. Glow Discharge Plasma

Plasma by definition is a fully or partially ionised gas. Plasma contains atomic and/or molecular ions, electrons, neutrals (atoms, molecules), radicals, photons and excited particles and meta-stable species.

Plasma may be generated in two ways: thermally, so called hot plasma, which has high degree of ionization and its bulk has very high temperature; or electrically under vacuum, referred to as cold plasma with low degree of ionisation and cool plasma bulk.

The energy of an electron in typical PVD plasma varies from 1eV to 10 eV that is equivalent to about 11600 K, [63] but because the electrons have virtually no mass, there is no heat transfer. Ions and neutrals by contrast have energies of 0.04 eV and 0.025 eV respectively and therefore are only just above ambient temperature of about 464 and 290 K.

3.1 Plasma Potential

A plasma consists of neutral gas atoms and molecules, ions and electrons. The number of ions and electrons within plasma body is roughly equal; therefore plasma in general is neutral. This condition is called quasi-neutrality and any changes in charge within the plasma body can only occur on a very small scale. However at the edge of the plasma the difference in potential can be much higher. If we consider plasma as an electrical conductor which has only limited electrical resistance, therefore any areas of charge imbalance within the plasma body will be immediately compensated by movements of charges within the plasma. Electrons are the dominant charge carrier due to their low mass and high mobility, hence they can respond more quickly to electric fields than heavier ions. [63-65]

In a plasma the density of ions and electrons is equal $n_i = n_e$ otherwise an electric field would be generated. From Boltzmann's relation electron density can be described as:

$$\boldsymbol{n_e = n_{e_0} exp\left(-\frac{eV}{k_B T_e}\right)} \qquad \text{Equation 1}$$

Where n_e is the electron density, n_{e0} is the electron number density in the remote plasma, which is unperturbed by the test charge, e is the electron charge, V the retarding potential and k_B and T_e are the Boltzmann constant and electron temperature respectively. [63]

In vacuum systems electrons are easily lost to the chamber walls. To compensate for this lost plasma assumes a positive electrical potential compared to the anode (chamber walls). It results in a slow increase in the net positive charge in the plasma. As plasma charges positively it is less energetically possible for electrons to leave, as now the chamber walls are more negative than the plasma. Therefore a steady state is reached and the plasma remains neutral. Consequently, an average plasma potential is several volts more positive than any surface in contact with it. This results in ions being accelerated from the plasma edges to the chamber walls with the same voltage. [65] It results in an equal rate of loss of both ions and electrons.

3.1.1 Debye Screening

Plasmas are conductive hence can respond to local changes in potential. The distance over which a small potential can perturb plasma is known as the self-shielding or Debye length. [65] In Debye screening a positive test charge (Ze) will attract electrons and repel ions due to the Coulomb electrostatic fields it creates. The number of charged particles affected by this force is determined by the potential profile in the neighbourhood of the test charge. The Debye length (λ_D) is found by solving the one dimensional Poisson's equation [24, 63, 66]:

$$\boldsymbol{\lambda_D = \sqrt{\frac{\varepsilon_0 k_B T_e}{n_{e_0} e^2}}} \qquad \text{Equation 2}$$

Where n_{e0} is the electron number density in the remote plasma, which is unperturbed by the test charge, e is the electron charge, ε_0 is a permittivity of free space, $k_B T_e$ is the electron energy (eV).

The time needed for electron to move in response to a plasma perturbation is the time an electron needs to move a Debye length and is equal to λ_D divided by electron velocity. [65]

The Debye length is typically equal ~0.1 mm for a magnetron discharge.

The test charge has no influence on electrons greater than several Debye lengths. Therefore every charged particle in the plasma experiences Coulomb interactions with every other charged particle in its Debye sphere. Ions can feel the potential inside the Debye length but not on the outside.

Figure 3.1 shows a schematic representation of Debye screening within a plasma.

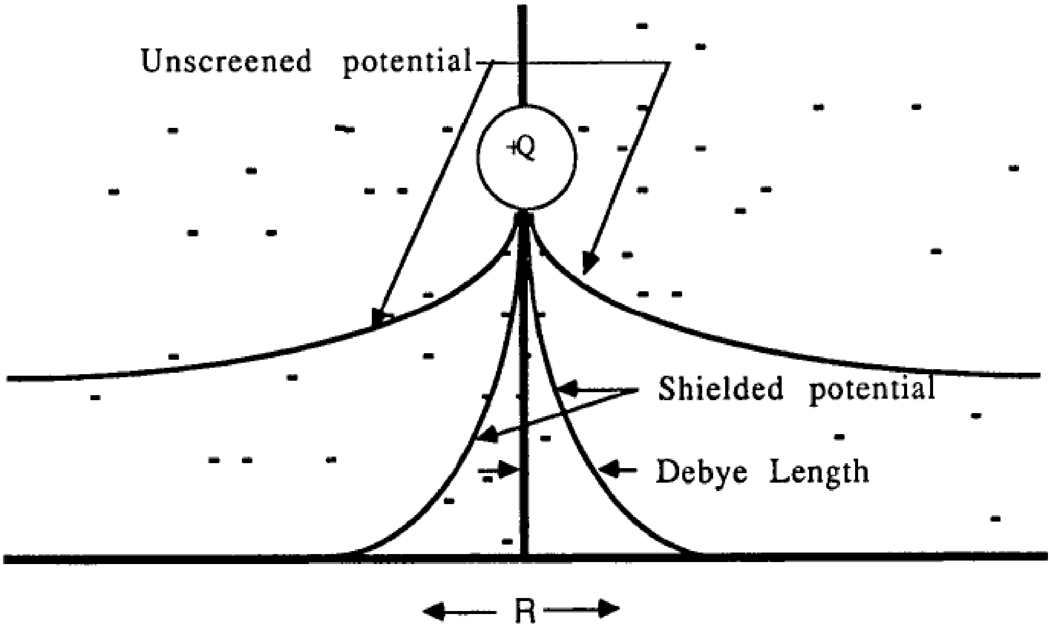

Figure 3.1: Unshielded electrostatic potential from a point charge Q compared to Debye screening potential, which occurs when a charge is placed in a plasma. [63]

A plasma is quasi-neutral ($n_i = n_e$) almost everywhere except in the sheaths next to electrodes or surfaces where the potential changes over several Debye lengths.

3.1.2 Sheaths

The edge of the plasma in contact with chamber walls or other surfaces is significantly different than the bulk plasma region. The sheath is the region within which significant voltage drop is observed, hence there is an extremely low electron density. The lack of electrons results in low levels of excitation of the gas species in that region, therefore the area appears dark. This phenomenon occurs due to the uniformity of plasma potential. All of the voltage change from the plasma to the region of its contact with a wall surface or electrode occurs in the sheath. Therefore the sheath is a region of high electric fields and high current flow. This flow consists of ions and electrons from the plasma and secondary electrons produced at the wall or electrode surface due to particle bombardment that are subsequently accelerated back into the plasma sheath. [65] The maximum current flow (j_{max}) is determined by the potential across the sheath and sheath thickness and is described by Child's Law:

$$\boldsymbol{j_{max}} = \sqrt{\left(\frac{4\varepsilon_0}{9}\right)\left(\frac{2e}{m}\right)}\sqrt[3]{\frac{v^2}{d^2}} \qquad \text{Equation 3}$$

Where m is an electron mass, V is a voltage across the sheath and d is a sheath width. Space-charged limited current flow described by Child's law can be used to characterise most of the cases of current flow between plasma and wall/electrode surfaces. [63, 65] The thickness of the sheath will be directly related to the applied potential, whereas current will be directly related to the plasma density. On the plasma sheath edge a weak potential is created which extends a Debye length into the plasma, with a value roughly related to electron temperature. This weak potential leads to 'pre-sheath' acceleration of the ions to the sheath edge known as a Bohm pre-sheath diffusion. The flux of ions to the sheath edge (j) is given by:

$$\boldsymbol{j = 0.6 n_e \sqrt{kT_e}} \qquad \text{Equation 4}$$

where n_e is an electron density. Increases in plasma density will significantly change the sheath thickness. [65]

At low pressures the cathode sheath is wide, ions are produced far from the target and their chances of being lost to the chamber walls are great. The mean free path between electrons is large, and electrons collected by the anode are not being replenished by secondary electron emission at the cathode. As a result discharges cannot be maintained at the pressure below 0.1 Pa, as ionisation efficiency is low. [66]

When the pressure is increased at a fixed voltage, the electron mean free path decreases, and more ions are generated which gives larger current flow. However when the pressure is too high the sputtered atoms are not efficiently deposited as they undergo increased collisional scattering and lose their energy.

Figure 3.2 shows a characteristic fall-out a plasma potential in front of the target surface.

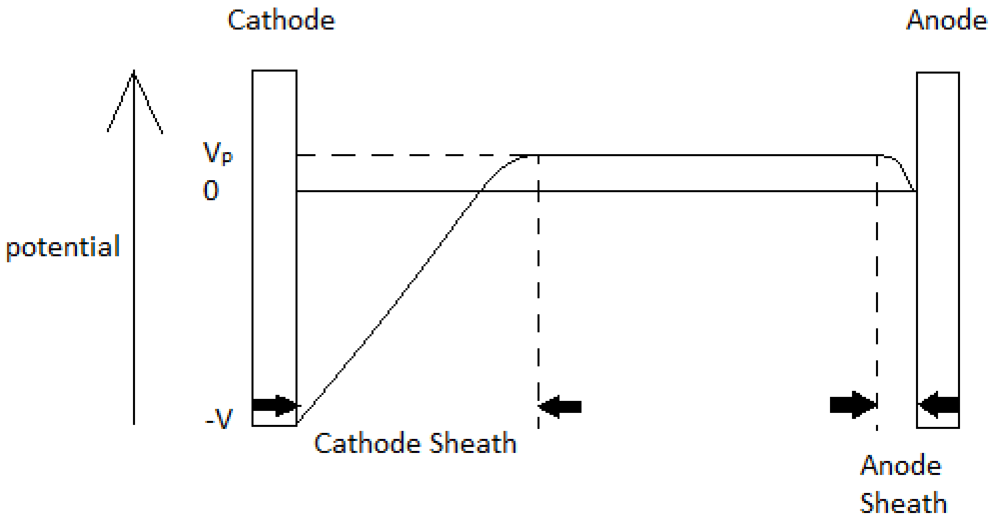

Figure 3.2: Schematic representation of a characteristic fall-off of the sheath potential in front of the target.

3.1.3 Floating Potential

An electrically floating substrate placed inside the vacuum system, which is in contact with plasma will rapidly become negatively charged due to the greater flux of electrons compared to ions. After a short while the substrate surface will become sufficiently negative that further electrons will be repelled to cause an equal flux of ions and electrons. The potential of this surface is called a floating potential (Φ_f) and it is negative compared to the plasma potential [65]:

$$\boldsymbol{\Phi_f = -0.5\left(\frac{kT_e}{e}\right) ln\left(\frac{2\pi m_e}{m_i}\right)\left(1+\frac{T_i}{T_e}\right)} \qquad \text{Equation 5}$$

Where m_i is an ion mass, m_e is an electron mass, T_i and T_e are ion and electron temperatures, respectively. The ion temperature is usually much smaller than the electron temperature (T_i<<T_e), hence the last part of the equation (*ln*) is neglected and the floating potential is linearly proportional to the electron temperature:

$$\boldsymbol{\Phi_f = -0.5\left(\frac{kT_e}{e}\right)} \qquad \text{Equation 6}$$

3.2 Ionisation

Under an appropriate gas density conditions the electron which will gain a sufficient energy, which is in excess of the ionisation energy of the working gas (ε_{iz}), and will collide with neutral gas atom (A), creating a positive ion (A^+). During the ionisation process a secondary electron will be ejected from the atom [63]:

$$\boldsymbol{A + e^- \rightarrow A^+ + 2e^-} \qquad \text{Equation 7}$$

When the energy of the electron colliding with the neutral molecule is less than its ionisation energy (15.8 eV for argon), then a metastable molecule is produced:

$$\boldsymbol{A + e^- \rightarrow A^* + e^-} \qquad \text{Equation 8}$$

Metastable A^* can then react with a sputtered atom, such as titanium:

$$\boldsymbol{A^* + Ti \rightarrow Ti^+ + e^- + A} \qquad \text{Equation 9}$$

This kind of reaction is called Penning ionisation and only occurs when the ionisation energy is less than the excitation energy of the exciting atom. Moreover two metastable particles can react together producing ionised molecules:

$$\boldsymbol{A^* + A^* \rightarrow A^+ + A + e^-} \qquad \text{Equation 10}$$

Also this may occur:

$$\boldsymbol{A^* + e^- \rightarrow A^+ + 2e^-} \qquad \text{Equation 11}$$

Finally, when a free electron collides with an atom, the atom gets excited and when relaxation occurs (electron from an excited state drops down to the ground state), then the energy is emitted as a photon of light (*hv*), which is the reason why a plasma glows:

$$\boldsymbol{A + e^- \rightarrow A^* + e^- \rightarrow A + e^- + hv} \qquad \text{Equation 12}$$

Ejected species will be accelerated by the electric field towards the cathode (ions) or anode (electrons). Secondary electrons will undergo further collisions to maintain the plasma. Ions accelerated towards the cathode may hit it with a high energy causing emission of secondary electrons, which may rapidly take part in ionisation process, causing the condition of ‘breakdown’. The flux of ions (*i*) to the anode will be:

$$\boldsymbol{i = i_0 \frac{exp(\alpha d)}{[1 - \gamma_e(exp\alpha d - 1)]}} \qquad \text{Equation 13}$$

Where i_0 is an electron flux starting towards the anode, α is a Townsend ionisation coefficient and it is probability per unit length that ionisation will occur. The Townsend secondary electron emission coefficient γ_e is defined as the number of secondary electrons emitted at the cathode per incident ion, so the α can be also described as:

$$\boldsymbol{\alpha} = \frac{\mathbf{1}}{\boldsymbol{\lambda}}\mathbf{exp}\left(-\frac{\mathbf{V_i}}{\mathbf{qE\lambda}}\right) \qquad \text{Equation 14}$$

Where λ is the collision mean free path, q is the electron charge, E is the electric field, V_i is the ionisation potential of the gas species, which is inversely proportional to the pressure. [24, 65, 67]

The breakdown voltage can be derived in terms of pressure and inter-electrode spacing:

$$\boldsymbol{V_B} = \frac{\boldsymbol{AP_d}}{\boldsymbol{ln(Pd)+B}} \qquad \text{Equation 15}$$

Where A and B are constants dependent on the gas. This equation is known as Paschen’s Law and has its representation in a curve (see Figure 3.3). It is a plot of V_B versus *Pd,* where *P* represents pressure and *d* electrode separation which indicates that at low values of *Pd* there are a low number of electrons, therefore ion collisions and secondary electron yield is too low to sustain ionisation in the discharge. Moreover at high pressures frequent collisions occur so electrons do not gain sufficient energy to ionise gas atoms. The discharge is self-sustaining typically at a few hundreds to a thousand volts, which means that for each electron at the cathode, exp(αd) electrons reach the anode and as a chain effect of collisions, new electrons at the cathode will be produced. [66] The lowest electron potential difference needed for a given gas to breakdown corresponds to the Pd value at the Paschen minimum (Ar~133 Pa cm).

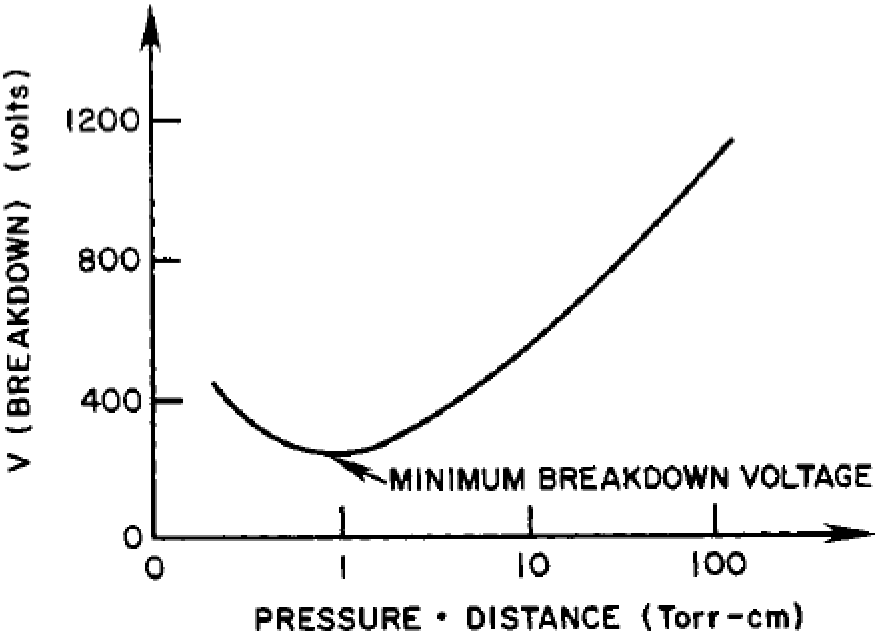

Figure 3.3: Paschen curve for the breakdown voltage for a gas between two electrodes separated by distance *d* at pressure *P*. [65]

4. Physical Vapour Deposition (PVD)

Physical vapour deposition (PVD) is the process, where atoms or molecules from a solid source are transported in the vapour state, through a vacuum or low pressure gas, or plasma environment and subsequently condense on the surface as a thin film or coating. [24] There are three main variants of the PVD process: vacuum evaporation, ion plating and sputtering. In this project magnetron sputtering (a development of the basic sputtering process) was used to produce coatings.

Evaporation is caused by absorption of thermal energy, whereas sputtering is an ejection of atoms from a solid surface by bombardment of the surface with energetic ions. In both ways the emitted atoms traverse a reduced pressure ambient and deposit on a substrate surface to form a film. [66]

4.1 Vacuum Evaporation

In vacuum evaporation atoms or molecules from a thermal vaporisation source, on average, reach the substrate without collisions with residual gas molecules in the vacuum chamber. This phenomenon is caused by the mean-free path being greater than the substrate to target separation. [24] In this process a typical operating pressure is about 0.01 Pa and deposition rates can be several microns per minute. Vacuum evaporation is a low energy process, which gives porous columnar structures of the deposited coating. It is used to deposit mostly metallic coatings.

In the vacuum evaporation technique films are formed by the evaporation of material from a molten source, usually heated by electron beam, hot filament or hot ‘boat’. Figure 4.1 presents a scheme of a typical vacuum evaporation system.

The process in general is restricted to low melting point materials. This is a ‘low energy process’ which results in weak coating adhesion. In vacuum the vapour travels from the source to the substrate in a straight line (line-to-sight) as the substrate holder is located directly above the source. Transport is collisionless prior to condensation due to the long mean free paths at typical operating pressures. [24, 65] Vacuum evaporation finds applications in reflective coating deposition for lighting, such as Al wire-fed onto ‘hot boat’ or E-beam Cr, Ni-Cr or stainless steel; EMI/RFI shielding, decorative coatings, Al coatings on glass beads for retro-reflective materials for safety jackets, traffic cones etc.; or Al films on food packaging materials.

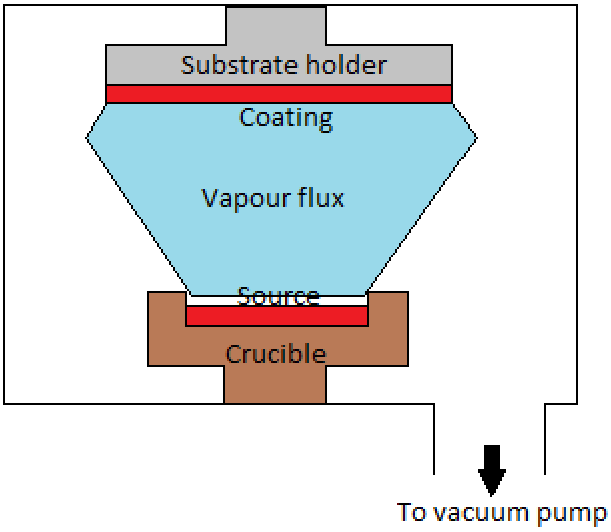

Figure 4.1: Schematic representation of a typical vacuum evaporation system.

4.2 Ion Plating

By definition ion plating is a coating process in which the substrate and growing film are subjected to continuous or periodic bombardment by energetic particles prior to and/or during the deposition process. The principle of energetic particles bombardment is to modify the film formation process and film proprieties. [24, 65] The typical operating pressure is 1 to 0.1 Pa and deposition rates are up to several microns per minute. Mostly metallic or ceramic coatings are deposited by this technique.

The technique is nowadays used to describe electron beam (E-beam) evaporation systems. Actual ionisation in early E-beam plasma was very low at about 0.1%. To produce dense coatings a very high bias voltage was needed (>1 kV), that caused significant re-sputtering and resulted in high stresses in the film. Although for some materials high evaporation rates could be achieved. It resulted however, in a poor film structure and low ion to atom ratios. Moreover the system design required that the evaporation took place from a point source and needed to take place upwards, which can lead to poor film uniformity on complex components. [24, 65-66]

Figure 4.2 gives a schematic representation of a typical ion plating source.

Current systems generally use low voltage/high current E-beam sources, which gives high plasma ionisation (10-50%). Dense coatings can be produce with a low (-100 V) bias. To improve film uniformity systems usually contain substrate rotation and crucible movement equipment. The ion plating technique is extensively used nowadays to deposit TiN and CrN layers onto large batches of tools and multi-layer oxide coatings for optical filters.

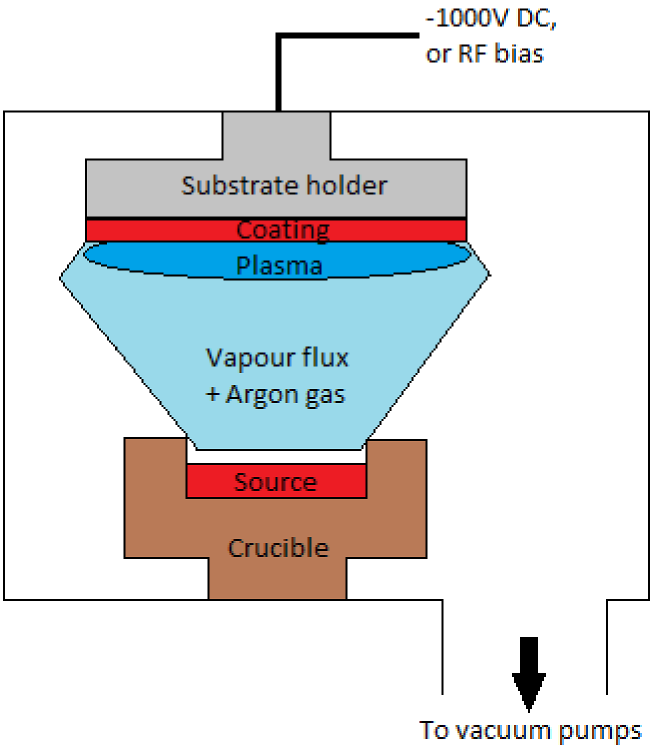

Figure 4.2: Schematic representation of typical ion plating system.

4.3 Cathodic Arc Evaporation

Arc evaporation processes use vaporisation from an electrode under arcing conditions as a source of vaporised material. A typical operating pressure is between 1 and 0.1 Pa and deposition is only possible from a conductive target; metallic or ceramic coatings can be deposited. [24] In the latter case, a reactive gas, such as nitrogen is introduced into the chamber while a metallic target is vaporised. Again, the growing film is subjected to ion bombardment.

Figure 4.3 presents a scheme of a typical cathodic arc evaporation system.

In cathodic arc systems, a high current/low voltage arc is initiated at the target surface that causes the emission of target atoms, ions and 'droplets' of target material. The cathode can be molten or solid with a water cooled solid target (cold cathode), which is the most common configuration. The arc voltage has to be near the ionisation potential of the gas or vapour (>25 V). [24] Each arc event lasts between 5 and 40 ns and for stable arc conditions a minimum current must passing through the arc, which varies from 50-100 A for metals with low melting point to 300-400 A for refractory materials. [68]

The arc can be initiated by applying high voltage between the electrodes, a so called trigger arc. There are three main arc sources distinguished in cathodic arc evaporation:

Random arc sources feature fixed permanent magnets behind target which gives uniform target erosion; steered arc sources feature varying magnetic fields which help reduce macro-particles emission. They cause arcs to move in a specific path and with greater velocity than in a random arc source. Filtered arc sources use additional magnetic fields to deflect charged particles and reduce macro-particles incident at substrate. The most common technique is to use a plasma duct in the form of 'bent knee' configuration. The plasma is bent out of the line of sight of the cathodic arc source by a magnetic field. As a result macros particles are deposited on chamber walls and only the charged coating flux particles get to the substrate. However the low point of this design is deposition rate which decreases by about one half. [24]

The process allows for very high ionization of coating flux, about 50-80%, with multiple ionisation possible (Me^{2+}, Me^{3+}). Cathodic arcs give the highest mean particle energy of all PVD processes, therefore good coating/substrate adhesion. It gives the possibility of low deposition temperatures (200^{o}C). The target can be mounted in any orientation; however it needs to be conductive. [24, 65, 68]

The main problem which arises during film deposition is formation of molten micron-size particles (macros) in the coatings. Magnets in the target are used to control the arc and keep it on the target surface. However there are a few possibilities to reduce macros, such as decreasing the arc current, increasing source-substrate distance, increasing gas pressure and using a co-axial magnetic field to increase plasma density. [24]

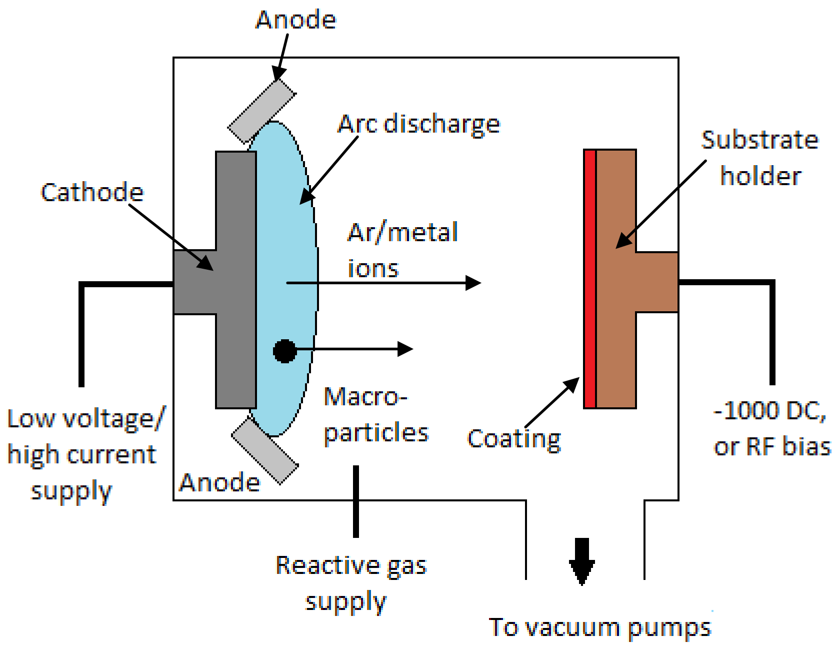

Figure 4.3: Schematic representation of cathodic arc evaporation system.

4.4 Sputtering

Sputtering is the physical vaporisation of atoms from a solid source by a mechanism of momentum transfer from bombarding energetic particles. These particles usually represent ions of a gaseous material accelerated in an electric field. [65] Sputter deposition is a process in which particles originating at a surface (target) are sputtered from the target and subsequently deposit onto a substrate. It was first reported in 1877 by Wright and was possible to perform because only a relatively poor vacuum is needed for sputter deposition. The process was patented by Edison in 1904 when he deposited silver onto wax photography cylinders. [24] Sputter deposition can be used to deposit films of compound materials either directly from a compound target or by reactive sputtering in which a metallic target is sputtered in a partial pressure of a reactive gas, such as oxygen or nitrogen. Sputter deposition is widely used for film deposition on magnetic media, semiconductor wafers and head surfaces, for coatings on window glass, inside of plastic bags and the surface of automobile parts, and for cutting surfaces for wear resistance, like razor blades or drills, and in many more applications. [69] The advantages of using sputter deposition as a thin film deposition techniques are excellent film uniformity, particularly over large areas; surface smoothness and thickness control, deposition of films with nearly bulk-like properties, which are predictable and stable;

versatility, good adhesion, high deposition rates (>10 nm/min) and deposition can take place at relatively low substrate temperatures (<150^{o}C). Moreover the sputter process is essentially a kinetic process involving momentum exchange rather than a chemical and/or thermal process and, therefore, virtually any material can be introduced into a gas discharge or sputtered from the solid. [65] However the sputtering process has a few disadvantages compared to other deposition techniques. As the process takes place under vacuum, the component size is limited by chamber size, there is the possibility of contamination of the coating during film deposition by Ar, O_2 or hydro-carbons (from the vacuum pumps) and dense coatings can be highly stressed, which can lead to wrinkling and peeling off the coating.

The event of sputtering is initiated by the first collision between an incident ion and target surface. The displacement of target atoms occurs due to successive collisions and atoms may escape from the surface. Figure 4.4 shows the schematic processes which occur at the surface and near-surface region of the bombarded target surface.

Bombarding particles can penetrate into the target surface. Particles create a cascade of collisions and some of the momentum is transferred to the surface atoms which can be ejected. Although most of the transferred energy (>95%) appears as heat in the surface and near-surface region. Some particles are reflected as high energy neutrals and some are implanted into the surface. These reflected highly energetic gas neutrals and high energy atoms ejected from a target bombard the growing film and affect its formation process. This can cause re-sputtering of a deposited material and, as a result, a decrease in sputtered yield from the target. If the flux of reflected energetic neutrals is anisotropic, then the growing film will have anisotropic proprieties. This may result in residual stress in post-cathode magnetron sputter deposited films, depending on the relative orientation of the film with respect to the post-cathode orientation. [24] However in magnetron sputtering system the target is water cooled and the cold surface minimises the amount of radiant heat in the system. This allows placing of thermally sensitive materials near to the sputter target. Cooling prevents diffusion in the target, which could lead to changes in elemental composition in the surface region while the target is being sputtered.

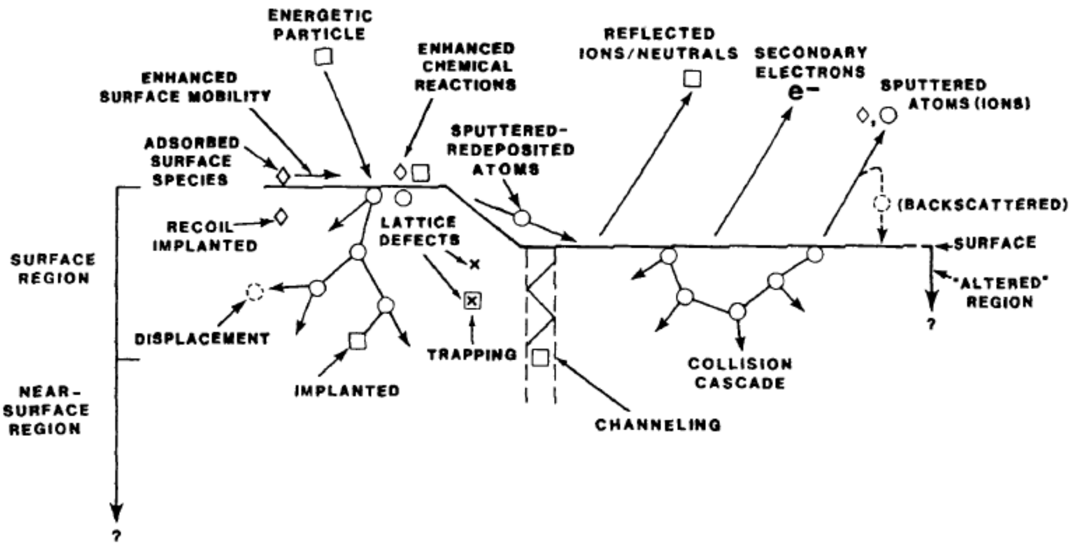

Figure 4.4: Schematic representation of the processes occurring on the target surface due to energetic bombardment. [66]

4.4.1 DC Diode Discharge

The simplest design of a sputtering system is a DC diode. It was historically first used to erode surfaces and for sputter deposition, but it was limited by low deposition rates and the difficulty of depositing insulators. Low deposition rates were due to secondary electron loss to the chamber walls, hence no new ions were formed from gas phase collisions. This limits net current flow and hence sputtering rate. Moreover if the cathode was an insulator (e. g. when sputtering oxides reactively, see Chapter 4.5.2) then the discharge current was extremely low and there was very little sputtering. [69]

The DC diode consists of two planar electrodes, an anode and a cathode, placed in the vacuum system (see Figure 4.5). In this design, the plasma is in front of the cathode surface, which consists of a plate made from the target material (the target and is made from metal in this case, as the glow discharge-current flow is maintained between two metallic electrodes). The reverse side of the cathode is water cooled. The substrate is placed in front of a target on a holder, and it can be electrically biased, floating or grounded. [67] The sputtering (or vacuum) chamber is evacuated and then backfilled with a sputtering gas; usually argon, at about 1.3-13 Pa. A DC voltage is applied between the electrodes to break down gas molecules into a glow discharge. The plasma potential is spatially uniform. Near the cathode is the dark space (sheath) in which an electric field is very large. The argon ions are accelerated rapidly in that region and strike the cathode with sufficient energy to remove atoms from the target, which may then condense on the substrate surface as a coating. The atoms that leave the target during sputtering have the typical energies of 2-5 eV. [24, 65, 69] Moreover secondary electrons (SE) may be also emitted from the target surface as a result of ion bombardment. These SE are the primary source of energy to the plasma and each one must generate significant number of ions to sustain the discharge. [69-70]

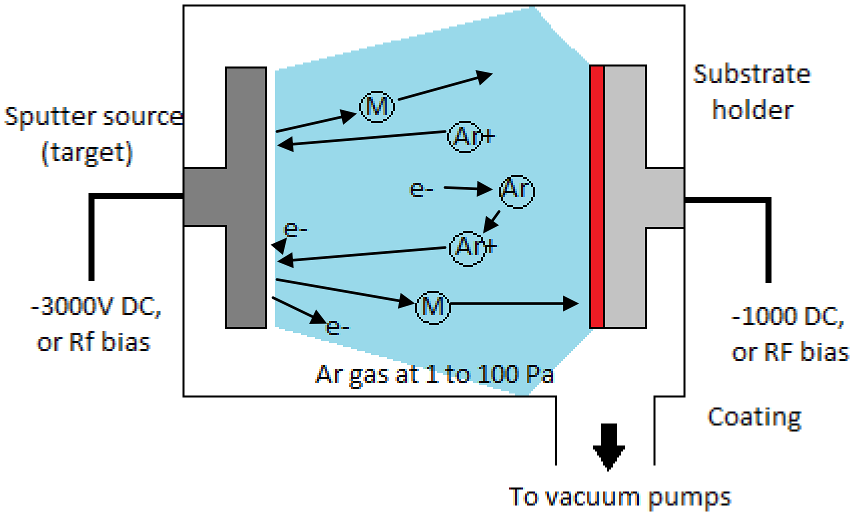

Figure 4.5: Scheme representation of the DC diode sputtering discharge.

4.5 Magnetron Sputtering

In magnetron sputtering a static magnetic field is located parallel to the cathode surface. One pole of a magnet is positioned at the central axis of the target and the second pole is formed by a ring of magnets around the outer edge of the target. [70] Secondary electrons emitted from the target are captured by this magnetic field and drift in a direction perpendicular to both electrical and magnetic fields (see Figure 4.6). This behaviour is known as an **E**×**B** drift and it causes electrons to move parallel to the cathode surface in a direction perpendicular to the magnetic field. [69] The magnetic field is orientated such that drift paths for electrons form a closed loop. This electron trapping effect increases the collision rate, and therefore the ionisation rate between the electrons and sputtering gas atoms, which results in denser plasma in the target region.

[66] This leads to increased ion bombardment of the target, giving higher sputtering rates, and therefore higher deposition rates at the substrate. [70]

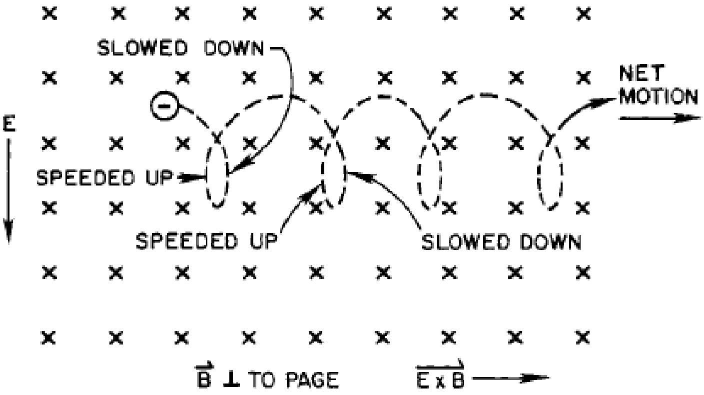

Figure 4.6: The motion of an electron in an electric and a magnetic field. The electric field is vertical, and the magnetic field is perpendicular to the plane of the page. [65]

The application of a magnetic field in sputtering has a significant impact on system control. A charged particle in a magnetic field is driven by a force:

$$\boldsymbol{F} = \boldsymbol{q}(\boldsymbol{E} + \boldsymbol{v} \times \boldsymbol{B}) \qquad \text{Equation 16}$$

Where q is the unit of electronic charge, **E** is the electric field vector, **v** is the velocity and **B** is the magnetic field vector. This force will cause the charged particles to move in an orbital path around the magnetic field lines. This path can be described by the Larmor radius:

$$\boldsymbol{r_L} = \frac{\boldsymbol{m_e v}}{\boldsymbol{Bq}} \qquad \text{Equation 17}$$

where m_e is the mass of an electron. [66, 69]

In an electric field **E** perpendicular to the magnetic field **B** charged particles will drift in a direction perpendicular to both fields at a constant drift velocity ν_H:

$$\boldsymbol{\nu_H} = \frac{\boldsymbol{E \times B}}{\boldsymbol{B^2}} = \frac{\boldsymbol{E}}{\boldsymbol{B}} \qquad \text{Equation 18}$$

This is called the Hall drift speed and increases the probability of collisions between electrons and molecules enabling the use of lower pressures during sputtering (about $1.3\text{x}10^{-3}$ Pa). Figure 4.7 represents the cycloidal motion of an electron in a magnetic field. [67]

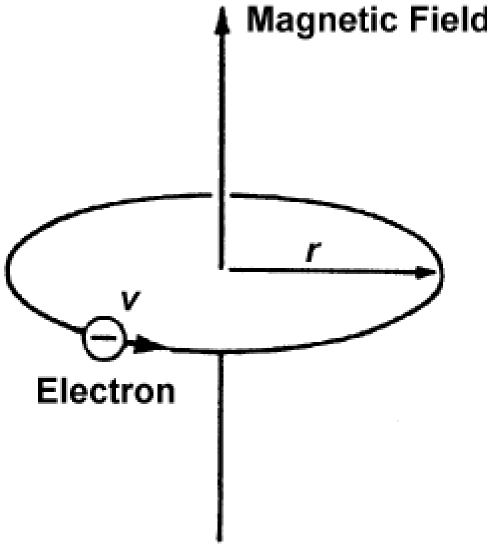

Figure 4.7: Cycloidal motion of an electron in a magnetic field. [67]

The drift speed is independent of the particle charge or mass, so electrons and ions drift with the same speed in the same direction. In the magnetron ions are not magnetised, as their Larmor radius is typically greater than the size of the chamber and so they are lost to the chamber walls before they can drift. This gives rise to an electron drift only, which takes place in a closed loop in front of the target surface. [69] Eventually these secondary electrons lose their kinetic energy due to collisions with gas atoms (ionisation) or with other electrons (electron heating). This results in the formation of the densest plasma and greatest ionisation between the inner and outer poles of the magnetron, and therefore the highest sputtering rate at the target is also in this region. This has the effect of causing non-uniform erosion of the target and the resulting area that is most heavily eroded is known as a race track. This circular drift increases the plasma efficiency what allows operations at low pressure and voltage.

The Figure 4.8 a) and b) represents the motion of electrons in a combined electric and magnetic field in a rectangular magnetron.

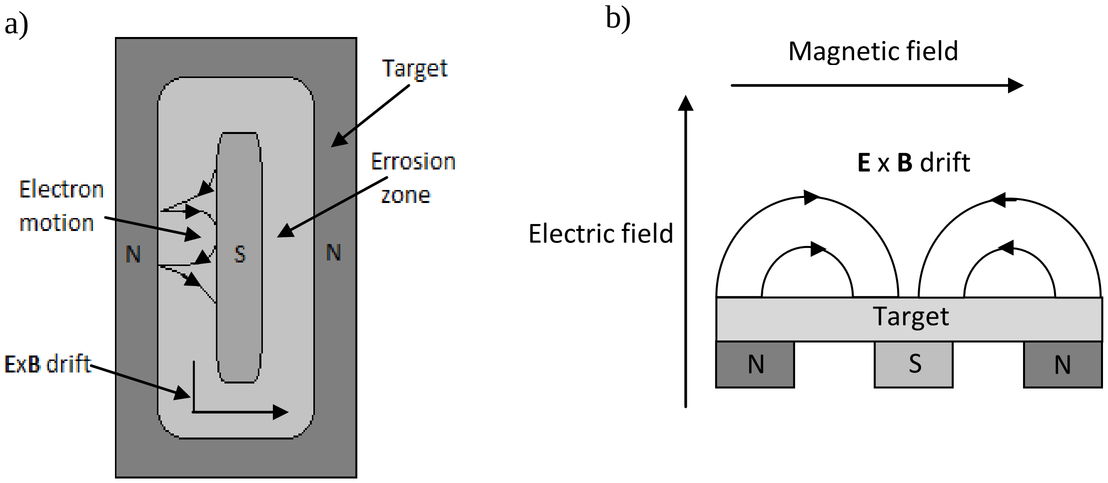

Figure 4.8: Schematic representation of electrons drift path in a rectangular magnetron: a) top view; b) side view.

4.5.1 Unbalanced Magnetron Sputtering

In conventional magnetrons the plasma is restricted to the target region. Substrates placed outside the dense plasma region, which typically extends 60 mm in front of the target, will lie in a low plasma density region, where ion currents incident at the substrate will not be great enough to modify the film structure. The energy of the bombarding ions can be increased by applying a negative bias to the substrate surface, but this can lead to defects in the film and increased film stress. Ion bombardment increases the surface mobility of the adatoms, during the film growth leading to enhanced nucleation and promotes dense film growth. However when the energy of the particles arriving at the substrate is greater than the threshold value for a particular material can cause an implantation of the surface atoms of the coating and entrapment of working gas atoms. This leads to distortions in crystal lattice and promotes compressive stress and strain within coatings. [71]

The unbalanced magnetron was developed in late 1980s to overcome this problem and it can be consider in two major types, both introduced by Window and Savvides. [72-75]

In the Type-1 configuration the central pole of the magnets is strengthened relative to the outer ring. In this case, the field lines are directed towards the chamber walls, charged particles are lost to ground and the plasma density in the substrate region is low. It results in low ion currents at the substrate, insufficient to modify the structure of the growing film, so consequently this design is not commonly used.

The Type-2 of unbalanced magnetron sputtering design has the outer pole of magnets strengthened relative to the central pole. In this case, most of the field lines are closed between the central and outer poles of the magnetron, but some of them are directed towards the substrate. The secondary electrons emitted from the target are able to follow those lines, which results in dense plasma flowing out towards the substrate. [70] Consequently, high substrate ion currents, which can densify the coating structure, can be extracted from the plasma. Typical ion currents for such arrangement are up to 10 mA/cm^2, which is an order of magnitude higher than for a balanced magnetron. [65-66] The ion current drawn at the substrate and deposition rate are directly proportional to the target current. As a result, the ion-to-atom arrival ratio at the substrate remains virtually constant with increasing deposition rate. [70] The ion flux configuration depends on magnetic field configuration, discharge current and substrate bias. [65]

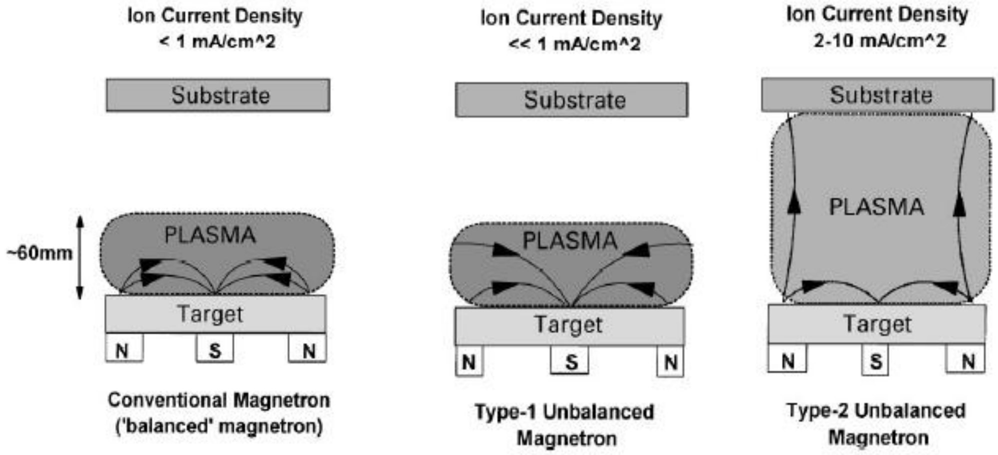

Figure 4.9: Schematic configuration of plasma in a 'conventional' or 'balanced' magnetron and in Type-1 and Type-2 unbalanced magnetrons, respectively. [70]

In multiple magnetron systems neighbouring magnetrons can have the same magnetic configuration or the opposite configuration. The former design is described as “mirrored” and in this case the field lines are directed towards the chamber walls, which causes a low plasma density at the substrate as secondary electrons which follow those lines and are lost to the chamber walls. [70]

In the latter case, the design is referred to as "closed field" unbalanced magnetron sputtering. In this case the field lines link across the chamber, preventing losses to the walls, confining a dense plasma to the substrate region, and ensuring high levels of ion bombardment of the growing film. Figure 4.10 shows schematically the field lines in both dual mode magnetrons.

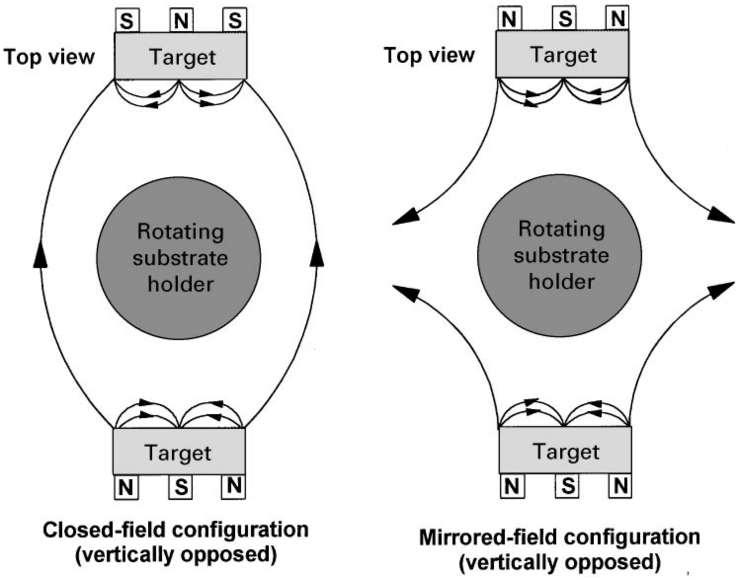

Figure 4.10: Dual unbalanced magnetron configuration. [70]

4.5.2 Reactive Magnetron Sputtering

The majority of commercially useful coating materials are compounds (oxides or nitrides), rather than pure metals or alloys. Compounds can be produced by radio frequency (RF) sputtering from a compound insulating target or by reactive sputtering from a metallic target. The latter technique has received a lot of attention mainly because of the relatively high sputtering rate, controlled deposition and ability to use DC power instead of RF power. [69] Reactive sputtering can be considered as the sputtering of elemental targets in the presence of chemically reactive gases that mass reacts with ejected target material and the target surface. [76] Reactive sputtering is commonly used for the deposition of oxide and nitride thin films. The principle of reactive sputter deposition is a chemical reaction between "metal" atoms ejected from a target surface and reactive gas molecules introduced into the system (i.e. O_2 or N_2). As a result of this reaction, the film created on the substrate surface is an either an oxide or a nitride.

4.5.2.1 Hysteresis Behaviour

A typical system would be operated with some partial pressure of an inert gas, such as argon, and a partial pressure of a reactive species, like O_2 or N_2. The operation of this system may be described by observing the changes in the plasma kinetics and the vacuum system, as a function of the partial pressure or a flow rate of reactive gas. [67] In Figure 4.11, the discharge voltage is plotted as a function of reactive gas flow rate. There is a constant inert gas pressure in the range of a few mTorr of Ar (~0.1 Pa).

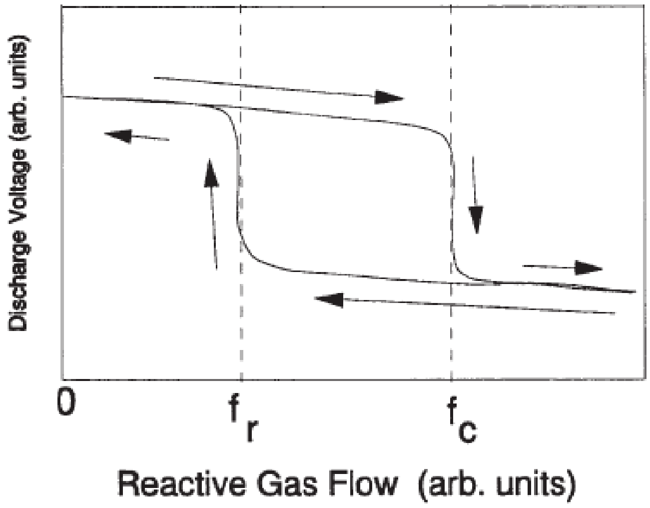

Figure 4.11: The discharge voltage as a function of reactive gas flow; f_c represents critical flow point and f_r transition point on the reversed curve. [69]

On the left side of the graph, the cathode is being sputtered with pure Ar, so the deposited films are purely metallic. During the deposition of oxide coating, as the reactive gas flow increases, the film is being partially oxidized and forms “sub-oxides”. Firstly, the target coverage with a reactive gas is very little, as the bombarding flux keeps the eroded part of the target clear of dielectric deposit. Any un-reacted oxygen is pumped away by an external pump. [65] Eventually, after further increases of reactive gas, the point will be reached where the fully stoichiometric (or very close to stoichiometric) oxide is formed. This is called the critical flow point (f_c) and it is highly unstable. Any additional increase of reactive gas will cause the film to become saturated with oxygen/nitrogen. The excess of reactive gas will result in complete coverage of the target surface with a layer of the compound material. This is the second critical point and it tends to reduce the deposition rate significantly as compounds sputter at a lower rate than metals (often significantly lower). Also, the discharge voltage usually changes significantly at this point (it can increase or decrease depending on the relative secondary electron coefficients of the metal target and its compound). [69] The best conditions to create fully reacted films, is deposition at the knee of the curve. This gives high deposition rates, while stoichiometric dielectrics are being deposited, but is a highly unstable condition and requires the use of process control systems if it is to be maintained during the deposition process. If the reactive gas flow rate is reduced after this transition the system does not cover back at the same flow, creating irreversible curve (hysteresis). This is due to the excess of a reactive gas on the target surface, which needs a sufficient time to be cleared of. Transition point on the reversed curve (f_r) is reached when the cathode is clear again and system converts back to a metallic mode. [69]

4.5.2.2 Reactive Sputtering Controlling System

To monitor parameters within the system and achieve stable deposition conditions, the feedback control of reactive gas flow is used. Monitored parameters are usually target voltage or chamber pressure. The reactive gas flow is also controlled to try to operate at the knee of the hysteresis curve. One of the most successful control systems in use is the optical emission monitor (OEM). A fibre optic cable is introduced into the chamber such that it can view the dense plasma in front of the target. The cable is connected to a monochromator box which is set to the appropriate wavelength in the emission spectrum of the target metal, e.g. in case of reactively sputtering titanium, the line is 507 nm. The Reactaflo (Megatech Ltd.) readout box gives information about the strength of the selected emission line, which is related in this case to the amount of the sputtered titanium in the plasma. The target is initially sputtered in argon only atmosphere and the readout is set to 1000 arbitrary units for convenience. This is referred to as the 100 % metal signal and subsequent reactive gas flow rates are set in relation to this figure. The Reactaflo is connected to the piezo valve (MV-112, Max Tech Inc.), which introduces the reactive gas to the system. The Reactaflo allows oxygen into the chamber until the OEM signal falls to a pre-determined proportion of the 100% metal signal. This value is referred to as the ‘turn-down’ signal and is usually determined empirically. The turn-down signal is then maintained at this value via a feedback control mechanism. Figure 4.12 shows the schematic system connection.

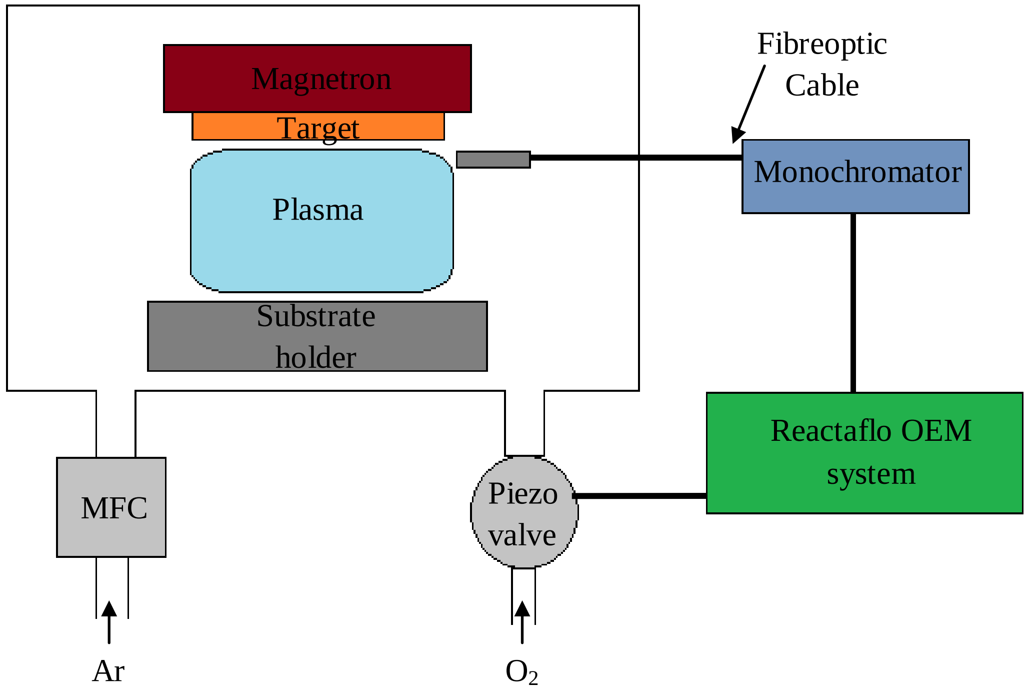

Figure 4.12: Diagram represents OEM layout system.

4.5.3 Pulsed Magnetron Sputtering

Pulsed DC magnetron sputtering was introduced in early 1990s to overcome problems associated with DC reactive sputtering of dielectric materials, such as arc formation. During pulsed sputtering the target potential is periodically switched either to ground (unipolar mode) or to a positive potential (bipolar mode) at frequencies in the range 20-350 kHz. The optimal frequency of pulsing, pulse duration and relative pulse heights depends on the target material. The most common mode of operation is an asymmetric bipolar mode where, during the pulse-off phase, the voltage is reversed to a magnitude equivalent to approximately 10% of the average voltage during the pulse-on phase. The asymmetrical bipolar mode can also be used in the dual magnetron sputtering configuration, where each of the magnetrons is driven at the same frequency and duty (always 50%) but are alternately biased positively and negatively. This approach helps to overcome the ‘disappearing anode’ effect whereby the chamber walls become coated with dielectric material, which results in the plasma and therefore deposition parameters drifting with time. [24, 77] Typical voltage and current waveforms for the asymmetric bipolar mode are shown in Figure 4.13. [77] In the pulsed DC frequency range ions and electrons can follow the cyclic potential changes at the target and in the plasma. Therefore during the 'pulse-on' phase an ion current flow towards target and the target is sputtered in normal manner, moreover the poisoned region on it may also charge up during the 'pulse-on' time. During the 'pulse-off' phase an electron current is drawn to the target surface that can discharge the poisoned regions before breakdown and arc formation.

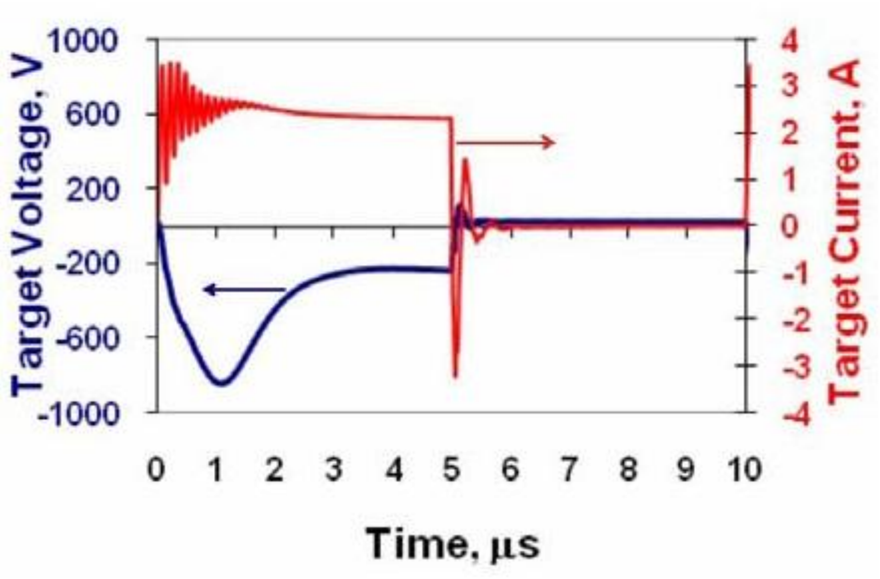

Figure 4.13: Current and voltage waveforms taken from the Advanced Energy Pinnacle Plus power supply operating in pulsed DC mode at 100 kHz pulse frequency, 50% duty.

Another important aspect in pulsed DC mode is a positive voltage overshoot at the beginning of the off phase. In this very short time (<250 ns) the target potential can reach several hundred volts, but the plasma potential will still remain above this value. This phenomenon has important impact on ion energy distribution functions (IEDF), which has been described in detail by Kelly *et al*. [77]

5. Thin Films

A thin film is defined as a low dimensional material produced by condensing, one-by-one, atomic/molecular/ionic species of material. The thickness is usually less than several microns. [67] Thin films have been used to make electronic devices, optical coatings, instrument hard coatings and decorative parts and many more.

The film growth and nucleation mode determines film proprieties such as density, surface area, and morphology and grain size. [67] Important aspects to the film growth are substrate surface roughness, surface temperature, adatom mobility and reaction, and mass transport during deposition such as void agglomeration and segregation effects. Basic film properties are controlled by parameters, such as film thickness, and microstructure and crystal structure and orientation. [67]

5.1 Initial Growth

Thin film deposition processes involve three main steps: production of appropriate molecules, ions or atoms; transport of those species onto the substrate surface and condensation on the substrate surface.

The sputtering process is responsible for the production of ions/atoms in an inert gas atmosphere. The sputtered species have energies ranging from 1-40 eV. In transporting species onto the substrate surface, gas pressure has a large impact as it affects the energy of the molecules arriving at the substrate surface. At higher pressure the mean free path for the travelling ions/atoms is smaller, which results in higher collision rates between molecules. Those collisions cause scattering and so reduce the particles' energy. The main factors which affect film growth on the substrate surface are the energy of the atoms/ions arriving on the substrate surface and substrate temperature. Film composition, adhesion, stress and structure depend on concurrent bombardment by energetic ions/atoms. [24, 67]

The film growth and nucleation mode determines film proprieties such as density, surface area, and morphology and grain size. [69] Condensation from the vapour phase involves incident atoms becoming bonded adatoms which diffuse over the film surface until they desorbs, or more likely are trapped at low energy lattice sites. Incorporated atoms reach their equilibrium position in the lattice by back diffusion motion. This atomic odyssey involves four basic processes: shadowing, surface diffusion, bulk diffusion and desorption. [66]

Areas, where the film grows faster shadow neighbouring slower growing areas and hence will expand and further starve the slow growing areas of the additional atoms. This results in columnar growth. The surface becomes textured and rough giving a matt surface. Columnar growth is mostly associated with thick films, as films below 1μm do not show many of the features seen in thicker films. [78]

When an atom arrives on the surface it may either stay where it is or move around the surface. This process is known as surface diffusion, and is determined by the energy of the arriving atom. The atom continues to move around the surface until it reaches the position which minimizes the total energy. As more atoms arrive they undergo a similar process but some connect with those adatoms already existing on the substrate surface and the size of the nucleated particle will grow. [78]

Coatings are formed by nucleation and growth processes. Three main forms of growth can be distinguished: island growth (Volmer-Weber type), layer growth (Frank-van der Merwe type) and mixed or Stranski-Krastanov growth. [66]

When the smallest stable clusters nucleate on the substrate and grow in three dimensions to form islands, this process it is referred to Volmer-Weber mechanism (island growth). This process occurs when atoms or molecules in the deposit are more strongly bound to each other than to the substrate. An example of island growth is metals and semiconductors deposited onto oxides. [66] The Van der Merwe mechanism describes the method where the atoms cover the whole surface before a second layer is grown. In this case atoms are more strongly bound to the substrate than to each other, which results in the creation of a less tightly bound second layer on the top of the first one. The other growth process is an intermediate combination of these two by first covering the surface by one or more monolayers, and then growing islands. This process is referred to as the Stranski- Krastanov (S-K) mechanism. [66, 78] Film growth by S-K mode is common and has been observed in metal-metal and metal-semiconductor systems. [66] The schematic pictures of three growing mechanisms can be seen below in Figure 5.1.

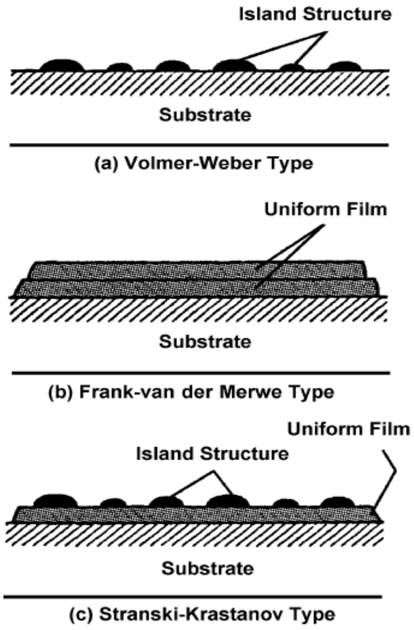

Figure 5.1: Schematic representation of different film growing techniques. [67]

5.2 Film Structure

This film growth and the nucleation mode determine many film properties such as film density, surface area, surface morphology and grain size. The microstructure and topography of a thin film depend on the kinetics of the growth and hence on the substrate temperature, the source of energy of impurity species, the chemical nature, the topography of the surface and gas ambient. These influence such features as surface mobility, kinetic energy of the molecules, deposition rate, and super-saturations of the vapour pressure to solution concentration, the condensation and the level of impurities. [24]

One very important aspect in thin film technology nowadays is the ability to control the crystallinity, grain size and morphology during the growth of the film. Surface morphology may vary from a very smooth, glassy-like structure to a very rough in many materials. In general surface roughness increases during film growth due to differences in growth between crystallographic planes or other features. Morphology is determined by surface roughness and the surface mobility of depositing atoms. Roughness increases while impinging species are incident at oblique angles instead of falling normally at the substrate. This happens due to the shadowing effect of the adjacent column being orientated towards the direction of the incident species. When the surface is rough the adatom flux hits the substrate from all directions, and if mobility is low then peaks grow faster than valleys, causing the shadowing effect. [24] When the nucleation barrier is high and super-saturation is low, then only a few nuclei are formed on the substrate surface. This results in coarse grained rough surface film creation, which becomes continuous at relatively large thickness. Due to high surface mobility the concavities are filled in, which increases the surface smoothness. [67]

When super-saturation decreases, grain size and surface mobility of the absorbed species are expected to increase. This results in well defined large grains formation at high substrate and source temperature (high mobility). Moreover, by increasing the kinetic energy of the incident atoms, surface mobility increases. Although at sufficiently high kinetic energy surface mobility may be reduced due to penetration of the incident species into the substrate. This causes smaller grain sizes, however the effect is more commonly seen in the systems with high substrate temperature and in relatively thick films. Post-deposition annealing at temperatures higher than the depositing temperature has a great impact on grain formation and size changes. Higher temperatures promote formation of larger grains causing re-crystallisation and sometimes abnormal grain growth. Grain growth is a diffusion related process that is thermally activated. Therefore higher annealing temperatures promote thermal diffusion of the condensed atoms in thin films. Finally grain sizes increase when film thickness increases under given deposition conditions for a given material-substrate combination. In thicker films re-nucleation takes place at the surface of previously grown grains, and each column grows multi-granularly causing possible deviations from normal growth. [67]

One of the ways to control the growth of the film is by changing the operating pressure. If pressure increases to the point where mean free path for elastic collisions between sputtering gas and sputtered atoms becomes much less than the source-substrate distance, the oblique component of the deposition flux increases due to gas phase scattering, which increases atomic shadowing at the substrate and encourages the formation of porous columnar coatings. A reduction in pressure increases energetic particle bombardment which results in denser film structures. [66]

During the deposition process, while atoms land on the substrate surface, they transfer the energy into the substrate causing a rise in the substrate temperature. Increasing substrate temperature will allow atoms to diffuse further and faster across the surface in search of the lowest energy nucleation site. It leads to fewer nucleation sites and to larger crystals in the final thin film. [78]

5.3 Structure Zone Models of Growth

The idea of describing coatings in terms of a structure zone model (SZM) was first applied by Movchan and Demchishin in 1969 for very thick films deposited by the vacuum evaporation process. [79] The model is schematically represented in Figure 5.2. In this case the only parameter considered was homologous temperature T_h (in Kelvin), defined as the film growth temperature divided by the melting point temperature of the deposited material:

$$\boldsymbol{T_h = {}^{T}/_{T_m}} \qquad \text{Equation 19}$$

Movchan and Demchishin concluded that the structures formed could be divided into three zones. In zone 1 at $T_h<0.3$, the atom mobility is low, which causes continuous nucleation of grains, and therefore formation of porous films with fine grained structure of textured and fibrous grains. Those grains point in the direction of the arriving vapour flux and ending with domed tops. [80] Zone 2 occurs at higher temperatures $0.3<T_h<0.5$. This time surface diffusion takes place leading to uniform columnar grains and the creation of a faceted film surface. The grain size increases with homologous temperature and may extend all the way through the film thickness. At even higher temperatures, $T_h>0.5$ bulk diffusion and crystallisation takes place leading to dense films with large grains reminiscent of bulk materials. [80]

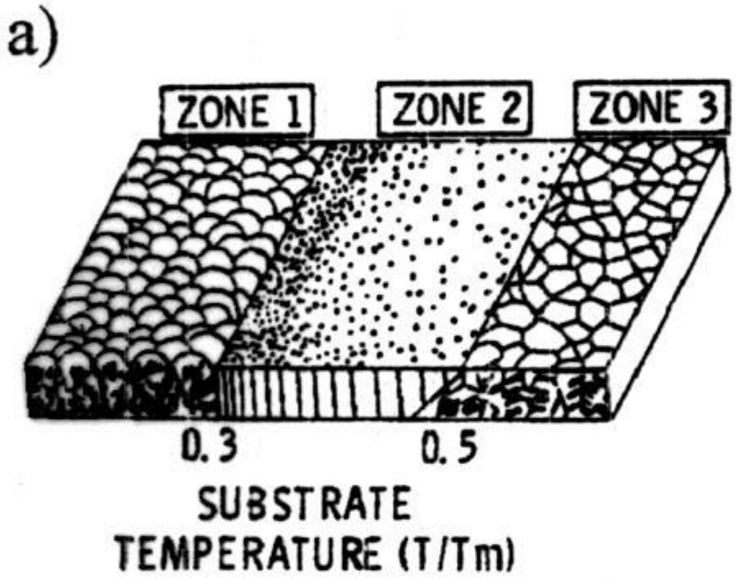

Figure 5.2: Schematic representation of structure zone model for vacuum evaporation processes introduced by Movchan and Demchishin. [79]

Thornton extended the original structure zone model to describe the structures of magnetron sputtered coatings. [81] This model describes sputtered coating structures in terms of temperature and pressure. The Thornton model is based on morphological development in 20-250 µm thick sputtered coatings of Ti, Cr, Fe, Cu, Mo, Al deposited at rates from 5-2000 nm/min. [66] The SZM consists of four structures: Zone 1, 2, 3 and Zone T.

Zone 1 (more open film structures) appears in amorphous and crystalline coatings and results from shadowing effects which overcome limited adatom surface diffusion at low temperatures and high pressures. This morphology produces coatings with a high surface area and with a columnar film surface appearance. [24, 66] Zone 2 results from surface diffusion, which indicates controlled growth. Surface diffusion allows the densification of the inter-columnar boundaries; however the basic columnar morphology remains. In zone 2 the grain size increases and the surface features tend to be faceted. [24] In Zone 3 lattice and grain boundary diffusion processes dominate at the highest substrate temperatures allowing re-crystallisation, grain growth and densification. Often a highly modified columnar morphology is detectable, with the columns being single crystals of material. Zone T, where the columns consist of single crystals of material forming dense array of poorly defined fibrous grains, may be considered as a transition region between Zones 1 and 2 in Figure 5.3 below. [66] The formation of the Zone T material is due to the energetic bombardment from reflected high energy neutrals from the sputtering target at low gas pressures. These energetic neutrals erode the peaks and fill-in the valleys to some extent. [24]

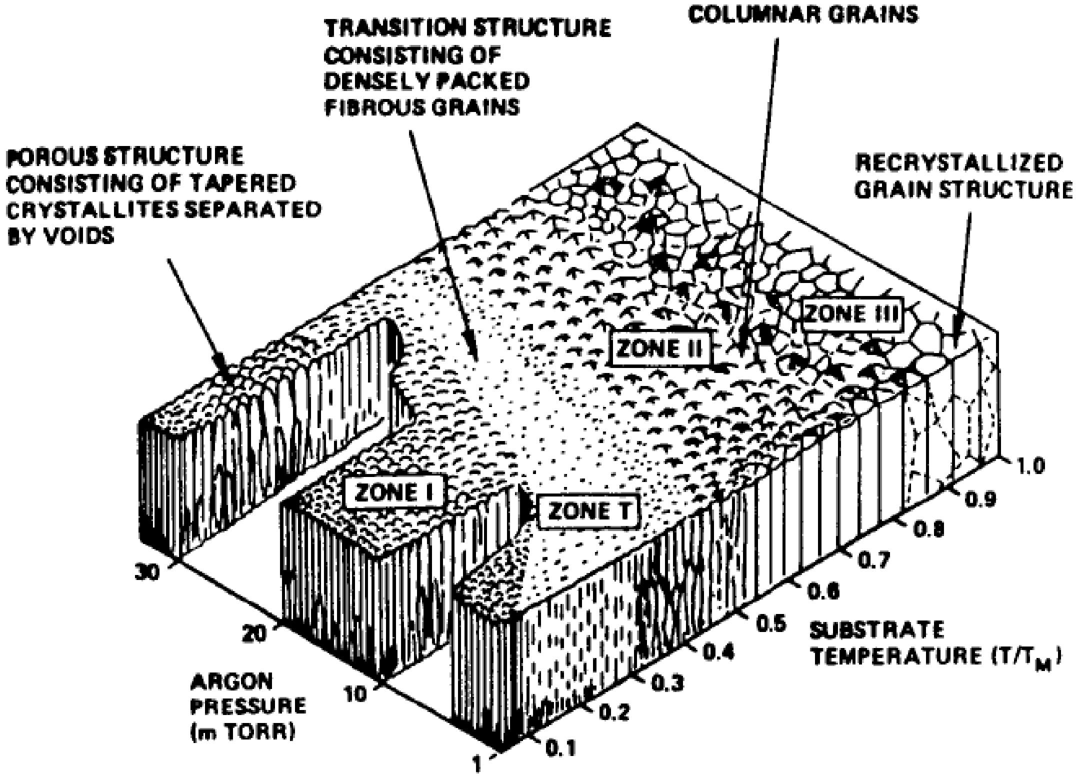

Figure 5.3: Schematic representation of structure zone model relating to magnetron sputter deposited films, introduced by Thornton. [24]

As the magnetron sputtering technique has been developed throughout the years further expansion of the Thornton zone model was needed. Coating deposition using “modern” sputtering techniques such as high power impulse magnetron sputtering (HIPIMS), which is a pulse sputtering technique where the peak power exceeds the time-average power by typically two orders of magnitude (~10^7 W/m^2). In this plasma conditions, it is likely for sputtered atoms to undergo ionisation, therefore the film is bombarded by large ion fluxes, which has forced the structure zone models to be considered as a rough generalisation and not an adequate representation for unique systems. [82]

In the 1990s Kelly *et al.* introduced a structure zone model that represents the structure of thin films deposited by the closed field unbalanced magnetron sputtering (CFUBMS) technique (see Figure 5.4). [70] In these model parameters such as homologous temperature T/T_m, bias voltage at the substrate (represents ion energy) and ion to atom ratio J_i/J_n (to represent ion flux) were considered. This structure zone model points out that films deposited by CFUBMS represent fully dense columnar structures at relatively low homologous temperatures, compared to other PVD processes (Zone 3 at temperature of 0.43, Zone 2 at 0.13).

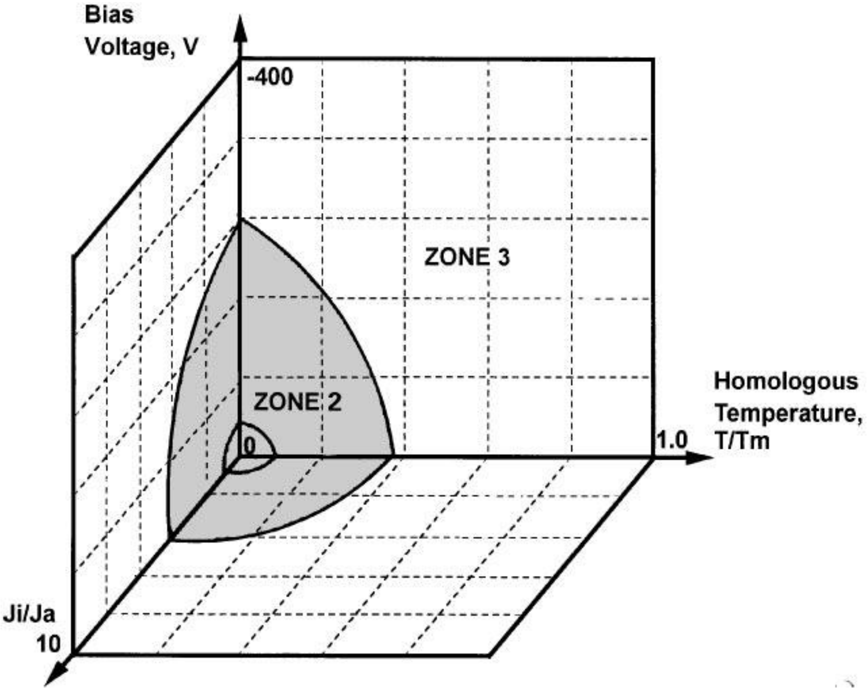

Figure 5.4: Schematic representation of structure zone model relating to closed field unbalanced magnetron sputter deposited films, introduced by Kelly *et al.* [70]

Recently Anders introduced a further expansion of the SZM by including plasma and ion effects on film growths. [80] He has pointed out than many other parameters such as target current, voltage, pressure, pulse frequency (if pulsed), substrate distance from the target will affect film growth processes. Therefore he proposed to extend and modify the Thornton SZM by replacing the linear T_h axis with a generalised temperature T^*, which consists of homologous temperature increased by a temperature shift caused by the potential energy of particles arriving on the surface. He replaced the linear pressure axis with a logarithmic axis for a normalised energy E^*, which describes displacement and heating effects caused by the kinetic energy of bombarding particles. Also, an unlabeled *z*-axis was introduced to represent a net film thickness t^* that will allow the familiar qualitative illustration of film structure to be maintained, while indicating thickness reduction by densification and sputtering. That also allows including ‘negative thickness' i.e. ion etching. [80] A schematic representation of this extended SZM diagram is presented in Figure 5.5.

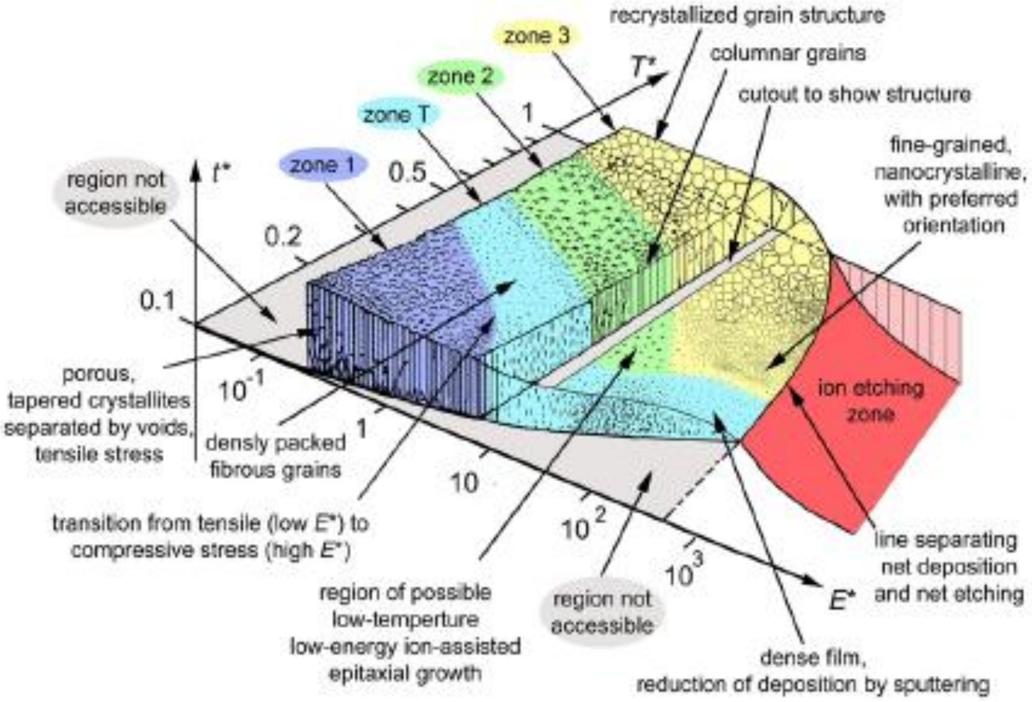

Figure 5.5: Structure zone diagram applicable to energetic deposition, where T^* is the generalized temperature, E^* is normalized energy flux and t^* represents the net thickness. [80]

6. Diffusion

Diffusion by definition “is a process by which matter is transported from one part of a system to another as a result of random molecular motions”. [83] In this chapter the physical process of diffusion, its laws, mechanisms and mathematical solutions for diffusion in thin films are explained.

6.1 History of Diffusion

The science of diffusion has it beginnings in 19th century when Thomas Graham was developing the first diffusion theories. He established that under similar conditions of temperature and pressure, the rates of diffusion of gasses are inversely proportional to the square root of their densities and depends on concentration difference:

$$\boldsymbol{Rate\ of\ diffusion} \propto \sqrt{\frac{\mathbf{1}}{\boldsymbol{Density}}} \qquad \text{Equation 20}$$

The rate of diffusion is equal to the volume of the gas, which diffuses per unit of time [84]:

$$\boldsymbol{Rate\ of\ diffusion} = \frac{\boldsymbol{Volume\ of\ the\ gas\ diffused}}{\boldsymbol{Time\ taken\ for\ diffusion}} \qquad \text{Equation 21}$$

Furthermore he established that at longer intervals of time the diffusion process decreases, and that the diffusion rates in liquids are much slower than in gases. [84]

The next important discovery in the theory of diffusion made Adolf Fick, who was interested in the movement of water confined by membranes in organic life. This work titled “Uber Diffusion” was published in 1855. [84] Albert Einstein based his Brownian motion in liquids theory on basics provided by Fick. [85]

Diffusion in solids was recognized in 1896 by W. C. Roberts-Austen, who reported the first diffusion measurement of gold in lead metal. [84]

Surface diffusion is one of the most important events in crystal and thin film growth, phase transformation, surface reactions, catalysis, condensation and evaporation phenomena and in all sorts of surface processes. [86] In 1918 Hamburger *et al.*

published work on films deposited in vacuum, and described the mobility of silver particles on a surface, which allows them to collide with other atoms to form crystallites. Only few years later in 1921 the importance of diffusion was recognized by Volmer and Estermann, who examined condensation of mercury on glass. They discovered that at relatively low temperatures molecules absorbed on the surface are able to migrate over it. In 1922 Volmer published his work about thin film growth which discussed surface diffusion of molecules adsorbed on a crystal. [86]

Nowadays diffusion is considered in all three states of matter. In materials of technological interest, diffusion has a great impact in their design, fabrication and performance. Diffusion research is full of examples from industry, such as sintering, power generation, lighting, metal forming, aviation, space, information technology and many more. [84]

Due to the broad diffusion field it is impossible to mention it in all scientific disciplines, however throughout the past hundred years many findings were published in the literature. [84, 87-91]

6.2 Diffusion in Thin Films

Diffusion in polycrystalline films occurs much faster than in bulk samples. This is caused by the physical proprieties of thin films, which may contain a high density of defects such as dislocations, vacancies and grain boundaries that can act as pathways for diffusion processes. [4] Also the mechanism of diffusion in thin films is different to that of bulk samples. In thin films, diffusion can occur through grains or along the grain boundaries, depending upon the microstructure of the film. In films with large grains, diffusion generally occurs through the grains and analysis of the process gives the lattice diffusion coefficients. As the grain size decreases, atomic transport occurs along the grain boundaries as well, and analysis yields grain boundary diffusion parameters. [11] Moreover diffusion must depend on the depth as size effects are associated with the influence of the surface. Thin film diffusion size effects are based on the fact that the mean square displacement of atoms in the neighbourhood of the surface is higher than for bulk, so the diffusion in the vicinity of grain boundaries must proceed more rapidly than in the bulk. [92]

Diffusion flux is a product of the density of the mobile defects, the diffusivity defects and the driving force. For thin films, flux divergence, which leads to localized depletion or accumulation of mobile defects, is usually related to the microstructure. The most common features are grain boundary junctions, a transient region which separates two areas of different grain sizes, the interface of two layers of different materials, and a surface exposed to a chemical environment which can react with one of the species in the film. [93]

As thin films are very sensitive to even the smallest changes in their impurity concentrations, diffusion may entail large differences in electrical conductivity, corrosion resistance or the optical proprieties of a film. [8] Hence the importance of studying diffusion processes in thin film systems. Techniques used to analyse diffusion include Auger depth profiling, X-ray photoelectron spectroscopy (XPS), energy-dispersive X-ray spectroscopy (EDS), X-ray diffraction (XRD) and secondary ion mass spectrometry (SIMS), Rutherford backscattering spectroscopy (RBS) and transmission electron microscopy (TEM). [4, 8, 11, 92-93]

6.3 Flux Equation-Fick's First Law

If an inhomogeneous single-phase alloy is annealed, species will flow and the concentration gradients will decrease. If the annealing time is long enough, the specimen will become homogeneous and the net flow of matter will stop. [91] Fick's first law defines the diffusion coefficient (D_l) of the component l and flux in an inhomogeneous single-phase binary alloy due to concentration gradient as:

$$\boldsymbol{J}(\boldsymbol{l}) = -\boldsymbol{D}(\boldsymbol{l})\left(\frac{\partial \boldsymbol{C}(\boldsymbol{l})}{\partial \boldsymbol{x}}\right) + \boldsymbol{C}(\boldsymbol{l})\boldsymbol{\nu}(\boldsymbol{l}) \qquad \text{Equation 22}$$

Where $J(l)$ is the flux at time t of atoms of the component l, $C(l)$ is its concentration, ν is the velocity of mass that moves due to the application of forces such as electromigration or a thermal or chemical potential gradient, and x is the distance into the sample taken parallel to the concentration gradient.

Thompson *et al.* studied the diffusion of Ni in Si [94] by defining a concentration of the diffusant at the entrance and exit surface of the sample separated by distance x in steady-state conditions. The diffusivity can be measured by monitoring the flux in the absence of a driving force. The measurements of the flux do not give any information about the distribution of the diffusant in the sample, microstructure and chemistry of the specimen or the path of diffusion. Fick's law can be expressed by measuring the diffusion coefficient in the absence of external forces, including chemical gradient, by isotope techniques, such as mass spectroscopy. Such measurements are defined as self-diffusion and in general are denoted by an asterisk or the isotope used. [84] In the case of diffusion due to a chemical gradient, the diffusion coefficient is affected by the motion of an atomic species and in consequence is defined as the interdiffusion coefficient $\widetilde{D}$. Fick's law will then reduce to:

$$\boldsymbol{J} = -\widetilde{\boldsymbol{D}}\left(\frac{\partial \boldsymbol{C}}{\partial \boldsymbol{x}}\right)_{\boldsymbol{T}} \qquad \text{Equation 23}$$

This equation fits the empirical fact that the flux goes to zero when the specimen becomes homogeneous, that is when the specimen reaches equilibrium. In this equation the flux across a given plane is proportional to the concentration gradient across that plane. [91]

Over the years many experiments were performed in order to prove the application of Fick's equation. Smith, for example placed a hollow cylinder of iron in the isothermal part of the furnace and passed a carburising gas through the inside of the cylinder, and decarburising gas over the outside. When the carbon concentration at each point in the cylinder no longer changes with time ($\frac{\partial \boldsymbol{C}}{\partial \boldsymbol{t}} = \boldsymbol{0}$), the quantity of carbon that passes through the cylinder per unit time ($\boldsymbol{q}/\boldsymbol{t}$) is a constant. Since J is determined as the flow per unit area it is a function of the radius described as: $\boldsymbol{J} = \frac{\boldsymbol{q}}{\boldsymbol{2\pi r l t}}$, where l is the length of the cylinder. Plotting gas concentration versus lnr, the diffusion coefficient should be found (see Equation 22). [91] Similar experiments have frequently been performed by passing a gas through a membrane. The experimental results consisted of measuring the steady-state flux, the pressure drop across the membrane and the thickness of the membrane, as it was impossible to determine a concentration as a function of distance in so thin membrane by chemical analysis. [91]

In three dimensional vector notations the general statement of Fick's first law is:

$$\boldsymbol{J} = -\widetilde{\boldsymbol{D}}\nabla\boldsymbol{C} \qquad \text{Equation 24}$$

6.4 Diffusion Equation-Fick's Second Law

Fick's second law, in general, is the basis of most diffusion measurements in solids. It has been widely used in samples of rod, plate and thin layer geometry, to give measurements of diffusion in single crystal specimens and along grain boundary dislocations. Fick's second law describes diffusion in non steady-state conditions, when the concentration changes with time but particles are neither created nor destroyed. It can be assigned by combining Fick's first law equation in three dimensional vectors with the continuity equation:

$$\frac{\partial \boldsymbol{C}}{\partial \boldsymbol{t}} = -\boldsymbol{\nabla J} \qquad \text{Equation 25}$$

In steady-state solution, for linear flow and constant D, Fick's second law can be written as [93]:

$$\frac{\partial \boldsymbol{C}}{\partial \boldsymbol{t}} = \boldsymbol{D\nabla^2}\mathbf{C} \qquad \text{Equation 26}$$

Where $\boldsymbol{\nabla^2 C}$ is called the Laplacian of C, and its representation in different systems can be found in Crank's book. [83] In a steady state $\boldsymbol{\partial C / \partial t = 0}$, and the problem is being reduced to solving the following equation:

$$\boldsymbol{D\nabla^2 C = 0} \qquad \text{Equation 27}$$

In non-steady-state the solution, for variable D, which is not a function of composition Fick's second law, is written as:

$$\frac{\partial \boldsymbol{C}}{\partial \boldsymbol{t}} = \frac{\partial}{\partial \boldsymbol{x}}\left(\boldsymbol{D}\frac{\partial \boldsymbol{C}}{\partial \boldsymbol{x}}\right) \qquad \text{Equation 28}$$

The concentration is determined as a function of position and time, that is, *c(x, t).* From the Equation 28, the constant D can be obtained by solving the error function, which will be described in more detail in the next chapters. Error function is used to describe D when the diffusion distance is relatively short, compared to the dimensions of the initial inhomogeneity. When complete homogenisation is approached, *c(x, t)* can be represented by the trigonometric series, but it will not be described in this work. [83]

6.5 The Analytical Solution to the Diffusion Equation

For the simple geometries the analytical solution to the diffusion equation can be found. In this work the one dimensional equation in semi-infinite couple, which will be described in the following chapters, as a solution to Fick's second law was solved. Other possible solutions of Fick's diffusion laws for the variety of geometries will not be described here, but can be found elsewhere. [83]

6.5.1 Gaussian Distribution in One Dimension

Equation 29 can be solved in the system in which the starting conditions are described by a layer of atom of a species in a plane at x=0 and zero concentration in the surrounding material. The total number of diffusing atoms per unit area in the internal layer represents a Gaussian distribution and equals A: [95]

$$\boldsymbol{c(x,t) = \frac{A}{2\sqrt{\pi D t}} \exp\left(-\frac{x^2}{4Dt}\right)} \qquad \text{Equation 29}$$

The total number of diffusing atoms can be also described as C_0l, where C_0 is the concentration in atoms/cm^3 in a layer that has a thickness l. In this case the Gaussian solution is only valid for $\sqrt{2D} \gg 1$. At the infinite concentration at x=0 that changes in time and concentration equals zero at x=+/-∞, and hence: [95]

$$\boldsymbol{\int_{-\infty}^{\infty} \exp\left(-\frac{x^2}{4Dt}\right) dx = 2\sqrt{\pi D t}} \qquad \text{Equation 30}$$

and:

$$\boldsymbol{\int_{-\infty}^{\infty} C(x,t)\, dx = A} \qquad \text{Equation 31}$$

Figure 6.1 represents concentration distribution as a function of distance, presented as initial concentration and the Gaussian profile at two subsequent times. When more diffusion occurs the C(x) curve broadens along the axis x. However since the total amount of solute in the sample is fixed, the area under the curve remains constant in time. In this case the distance is given by $x = \sqrt{2Dt}$. [91]

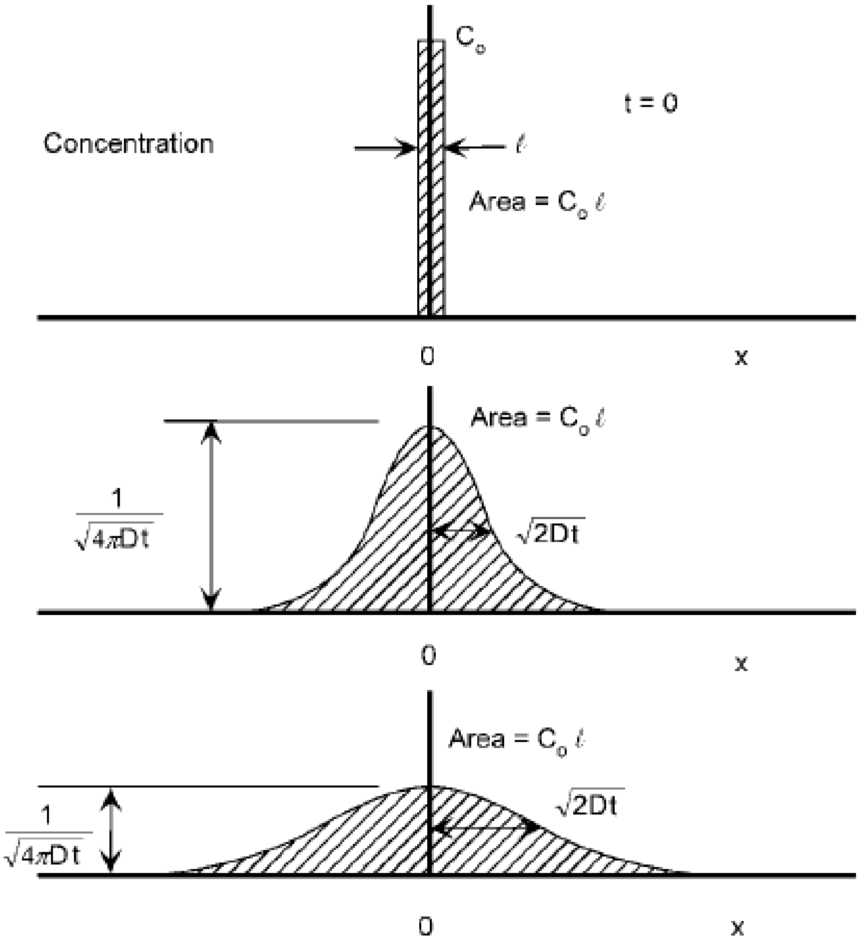

Figure 6.1: Gaussian diffusion profile (concentration-distance curve) for a plain source. The hatched areas show the dopant concentration which remains constant in time. [95]

Another example of the Gaussian concentration profile is when the thin layer is deposited on a substrate surface and all of the deposited material diffuses into the substrate. The total amount of the deposited material in the substrate stays constant. Figure 6.2 shows the Gaussian profile of the layer with a thickness l and composition C_0 atoms/cm^3.

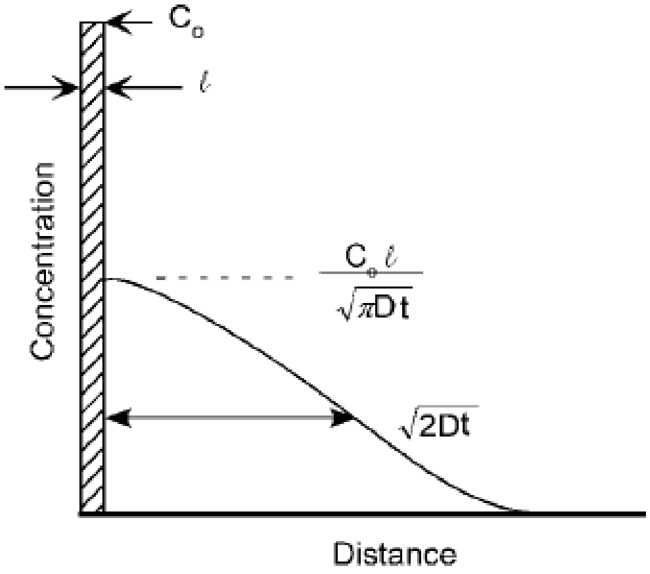

Figure 6.2: Gaussian profile of the thin layer deposited onto substrate surface after sufficient time. [95]

The concentration profile in the substrate is described as:

$$\boldsymbol{C(x,t) = \frac{C_0 l}{\sqrt{\pi D t}} \exp\left(-\frac{x^2}{4Dt}\right)} \qquad \text{Equation 32}$$

and since all of the deposited material diffuses into the substrate, the total amount of the material deposited onto the substrate surface (C_0l atoms/cm^3) is the total amount of the material in the diffusion profile:

$$\boldsymbol{\int_0^\infty \exp\left(-\frac{x^2}{4Dt}\right) dx = \sqrt{\pi D t}} \qquad \text{Equation 33}$$

This solution is valid for annealing drive-in diffusion, when the annealing time is long enough for the material to diffuse into the sample. The profile assumes that the diffusion coefficient is constant and there is no effect of clustering or variation in the density within the sample. [95]

6.5.2 Error Function: Semi-Infinite Couple Solution

The error function (*erf (z)*) concentration distribution gives a solution to the one-dimensional diffusion equation when the surface concentration stays constant. The solution is given by the complimentary error function (*erfc (z)*):

$$\boldsymbol{C = C_0 erfc \frac{x}{2\sqrt{Dt}}} \qquad \text{Equation 34}$$

where $erfc\ (z) = 1 - erf\ z$, and the $erf(z)$ is the integral of the Gaussian probability distribution function:

$$\mathbf{erf}\ \boldsymbol{z} = \frac{\mathbf{2}}{\sqrt{\boldsymbol{\pi}}}\int_{\mathbf{0}}^{\boldsymbol{z}} \mathbf{exp}(-\boldsymbol{\eta}^{\mathbf{2}})\, \boldsymbol{d\eta} \qquad \text{Equation 35}$$

Where $z = \frac{x}{2\sqrt{Dt}}$. [95]

Figure 6.3 shows the schematic representation of the *erf (z)* and the *erfc (z).*

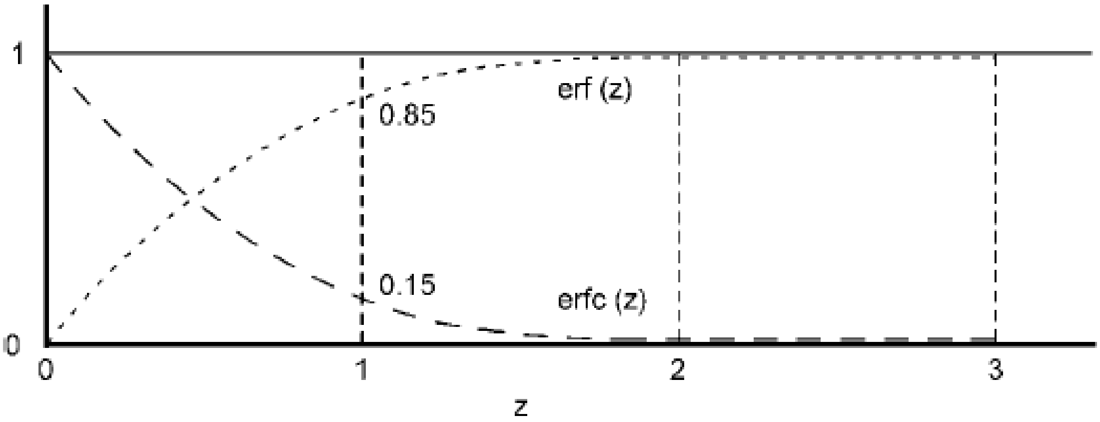

Figure 6.3: A scheme of error function and complimentary error function analytical solution. [95]

In the semi-infinite couple the distribution of two pure species A and B joined together without interdiffusion is represented. The diffusion problem in semi-infinite media was solved here using Laplace transformation (see Appendix 2). In semi-infinite medium x>0, whose surface is kept at a constant concentration C_0, and initially concentration C equals zero throughout the medium. The boundary conditions for this solution are as follows:

$$C = C_0, \qquad x = 0, \qquad t > 0$$

And the initial conditions are

$$C = 0, \quad x > 0, \quad t = 0$$

Fick's second diffusion law needs to be solved. By multiplying both sides of Equation 28 by $e^{-pt}$and integrating with respect to t from 0 to ∞ we obtained:

$$\int_0^\infty e^{-pt}\frac{\partial^2 C}{\partial x^2}dt - \frac{1}{D}\int_0^\infty e^{-pt}\frac{\partial C}{\partial t}dt = 0. \qquad \text{Equation 36}$$

By assuming that the orders of differentiation and integration can be interchanged, and this can be adjusted to the function we want to use then:

$$\int_0^\infty e^{-pt}\frac{\partial^2 C}{\partial x^2}dt = \frac{\partial^2}{\partial x^2}\int_0^\infty Ce^{-pt}dt = \frac{\partial^2 \overline{C}}{\partial x^2}. \qquad \text{Equation 37}$$

Moreover, integrating by parts gives:

$$\int_0^\infty e^{-pt}\frac{\partial C}{\partial x}dt = [Ce^{-pt}]_0^\infty + p\int_0^\infty Ce^{-pt}dt = p\overline{C}, \qquad \text{Equation 38}$$

The term in square brackets disappears at t=0 by virtue of the initial conditions and at t=∞ through the exponential factor, therefore Equation 28 is reduced to:

$$D\frac{\partial^2 \overline{C}}{\partial x^2} = p\overline{C}. \qquad \text{Equation 39}$$

Now considering the boundary conditions we see:

$$\overline{C} = \int_0^\infty C_0 e^{-pt}dt = \frac{C_0}{p}, \; x = 0. \qquad \text{Equation 40}$$

In Equation 40 $\bar{C}$ remains finite as x approaches infinity is:

$$\overline{C} = \frac{C_0}{p}e^{-qx}, \qquad \text{Equation 41}$$

Where $q^2 = p/D$. From Laplace transformation we know that the function given in Equation 41 is described by complimentary error function as shown in Equation 34.

The proprieties of the error function are as follow:

$$\mathbf{erf}(-z) = -\,\mathbf{erf}\,z, \qquad \mathbf{erf}(0) = 0, \qquad \mathbf{erf}(\infty) = 1, \qquad \text{Equation 42}$$

And hence:

$$\frac{2}{\sqrt{\pi}}\int_z^\infty \exp(-\eta^2)\,d\eta = \frac{2}{\sqrt{\pi}}\int_0^\infty \exp(-\eta^2)\,d\eta - \frac{2}{\sqrt{\pi}}\int_0^z \exp(-\eta^2)\,d\eta = 1 - \mathbf{erf}\,z = erfc\,z, \qquad \text{Equation 43}$$

Where $erfc\ z$ is the error function complement hence the diffusion equation is usually written as:

$$\boldsymbol{C(x,t)=\frac{C_0}{2}erfc\frac{x}{2\sqrt{Dt}}} \qquad \text{Equation 44}$$

Where C(x, t) is the concentration of the diffusing species at penetration distance x at time t, and C_0 is the original concentration in the solid. D is the diffusion coefficient of the diffusing species, and it is described in m^2/s. [11, 14, 83, 91]

Figure 6.4 shows the error function solution for a diffusion couple, where two different materials are joined at x=0.

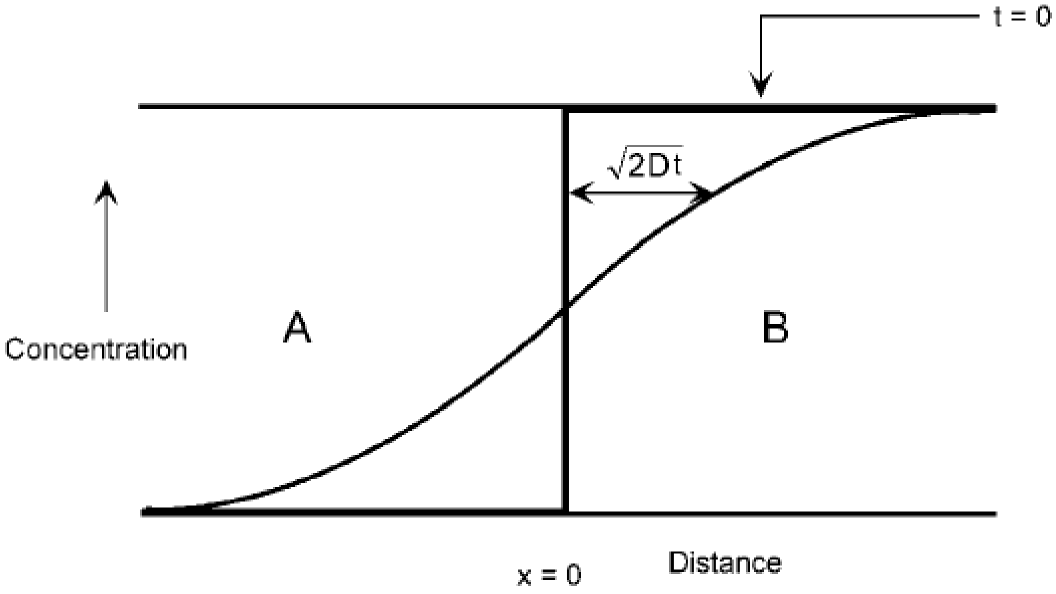

Figure 6.4: Diffusion profile for a diffusion couple, where the concentration at the interface is initially half way between the concentrations of either side. The concentration in each half of the couple is given by a complimentary error function starting at C=0.5 at x=0 and increasing to C=1 at x=−∞ and at x=∞ for A and B, respectively. [95]

6.6 Temperature Dependent Diffusion. Arrhenius Plot.

The temperature dependence of the diffusion coefficient D is described by the Arrhenius equation:

$$\boldsymbol{D = D_0 exp(-{}^{Q}/_{k_B T})} \qquad \text{Equation 45}$$

where D_0 is the temperature independent frequency factor, Q is the activation energy, k_B is the Boltzmann constant and T is the temperature in Kelvin. [84, 93] The Boltzmann constant gives the fraction of atoms (molecules) in the system, which has energy greater than Q at the temperature T. Therefore the diffusion rate depends on the frequency factor, which in turns depends on geometric details of the path and the atom density multiplied by the number of atoms that have enough energy to diffuse through the material. [95] The D_0 and Q values are dependent on diffusing and host species therefore are different for every solute or solvent pair.

By taking natural logarithm of both sides of Equation 45 the formula will become:

$$\boldsymbol{lnD = lnD_0 - {}^{Q}/_{k_B T}} \qquad \text{Equation 46}$$

Hence plotting lnD as a function of reciprocal temperature a linear graph should be obtained, where the gradient represents $-{}^{Q}/_{k_B}$. Figure 6.5 shows an example of an Arrhenius plot, which represents a straight line with negative gradient suggesting that the diffusion process in this case has a single activation energy Q over the range of measurements. In the case when the slope changes, or becomes a discontinuous curve, this would suggest that the mechanism controlling the rate has changed. [95]

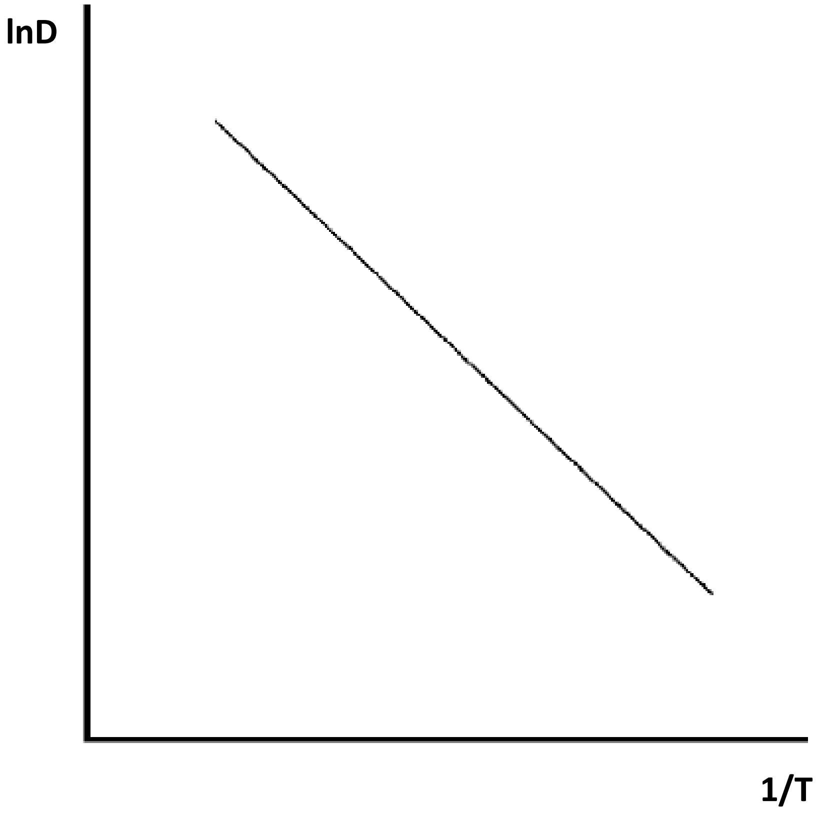

Figure 6.5: An example of the Arrhenius plot. [95]

6.7 Diffusion Mechanisms

Atoms in a crystal oscillate around their equilibrium positions, however sometimes these oscillations become large enough to allow an atom to change position. These jumps from one lattice site to another are responsible for diffusion in crystalline solids. [91] The main possible diffusion mechanisms considered for atoms in single crystals presented in Figure 6.6 are as follows:

Interchange and ring mechanism. The diffusive motion in this mechanism takes place through a correlated rotation of two or more atoms about a common centre without causing a defect. It has been found energetically unfavourable in most solids. [84]

The second type is the interstitial mechanism, where small atoms can pass from one interstitial site to its nearest-neighbour interstitial sites without permanently displacing any of larger matrix atoms. [91] Usually gas atoms such as O, N, H and C diffuse easily in the open lattices of bcc metals, like Fe, Ta, W and Mo. If a relatively large atom, such as a matrix atom gets into an interstitial position it will cause a very large distortion when it jumps from one interstitial site to a neighbouring interstitial site. This mechanism may cause displacement of a neighbouring atom to an interstitial position, which is called an interstitialcy or kick out mechanism. [84] The Crowdion mechanism occurs when the extra atom placed in a close-packed direction displaces several atoms from their neighbouring positions. This configuration resembles the correlated motion of a line of displaced atoms. [84] However, it is worth pointing out here that the interstitial atom means only that there is one more atom than there are sites in a given small region. Similarly, that a vacancy does not have to mean that a particular site is vacant but that the region contains one fewer atoms than sites. [91]

The vacancy mechanism, which has been found as the most favourable in metals, involves atomic diffusion into the missing atomic sites (vacancies). Vacancies are present in pure metals and alloys at all temperatures; their concentration at the melting temperature (T_m) is about 0.01%. The vacancies may exist as dimmers (hence divacancies), particularly near to T_m. [84] If one of the atoms on an adjacent site jumps, into the vacancy, the atom is described as having diffused by a vacancy mechanism. [91] The vacancy mechanism is the mechanism of self-diffusion for all pure metals and for substitutional solutes in alloys. It can also be found in ionic compounds and oxides.

Another diffusion mechanism is known as the sub-boundary mechanism. The diffusing atom moves along interconnecting dislocation pipes (which are more spacious for diffusing atoms than bulk or dislocation lines), which results in naturally occurring low-angle boundaries. This mechanism has been found to operate at low temperatures, typically $<0.5\ T_m$, the absolute melting temperature, in metals such as Au, Ag and Cu. [84]

The relaxation mechanism is the one where the diffusing atom moves more or less freely within a disordered group of atoms in the lattice. The relaxation mechanism dominates in most crystalline solids but lately has been considered in the context of radiation damage in amorphous metallic alloys and some polymers. [84]

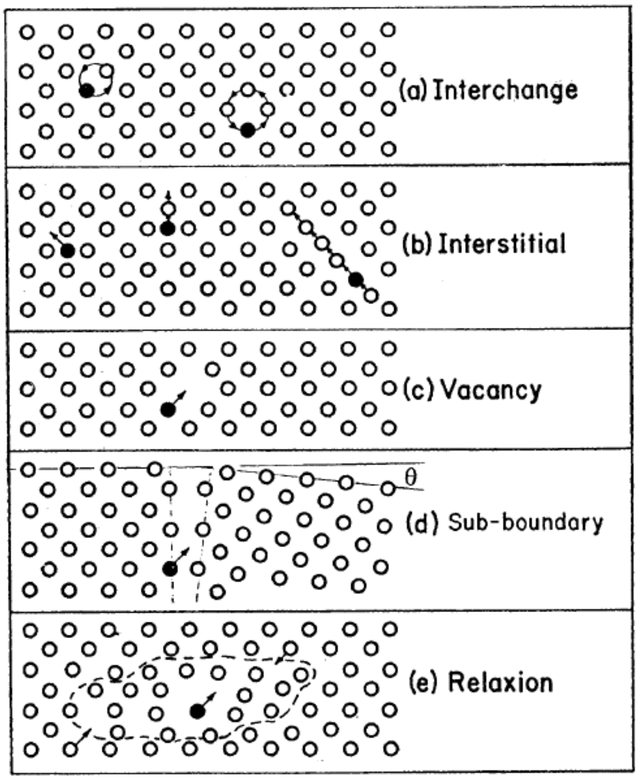

Figure 6.6: Diffusion mechanisms in solids. [84]

In amorphous materials diffusion generally occurs faster than in crystals. This is directly related to the random arrangement in the lattice and lower density (more open structure) than in the crystalline materials. Atoms can move through interstitials (open spaces between atoms in the matrix) and this type of diffusion is the most rapid and depends on the matrix density. If the structure is rather open, then not only small ions but also many metals can undergo diffusion through interstitial sites in amorphous materials. Substitutional and vacancy mechanisms are rather slower, as substitutional atom needs to replace other atoms in the matrix, which requires relatively high energy, whereas the probability of finding atom-size open spaces in the amorphous structure is rather small. Dangling bonds, which are a defects created in glassy forms (see Figure 6.7) promotes the diffusion in amorphous materials by creating a free spaces for diffusing atoms. They are not obtained in crystalline structures as removing an atom from the lattice creates a vacancy and more dangling bonds. The bonds would pair up, leaving no vacancies or dangling bonds. [95]

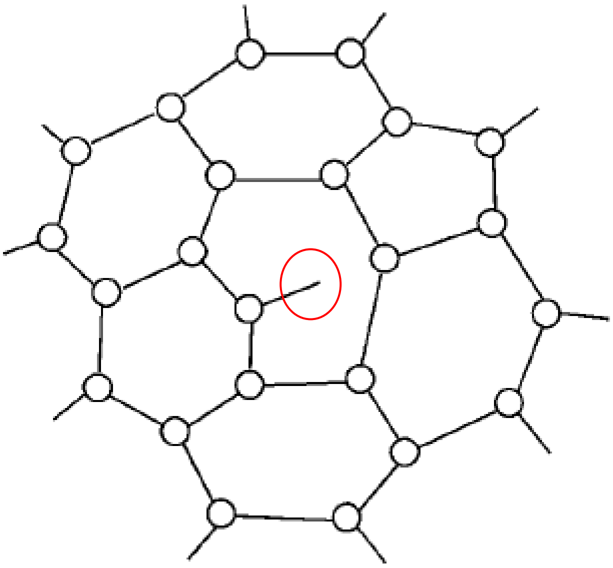

Figure 6.7: Dangling bond in an amorphous structure network. [95]

6.8 Grain Boundary Diffusion

It is well known that grain boundaries (GB), dislocations or surfaces acts as rapid diffusion “short circuits” in metals and non-metals. Short circuit diffusion occurs with lower activation energy than lattice diffusion, which is why GB diffusion becomes particularly important at relatively low temperatures. [96] In solid materials two types of GB structure have been recognized: periodic and glassy, as a material can be observed in crystalline or amorphous/glassy phases. GBs have been assumed to have orientated structures. In the literature there is plenty of work presented about structural models of grain boundaries, which will not be presented in this work. [13, 97-100]

The first direct proof of GB diffusion was obtained in the early 1950s using autoradiography [101] and then developed by Fisher who described first model of grain boundary diffusion (see Figure 6.8). [102]

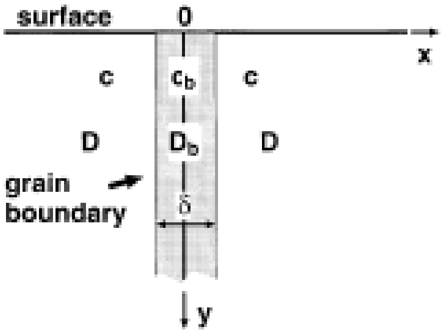

Figure 6.8: Schematic geometry from the Fisher model of grain boundary diffusion, where δ is the GB width, D_b is the GB diffusion coefficient, D is the volume diffusion coefficient and C and C_b represents concentration of the diffusion atoms in the volume and in the boundary respectively. [102]

GB diffusion in inter-metallic compounds has not been studied in such a broad field like bulk diffusion, and the mechanism of diffusion in grain boundaries is still not well understood. It is not clear if the local disorder at GBs is caused by anti-structure atoms or structural vacancy formation in the bulk lattice. [103] However in the literature there is some information about grain boundary diffusion for Ni [104-107], Ti [108] and Fe [109] aluminides.

GB diffusion experiments include direct volume diffusion from the surface, diffusion along the GBs, partial leakage from the GBs to the volume and subsequent volume diffusion near the GBs. [102] Different regimes of kinetics have been determined depending on the processes which occur subsequently with GB diffusion. Harrison *et al.* described the GB diffusion measurements by classification of diffusion kinetics into three regimes called Type A, B and C, considering the regular array of grain boundaries of radius δ and d-spacing as shown in Figure 6.9. [102]. The section represents three different types of solute distribution, which depends on the ratio of the mean diffusion distance in the lattice $(Dt)^{1/2}$ to the separation d. [91]

Type A kinetics occur when the temperatures are high and/or during very long anneals, and/or for small grain sizes. The volume diffusion length $(Dt)^{1/2}$ is greater than the d-spacing between the grain boundaries and the volume diffusion fields around adjacent GBs overlap each other $(DT)^{1/2} \gg d$. [102] In this type of kinetics atoms interact with several dislocations diffusing through the lattice. The dislocations increase the effective diffusivity D_{eff} for the solid, so the penetration depth is greater that it would be without dislocations. [91]

Type B occurs at lower temperatures and/or shorter annealing time, and/or when the grain size is larger than in Type A. The volume diffusion to the adjacent grain boundaries do not overlap with each other. [102] The solute field around each dislocation develops independently of its neighbour $\delta \ll (Dt)^{1/2} \ll d.$ [91]

Type C is when the temperature is even lower than in Type B kinetics, and/or the annealing time is shorter. These conditions cause the volume diffusion to be almost 'frozen out' and the diffusion takes place only along the GBs, without essential leakages to the volume $(Dt)^{1/2} < \delta.$ [102] This is rare in bulk samples but may be a very significant in thin films where the diffusion through one micron thick film can occur without any solute being lost to the lattice. [91] The Harrison's B-regime conditions are most common for diffusion mechanisms for inter-metallic compounds. In such a case the trace atoms diffuse fast along GBs. When those atoms reach some depth, they penetrate into the bulk of the grains and diffuse even further, over a distance that is much larger than the GB width, δ. The rate of diffusion in the bulk is slower than in the GBs. It results in determination of the so-called triple product from the detected diffusion profile:

$$\boldsymbol{P = s\delta D_{gh}} \qquad \text{Equation 47}$$

Where s is a segregation factor and D_{gb} is the GB diffusion coefficient. [110]

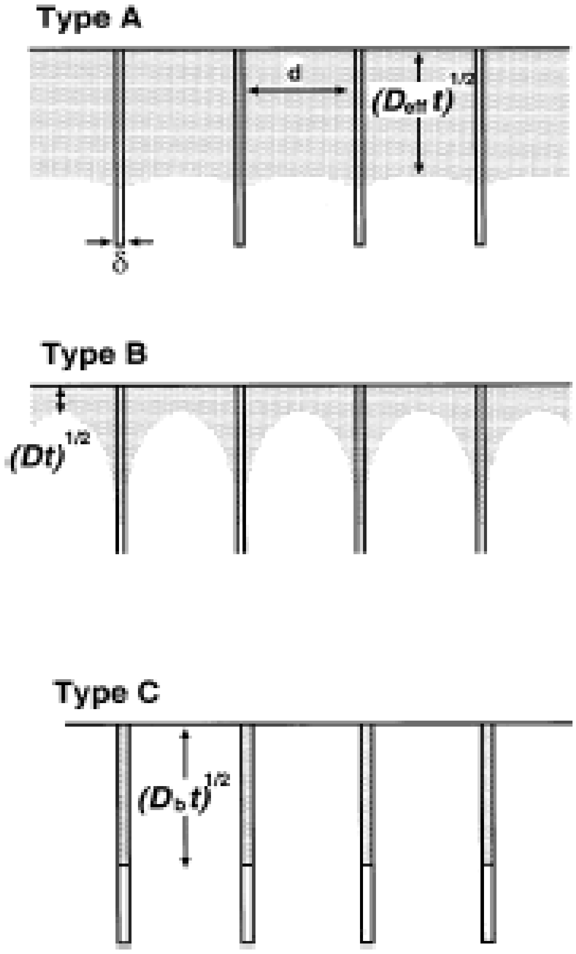

Figure 6.9: Schematic illustration of the Harrison's classification of diffusion kinetics. [102]

6.9 Diffusion Summary

Diffusion is a movement of an atom from one lattice site to another, which occurs when there is an adjacent space in the lattice or the atom has sufficient energy to move. Factors that influence diffusion are diffusion mechanisms, diffusing and host species, temperature, annealing time and the microstructure (the fastest diffusion rates has been found in amorphous materials due to more open structures and random arrangements in the lattice, however in crystals diffusion occurs faster in polycrystalline materials than in single crystals due to GBs and dislocation cores). Therefore it can be generalised that diffusion occurs faster in more open crystal structures, in materials with lower density, relatively low melting temperatures and bonded by weaker secondary bonds. Moreover smaller sizes of diffusing atoms increases diffusion rates and cathions diffuse faster than anions.

Diffusion in thin films occurs faster than in bulk materials due to the higher degree of defects such as dislocations, vacancies or GBs, which may serve as short circuits for diffusion processes. The short circuits diffusion occurs at lower activation energies than through the lattice, therefore thin films microstructure is one of the factors especially important at relatively low temperatures. And hence in the thin films, in which larger grains can be distinguished, the diffusion occurs mainly through the lattice as there are fewer GBs. On the other hand, in films with smaller grains, and therefore increased number of GBs diffusion rates are higher, as the diffusion occurs through the lattice and through GBs. Diffusion is depth and size dependent in this case, due to higher probability of the appearance of atom displacement in the neighbourhood than in the lattice with larger grains. Vacancies are the most favourable path for lattice diffusion, but the probability of a vacancy is related to the degree of defects in the lattice. The interstitial diffusion occurs relatively easy (especially if the diffusing atoms are small), partly because there are more interstitials than vacancies in the lattice. In the case of amorphous materials another path for diffusion to occur are dangling bonds in the structure.

Fick's second law is a basic equation to describe most of the diffusion cases in solids in non-steady state conditions. This equation describes concentration as a function of position and time, and for a given diffusing couple the diffusion coefficient remains constant. Error function is the most common way to find diffusivity in the case of relatively short diffusion distances. Both Gaussian and error function solutions involve $\frac{x^2}{Dt}\ (or\ \frac{x}{\sqrt{Dt}})$, and this group of variables is dimensionless. If the diffusion distance $(\sqrt{Dt})$ is large compared to the film thickness, then the concentration remains uniform throughout the thickness after time t. However if the $\sqrt{Dt}$ is small compared to sample thickness, then the other side of the sample effectively becomes at infinity and the Gaussian and error function solutions are appropriate to use.

In the Arrhenius equation the diffusion rate depends on temperature and the frequency factor, which in turns depends on geometric details of the path (atom density × number of atoms that have enough energy to diffuse). The D_0 and Q are parameters independent of temperature. When the Arrhenius plot becomes a discontinuous curve it suggests that the mechanisms controlling diffusion rate have changed.

7. Experimental Equipment

This chapter details the equipment used for coatings deposition during this project. The vacuum chamber, magnetron designs and power delivery modes are described here.

7.1 Vacuum Chamber

The vacuum system consisted of a rectangular stainless steel vacuum vessel with internal dimensions of 1800 mm in length; 650 mm in width and 300 mm height (see Figure 7.1). This vacuum rig is known as the Large Area coating chamber and was manufactured by PREVAC Sp.z.o.o. The chamber has the capacity for the installation of two rectangular magnetrons and one ion source mounted on the top of the chamber. This design allows multilayer stacks to be deposited in a similar way as in industrial applications.

Figure 7.1: Large Area coating chamber (Prevac Sp. z.o.o.)

The chamber was pumped down using a diffusion pump, which was backed up by a rotary pump. The typical base pressure reached by this chamber was about 2-3×10^{-5} Pa, as measured by a Penning gauge connected to a Penning gauge readout, both manufactured by Edwards Ltd. To reduce the pumping speed and enable coating deposition under higher operating pressures, baffle could be partially closed over the diffusion pump entrance. During sputter deposition, the chamber would be backfield with 99.95% purity argon gas to achieve the desired operating pressure, which was monitored by a Baratron® capacitance manometer pressure gauge (MKS Instruments) connected to a MKS Instruments PR 4000 pressure control unit. The gas flow into the chamber was controlled by a MKS mass flow controller connected to a readout unit (MKS Instruments PR 4000). During reactive sputtering the reactive gases (oxygen, nitrogen) could be either controlled by MKS mass flow controllers or via an optical emission monitoring system (OEM), described in Chapter 4.5.2.2.

The substrate onto which the thin films were deposited was placed onto an aluminium substrate holder directly under the magnetron. The target/substrate distance was 90 mm and the substrate was covered by a shutter during target cleaning prior to coating deposition.

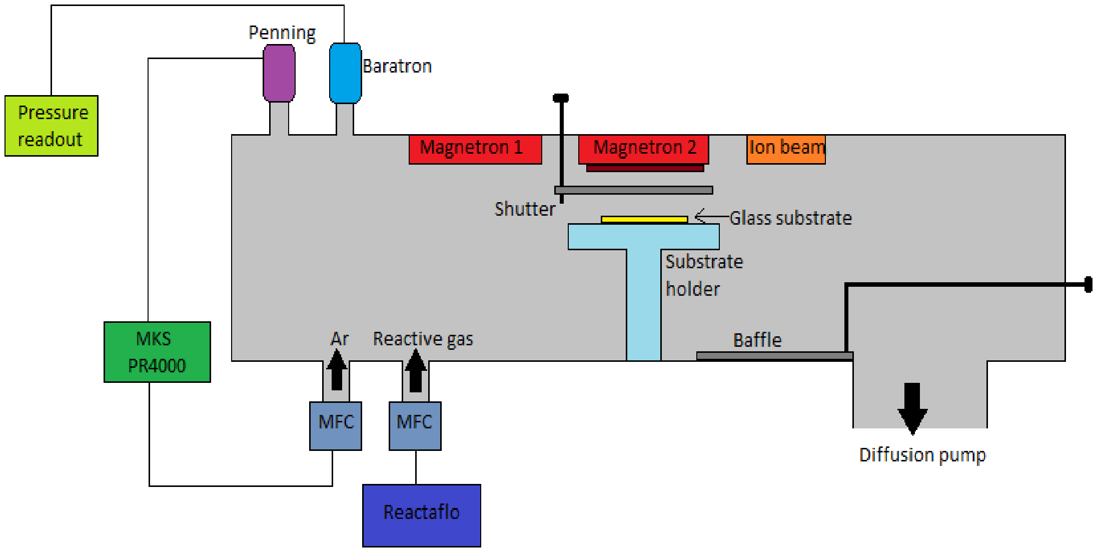

Figure 7.2: Schematic design of the Large Area coating chamber.

7.2 Magnetron Designs

Standard planar and full face erosion (FFE, Gencoa Ltd.) magnetrons were used during thin film depositions. The target sizes for the magnetrons were 100 mm×300 mm and 125 mm×350 mm, respectively.

The full face erosion (FFE) magnetron design incorporates a means of scanning the magnetic field across the face of the target. This improves target usage to the order of 45% - 60%, which is a significant increase compared to a standard planar magnetron. Consequently there are no areas of re-deposited coating material in the centre of the target surface. This promotes process stability during reactive sputtering and reduces arc-induced defects in the growing film. The FFE is equipped with a mechanism to rotate a pair of magnets, which make up the central pole, as shown in Figure 7.3. As a consequence, during sputtering the plasma is seen to sweep across the surface of the target (from side to side in Figure 7.3). This broadens the racetrack, which increases target utilisation and decreases the re-deposition zone in the centre of the target, which helps to reduce arcing. Moreover, due to the constant movement of plasma density, it allows the deposition of more uniform coatings in stationary substrate mode. [111]

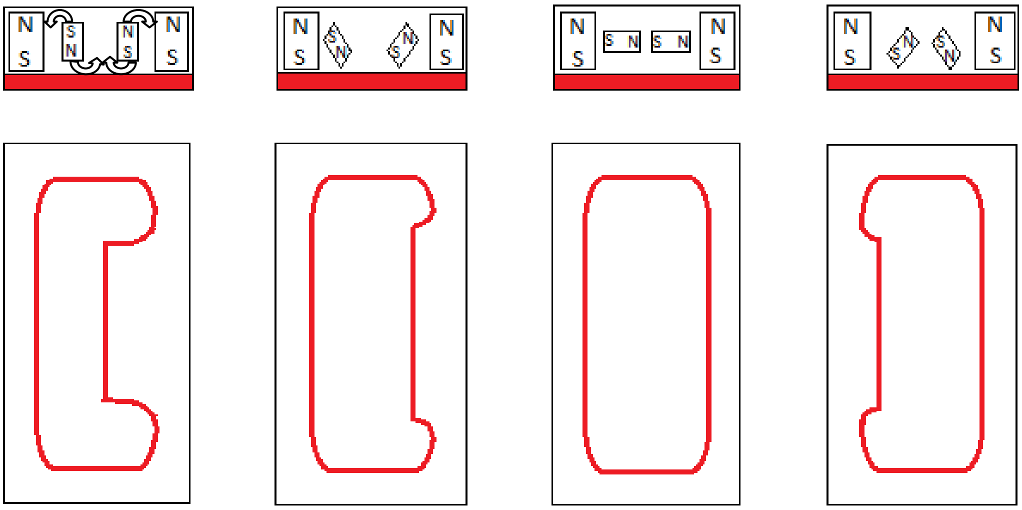

Figure 7.3: Schematic design of rotating cycle in FFE magnetron.

Cylindrical rotatable magnetrons (C-mags) were used to deposit zinc stannate samples within the Pilkington Technology Management Ltd. laboratories in Lathom. The size of the target required was 1000 mm in length and 300 mm in radius. Cylindrical rotatable magnetrons incorporate a stationary magnet array within a moving (rotating) cylindrical target. The plasma is confined to the region in front of the magnetic array. As the target rotates the whole circumference of the target passes through this region and is sputtered in turn. Thus, there is no re-deposition zone on the surface and target utilisation is very high (>80%), with only the end of the tube remaining unsputtered (see Figure 7.4). C-Mags are also known for their high film uniformity along the length of the tube (±2%). Rotatable magnetrons have advantages over planar magnetrons in terms of target life and cleanliness of the target surface. This cleanliness is most important when sputtering oxides from either ceramic oxide targets or with reactive process gases. It results in better long term stability and fewer defects in the growing film. [111]

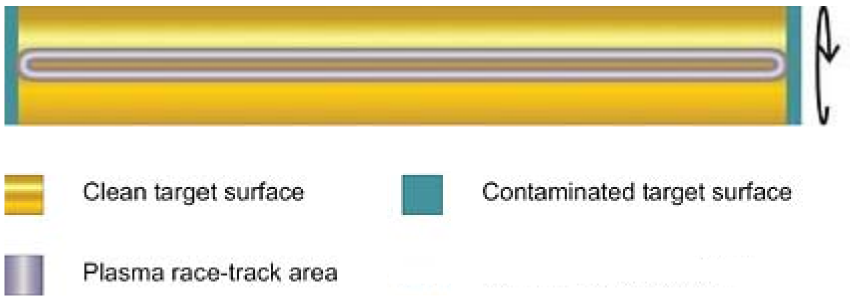

Figure 7.4: Schematic representation of cylindrical rotatable target.

7.3 Power supply

The magnetrons were driven using an Advanced Energy Pinnacle Plus power supply. It has a dual channel output for multi-source processing with a maximum output power of 5 kW per channel. This power delivery mode allows sputtering in both DC and pulsed DC modes in an adjustable frequency range of 5 to 350 kHz and variable duty cycle down to a minimum of 50%. Due to its superior arc control, the Advanced Energy Pinnacle Plus power supply reduces substrate damage caused by arcing, as described in section 4.5.3.

8. Analytical Techniques

Various analytical techniques were used to investigate the structure of the deposited coatings. X-ray diffraction and Raman scattering were used to determine crystalline structure. Scanning electron microscopy and energy dispersive X-ray spectroscopy measurements were performed to obtain surface morphology and stoichiometry, respectively. Secondary ion mass spectrometry and X-ray photoelectron spectroscopy were used to perform depth profiling analysis to describe the diffusion of silver and sodium atoms.

8.1 Dektak Profilometry

The thicknesses of the coatings produced were measured by a Dektak profilometer. The measurements are performed by traversing the sample under a stationary stylus, which is deflected vertically and this movement relates to the height of surface features. The thickness of the deposited film can be measured from the step-height when traversing from the substrate to the coating. The figure below shows the Dektak® 3 stylus profilometer manufactured by Vecco Instruments Inc.

Figure 8.1: Picture represents Dektak 3 stylus profilometer used to physically measure coating thickness after deposition.

8.2 Raman Spectroscopy

Raman scattering is a spectroscopic technique to detect vibrations in molecules. It is widely use to provide information about chemical structures, physical forms, for fingerprinting and for quantitative or semi-quantitative analysis. Samples can be measured in a whole range of physical states, as solids, liquids or in vapour state. [112]

Light from a laser interacts with sample molecules and polarizes the cloud of electrons around the nuclei. Polarized electrons go to higher energy states, so the energy present in the light wave is transferred to the molecule. A short-lived “complex”, called a virtual state is created between light energy and electrons in the molecule in which nuclei do not have time to move. As the state is not stable the light is released immediately as scattered radiation. The shape of the distorted electron arrangement depends on the energy transferred to the molecule, and hence on the laser frequency.

Two types of scattering can be defined: first and most intense is Rayleigh scattering. It is an example of elastic scattering, which means that there is no energy change. The process occurs when the electron cloud relaxes without nuclei movements. The second type, Raman scattering, is much rarer, involving only one in 10^6-10^8 of the photons scattered. It occurs when electrons and light interact with each other and the nuclei begin to move at the same time. Large changes in the energy of the molecule occur, which can be to either lower or higher energy depending on whether the process starts with a molecule in ground state (Stokes scattering) or in a vibrational excited state (anti-Stokes scattering). The major type of Raman scattering is Stokes Raman scattering, as most molecules at room temperature before interacting with the laser are likely to be in the ground vibrational state. Figure 8.2 shows a schematic representation of Raman energy states.

The ratio between Stokes and anti-Stokes scattering depends on the number of molecules in the ground and excited vibrational states. This can be calculated from the Boltzmann equation:

$$\frac{N_n}{N_m} = \frac{g_n}{g_m} exp\left[-\left(\frac{E_n - E_m}{k_B T}\right)\right] \qquad \text{Equation 48}$$

where N_n is the number of molecules in the excited vibrational energy level (n), N_m is the number of molecules in the ground vibrational energy level (m), g is the dependency of the levels *n* and *m*, E_n-E_m is the energy difference between the vibrational energy levels, k_B is the Boltzmann constant, which equals 1.3807×10^{-23} JK^{-1}. [112]

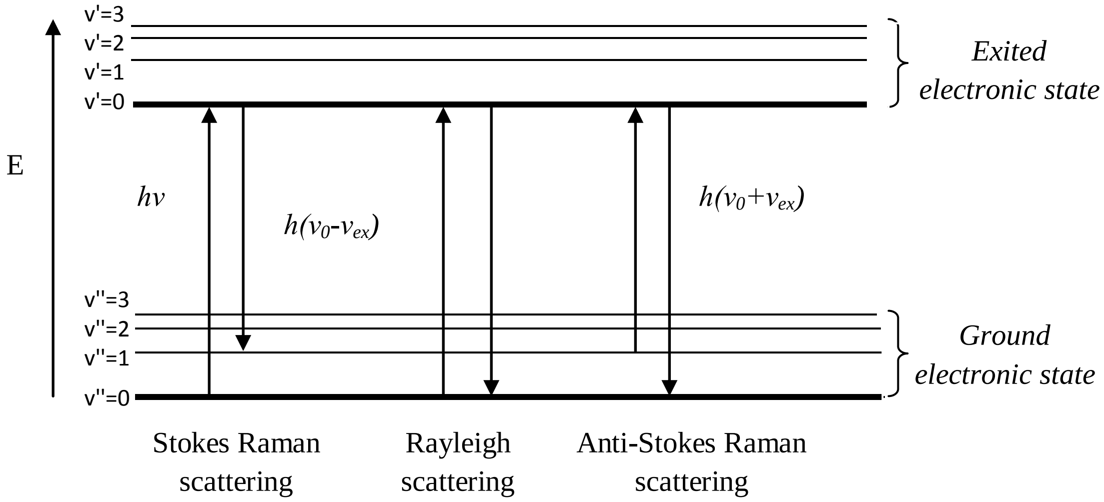

Figure 8.2: Raman energy state scheme; v'' and v' refer to the vibrational levels in the ground and excited electronic states, respectively.

8.3 Scanning Electron Microscopy (SEM)

Scanning electron microscopy is one of the most powerful techniques for microstructural analysis and characterisation of solid objects. It gives excellent topographical information and near-surface region composition. SEM has a high resolution - down to 2-5 nm. It can operate at magnifications from about 10×-300000×, but most SEM images are produced with magnification below 8000×. The large depth of field results in images having a three dimensional appearance. [113]

The source of electrons is focused onto a sample surface with energy between a few hundred eV up to 30 keV. As primary electrons penetrate the surface of the specimen several interactions occurs which may results in the emission of electrons or photons from (or through) the surface. A fraction of the emitted electrons can be collected and processed by a detector, producing an image. Every point that the beam hits on the sample is mapped directly onto a corresponding point on the screen. [114]

SEM images can be produced as secondary electron (SE) images, backscattered electron (BSE) images and elemental X-ray maps. When high energy primary electrons interact with an atom either inelastic scattering with the atomic electrons or elastic scattering with the atomic nucleus occurs. If the energy of the emitted electron is less than 50 eV, by convention it is referred to as SE, if the emitted electron energy is higher than 50 eV then BSE images are produced.

8.4 Energy Dispersive X-ray Spectroscopy (EDX)

SEM can be combined with EDX to provide simultaneous examination of the morphology of an object and analysis of its elemental composition. The X-ray microanalysis can be done in the spot mode (elemental composition), in the area mode (bulk composition), in dot mapping mode (to study the distribution density of different elements in a particular region or phase), or in linear traverse mode (to determine the variation in concentration of one or several elements along the line).

A conventional detector is maintained under cryogenic conditions and is made of lithium drifted silicon, with a beryllium window which separates the spectrometer and the microscope. The Si-Li detector collects X-rays photons originated from the specimen, which are then transformed into counts after conversion into a voltage pulse output. [114]

EDX is based on the detection of X-rays emitted by the specimen. Since each element has its own characteristic position EDX can simultaneously detect all elements with energy higher than 1 keV ($Z \geq 11$). Lower energy elements will be absorbed by the Be window. Modern EDX detectors are windowless; therefore it is possible to detect lower atomic number elements, such as carbon or oxygen.

Most EDX systems are equipped with software for quantitative analysis, called ZAF. It consists of three major corrections: atomic number (Z), absorption (A) and fluorescence (F). However to avoid large errors, quantitative analysis must be carried out on a flat polished surface. [114]

8.5 X-ray Diffraction (XRD)

X-ray diffraction is a powerful technique to measure crystalline structures present in materials and also to determine structural proprieties such as strain state, grain size, phase composition, preferred orientation and defect structures of those phases. It can be also used to determine film thickness, multilayer periods, and interfaces. [115] The sensitivity of the XRD analysis depends on the material of interest, as it is most sensitive for the elements with high atomic number Z.

X-ray diffraction is the elastic scattering of X-ray photons by atoms in a periodic lattice. In XRD an incident X-ray beam penetrates many micrometers into the bulk of the sample and the direction of the diffracted beam is determined by the periodicity of the planes of atoms in the crystalline solid. [116] By measuring the angles, under which X-rays leave the crystals the crystal lattice spacing d can be calculated from Bragg's law equation:

$$\boldsymbol{2d\sin\theta = n\lambda} \qquad \text{Equation 49}$$

Where λ is the wavelength of the incident X-ray beam applied to the crystal surface, θ is the angle of incidence/reflection, which produces a diffracted beam at the same angle, d is the crystal lattice spacing.

In order to identify the unknown species, the data obtained from XRD analysis can be compared with the standard line patterns available for various compounds in the Powder Diffraction File (PDF) database. This file contains line patterns for over 60,000 different crystallographic phases and it is updated annually by the International Centre for Diffraction data (ICDD). [114]

Figure 8.3 shows a simplified X-ray diffractometer.

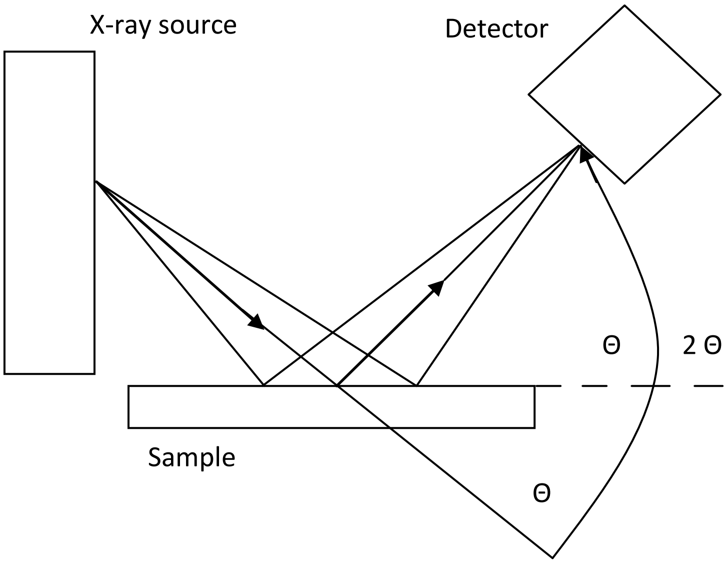

Figure 8.3: Schematic representation of simplified XDR apparatus.

Peak position and intensity measurements are useful to describe lattice constant and stress of the measured sample. Moreover peak angles and profiles may be used to find grain size and the degree of crystallisation. It is known that sharp narrow peaks represent perfect crystals. When the crystal size is below 100 nm the peaks become wider due to incomplete destructive interfaces in the scattering directions where X-rays are out of phase. [114] The Debye-Scherrer equation allows estimation of crystal size to line width:

$$\boldsymbol{\beta} = \frac{\mathbf{0.98}\boldsymbol{\lambda}}{\boldsymbol{FWHM}\ \mathbf{cos}\ \boldsymbol{\theta}} \qquad \text{Equation 50}$$

Where β is the grain size, λ is the wavelength (0.154056 nm for copper Kα radiation), FWHM is the Full Width Half Maximum of the peak and θ is the angle of incidence/reflection to the planes. [117] X-ray line broadening provides a quick but not always reliable estimate of an actual grain size within the crystal. To obtain actual grain sizes line profile analysis with Fourier transformation needs to be performed.

8.6 X-ray Reflectivity (XRR)

X-ray reflectivity (XRR) is a non-destructive and non-contact technique to determine the thickness of the thin film (between 2-200 nm), film roughness and density. A monochromatic X-ray beam of wavelength λ irradiates the sample surface at a grazing angle ω, and the intensity of the beam reflected by the sample at a 2θ angle is measured by a detector. The detector rotates at twice the speed of the sample mounted on the sample holder. The reflection at the sample surface and at the interfaces is due to the different electron densities in the different layers (films), which correspond to different reflective indices in the classical optics. [118] To determine thickness and roughness with high accuracy the sample alignment to the X-ray beam position is critical. The alignment process is carried out automatically by a computer, repeatedly adjusting the z axis (sample distance from the beam), ω (or θ) positions. The optimum position is reached when the sample is located at the centre of the X-ray beam and only half the X-ray beam is reflected back to the detector. Then, the detector (2θ) is set at an appropriate position and the total external reflection adjustment starts by further optimisation of the z, ω and λ positions, until the maximum reflection, which equals the intensity of the incident beam is reached. [119]

Thickness is usually determined by XRR with a precision better than 0.1 nm for measurements exhibiting interfacial fringes in a bigger angular range. For incident angles greater that the critical angle θ_c, ($\theta > \theta_c$) the X-ray beam penetrates inside the film, and therefore reflection occurs at the top and the bottom surfaces of the film. The interface between the rays reflected from the top and the bottom of the film surfaces results in the interface fringes, which are angle dependent. [118]

In XRR measurement roughness gives rise to diffuse scattering. At interfaces the interfacial roughness and diffuseness reduce the specular reflectivity of an interface either by scattering X-rays into non-specular directions, in the case of interface roughness, or by increasing the transmissivity of the interface in the case of interfacial diffuseness. In general roughness σ consists of the interfacial roughness σ_r and interfacial diffuseness σ_d, i.e. $\sigma = \sqrt{\sigma_r^2 + \sigma_d^2}$. However XRR only records specular reflection intensity and it is only sensitive to the normal surface direction, therefore it cannot distinguish interface compositional grading or diffuseness from the interface roughness. [119]

One of the most reliable methods in determining density of uniform thin films is XRR mass measurement. The thickness of the film and its area must be known to provide reliable analysis. Density (δ) measurements by XRR are mainly determined by the critical angle (θ_c) using Snell's law:

$$\boldsymbol{\delta = {\theta_c^2}/{2}} \qquad \text{Equation 51}$$

and noting that the θ_c is usually very small. Hence the instrument alignment is the crucial limiting factor in precisely determining the density of thin films using XRR. A misalignment of 0.005^{o} in sample tilt, with respect to the incoming X-ray beam can change the final value of the electron density by 5%. [119]

Figure 8.4 shows a simplified representation of XRR instrument.

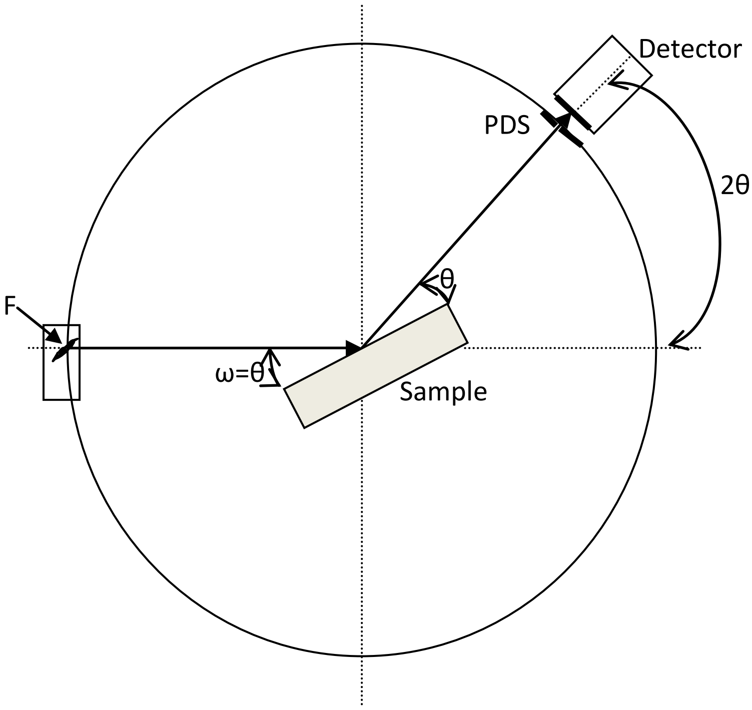

Figure 8.4: Schematic representation of XRR instrument, where the incident angle ω equals outgoing angle θ and the reflected intensity of 2θ angle is measured. The anode focus, F of the tubes lies on the detector circle, which is fixed through the detector slit, PRS (programmable receiving slit).

8.7 Atomic Force Microscopy (AFM)

Atomic Force Microscopy is a surface characterisation technique that uses a very sharp probe to scan across the surface of interest. Interactions between the probe and the sample surface are being used to produce a very high resolution three dimensional topographic image of the surface. AFM is designed to take measurements in air or fluid environments instead of a vacuum. It can be used as a static technique, measuring a sample surface in a contact mode or as a dynamic technique, in which case the cantilever is oscillating in an intermittent or a non-contact mode. In a contact mode the probe remains in contact with the sample by all times. This type of AFM analysis is used to scan hard and relatively flat surfaces. [120]

In a basic AFM set up a probe is mounted at the apex of a flexible cantilever made of silicon or silicon nitride. The cantilever or the sample surface is mounted on a piezocrystal, which allows the position of the probe to move in relation to the surface. Deflection of the cantilever is monitored by the change in the path of a beam of laser light, which is deflected from the upper side of the end of the cantilever by a photodetector. The piezocrystal moves the tip to be in contact with the sample surface and its deflection is being monitored. This deflection is used to calculate the interaction forces between the probe and the sample surface. This type of AFM analysis is called tip or surface scanning. [120]

8.8 Optical Spectroscopy

In optical spectroscopy the incoming photon (or light) can interact with the valence electrons of the material in three different ways, causing reflection, absorption or transmission of light. Therefore the intensity of the incident light (I_0) can be written as a sum of those three effects [121]:

$$\boldsymbol{I_0 = I_r + I_a + I_t} \qquad \text{Equation 52}$$

Where I_r, I_a and I_t represent light that was reflected, absorbed and transmitted respectively.

Reflection occurs when the beam of light strikes the material; the photons interact with the valence electrons and give up their energy causing emission of the electrons of almost identical wavelength, as the excited electrons return to their lower energy levels.

The reflectivity R gives the fraction of the incident beam that is reflected. In vacuum or in air it is described as:

$$\boldsymbol{R} = \left(\frac{\boldsymbol{n}-\mathbf{1}}{\boldsymbol{n}+\mathbf{1}}\right)^{\mathbf{2}} \qquad \text{Equation 53}$$

Where n is the refractive index. If the material is in some other medium with the refractive index n_i then:

$$\boldsymbol{R} = \left(\frac{\boldsymbol{n}-\boldsymbol{n_i}}{\boldsymbol{n}+\boldsymbol{n_i}}\right)^{\mathbf{2}} \qquad \text{Equation 54}$$

These equations apply to the reflection from a single surface with a beam of incidence perpendicular to the surface. The value of R depends on the angle of incidence and the wavelength. Materials with high refractive index have a higher reflectivity than materials with a low index of refraction. [121]

Absorption defines the portion of the incident beam, which has not been reflected by the material, but is either absorbed or transmitted. The fraction of the absorbed beam is related to the thickness of the material and the means of interactions between the photons and the material. The intensity of the beam after passing through the material is given by the Bouguer's law:

$$\boldsymbol{I} = \boldsymbol{I_0}\mathbf{exp}\,(-\boldsymbol{\alpha x}) \qquad \text{Equation 55}$$

Where x is the path, through which the photons move, usually described by the thickness of the material, α is the absorption coefficient of the material for the photons, I_0 is the intensity of the beam after reflection at the front surface and I is the intensity of the beam at the back surface. [121]

Transmission describes the situation when a beam of light is not reflected or absorbed but passes through the material. To determine the fraction of the transmitted beam the reflectivity and absorption of light by the material needs to be considered at first. If the incident intensity is I_0, then the loss due to the reflection at the front of the material is RI_0. Therefore the fraction of the beam which actually enters the material is [121]:

$$\boldsymbol{I_0} - \boldsymbol{RI_0} = (\boldsymbol{I} - \boldsymbol{R})\boldsymbol{I_0} \qquad \text{Equation 56}$$

Because $I_{\text{reflected at front surface}}=RI_0$ and $I_{\text{after reflection}}=(1-R)I_0$.

Moreover a portion of the beam that enters the material is partially lost by absorption, therefore the intensity of the beam after passing the material having a thickness x is:

$$\boldsymbol{I_{after\ absorption} = (1-R)I_0 exp(-\alpha x)} \qquad \text{Equation 57}$$

Before the partially absorbed beam exits the material the reflection occurs at the back surface of the material. The fraction of the beam which reaches the back surface and is reflected is:

$$\boldsymbol{I_{reflected\ at\ the\ back\ surface} = R(1-R)I_0 exp(-\alpha x)} \qquad \text{Equation 58}$$

Consequently the fraction of the beam that is completely transmitted through the material is equal $I_{after\ absorption} - I_{reflected\ at\ the\ back\ surface}$, therefore:

$$\boldsymbol{I_t = I_0(1-R)^2 exp(-\alpha x)} \qquad \text{Equation 59}$$

The intensity of the transmitted beam depends on the wavelength of the photons in the beam and also on the microstructure of the material that the beam is passing through. [121]

Figure 8.5 shows the schematic representation of what happens to the beam while it is passing through the material.

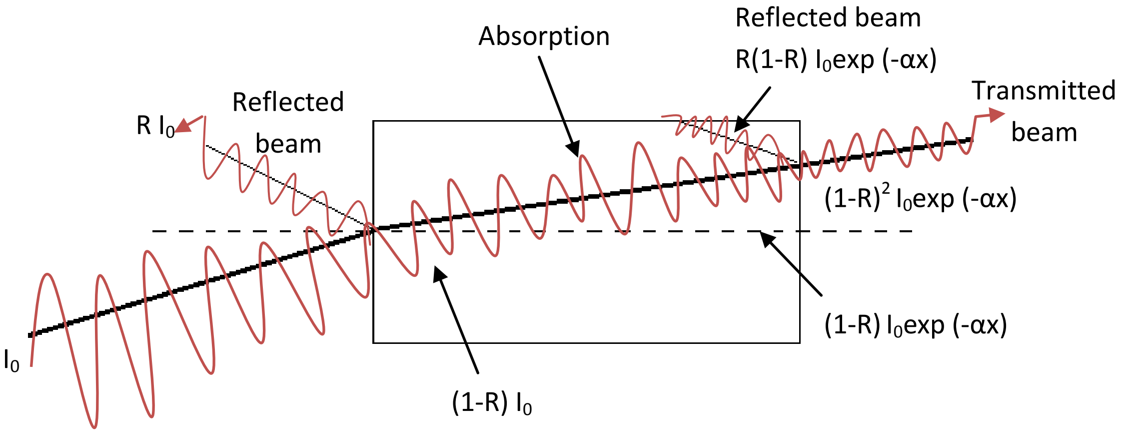

Figure 8.5: The beam fractions which are reflected, absorbed and transmitted through the material.

Refraction occurs even when the photon is transmitted, it causes polarisation of the electrons in the material and loses some of its energy due to interaction with the polarised material. If θ_i is the angle of incidence and θ_t the angle of refraction of a beam which penetrates through the material, then:

$$\boldsymbol{n = \frac{c_0}{c} = \frac{\lambda_{vacuum}}{\lambda} = \frac{sin\theta_i}{sin\theta_t}} \qquad \text{Equation 60}$$

where n is the index of refraction, c_0 is the seed of light in a vacuum (3×10^8 m/s), and c is the speed of light in the material. Refractive index can be also described using other parameter such as absorption index κ, and then n^* is called a complex refractive index:

$$\boldsymbol{n^* = n(1 - i\kappa)} \qquad \text{Equation 61}$$

Where $i = \sqrt{-1}$ and is called the imaginary number. The absorption index is defined as:

$$\boldsymbol{\kappa = \frac{\alpha\lambda}{4\pi n}} \qquad \text{Equation 62}$$

Where α is the linear absorption coefficient, λ is the wavelength of light, n is the refractive index. However if photons travel through Material X instead of in a vacuum, and then pass through Material Y, the velocities of the incident and refracted beams depend on the ratio between their refractive indices:

$$\boldsymbol{\frac{c_1}{c_2} = \frac{n_2}{n_1} = \frac{sin\theta_i}{sin\theta_t}} \qquad \text{Equation 63}$$

Equation 63 is known as a Snell's law. [121]

The refractive index is not a constant for a particular material but it is dependent on the frequency and wavelength of the photon. The dependence of the refractive index on wavelength is nonlinear. Dispersion of the material is a variation of the refractive index with wavelength:

$$\boldsymbol{(Dispersion)_\lambda = \frac{dn}{d\lambda}} \qquad \text{Equation 64}$$

The dispersion can be defined as pulses of light of different wavelengths in the material, which starts at the same time at one end and will arrive at different times at the other end of the material. [121]

8.9 Secondary Ion Mass Spectrometry (SIMS)

SIMS is a destructive analytical technique with high sensitivity which can be used to determine the composition and chemical state of the atoms at the sample surface. In dynamic SIMS, the focused primary ion beam is used to sputter material from the samples. The sample is placed in the vacuum chamber and is bombarded by primary ions, which knock atoms from their lattice position and they are then ejected from the material. [116] Secondary ions are accelerated into the mass spectrometer and separated according to their mass-to-charge ratio (m/e). The most probable energy of secondary ions is <10 eV. Secondary ions are emitted as a result of momentum transfer through collision cascades initiated by energetic primary ion bombardment on the sample surface. Due to collisions with sample atoms, primary ions become neutralised and lose their kinetic energy. [122] The in-depth concentration profile is obtained by monitoring the intensity of the mass peaks as a function of bombardment time. In dynamic SIMS the primary ion current used is >1 µA/cm^2, which removes more than one monolayer of material. The sputter yield depends on mass, energy, angle of incidence of the primary ions, crystal structure, lattice orientation, surface roughness etc. and it is described as the amount of sample material removed (measured as number of atoms) per incident ion. Heavier elements sputter more easily than light ones. It is one of the most sensitive analytical techniques with elemental detection limits in the ppm range. The most common application of SIMS is depth profiling elemental dopants and contaminants in materials at trace levels.

A magnetic sector analyzer is used to distinguish the analyzed elements. These types of mass spectrometers use an electrostatic analyzer for energy filtering and a magnetic sector for mass separation. They are capable of achieving high mass resolution with a typical range of 250 amu. [8] Ions of mass M, charge e and velocity v go through the entrance slit of the analyzer and are deflected by a magnetic field B. The radius R followed by the ions is given by [116]:

$$\boldsymbol{R = \frac{Mv^2}{eV_iB}} \qquad \text{Equation 65}$$

Only ions with a specific velocity and charge continue to the exit slit for any given magnetic field. All ions entering the exit slit have the same charge-to-mass ratios, so the magnetic field is kept constant.

Time of Flight (TOF) analysers are capable of high mass resolution and extended mass range. High mass resolution is enabled by the introduction of a pulsed ion beam (1-10 ns), which strikes the sample surface and ejects the secondary ions. Extracted ions travel through a drift tube to a large area detector, where mass separation analysis is accomplished by assigning different time of travel to the mass of different ions. Lighter ions need less time to travel through the tube and reach the detector faster than heavier ions. TOF analysers enable the entire spectrum to be collected in few μs, providing alongside a very high resolution. They enable separation of fragments with similar masses into different peaks and enable more exact mass determination. [115]

8.10 X-ray Photoelectron Spectroscopy (XPS)

In XPS electrons are ejected from a core level by an X-ray photon of energy hν. When hν is larger than the binding energy (BE), an electron is freed from the atom and the difference between the energy of excitation and BE is represented by kinetic energy (KE). The energy of the emitted electron is measured and calibrated against standard energy references.

The XPS apparatus usually consists of a X-ray source and a highly stable KE analyser placed in ultra high vacuum. The X-ray source is a diode system with a coated anode, usually with Mg or Al to produce Mg or Al Kα X-rays (0.7 and 0.85 eV, respectively). [122] The spectrometer measures the experimental value of kinetic energy, whereas binding energy (BE) is a characteristic parameter which identifies electrons specifically. The Einstein photocatalytic law express the dependency between KE and BE [117]:

$$\boldsymbol{KE = h\nu - BE} \qquad \text{Equation 66}$$

A hemispherical sector analyser (HSA) is usually used to determine the low-energy electrons (generally in the range of 20-2000 eV). The HSA consists of a pair of concentric hemispherical detectors between which there is a gap for electrons to pass. A potential difference is applied across the two hemispheres with the outer being more negative than the inner hemisphere. [123] Electrons which travel the distance between the entrance and exit slits of energy analyser are collected and measured using an electron multiplier.

9. Project Plan and Methodology

The aim of this project was to investigate the diffusion of silver and sodium atoms through dielectric coatings. Silver atoms diffused from the deposited silver layer, whereas sodium diffusion occurred from float glass substrates upwards through the deposited coatings.

Dielectric coatings were chosen by the project industrial sponsors and are used worldwide in Low-E glass production. These coatings are titanium dioxide, aluminium doped zinc oxide, zinc stannate and silicon nitride. Those films represent a broad range of physical and structural proprieties required in Low-E coatings production.

9.1 Standard Experimental Procedure

Dielectric films were deposited onto 4 mm thick soda-lime glass, at ambient temperature by reactive pulsed DC magnetron sputtering. Samples were placed in a vacuum chamber, which was pumped down to a base pressure of about 2×10^{-4} Pa. During reactive sputtering, a metallic target was sputtered in the presence of a reactive gas, e.g. oxygen, and a compound film is deposited. [4, 11] The compound film may also form on the target, which can lead to arcing at the target and cause process instabilities. This can be avoided through the use of mid-frequency (20-350 kHz) pulsed sputtering. [4] In this project, therefore, coatings were mainly deposited using a pulsed DC power supply, but some materials, such as zinc stannate, have been deposited in AC (40 kHz) mode using a dual channel Huettinger (Tig 20/100PSC) power supply as well. Although the basics of the technique stay the same, the operating conditions vary between deposited materials and will be illustrated in the following chapters.

Titanium dioxide films were sputtered from a full face erosion (FFE) magnetron (125 mm×350 mm, Gencoa Ltd.) using a 99.5% purity metal target, driven by an Advanced Energy Pinnacle Plus power supply operating in pulsed DC mode at an average power of 1 kW and a pulse frequency of 100 kHz and 5.0 µsec off time (i.e. 50% duty). The optical emission monitoring (OEM) system was used to control the amount of oxygen introduced into the system during films deposition. The optimal conditions were found to be when the OEM signal was set to 20% of the full metal signal. The amount of argon introduced into the chamber was control by a MKS mass flow controller, and was set at 65 standard cubic centimetres per minute (SCCM).

Zinc oxide coatings (2 wt % Al doped) were sputtered from a FFE magnetron using a 99.5% minimum purity metal target. The magnetron was driven by an Advanced Energy Pinnacle Plus power supply operating in pulsed DC mode at a frequency of 100 kHz and 5.0 µsec off time. The power range used during the deposition varied from 300-500 W between the coatings. Stable operating conditions could not be obtained using OEM system for this target material. Consequently, the amount of argon and oxygen gases introduced into the chamber during sputtering was controlled by MKS mass flow controllers, and varied from 8-15 SCCM of oxygen, in constant argon flow rate of 10 SCCM. Coatings were produced using the range of operating pressure from 0.2-0.9 Pa. The operating pressure was changed by closing the baffle over the diffusion pump, which slowed down the pumping speed significantly.

Zinc stannate coatings were deposited onto float glass within a second coating chamber at Pilkington Technology Management Ltd. laboratories in Lathom. Films were sputtered from single planar magnetrons in DC mode using an Advance Energy Pinnacle Plus power supply, and from dual rotatable (with cylindrically shaped targets) and dual planar magnetrons in 40 kHz AC mode using a dual channel Huettinger (Tig 20/100PSC) power supply. The power range used during film deposition varied from 1-5 kW. Zinc-tin coatings were sputtered from targets with the 50:50 wt % ratios between Zn and Sn for single planar and rotatable magnetrons, whereas for dual planar magnetrons the ratio was 52:48 wt % respectively. The amount of oxygen introduced into the chamber during sputtering was controlled by MKS mass flow controllers and varied from 80-170 SCCM between the runs, whereas the argon flow rate was held constant (120 SCCM). The operating pressure was changed by slowing down the turbo pumps to reduce the pumping speed of the vacuum chamber. Coatings were deposited at pressures of 0.3, 0.8 and 1.2 Pa.

Silicon nitride films were sputtered from a FFE magnetron using a 99.5% purity silicon target, driven by an Advanced Energy Pinnacle Plus power supply operating in pulsed DC mode at a frequency of 100 kHz and 5.0 µsec off time. The power range used during deposition varied from 150-300 W between the coatings. The amount of argon and nitrogen gasses introduced into the chamber during sputtering was controlled by MKS mass flow controllers, and varied from 9-12 SCCM of nitrogen, with an argon flow rate of 35 or 50 SCCM. Coatings were produced using the range of operating pressures in the range of 0.25-0.9 Pa. The operating pressure was changed by closing the baffle over the diffusion pump.

Dielectric coatings investigated in this study were post deposition annealed in air at 650°C for 5 minutes and then over-coated with silver- these films will be referred to as annealed films in this thesis. However titania samples were annealed over a broader temperature range and that will be fully described in Chapter 10. The dielectric layers were over-coated with silver, which was deposited by DC magnetron sputtering from a 99.95% pure Ag target. The standard planar magnetron was driven by an Advanced Energy Pinnacle Plus power supply at an average power of 100 W. The thickness of the metal layer was ~100 nm. Dielectric/silver stacks were re-annealed at 250°C for 5 minutes to allow the diffusion of silver and sodium atoms through the coatings.

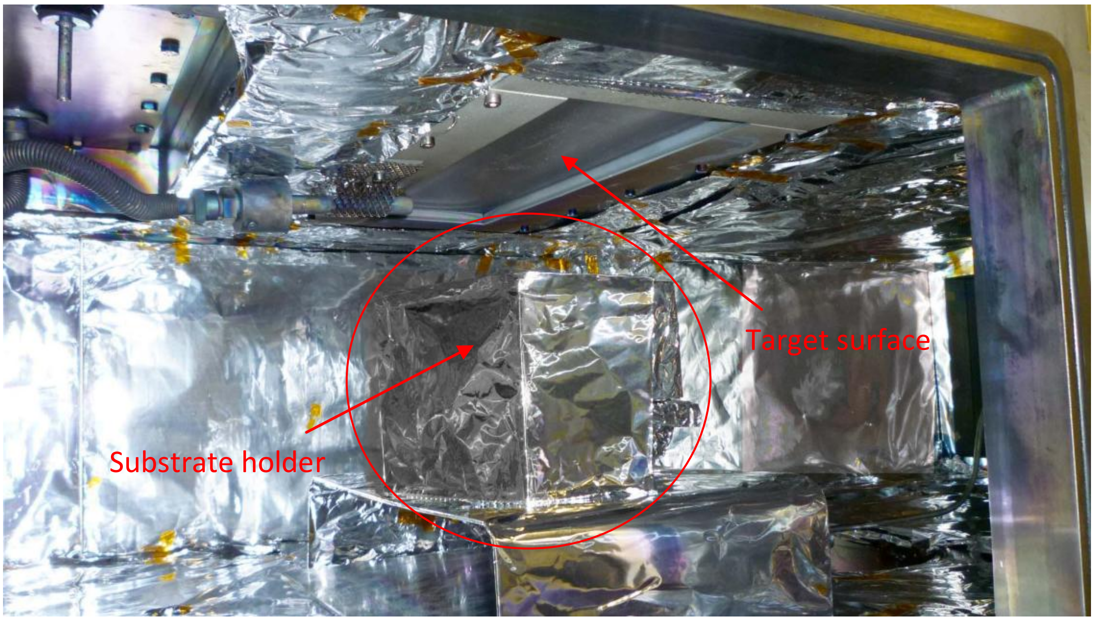

Figure 9.1: Picture shows the substrate holder placed directly under the magnetron in the Large Area coating chamber.

9.2 Standard Analytical Techniques

In order to describe the coatings crystalline structure, topography and composition analytical technique such as Raman, SEM, EDX, AFM, XRD and XRR were performed. To measure silver and sodium diffusion XPS and SIMS depth profiling analysis was completed.

9.2.1 Structural Analysis

The coating thickness was measured by a Dektak® 3M stylus profilometer (Vecco Instruments Inc.) and was determined to be around 1 µm for the titania films and 80 nm for the ZTO, AZO and Si_3N_4 samples. The difference in thickness between titania and remaining coatings was due to analytical requirements. Titanium dioxide coatings were measured by Raman spectroscopy to determine their crystalline structure after annealing at different temperatures. An argon ion laser (green light, 514.5 nm wavelength) penetrates samples to a depth of about 1 µm. Therefore to minimise the signal picked up from the substrate, deposited coatings needed to be around 1 µm thick. For each sample an average of six scans were taken to determine the thickness of the coating.

The crystallographic proprieties of the TiO_2 films were investigated using Bragg-Brentano (B-B) mode on a URD6 Seifered & Co X-ray diffractometer with Cu Kα radiation and flat graphite monochromator on the diffraction beam. The angular step of the sample rotation in respect to the incident beam was 1.5^0 and counting time was 10s/step. To investigate the crystallographic proprieties of the remaining films, coupled θ-2θ X-ray diffraction (XRD, X'Celerator detector) scans were performed using Ni-filtered Cu Kα radiation at 0.154056 nm, scanning the samples from 5 to 75 degrees 2θ for times from 30 minutes up to 5 hours. The analysis was performed under ambient conditions of temperature and pressure by directing an X-ray beam onto a specimen, which is diffracted by the regularly repeating atomic structure of the crystalline phases within the specimen, which produces diffraction patterns. The X-ray diffractometers used in these studies detects X-ray intensity as a function of 2θ angle and the data is displayed as a diffractograms. Each crystalline phase in the diffractograms was identified by search matching using a database of 300,000 reference patterns. XRD measurements were taken at Sofia University in Bulgaria (titanium dioxide films) and at

Pilkington's Technology Management Ltd. Analytical Centre in Lathom (Al-doped ZnO, zinc stannate and silicon nitride coatings).

Raman (Renishaw inVia spectrometer with 514.4 nm wavelength of argon ion laser) analysis was carried out to determine the structure of selected dielectric coatings before and after annealing. The analysis was performed to determine the crystalline structure of the coatings and possible isotopic form of the material.

To determine the surface morphology, the dielectric coatings were investigated using scanning electron microscopy (SEM, Zeiss Supra 40VP) operating at 1-3 kV. Energy dispersive X-ray analysis with 40 mm^2 silicon drift detector (SDD, Zeiss Supra 40VP) with the ion beam energy of 8 keV was used to determine the stoichiometry of the deposited materials.

Spectrophotometric analysis was carried out to find the refractive index n and extinction coefficient k values of the transparent coatings. Transmission and reflection spectra were acquired using a Hunterlab Ultrascan spectrophotometer and modelled using CODE software.

Atomic force microscopy (AFM, Multimode SPM with Nanoscope III controller with the WSXM software) was used to measure the roughness of the zinc stannate selected samples. The AFM was operated in jumping mode (JM), which is the midpoint between classic contact and dynamic modes. It works similar to pulse force microscopy (PFM), which uses scanning mode to minimise shear forces. The difference between PFM and JM is that the first one is implemented electrically, whereas JM is a software method running in the processor memory. JM operates in cycles repeated at each image point with the following steps: tip-sample separation, lateral tip motion at the furthest tip-sample distance, tip-sample approach and feedback, which is performed on the cantilever deflection. Most AFM heads use optical beam deflection to detect the cantilever bending, but in JM mode, the voltage corresponding to the zero force level when the tip-sample distance in the maximum is measured. The set point is then recalculated to correct the zero force level fluctuations. [124]

Silicon nitride samples were analysed by X-ray reflectometry (XRR) to find the thickness, surface roughness and the density of the thin films. Reflectograms were obtained by scanning samples for 2 hours by phase detector. The measurements were performed under ambient conditions of temperature and pressure by directing an X-ray beam onto a specimen. The detector measures the intensity of the X-ray beam at an angle equal to the incident angle from the sample surface (ω=θ). The criteria on which the XRR assignments are based on the correlation of the model fit to the measured data, and the correlation between the model stack to the expected stack. Hence, an excellent fit means that the model fit strongly corresponds to the measured data line giving very low level of uncertainty of the modelled data. Thickness, roughness and density values for every layer are close to that of the expected stack. Good fit shows model fit, which largely corresponds to the data line with some discrepancies, giving low levels of uncertainty for the model data. Thickness, roughness or density values of some layers are different than expected. Satisfactory fit represents model fit that roughly corresponds to the measured data line and hence shows an average level of uncertainty. Thickness, roughness or density of most layers varies from the expected. And finally poor fit express model fit, which only corresponds to a small amount of the measured data. Thickness, roughness or densities of all layers are doubtful; therefore high levels of uncertainty are assigned to the model data.

9.2.2 Diffusion Measurements

The amount of diffusion in most of the samples was measured using time of flight secondary ion mass spectrometry (ION TOF 5) with a Bi_3^+ analysis beam and a 1 keV Cs^+ sputter beam. The sputtered beam was rastered over a 200 µm×200 µm area and the bismuth beam was rastered over a 50.8 µm×50.8 µm area at the centre of the sputtered area for each sample. Caesium creates positive and negative ion clusters with neutral species which are sputtered from the surface. The signal level of CsM^+ clusters are less matrix dependent than from M^+ ions and are the ions species of choice taking into account other factors such as peak intensity and peak overlaps. In TOF-SIMS a pulsed beam of bismuth ions is directed into a sample surface. The ions liberate neutral and charged elemental and molecular species from the surface. Ions can be selectively extracted and detected using a TOF system in which ions are separated according to their mass. [125] A separate rastered beam of caesium ions is used to remove material from the surface over a defined area. Analysis on the centre of the crater is carried out using the bismuth beam. The process is repeated every second or so until the coating has been penetrated and the glass substrate has been reached.

Diffusion in titania samples was measured using secondary ion mass spectrometry (SIMS, Cameca ims 3f spectrometer) with magnetic sector detector and X-ray photoelectron spectrometry (XPS VG-ESCALAB 220iXL spectrometer). In SIMS the primary ion energy of oxygen ion gun used to sputter material from the samples was 10 keV. An automatic routine was used to adjust the sample voltage to compensate for sample charging effect. The routine maximises the signal (50 Ti in this case) by varying the sample potential, thus effectively compensating for the drift in sample potential away from the optimum. This accounts for the lack of signal at the very surface of the sample. When the routine finds the right potential the signal appears. The routine checks the sample potential every 10 to 20 cycles.

XPS depth profiling was carried out to determine the silver and sodium diffusion. The pressure in the analysis chamber was typically 1.066×10^{-8} Pa and photoelectrons were collected from a 10 mm^2 sample area. The Al Kα monochromatic X-ray source was used with an argon ion gun, which bombarded the sample surface with energies of 3-5 keV. Ejected material travelled to the hemispherical sector analyser (HSA), where it was analyzed.

In order to find diffusion coefficient values for Ag and Na in the analysed samples Fick's second law equation for infinite couple with constant surface composition was solved. [84] Calculations were performed using a macro programme configuration written for commercially available software[1]. However before the diffusion coefficient values were found the diffusion calculator has normalised the raw SIMS depth profiling data converting intensity measured in counts per second into relative silver concentrations. Values were standardised to the highest value of pure Ag (used as a 100% of the total intensity measured by SIMS) by multiplying raw silver, matrix (dielectric coating) and silicon (detected from the glass when the substrate surface was reached) data by the factor that scales relative concentration values from 0 to 1. Sputter time has been converted to depth (nm) using empirically measured thickness value of the dielectric coating (matrix) prior to the silver layer deposition as a reference value. Then the diffusion calculator fits the analytical solution of Fick's second law curve into the data finding the concentration of Ag by solving the complimentary error function. Figure 9.2 presents an example of normalised raw SIMS depth profiling data, where the counts are scaled from 0 to 1, and where 1 is equivalent to the highest (100%) silver signal. The circled region shows the area where the calculator fits the analytical

[1] Written by Dr. John Ridealgh from Pilkington Technology Management Ltd.

solution of Fick's second law curve (light blue line marked as 'Fit Ag counts' on the spectrum). The complimentary error function equation is solved at the knee of the curve, at concentration C between 0-0.1 and magnified spectra of that region is shown in Figure 9.3. The entire spectrum was not taken into account due to the analysis (more than one layer is sputtered off the material at once during SIMS depth profiling) and surface effects at the interfaces such as roughness, which does not describe the diffusion mechanism. A similar approach was used for finding the diffusivity of sodium.

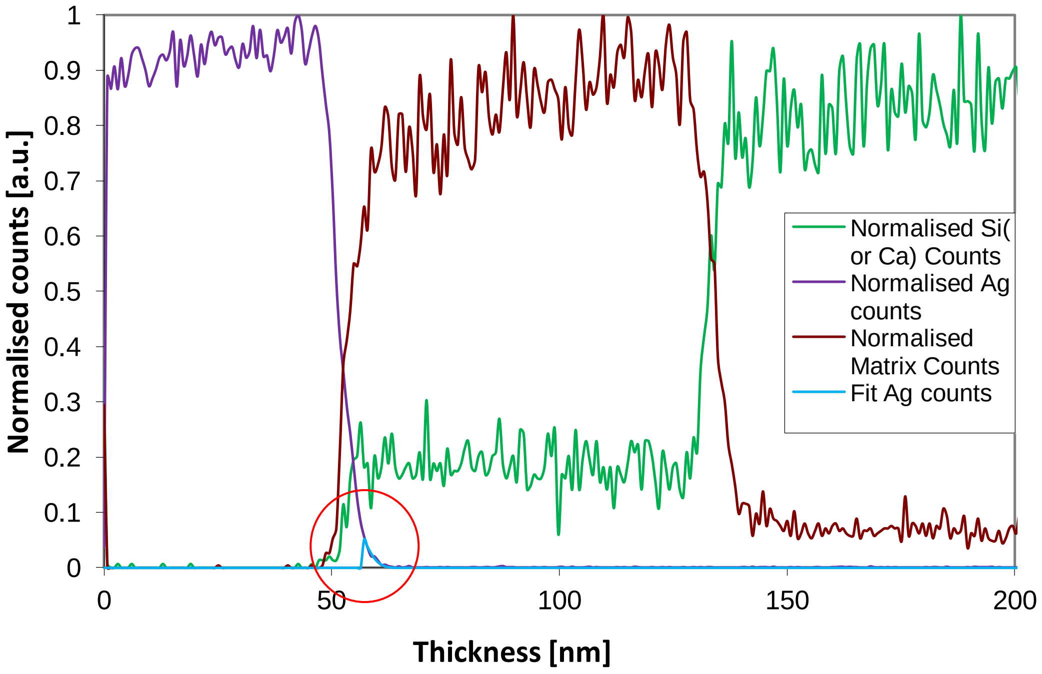

Figure 9.2: Example of diffusion modelling and curve fit into Fick's analytical solution.

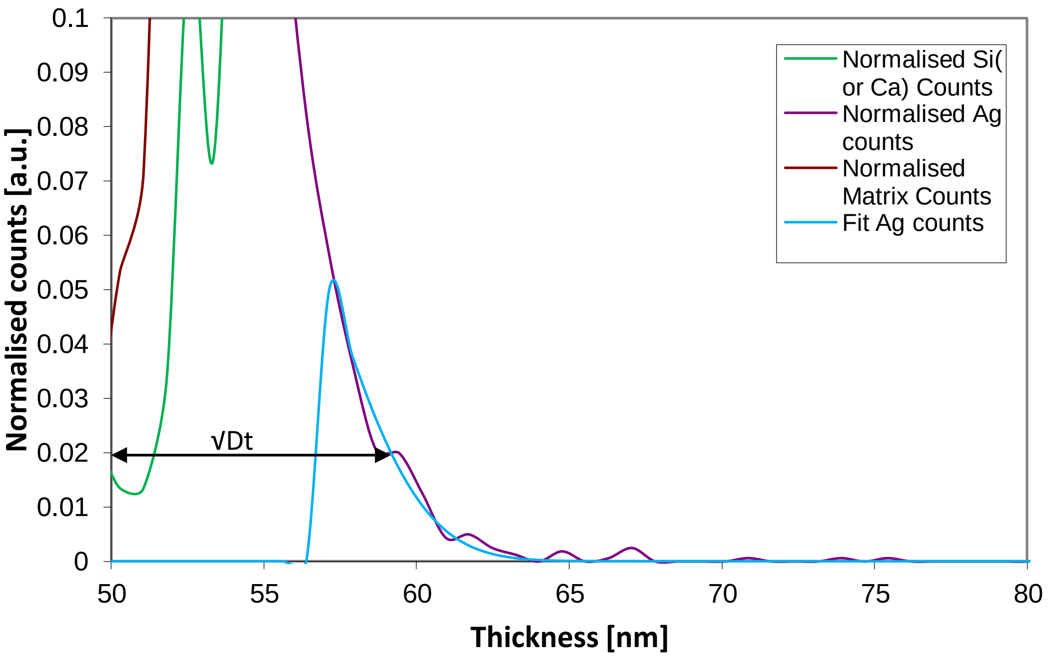

Figure 9.3: Ag counts fitted into Fick's second law analytical solution.

10. Results: Titanium Dioxide Coatings

In this chapter titanium dioxide films deposited by pulsed DC magnetron sputtering will be described. Two independent batches were produced. The first batch was used to determine changes in the crystal structure of sputter deposited titania films after annealing. The second batch was prepared to study the diffusion of silver and sodium atoms through titanium dioxide coatings.

10.1 TiO_2: Annealing Studies

TiO_2 films were deposited onto float glass substrates as described in Chapter 9.1. Coatings were sputtered at pulse frequencies of 100 and 350 kHz at 50% duty, whereas the OEM signals was varied between 10 and 30% of the full metal signal. The operating pressure during sputtering was set to 0.2 Pa. Run details are listed below in Table 10.1. Selected samples were post-deposition annealed in air at the range of temperatures of 100-800^{o}C for 10 minutes using a furnace (Omegalux LMF 3550). The purpose of this study was to investigate changes in the crystal structure of the titania coatings. Raman and X-ray diffraction analysis were carried out to describe the crystal structure of TiO_2 coatings after heat treatment. EDX analysis was carried out to investigate the composition of titania structures deposited under different OEM settings, i.e. different oxygen/argon ratios.

Table 10.1: Run conditions for the deposition of titania samples.

Sample number	Frequency [kHz]	Deposition time [minutes]	OEM signal [%] at λ =507 nm	Thickness [µm]
1	100	180	20	1.55±0.02
2	100	180	30	3.37±0.07
3	350	180	20	2.46±0.05
4	100	180	10	1.41±0.03
5	100	180	15	1.64±0.05

All of the samples were deposited for a period of three hours, and the variations in thickness are due to the differences in the metal content during sputtering. The thickness of the samples varied from 1.41 to 3.37 µm and the thickest sample was deposited at the highest OEM signal (lowest oxygen flow rate). This agrees with a general rule that pure metals have higher deposition rates when sputtered, than their oxides/nitrides deposited reactively by magnetron sputtering techniques. The stoichiometric composition of synthesised TiO_2 consisted of 33.3 at % (60 wt %) of Ti and 66.6 at % (40 wt %) of O_2. The EDX analysis showed that the composition of titanium dioxide samples deposited in this study is close to the stoichiometric composition, however samples 1, 4 and 5 present the nearest values. Results from EDX analysis are shown in Table 10.2. It can be seen that the relatively small changes in the OEM signals did not make much difference to the film composition according to EDX results, however this could be related to the detection limit and the accuracy of EDX analysis. There was quite significant difference obtained in coatings colouring, which is related to the oxygen flow rate used during coatings deposition. The titania deposited under the lowest oxygen flow rate was the darkest (metal rich), therefore the transparency of the glass was significantly decreased.

Table 10.2: EDX elemental analysis of TiO_2 coatings.

	Sample 1	**Sample 2**	**Sample 3**	**Sample 4**	**Sample 5**
O at %	66	65	65	67	66
O wt %	39	38	38	40	39
Ti at %	34	35	35	34	34
Ti wt %	61	62	62	61	61

As-deposited samples were analysed using Raman spectroscopy and then annealed and re-analysed by Raman and X-ray diffraction.

Titanium dioxide can form three main crystalline structures: tetragonal anatase and rutile, which belong to the space group D_{4h}^{19} and D_{4h}^{14} respectively, and lower symmetry orthorhombic brookite (D_{2h} space group representation). [126-127] Factor group analysis of anatase indicates the existence of 15 optical modes with the following representation of normal vibrations: $1A_{1g}+1A_{2u}+2B_{1g}+1B_{2u}+3E_g+2E_u$ [128]

Within this representation $1A_{1g}$, $2B_{1g}$, $3E_g$ are Raman active, whereas the remaining modes are active in Infrared. [128] Table 10.3 shows characteristic Raman shifts assigned for the anatase, rutile and brookite forms of titanium dioxide found in the literature and also provided from Millennium Chemicals Ltd., obtained from nanocrystalline powder standards.

Table 10.3: Observed Raman shifts assigned to titania crystalline structures. Letters assigned to the peak positions for anatase, rutile and brookite standards determine the intensity of the peaks and so vs means very strong peak, s-strong, m- medium, w-weak and sh-shoulder, whereas c represents the combination.

	Millennium Chemicals	**Giolli *et al.*** [127]		**Li Bassi *et al.*** [126]	
	Frequency [cm^{-1}]	Frequency [cm^{-1}]	Symmetry	Frequency [cm^{-1}]	Symmetry
Anatase	144 vs	144 vs	E_g	144	E_g
	197 w	197 w	E_g	197	E_g
	320 vs				
	399 s	400 m	B_{1g}	399	B_{1g}
		507 m	A_{1g}		
	515 m	519 m	B_{1g}	519	
	639 m	640 s	E_g	$A_{1g}+B_{1g}$	
	795 w			639	E_g
Rutile	143 w	143 w	B_{1g}	143	B_{1g}
	273 sh	247	w		
	320 w	$B_{1g}+B_{1g}$			
	357 w				
	447 s			447	E_g
	519 m	447 s	A_{1g}		
	612 s			612	A_{1g}
	826 w	616 m	A_{1g}	826	B_{2g}
		826 w	B_{2g}		
Brookite	128 s	128 s	A_g		
	135 w				
	153 vs	153 vs	A_g		
	214 w				
	235 m(c)				
	247 m	247 m	A_g		
	288 w				
	322 w				
	366 w	366 w	B_{2g}		
	396 sh				
	412 w				
	454 w				
	461 w				
	502 w				
	545 w				
	585 w				
	636 s	636 s	A_g		
	950 sh				

There are many papers in the literature, which indicate that the peak position, shape and intensity of Raman peaks are related to sub-stoichiometric defects, quantum confinement effects, crystal sizes, nanocrystallinity and large interfacial areas. [126-127, 129-130] As Raman analysis gives information about the nature of bonds, which are affected by the structure of a particular phase and the local surroundings around atoms, it implies that indeed peaks shapes and positions obtained from Raman thin film analysis would have to be influenced by film stoichiometry and crystal related distortions. Moreover peaks obtained from titania films produced in this work are compared against pure titania nano-crystals, therefore any impact from phase mixtures, stoichiometry or degree of crystallisation in the analysed films can have a quite significant impact in Raman shifts against the powder standard.

The Raman spectra presented in Figure 10.1 were collected from as-deposited samples 1-5. Samples are aligned with nanocrystalline rutile and anatase powder standards (provided by Millennium Chemicals Ltd.) to compare the shape, peak position and intensity, and therefore the structure of the titania coatings.

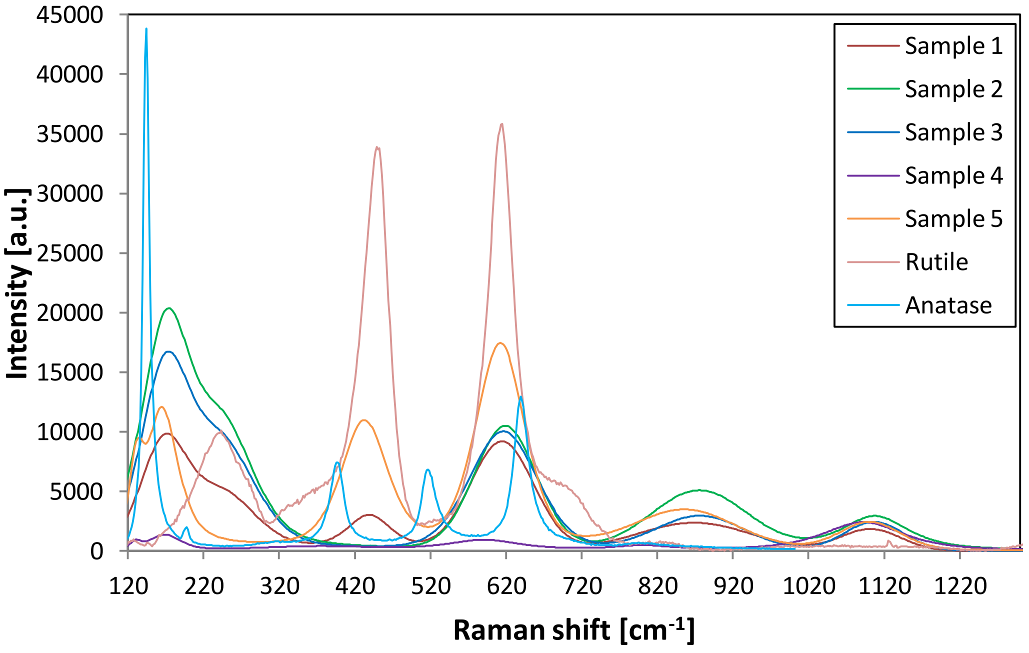

Figure 10.1: Raman spectra of titania coatings collected from samples 1-5 and rutile and anatase standards.

Comparing the spectra analysed by Raman with the rutile standard in Figure 10.1, it is seen that the rutile standard peak situated at about 612 cm^{-1} can be obtained in all samples. However the peak at 448 cm^{-1}, is shifted to a lower number and has relatively low intensity for most of the samples. The rutile shoulder peak at 237 cm^{-1} can be barely seen in sample 1 and sample 2, as it is overlaid with a lower Raman shift peak situated at about 185 cm^{-1}. Furthermore sample 2 does not show evidence of a peak at 448 cm^{-1} shift, which may suggest that peaks detected in this samples come from amorphous vibration in the molecules. Moreover strong peaks at lower shifts (185-200 cm^{-1}) detected in most of the samples may indicate a mixture of a weak anatase or brookite formation. Anatase is represented by a high intensity peak at 144 and a weak peak at 197 cm^{-1}, whereas brookite shows a strong shift at 153 cm^{-1}. Samples 3 and 4 show no evidence of the characteristic peak at 448 cm^{-1} shifts for rutile either. Sample 4 represents a very flat spectrum with a very weak structure at about 620 cm^{-1} shift. These spectra may suggest that there is no significant crystallinity in the TiO_2 in the analysed samples and the peak obtained from Raman spectroscopy comes from amorphous vibrations. On the other hand sample 5 shows the characteristic rutile shift with relatively high peak intensities, and the position of these peaks is in good agreement with the crystalline rutile standard.

For the most of the peaks obtained by Raman in this work, peak broadening and shifting to higher wavenumber can be seen (see Table 10.4). Giolli *et al.* [127] showed that peaks up shifting and broadening in nanocrystalline anatase are caused by non-stoichiometric composition of the material or by small particle sizes. Khan *et al.* [129] also suggested that peak broadening occurs due to nanocrystallinity and quantum confinement effects. The quantum size effect in the Raman spectra of nanocrystalline anatase and rutile thin films was measured by Balaji *et al.* [131] It was found that there is a characteristic dependency between grain size and peak position and broadening in Raman analysis. Finally Li Bassi *et al.* [126] pointed out that materials with smaller particles (~4.4 nm) have Raman spectrum similar to that of amorphous materials. Very broad peaks may be, therefore, caused by background noise indication, which is quite characteristic of amorphous materials.

Broad and weak peaks at about 1100 cm^{-1} arise from the glass surface, as found by Xie *et al.* [132]

Table 10.4 summarises the peak positions obtained from Raman analysis for samples 1-5, assigned with peak positions for anatase, rutile and brookite.

Table 10.4: Raman peak positions for the as-deposited titania samples and powder standards.

Anatase	**Rutile**	**Brookite**	**Sample 1**	**Sample 2**	**Sample 3**	**Sample 4**	**Sample 5**
144 vs 197 w	143 w	153 vs	185	190	200	200	190
	273 sh		270	270	275		270
	320 w	322 w				330	
	447 s	454 w	455	450	460		450
		585 w				575	
	612 s		615	605	605		610
	826 w		830	820	830		855

Figure 10.2 shows Raman images collected from as-deposited sample 1 and the same sample heat treated at 200 and 300°C. Samples are aligned with the rutile standard. It is clearly seen that the sample annealed at 200°C no longer indicates rutile-like shifts in the Raman spectrum. However the same sample annealed at 300°C shows similar shifts to the as-deposited one. This may suggest that, during annealing at a relatively low temperature range, titania loses its rutile-like structure and becomes amorphous, and that the rutile-like structure seen here is detectable again, after annealing at higher temperatures. This would mean that at relatively low annealing temperature we have seen the dissolution of the rutile-like structure which was formed in magnetron sputtered titania samples. However it would be more likely to assume that the as-deposited titania as well as those annealed at the temperature range of 100-300°C show Raman shifts which are represented by an amorphous vibrations.

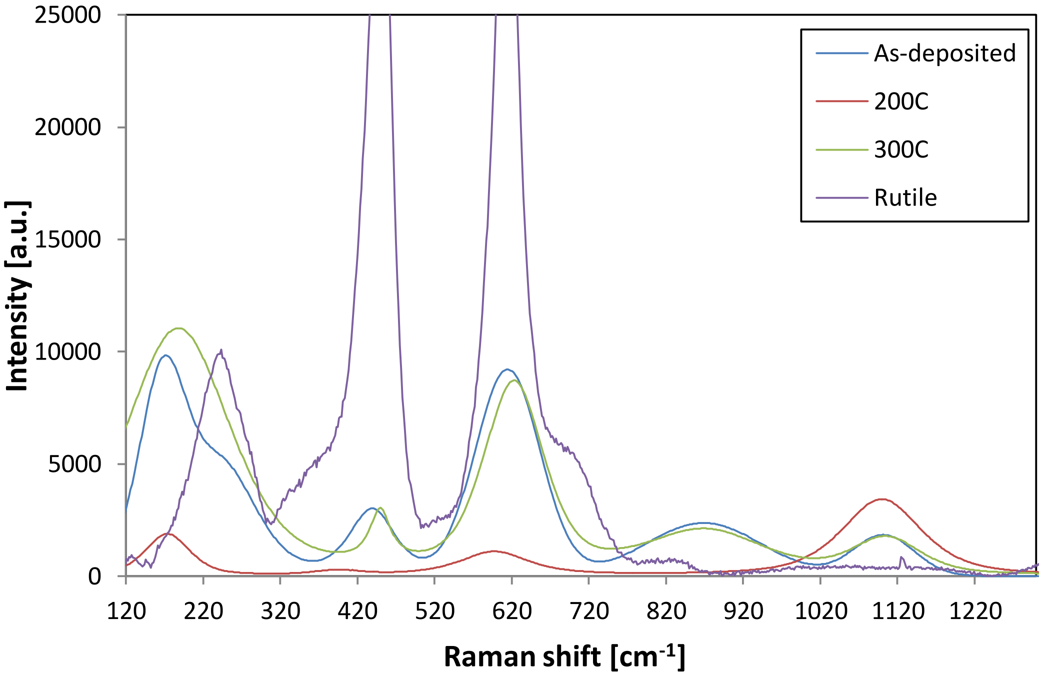

Figure 10.2: Raman spectra of sample 1, as-deposited and annealed at 200 and 300°C compared with a rutile standard.

Samples annealed at the temperature range of 400-800°C show similar Raman spectra. The rutile-like structure has disappeared, but instead very strong anatase peaks have been obtained. Figure 10.3 shows results obtained for samples annealed at 400, 700 and 800°C, aligned with the anatase nanocrystalline powder standard.

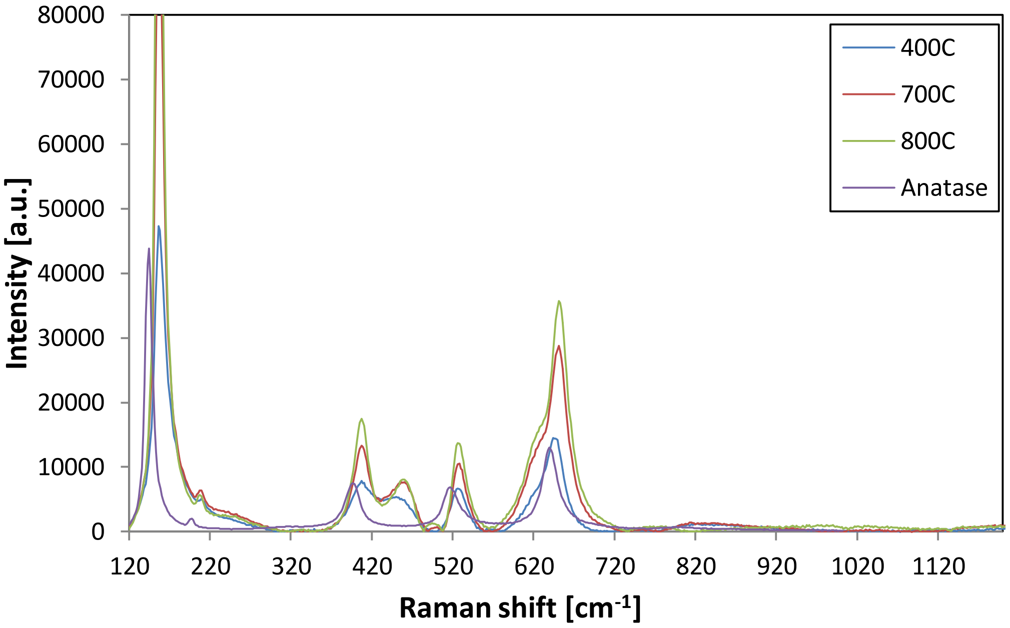

Figure 10.3: Raman spectra of TiO_2 coatings annealed over the range of temperatures from 400 to 800^o C aligned with the anatase standard.

For each sample the peaks have been shifted to higher positions than those characterised by the nanocrystalline anatase powder standard. Moreover an extra peak appears in samples annealed at relatively high temperatures at about 460 cm^{-1}, which probably indicates the presence of the rutile or brookite phase in the crystal structure. This peak increases with rising annealing temperature. Moreover a very weak shoulder is presented at 620 cm^{-1} which also represents one of the characteristic shifts in the rutile structure. This may suggest that the titania structure is shifting from anatase to the rutile phase, as it is known that rutile tends to form in highly energetic processes, therefore high temperature annealing may initiate the rutile forming process. Nevertheless comparing peak positions found from Raman analysis with standard peak positions for anatase, rutile and brookite assigned to the analysed samples in Table 10.5, there is quite significant peaks up-shifting detected. As mentioned earlier in this chapter similar results were found in the literature and were attributed to non-stoichiometric composition of the material and/or small particle sizes. [126-127]

Table 10.5: Raman peak positions for powder standards and titania samples annealed at temperature range of 100-800°C.

Anatase	**Rutile**	**Brookite**	**100**	**200**	**300**	**400**	**500**	**600**	**700**	**800**
144 vs	143 w	135 w 153 vs		136		158	158	158	157	157
197 w			188	178	187					
		214 w				211	210	210	208	208
399 s		396 sh 412 w				406	407	407	407	407
	447 s	454 w 461 w	457		452	458		460	462	462
515 m	519 m					527	527	528	528	528
	612 s		626		624					620
639 m		636 s				645	648	649	652	651
	826 w									

To help clarifying results obtained from Raman spectroscopy, XRD analysis was also performed, as described in Chapter 9.2.1.

Figure 10.4 shows the peak positions for rutile and anatase obtained from sample 1 annealed at 100, 200, 300, 400 and 700°C for 10 minutes, then analyzed by XRD.

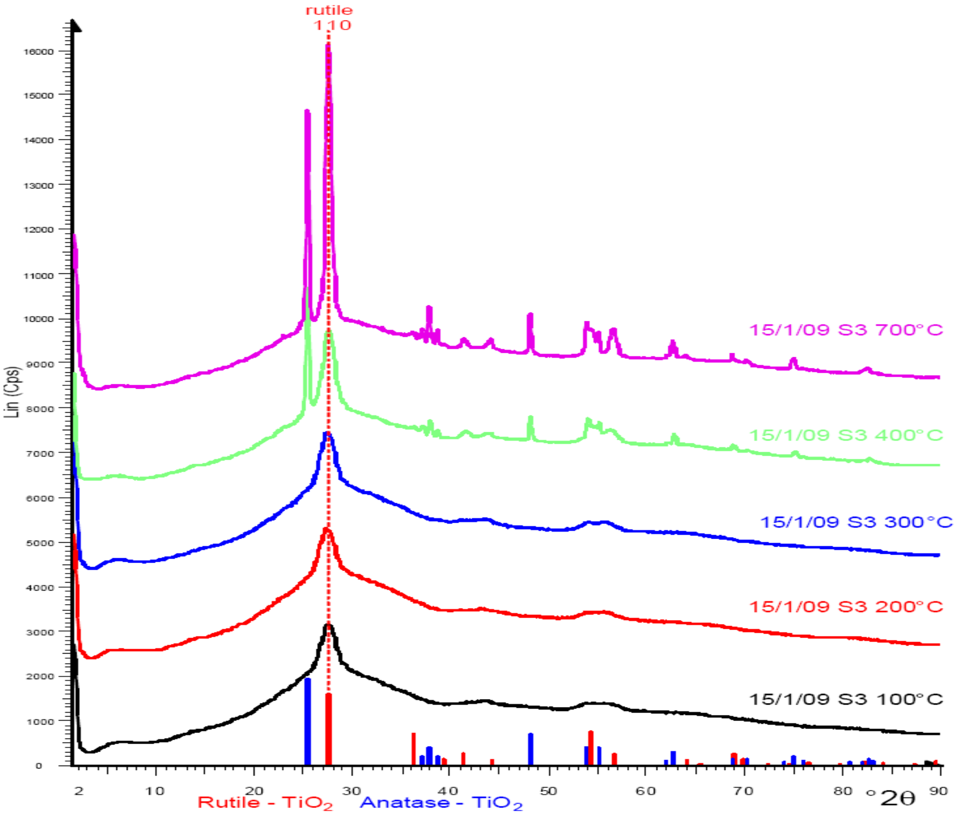

Figure 10.4: XRD spectra collected from sample 1 annealed at the range of temperatures between 100-700^{o}C.

XRD analysis indicates that samples, which were treated at temperatures below 400^{o}C, show an unknown or amorphous phase. This structure has been determined as consisting of a very small grain size (~3 nm). In samples annealed at temperatures higher than 400^{o}C, evidence for a two-phase structure can be distinguished. In both cases rutile is the main constituent of the structure, but this contribution is smaller in samples treated at relatively high temperatures. Also, based on the peak widths, the crystal size for anatase is much larger than for rutile, which may be the reason why in Raman analysis anatase was detected more easily than rutile.

XRD analysis did not show a brookite presence in any of the analysed samples, which discredits the possible presence of brookite suggested by the Raman analysis. Furthermore, this phase is extremely rarely obtained in magnetron sputtered thin TiO_2 films. It is most likely, therefore, that the peaks assigned to samples annealed at the range of temperatures from 100-800^{o}C in Table 10.5 consist of vibrations obtained from anatase and rutile structures only. Moreover brookite has been characterised in the literature by showing its most characteristic peaks at 128 cm^{-1} and 247 cm^{-1}, which have not been detected here. [127] Finally XRD results show that rutile is the dominant phase in the coatings, whereas Raman spectra collected from samples annealed at relatively high temperatures suggested that anatase is the leading form of titania presented in these samples. This may be caused by the significant difference in the grain sizes between rutile and anatase. As mentioned earlier in this chapter, particle sizes are one of the main factors which influence Raman analysis as well as XRD. Generally relatively small grains represent broader, lower intensity peaks, which furthermore in Raman may also cause peak shifting. Therefore, if the anatase component of the films has significantly larger grains than the rutile component it would be the phase easier to pick up and determine by the analytical techniques used in this work.

Table 10.6 shows XRD results obtained from sample 1 annealed at the temperature range of 100-700^{o}C. Crystal sizes are assigned to each coating.

Table 10.6: XRD results obtained from samples annealed at the temperature range of 100-700^o C.

Sample	**% Rutile**	**% Anatase**	**% Amorphous Phase**	**Crystallite size (110) Rutile [nm]**	**Crystallite size (101) Anatase [nm]**	**Crystallite size Amorphous Phase [nm]**
100^o C	-	-	100	-	-	3.3
200^o C	-	-	100	-	-	3.4
300^o C	-	-	100	-	-	3.5
400^o C	70	30	-	4.7	77	-
700^o C	56	44	-	14	110	-

SEM studies were carried out on samples 1-5 and the sample annealed at 800^{o}C, as noticeable changes in film morphology were observed under the optical microscope while Raman images were taken.

Figures 10.5-10.12 show SEM micrographs of the surface and fracture sections of titania samples deposited on float glass. In each case the film appears to have a fully dense structure. In some cases grains can be distinguish on the coating surface. Sample 2 presented in Figure 10.6-10.7 shows very smooth surface with some occasionally pores in the structure, which may be regions were some crystallisation took place. The difference in film surfaces may be due to the higher metal content during film deposition, as this sample has been deposited at a higher total metal OEM signal than the remaining samples. Furthermore, higher metal content while sputtering is also the reason that sample 2 is about twice as thick as the remaining samples. Moreover sample 3, which was sputtered at the higher frequency of 350 kHz, presents more defects (grains and holes) on the sample surface than samples deposited at a pulse frequency of 100 kHz. It can be found in the literature that increasing pulse frequency in magnetron sputter deposition can lead to increased surface roughness due to argon inclusion and re-sputtering of the growing film. [133-135] This may be the reason for the surface defects and non-uniformity of sample 3.

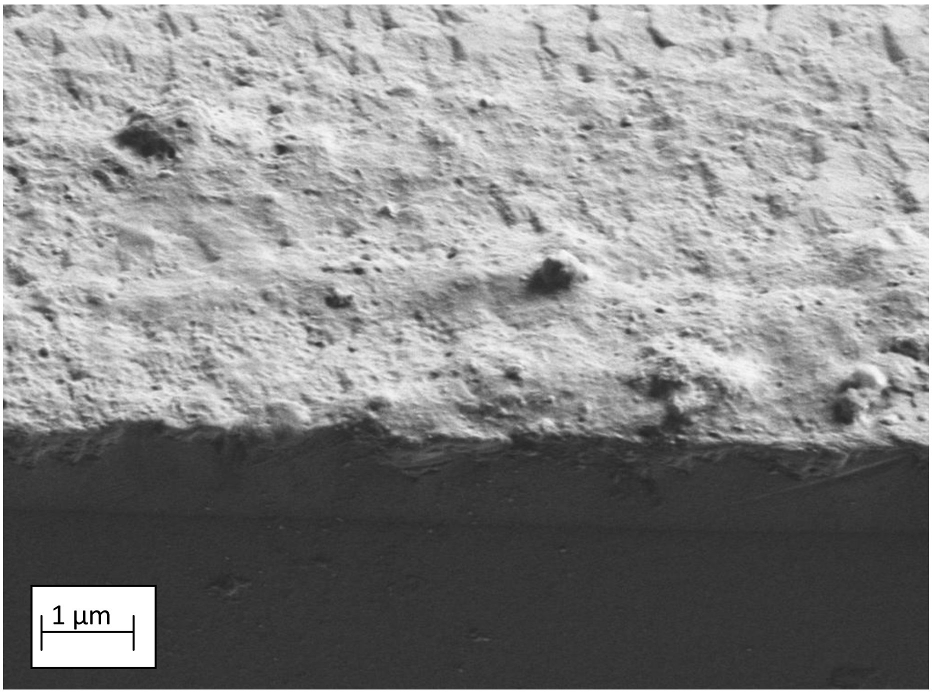

Figure 10.5: SEM micrograph of the fracture section of titania sample 1, deposited onto float glass substrate.

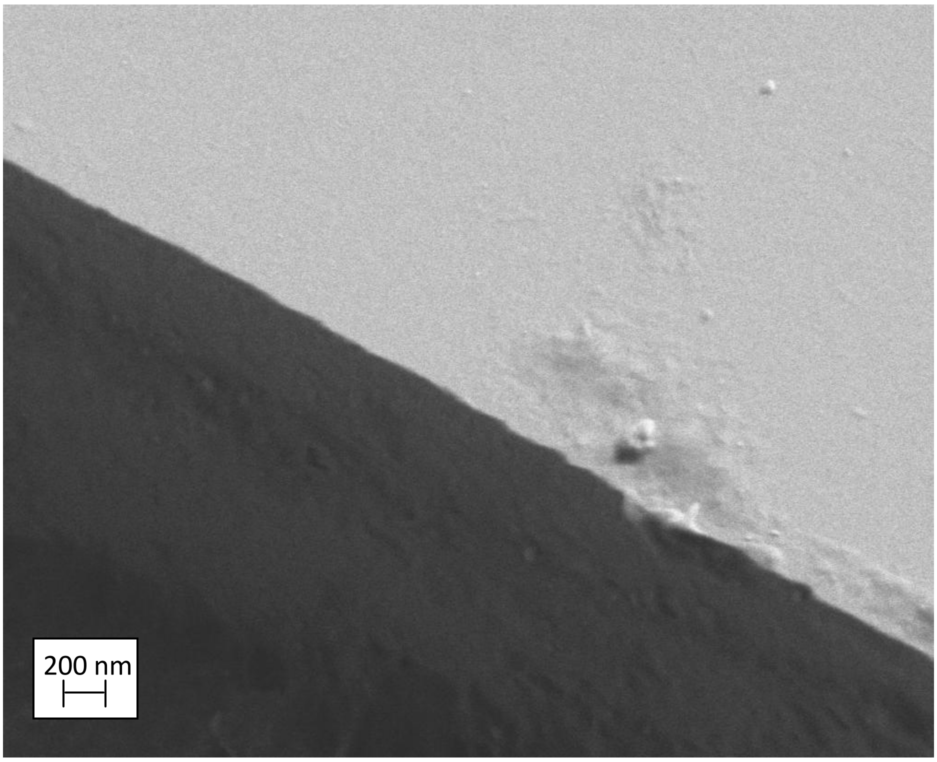

Figure 10.6: SEM micrograph of the titania sample 2 deposited onto float glass substrate, top view.

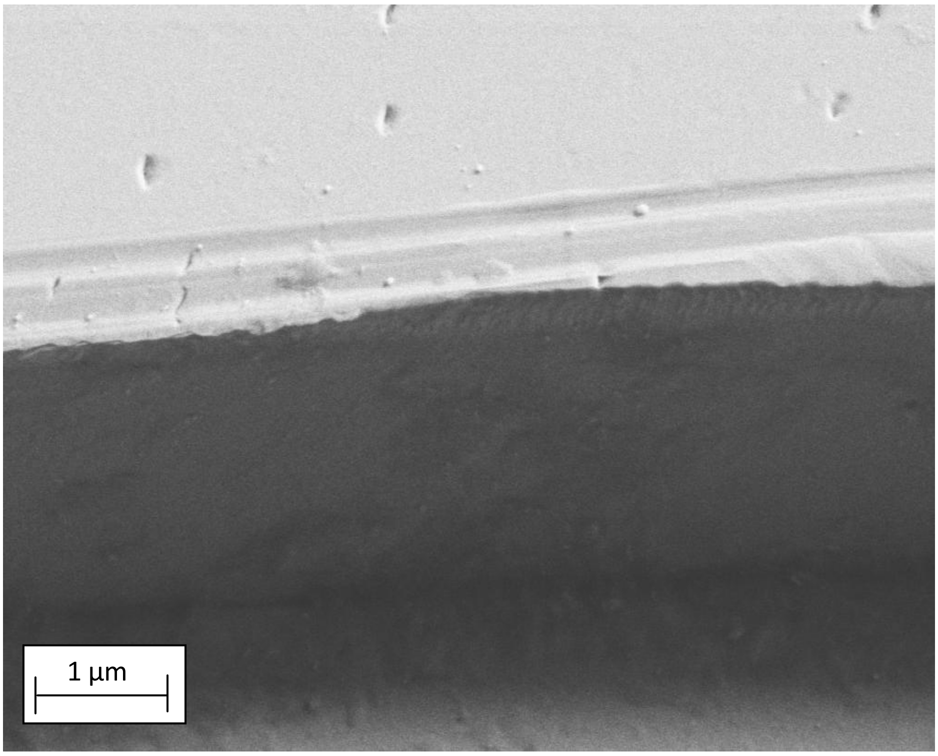

Figure 10.7: SEM image fracture view collected from titania sample 2, deposited onto float glass substrate.

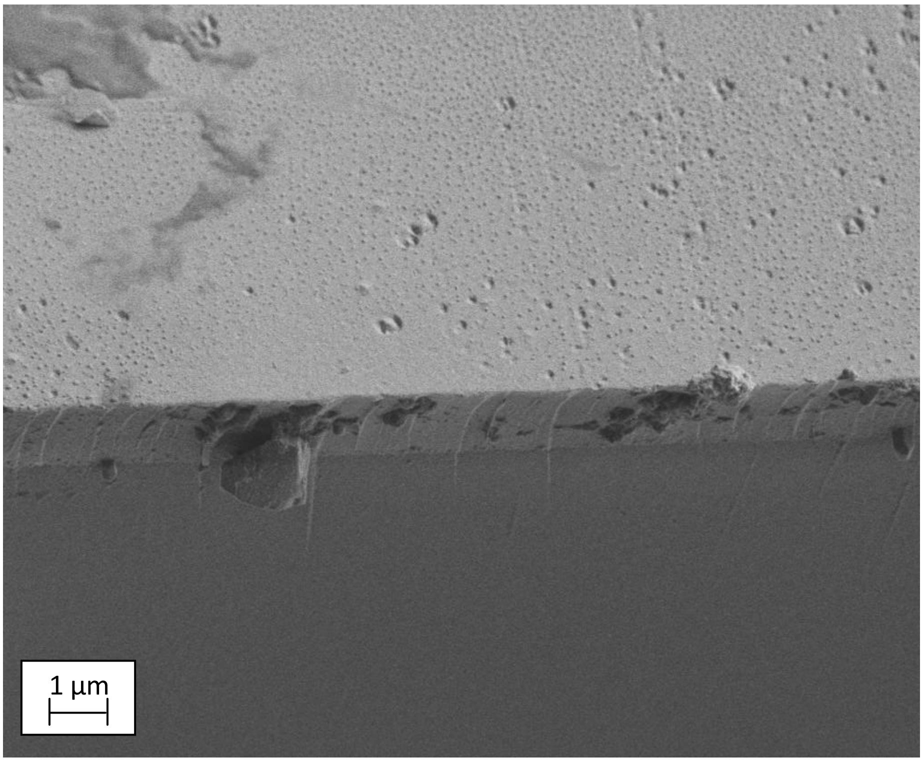

Figure 10.8: SEM image of the top surface of titania sample 3, deposited onto float glass.

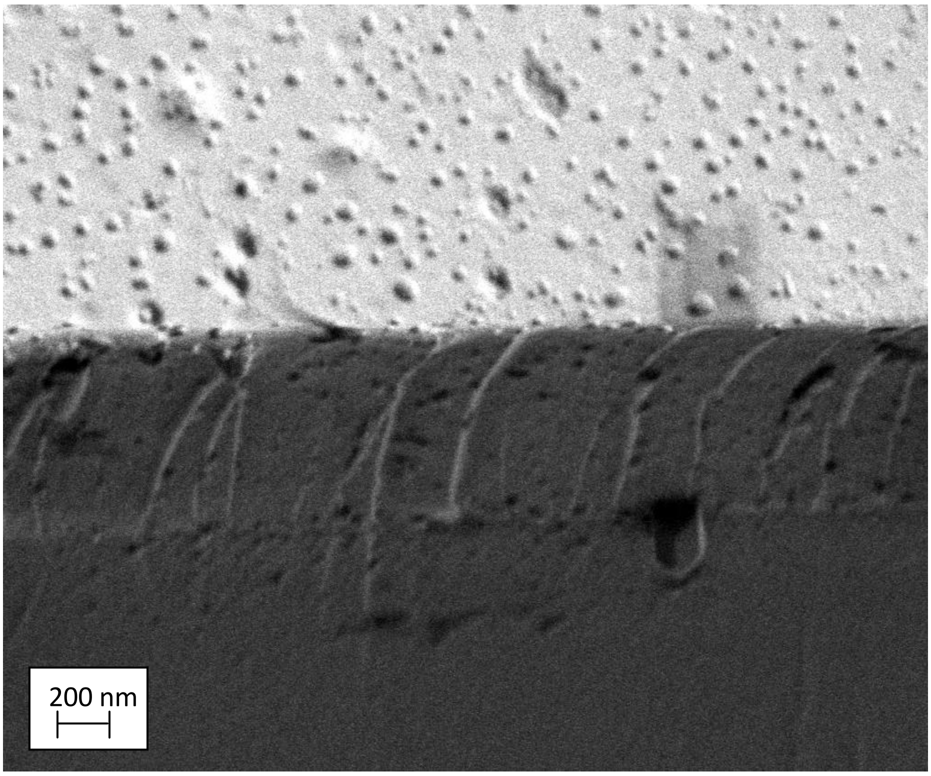

Figure 10.9: SEM micrograph of fracture section of titania sample 3, deposited onto float glass substrate.

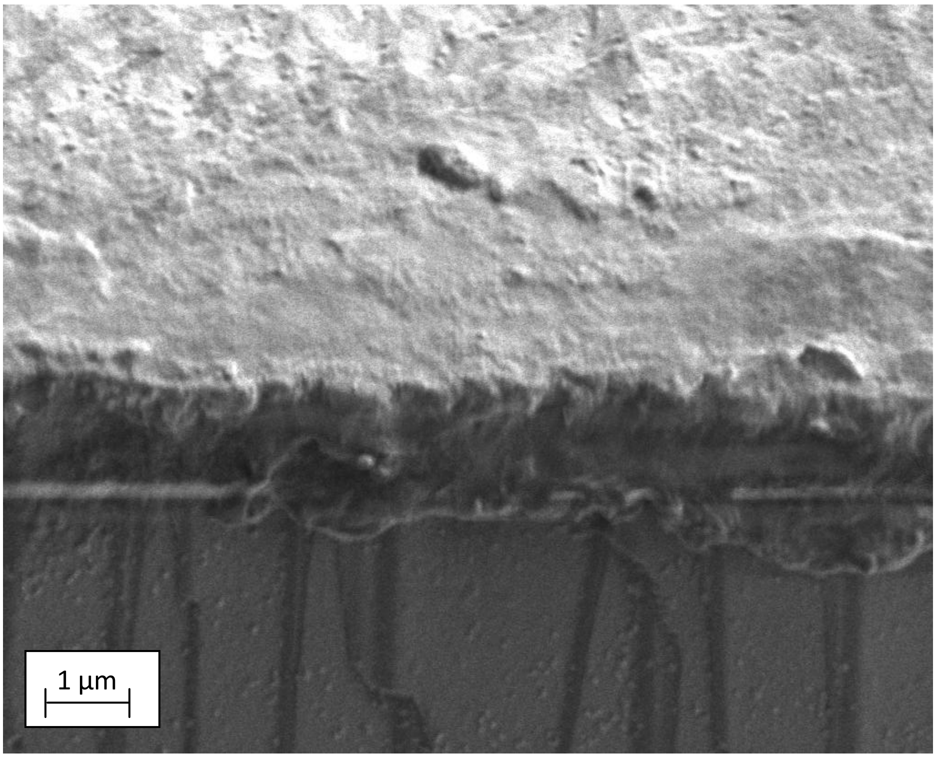

Figure 10.10: SEM image of fracture section of titania sample 4, deposited on float glass substrate.

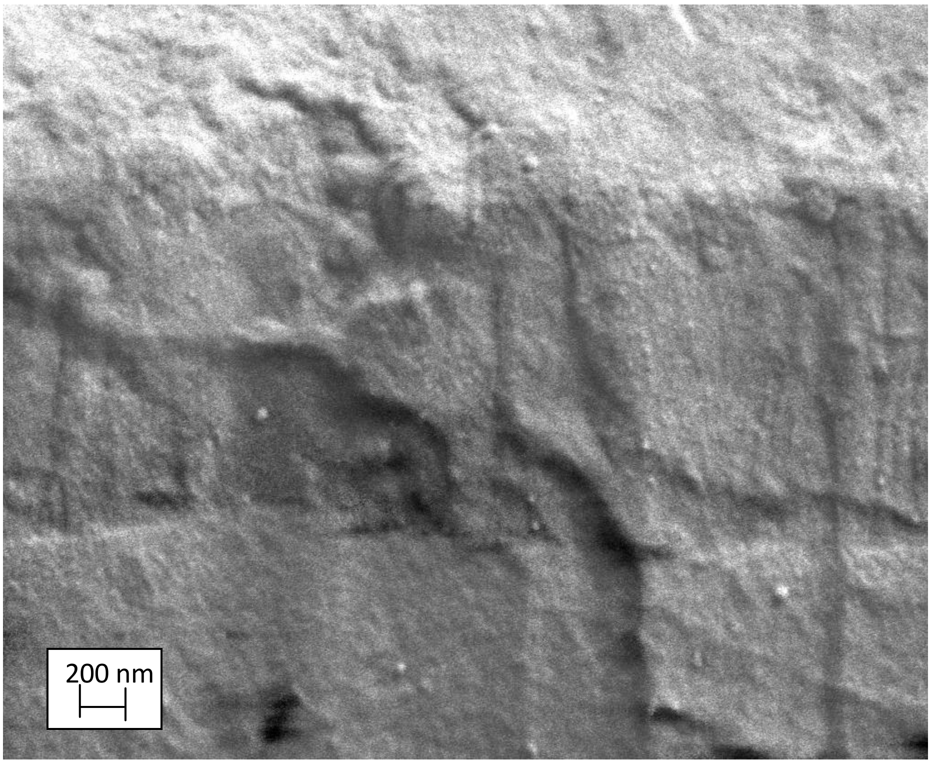

Figure 10.11: SEM micrograph of top surface of titania sample 5, deposited onto float glass.

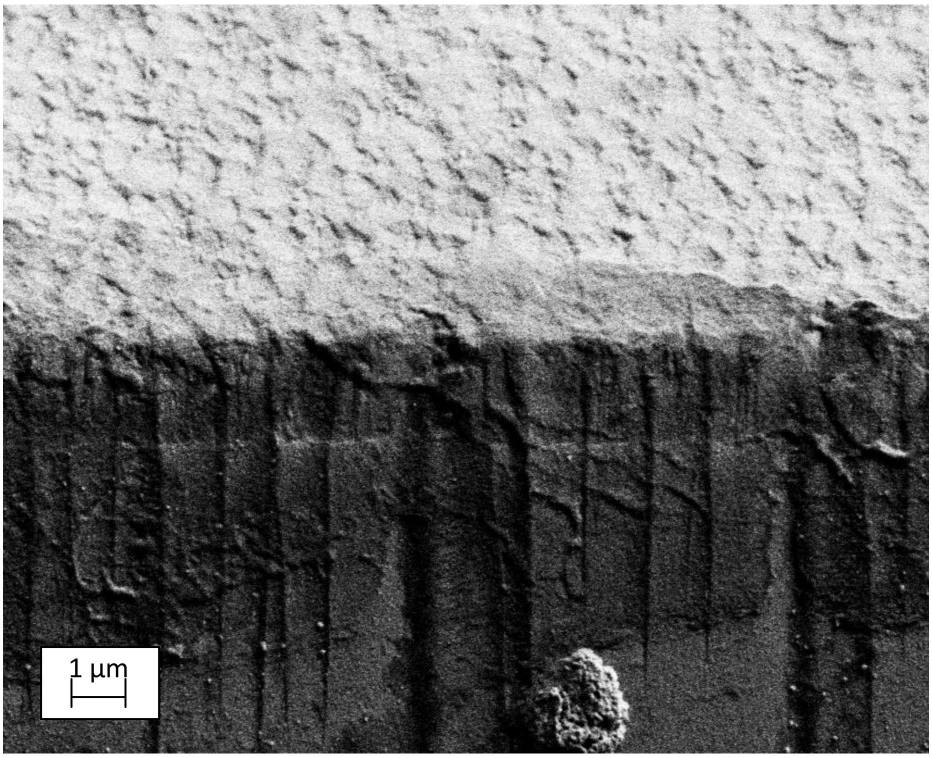

Figure 10.12: SEM fracture view image of titania sample 5, deposited onto float glass substrate.

Visible changes in the surface topography were obtained in samples annealed at temperatures above 600^{o}C. For example, Figures 10.13 to 10.15 show SEM micrographs of the surface of sample 5, annealed at 800^{o}C. Features on the film surface appear to have been caused by post deposition crystallisation processes after treatment at relatively high temperatures, because the surface area of these features increased with temperature, therefore it is clear that the structural changes on the coating surface occurred due to post deposition crystallisation after temperature treatment. Faceted regions or grains (Figure 10.14) and whiskers (Figure 10.15) were observed on sample surface.

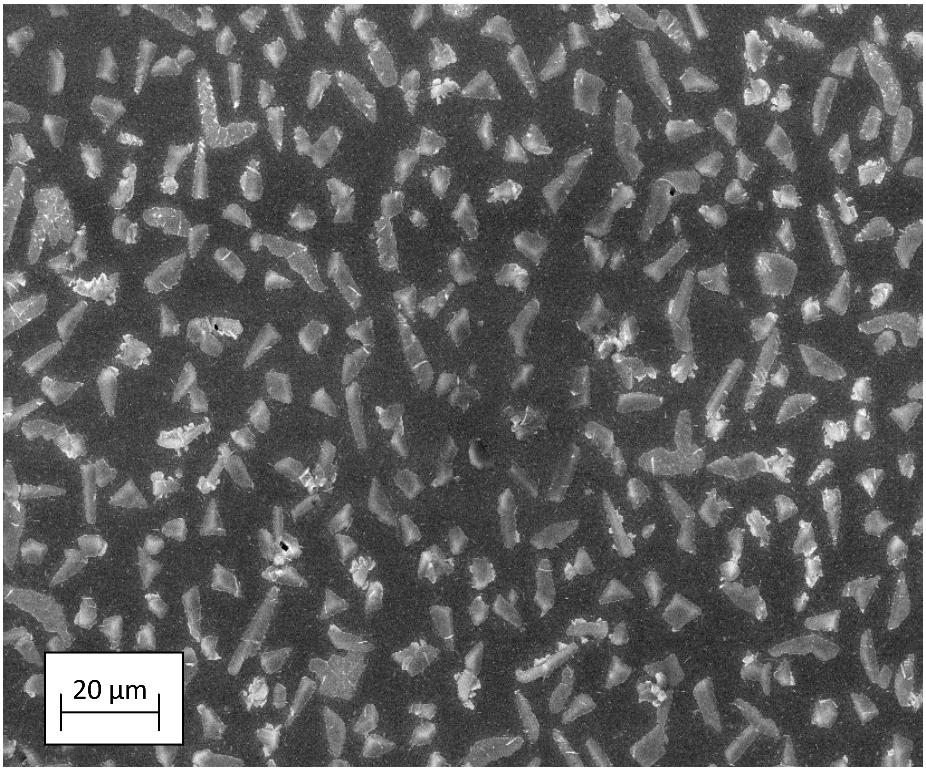

Figure 10.13: SEM top image of TiO_2 sample 5, deposited onto float glass, post-deposition annealed at 800°C.

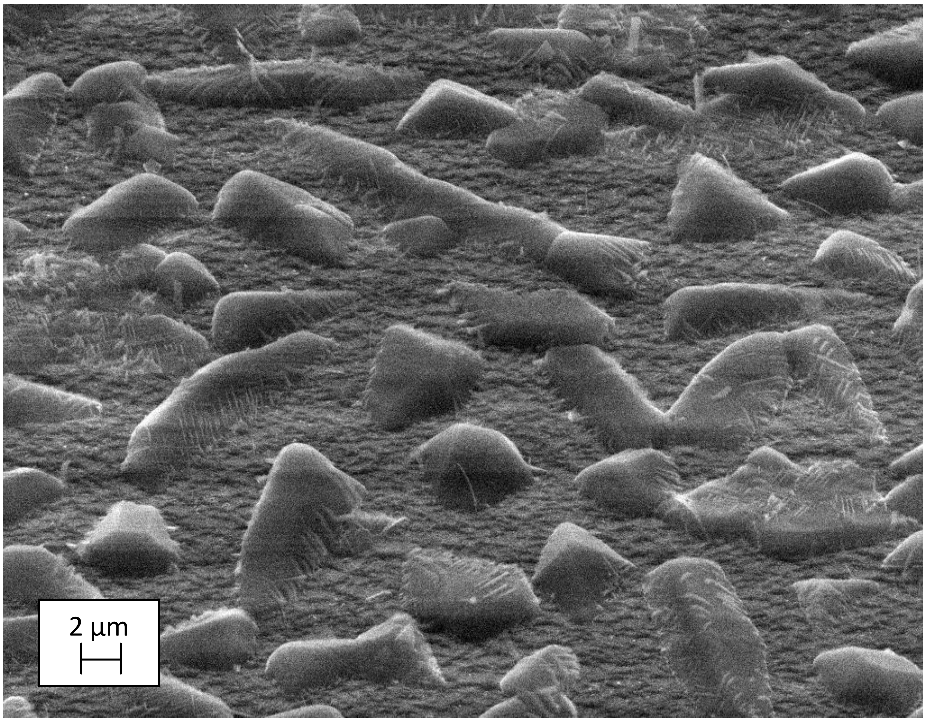

Figure 10.14: SEM micrograph of the surface of the titania sample 5, deposited onto float glass and annealed at 800°C.

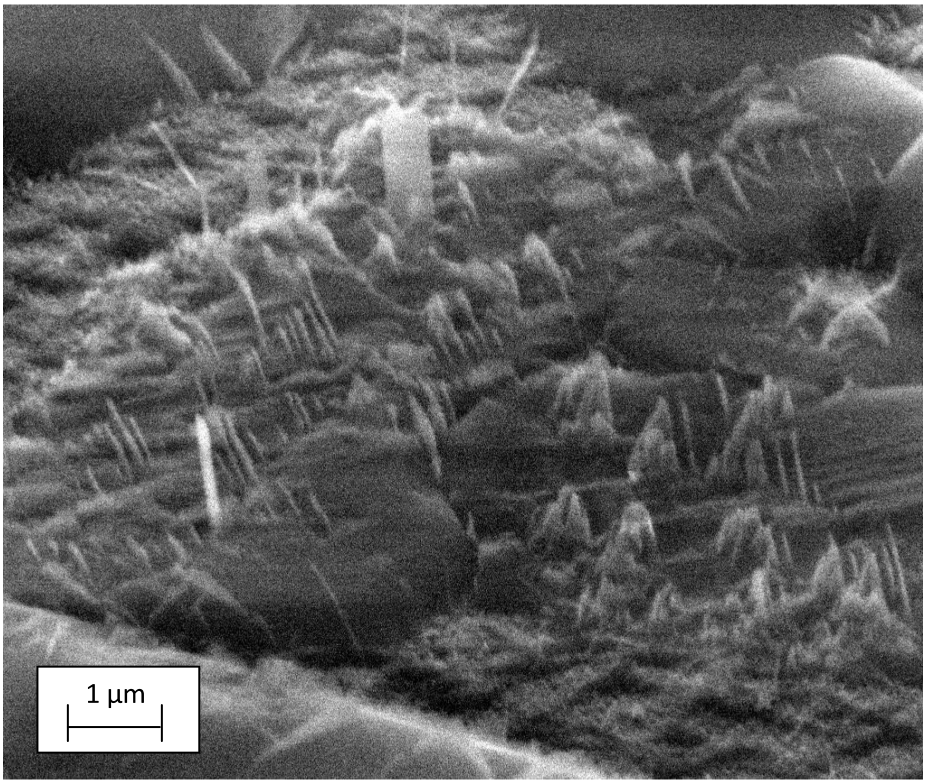

Figure 10.15: SEM image of the surface of the titania sample 5, deposited onto float glass, annealed at 800°C.

To compare if there is any difference in crystal structure between the surface region and the features observed by SEM, Raman scans were taken from the faceted area and the surrounding surface region, respectively. In both cases analysis showed that the crystalline structure stayed the same, but there are differences in peaks intensities. It may suggest that these regions have the same crystal structure as the surrounding surface. On the other hand micro-Raman is not a surface specific technique, and the laser which penetrates to a depth of about 1 µm picks up signals not just from the sample surface but also from the grains underneath.

Spectra obtained from the sample annealed at 700°C are shown in Figure 10.16. Both grain and surface scans present the same shape of the Raman peak (same shifts detected), however they differ slightly in the intensities. This may be due to higher concentration of the detected mixed anatase/rutile crystals in grain areas, as sharper and more intensive peaks indicate higher crystallinity. This suggests that the grains are regions of improved crystallinity, which arose during high temperature treatment.

Following that, Figure 10.17 shows similar results obtained from Raman scans collected from the surface and the faceted regions for the same sample annealed at 800^{o}C. On this spectrum, both on-grain and on-surface Raman scans are identical. This suggests that there is no difference in crystallite concentration between the grains and the surface area. Moreover the sample annealed at 800^{o}C shows more intensive Raman shifts than the sample annealed at the lower temperature. This is related to grain formation, i.e. re-crystallisation due to post-deposition high temperature treatment, as grains grow with increasing annealing temperature, and further crystallisation occurs. Rutile is known to be formed by high energy processes; therefore increasing temperature allows transformation to occur from meta-stable anatase to rutile. Unfortunately further investigations of titania films phase transformation due to high temperature treatment was restricted by the substrate properties. Float glass has softened when was annealed at 800^{o}C.

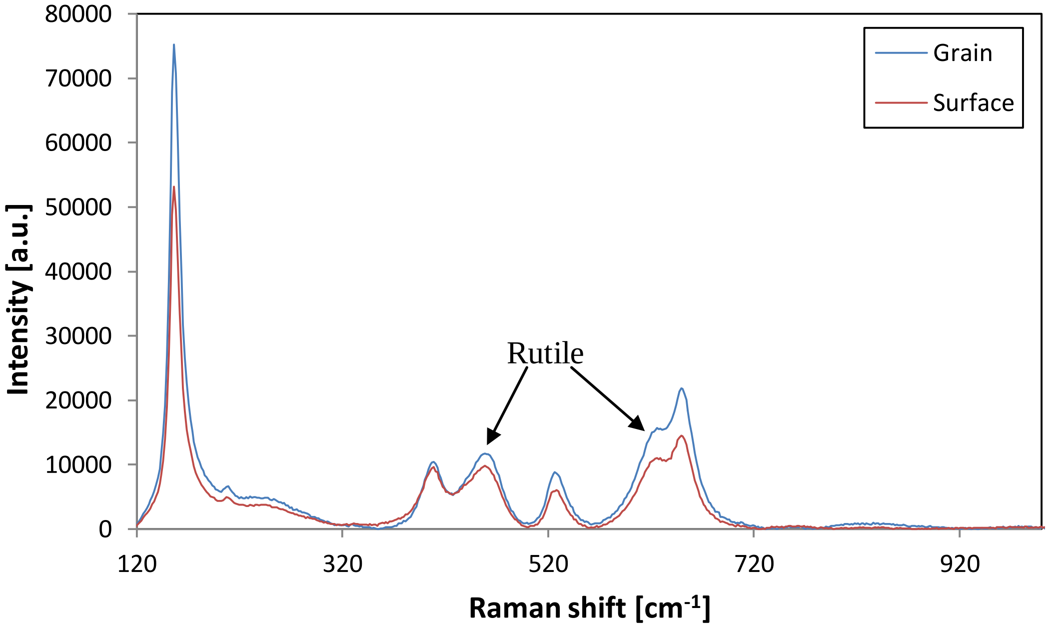

Figure 10.16: Raman images of sample annealed at 700^{o}C. Red- collected from surface, blue- from grain.

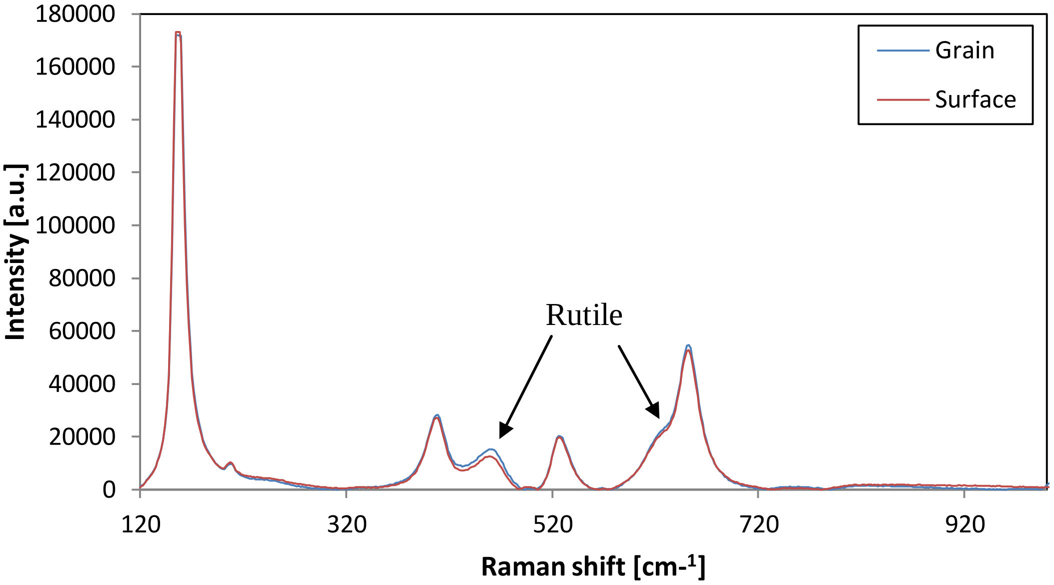

Figure 10.17: Raman images of sample annealed at 800°C, red- obtained from surface, blue- from grain.

10.2 TiO_2: Diffusion Studies

Titanium dioxide films were deposited onto soda-lime glass, at ambient temperature by reactive pulsed DC magnetron sputtering. Samples were post-deposition annealed at the temperature range between 200-600°C for 10 and 30 minutes. Table 10.7 shows annealing conditions for the deposited titania samples.

The temperature range selected for the TiO_2 study was inspired by studies discussed in previous chapter. These temperatures represent the transition points in the crystalline structures of titania coatings. However, an additional annealing time of 30 minutes was introduced here, as the second batch of TiO_2 coatings deposited did not directly follow the trend obtained in the previous studies. This may be due to environmental differences, as both batches were prepared in different vacuum chambers. The second batch was produced in the Teer Coatings rig (UDP450), which differs in shape and capacity from the Large Area rig (see Chapter 7.1), which was used to deposit the previous batch of titania samples. The UDP450 is a cylindrically shaped vessel with a diameter of 660 mm, and 595 mm high. The rotatable substrate holder is placed in the middle of the chamber, and the chamber is designed to take four standard planar magnetrons with target sizes of 100 mm×300 mm. Moreover the base pressure that the Teer rig can be pumped down to is about $5\text{-}6\times10^{-4}$ Pa.

As-deposited and annealed titania samples were analysed by Raman and then were over coated with silver and re-annealed at 250°C for 10 minutes. Samples were then analysed by X-ray diffraction (URD6 Seifered & Co X-ray diffractometer) to investigate the crystal structures of the titania coatings and depth profiling analysis was performed by dynamic secondary ion mass spectrometry (SIMS, Cameca ims 3f spectrometer, see Chapter 9.2.2) to investigate the diffusion of silver and sodium atoms through the titanium dioxide films.

Table 10.7: Titania samples annealing conditions and thickness measured by Dektak profilometer assigned to each sample.

Sample number	**Titania annealing conditions**	**Thickness [μm]**
1.1	as-deposited	1.19±0.05
2.1	200°C for 10 minutes	1.19±0.05
3.1	400°C for 30 minutes	1.19±0.05
4.1	400°C for 10 minutes	0.97±0.03
5.1	600°C for 10 minutes	1.19±0.05
6.1	600°C for 30 minutes	1.17±0.06

10.2.1 TiO_2: Coating Characterisation

Raman spectra shown in Figure 10.18 were collected from the as-deposited sample, and samples annealed at 200°C and 400°C for 10 minutes. Spectra are aligned with the nanocrystalline rutile powder standard. Sample 1.1 presents rutile characteristic peaks at 430, 616 and 868 cm^{-1}, whereas the broad peak at about 168 could be mixed brookite phase, or shifted rutile peak from about 273 cm^{-1}. Samples 2.1 and 4.1 show a rutile-characteristic peak shifted to a lower wave number, which at first may suggest that this peak characterises brookite not rutile structure. However, as pointed out in the previous chapter, brookite is usually characterised by two strong peaks at 128 cm^{-1} and 247 cm^{-1}, which have not been seen here, therefore this phase will not be considered.

Broad, shifted peaks presented in the spectrum below may suggest that there is no crystalline structure, or that very weak, small crystallites are presented in these samples. Peaks obtained from Raman may come from vibrations from amorphous areas within the coating.

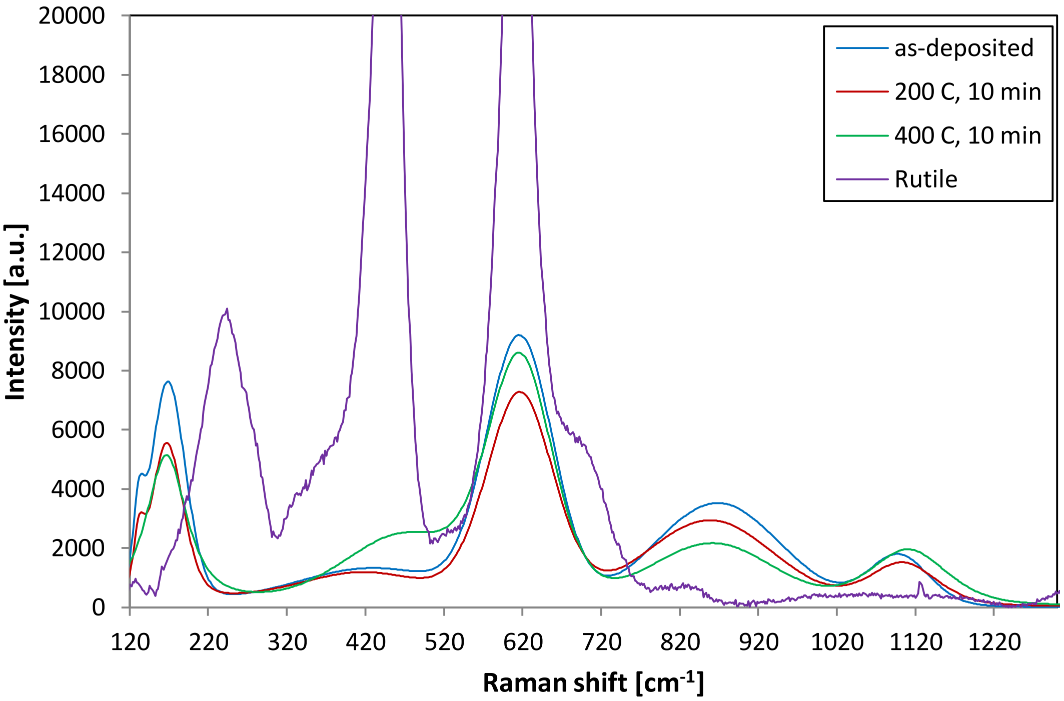

Figure 10.18: Raman spectra of titania coatings from the as-deposited sample and samples annealed at 200 and 400°C, aligned with the rutile standard.

In Figure 10.19 images of samples annealed at 600°C for 10 minutes and 30 minutes and at 400°C for 30 minutes are presented and aligned with the anatase nanocrystalline powder standard. For all samples a distinct anatase structure has been obtained. All samples are in good agreement with the standard sample, however the sample annealed at 600°C for 30 minutes shows much higher peak intensities. This may be due to abnormal grain growth during the longer annealing time, or a higher degree of crystallinity in this sample, than in the remaining ones.

Table 10.8 shows the characteristic peaks obtained from Raman analysis assigned to the standard peak positions for different crystalline structures of titania. It can be seen that samples annealed at relatively high temperatures (400°C for 30 minutes and at 600°C for 10 and 30 minutes) show that anatase is the main phase formed.

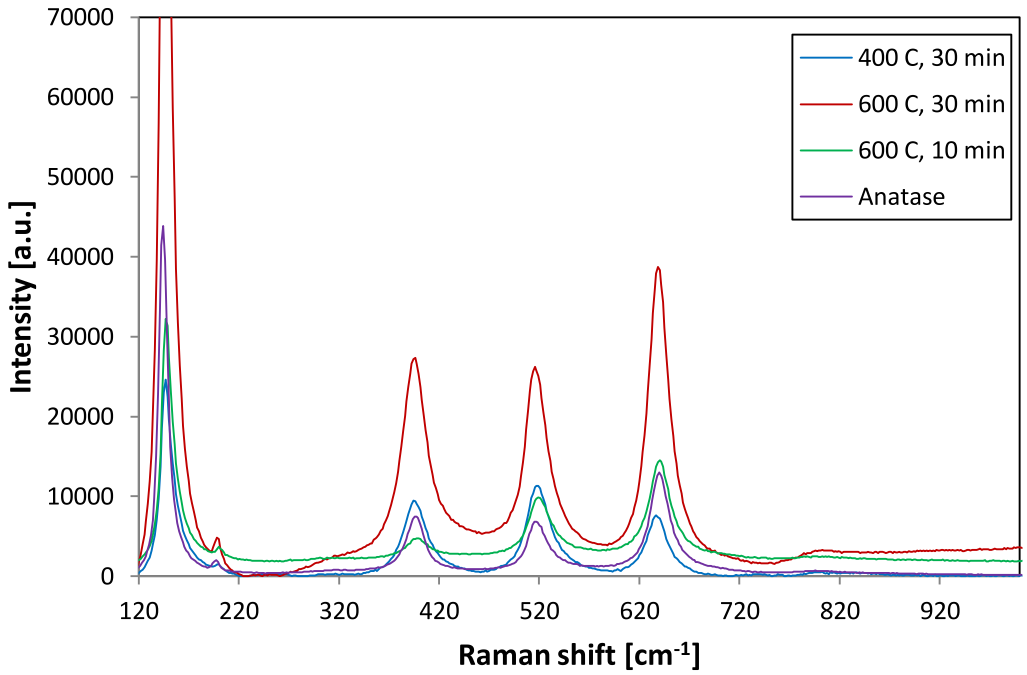

Figure 10.19: Raman spectra collected from samples annealed at 400 and 600^{o}C and anatase standard.

Table 10.8: Raman peak positions detected from samples 1.1-6.1 assigned to TiO_2 crystalline powder standards.

Anatase	Rutile	Brookite	Samp. 1.1	Samp. 2.1	Samp. 3.1	Samp. 4.1	Samp. 5.1	Samp. 6.1
144 vs	143 w	128 s 135 w	131.35	132.55	146.80		146.77	148.93
		153 vs	168.68	165.38		166.6		
197 w					199.70		198.97	199.83
399 s		396 sh			396.17		395.90	397.74
		412 w		414.14		414.54		
	447 s		430.92					
515 m	519 m				519.30		517.312	519.93
	612 s		616.57	616.87		617.44		
639 m		636 s			637.59		639.36	640.33
	826 w		868.11	859.20	828.50	861.61		

The XRD analysis was carried out to determine the crystalline structure of titania coatings. High intensity peaks that can be seen in each spectrum at 38^{o} 2θ represents the silver (111) peak, as samples were measured after Ag deposition. Figure 10.20 show diffraction patterns measured from the as-deposited sample and samples annealed at 200^{o}C, whereas in Figure 10.21 samples annealed at 400^{o}C for 10 and 30 minutes are presented. Finally Figure 10.22 shows samples annealed at 600^{o}C for 10 and 30 minutes. In the region where TiO_2 normally shows diffraction peaks, the patterns of the as deposited sample and the sample annealed at 200^{o}C for 10 min contain distinct halo-like regions (at 2θ between 20 and 50^{o} and between 53 and 75^{o}). This suggests the formation of a disordered amorphous-like structure; however, some relatively low intensive peaks have been also registered. The qualitative phase analysis performed showed that those peaks correspond to a few crystalline polymorphous modifications of TiO_2 namely anatase (tetragonal unit cell), rutile (tetragonal unit cell, but with different parameters and group symmetry from anatase) and β-TiO_2 (monoclinic). Thus, the initial coating has a predominately amorphous structure, but contains a smaller share of a mixture of these three crystalline polymorphs of TiO_2. Annealing at 200^{o}C almost does not change the phase composition and the two patterns are very similar. During the annealing at 400^{o}C the intensity of the TiO_2 peaks increases, which indicates an increase of the share of the crystalline phase. While in the coating annealed for 10 min the intensity of the peaks corresponding to the crystalline phase is still relatively low (the maximum intensity is for the peak corresponding to β-TiO_2), i.e. the contribution of the amorphous phase is still high, in the pattern obtained after 30 min annealing two peaks with relatively high intensity and a few peaks with lower intensity corresponding to anatase have been registered. This points out that in the coating annealed at 400^{o}C for 30 min a predominately polycrystalline anatase phase has been formed. Annealing at 600^{o}C leads to the almost complete transformation of the amorphous phase into a crystalline phase. Peaks corresponding to anatase are the biggest in number and have the highest intensity, which suggest that this is the predominating phase in these two coatings. The best result is obtained when the annealing time is 30 min. After that, anatase is the only crystalline phase in the coating. After 10 min annealing at 600^{o}C besides anatase, there are some rutile and particularly β-TiO_2 peaks present.

Both Raman and XRD showed similar results, in that a higher degree of crystallization occurs in samples which have been subjected to relatively high temperature treatment for longer times. Both time and temperature play an important role in titania phase transformation, allowing total transformation from a firstly amorphous structure through predominantly mixed phase crystals to finally pure anatase phase.

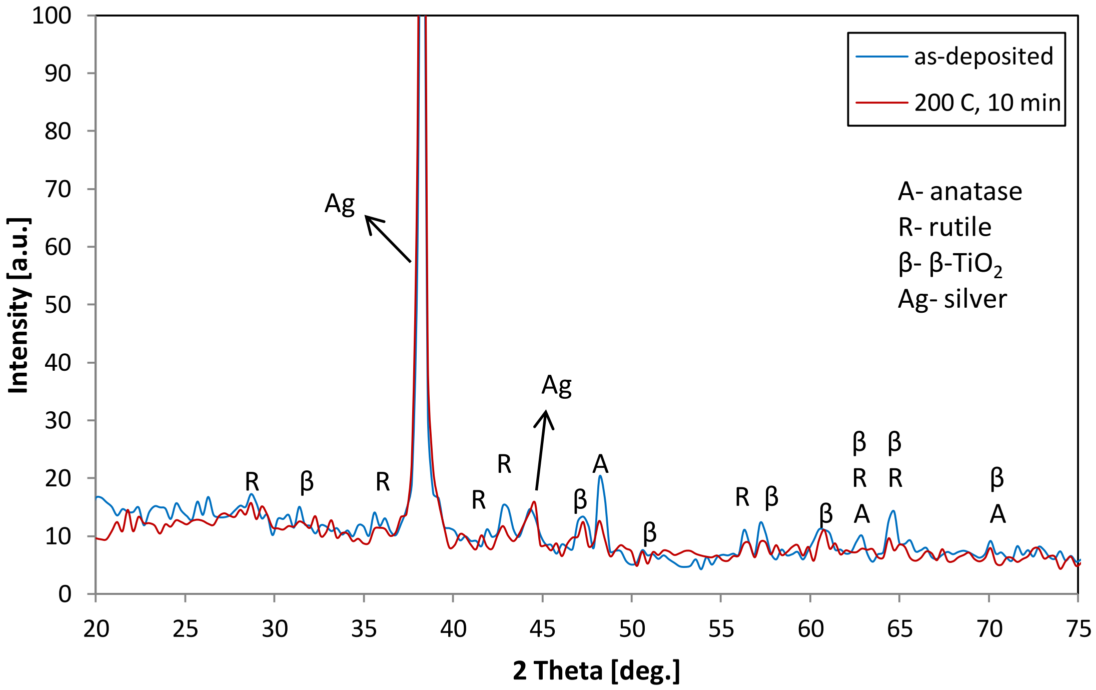

Figure 10.20: XRD diffractograms collected from TiO_2 as-deposited sample and annealed at 200^oC for 10 minutes.

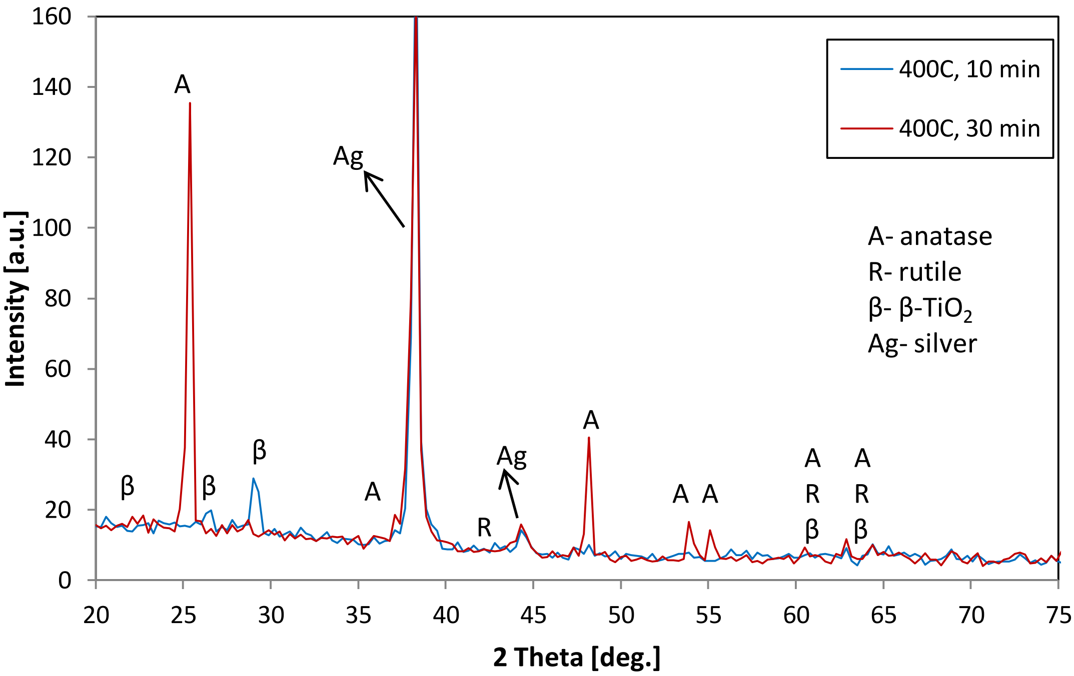

Figure 10.21: XRD diffractograms collected from TiO_2 annealed at 400^oC for 10 minutes and 30 minutes respectively.

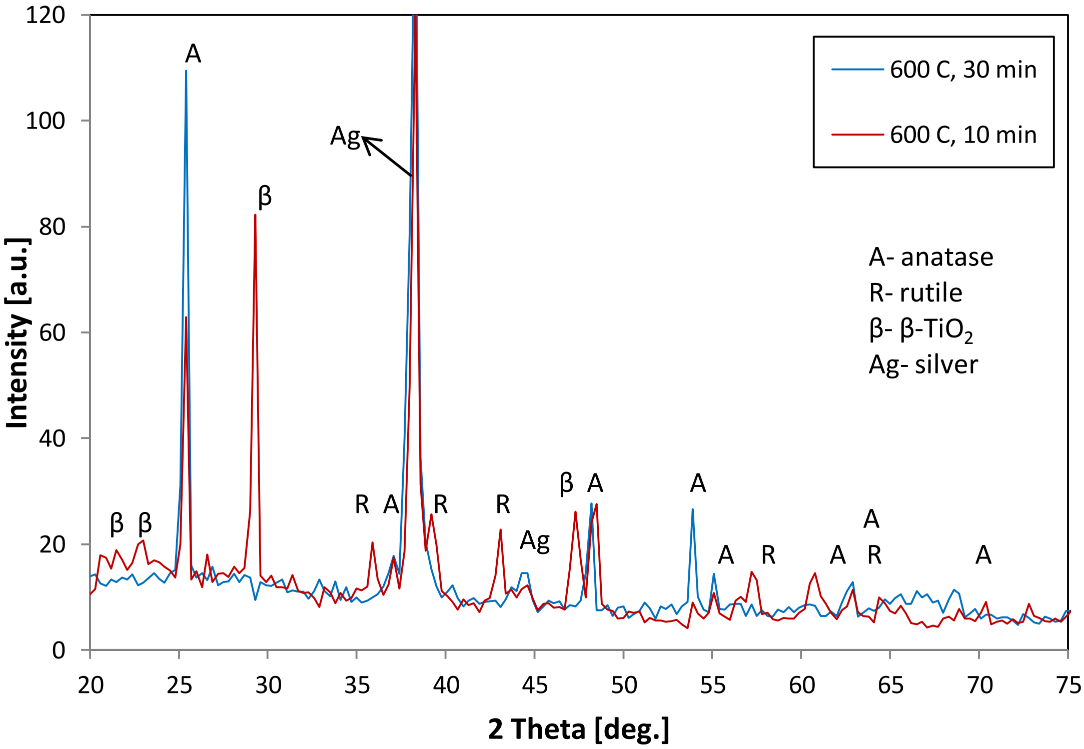

Figure 10.22: XRD diffractograms collected from samples annealed at 600^oC for 10 and 30 minutes respectively.

In order to investigate surface roughness Atomic Force Microscopy (AFM) analysis was conducted (see Chapter 9.2.1). Surface roughness was investigated in the as-deposited sample and the sample annealed at 600°C for 10 minutes. Large differences in surface roughness between samples may play an important role in diffusion processes, as bigger valleys existing on the film surface could serve as pockets, or free spaces for diffusing atoms to accumulate at. Consequently, at this point concentration of silver would be falsely higher suggesting that the silver diffusion rate is higher. Figure 10.23 shows 5 μm×5 μm images of the titania coating as-deposited and post-deposition annealed at 600°C for 10 minutes, respectively. Table 10.9 shows root-mean-square (RMS) and roughness average (Ra) values for both samples. Values are slightly higher for the as-deposited sample, which suggests that during heat treatment grain sizes increase filling the free spaces and/or valleys on the coating surface, and hence surface roughness decreases in the annealed film. However the difference is not very large, therefore, differences in roughness between the titania samples should not play an important role in silver diffusion.

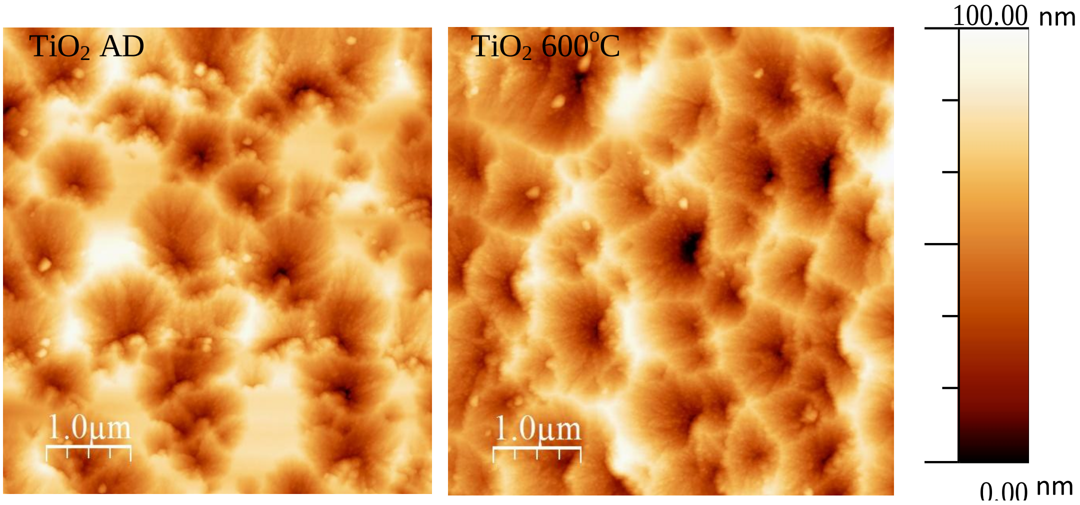

Figure 10.23: AFM images collected from titania samples: as-deposited (left) and annealed at 600°C (right).

Table 10.9: Roughness average and root-mean-square values obtained from AFM analysis for as-deposited and annealed at 600°C titania samples.

TiO_2 sample	Ra [nm]	RMS [nm]
As-deposited	13.8	16.9
Annealed at 600°C	13.1	16.4

10.2.2 TiO_2: SIMS Diffusion Studies

The Ag/TiO_2/glass samples were characterised using secondary ion mass spectrometry with a magnetic sector detector as described in Chapter 9.2.2 to investigate silver and sodium diffusion. Figure 10.24 shows an Ag/TiO_2/glass sample, which will be described as a standard in this work. The standard sample has been measured by SIMS without being subjected to post-deposition heat treatment. This sample was measured after 24 hours after deposition, so any diffusion of Na or Ag atoms will be due to storage at room temperature. Diffusion measurements in the remaining samples will be characterised against diffusivity values obtained from the standard sample. Figure 10.25 represents the diffusion profile for two Ag/TiO_2/glass samples post-deposition annealed (before silver over-coating) at 200 and 600°C respectively. The annealing temperature and, therefore, film structure does not cause drastic differences in the silver diffusion profiles, but it has a great impact on sodium diffusion. Sodium, which is one of the constituents of glass, could have diffused through the titania coating during first annealing, before silver over-coating has taken place. Raman analysis showed that the sample annealed at 200°C did not have a crystalline structure, whereas samples annealed at 600°C appeared to be predominantly anatase. This suggests that in the case of silver migration, it is harder to diffuse through amorphous titania, as the diffusion rates in crystalline samples are higher. Figure 10.26 compares the difference between sodium profiles in the as-deposited sample, the sample annealed at 200°C for 10 minutes and the sample annealed at 600°C for 10 minutes. All of these samples were over-coated with Ag and annealed for the second time at 250°C for 10 minutes. From the graph it is clearly seen that the biggest difference in sodium diffusion rates exists while comparing the sample annealed at 600°C with the two remaining samples. The difference in the sodium profile is not that crucial for the as-deposited sample and the one annealed at 200°C. This indicates that doubling the diffusion time at relatively low temperatures does not have a crucial impact on sodium migration. Whereas annealing at temperatures significantly higher causes major increase in sodium diffusivity. Therefore we can say that the significant increase in sodium diffusion in samples annealed at higher temperatures is mainly caused by the first annealing process, whereas the second annealing may cause only insignificant further increase in the sodium diffusion rates. Moreover, a very surprising peak occurs in the sodium profile collected from the sample annealed at 600°C close to the zero value on the x-axis (i.e., very close to the sample surface). It suggests that some Na could be on the film surface. This happens because the system is very sensitive to sodium. Na is easily picked up from the environment, which may be the reason why it was detected on the sample surface. The other possibility is that it is due to a speck of fracture debris from sample preparation, or it might have been produced by the routine used to compensate the sample charging effect. This means that the detected sodium signal may not indicate the real amount of sodium in the very top layer of the film.

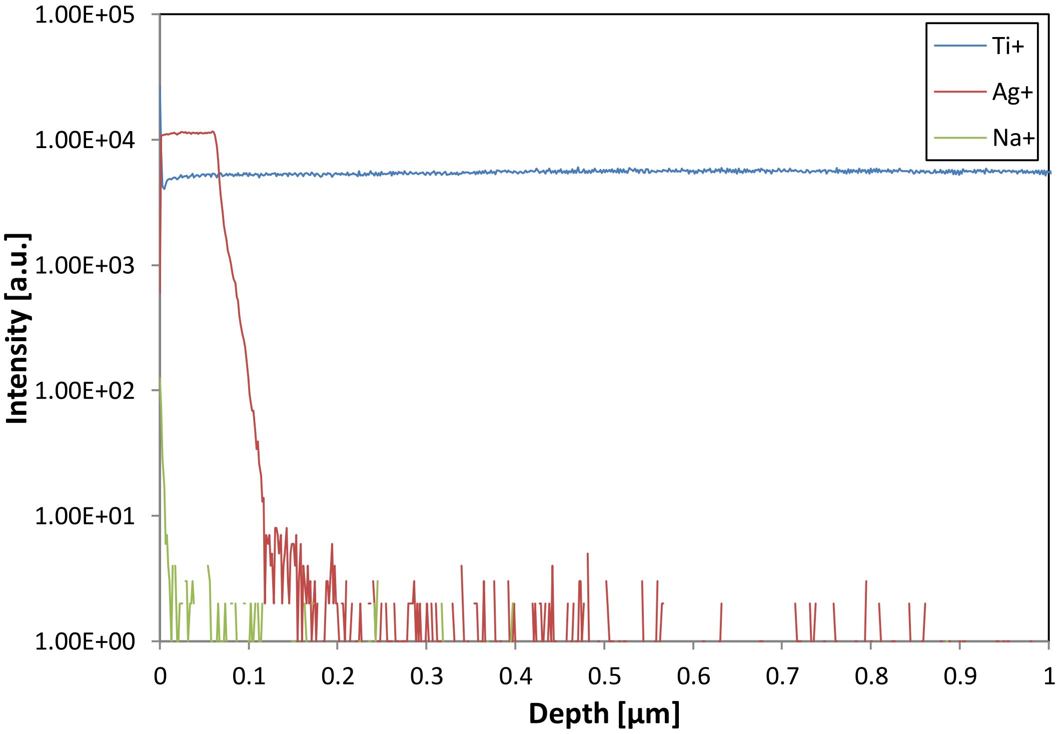

Figure 10.24: SIMS depth profiling of as-deposited Ag/TiO_2/glass sample, referred to a standard sample in the text.

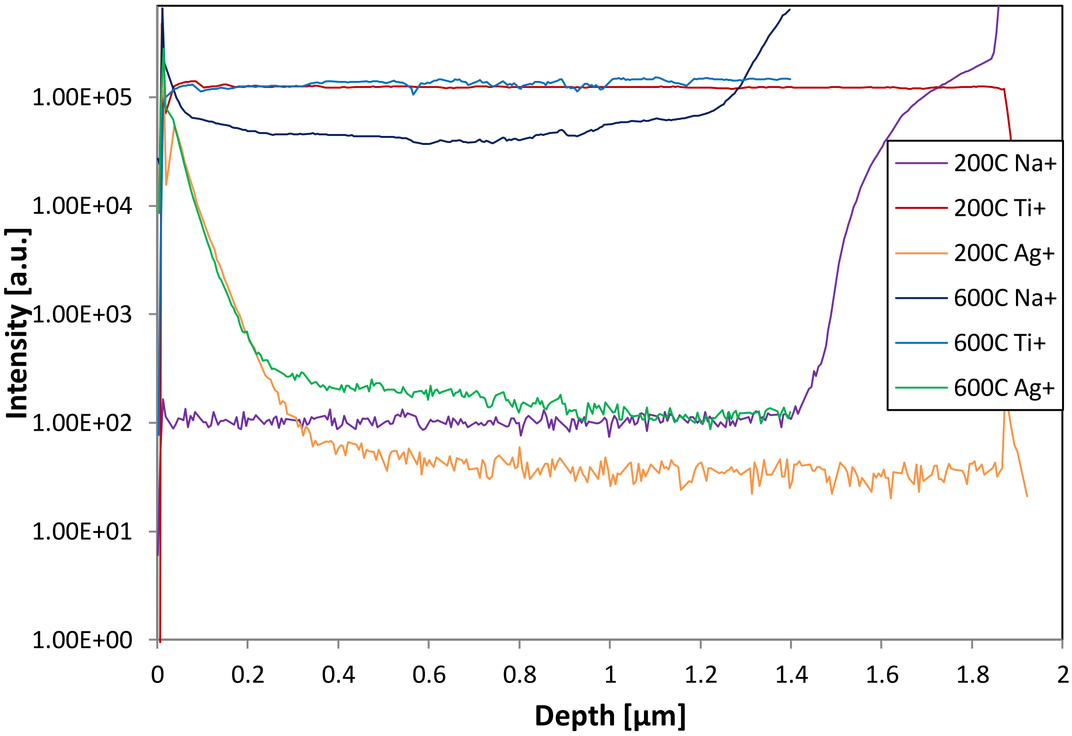

Figure 10.25: Silver and sodium SIMS profiles for samples 2.1 (annealed at 200^{o}C) and 6.1 (annealed at 600^{o}C).

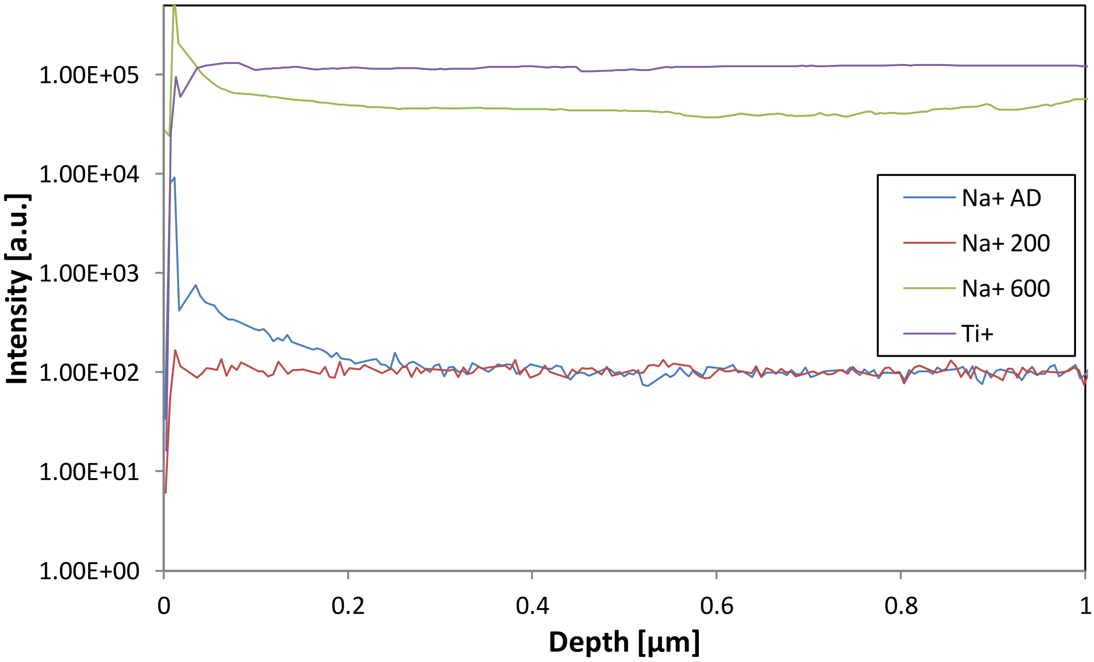

Figure 10.26: Na SIMS profiles for samples 1.1 (as-deposited), sample 2.1 (annealed at 200^{o}C) and 6.1 (annealed at 600^{o}C).

Figure 10.27 shows the difference between samples annealed at 400°C, but for different times. As found from the Raman and XRD analysis, the annealing time has also a big impact on film structure. The sample which was annealed for 10 minutes did not show a fully crystalline structure, whereas the sample annealed for 30 minutes showed a strong anatase structure in the Raman spectrum, and stronger crystallinity in XRD. As shown in the spectra below, the diffusion profile has also changed in these samples. There is still smaller difference in silver diffusion, but for sodium the diffusion rate is two orders of magnitude higher for the sample annealed for 30 minutes. This confirms that while annealing at relatively high temperatures both time and temperature plays important role in the diffusion process. It is obvious that changes in the sodium diffusion rate are due to the first annealing condition, therefore in this case the vast difference (two orders of magnitude) in sodium profiles must be due to the threefold increase in annealing time, as the temperature was the same for both samples. The reason for the increased diffusivity may be also the structural changes in the dielectric coating, as the titania becomes semi-crystalline and therefore grain boundaries might have served as migration short circuits for diffusing atoms. The diffusion coefficient values have been calculated by fitting experimental data into Fick's second diffusion law, values obtained have been summarised in Table 10.10.

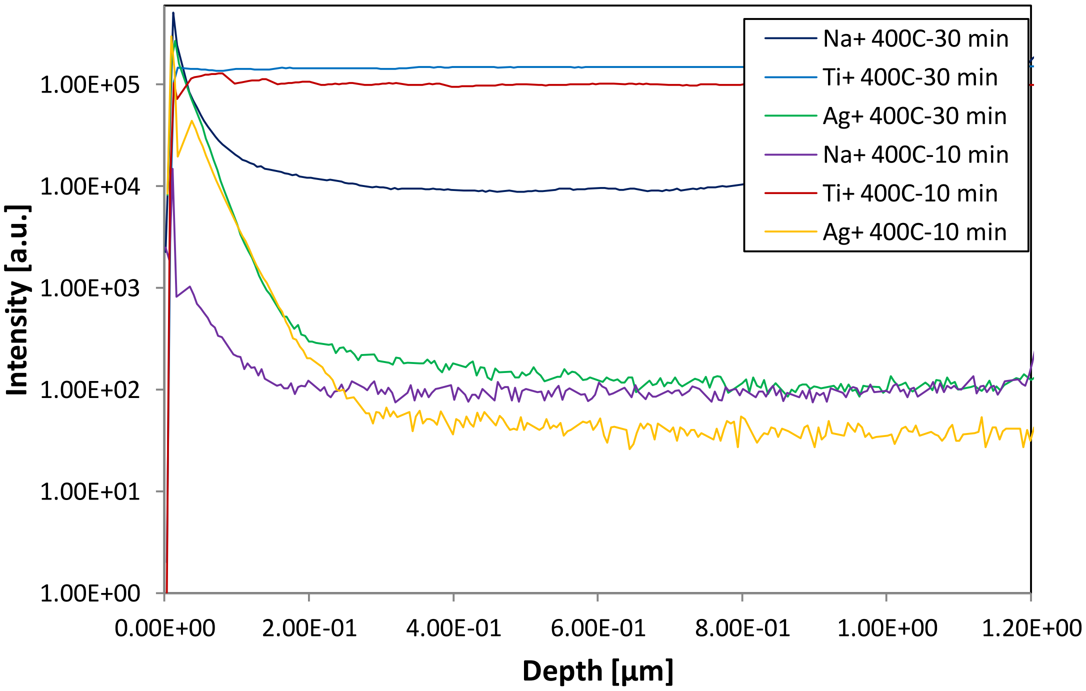

Figure 10.27: Na and Ag SIMS profiles for samples 3.1 and 4.1 annealed at 400°C for 10 and 30 minutes respectively.

Table 10.10 represents the diffusion coefficient values calculated for sodium and silver using Fick's second law of diffusion for an infinite couple with constant surface composition (see Chapter 6.5.2). Values calculated for silver atoms are not very different between samples. For the most of the samples diffusivity stays between 5.5 and 8.5×10^{-19} m^2/s, whereas for sample 6.1 the diffusivity of silver is significantly higher and equals 1.6×10^{-18} m^2/s. This increase must be due to structural changes in the titania coating during first annealing (before the silver coating was deposited). As XRD and Raman analysis showed that the titania has transformed from amorphous to a fully crystalline structure in sample 6.1 (annealed at 600^{o}C for 30 minutes). Moreover in this sample anatase has developed to be the only crystalline phase in the coating. After 10 min annealing at 600^{o}C, beside anatase there is evidence of rutile and particularly β-TiO_2 structures present. In general, diffusion may occur through the lattice (through point defects such as vacancies or interstitial sites) or along line and surface defects, such as grain boundaries or dislocations. The latter are known as diffusion short circuits, as diffusion occurs faster along line and surface defects than through the lattice. [136] In the mixed-phase titania crystals, which include different orientation in the crystalline lattice, silver atoms diffuse through grain boundaries of a limited length, due to grain orientation, which effectively serves as the end of the diffusion path. On the other hand pure anatase, which was found from XRD to be represented by the (101) peak, shows a more regular crystalline structure. This means that grains in the crystal lattice are more regularly orientated, therefore grain boundaries provide longer lasting short circuits for diffusing silver atoms than in amorphous or mixed-phase crystalline titania. This could be the reason for higher silver diffusivity obtained in sample 6.1 than in the remaining samples.

Sodium diffusion calculations were not that successful, which most likely is due to the first annealing conditions. Fitting the data into Fick's second law was particularly difficult for samples annealed at relatively high temperatures. However the sample annealed at 400^{o}C for 10 minutes did not cause problems while fitting raw data into the diffusion calculator program. In samples annealed at 600^{o}C and the one annealed at 400^{o}C for 30 minutes the concentration of sodium atoms in the titania coating was higher than the range in which the diffusion calculator operates. Therefore diffusivity values were only calculated for samples annealed at lower temperatures. Sodium consists of small and very mobile atoms; therefore even at relatively low temperatures it diffuses fairly easily through host lattices. Hence quite high diffusivity under relatively low temperatures in this study is rather reasonable. The most obvious diffusion path here would be grain boundaries, as the atom packaging is poor in the grain boundaries and atoms can easily squeeze through it at low activation energies. [121] However due to the size of sodium atoms and their high mobility they can also easily travel through interstitials between atoms in crystals, also at relatively low activation energy.

Differences in diffusion coefficient values for silver and sodium obtained from analyzed samples are plotted in Figure 10.28. It can be seen that silver diffusivity values between samples 1.1-5.1 are quite similar, whereas sample 6.1 shows a significant increase. On the other hand, values for sodium are rather scattered and could only be calculated for samples annealed at relatively low temperatures.

Figures 10.29-10.30 represents an example of analytical solution to Fick's second diffusion law, for silver and sodium, respectively. 'Fit Ag/Na counts' curve represents concentration of silver/sodium found by diffusion calculator (method closely described in Chapter 9.2.2), which represents an analytical solution of Fick's law. The curve is fitted into normalized SIMS depth profiling data.

Table 10.10: Diffusion coefficient values (D) calculated from SIMS analysis for silver and sodium atoms in titania coatings.

Sample number	D_{Ag} [m^2/s]	D_{Na} [m^2/s]
Standard	1.35×10^{-21}	4.00×10^{-21}
1.1	7.00×10^{-19}	6.00×10^{-19}
2.1	7.50×10^{-19}	2.10×10^{-18}
3.1	8.50×10^{-19}	-
4.1	5.50×10^{-19}	4.50×10^{-19}
5.1	6.00×10^{-19}	-
6.1	1.60×10^{-18}	-

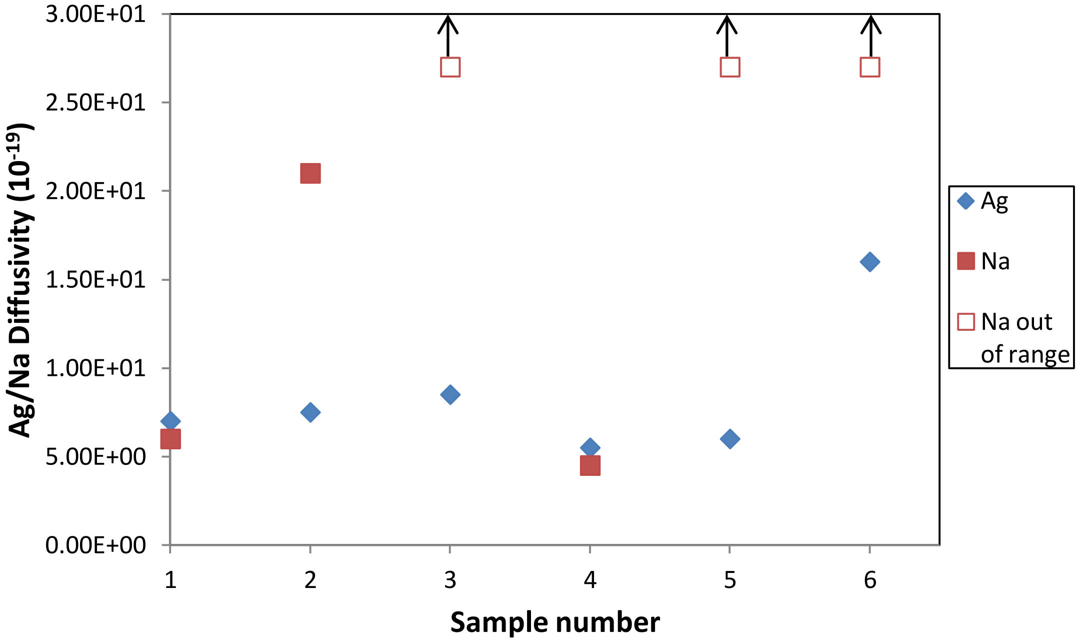

Figure 10.28: Silver and sodium diffusion values calculated from selected titania samples.

Empty red squares in the graph above represent sodium diffusivity in samples annealed at relatively high temperatures. It was not possible to obtain these values using diffusion calculator. Annealing conditions for the samples were as follow: sample 1.1- as-deposited, sample 2.1- 200°C/10 min, sample 3.1- 400°C/30 min, sample 4.1- 400°C/10 min, sample 5.1- 600°C/10 min and sample 6.1- 600°C/30 min.

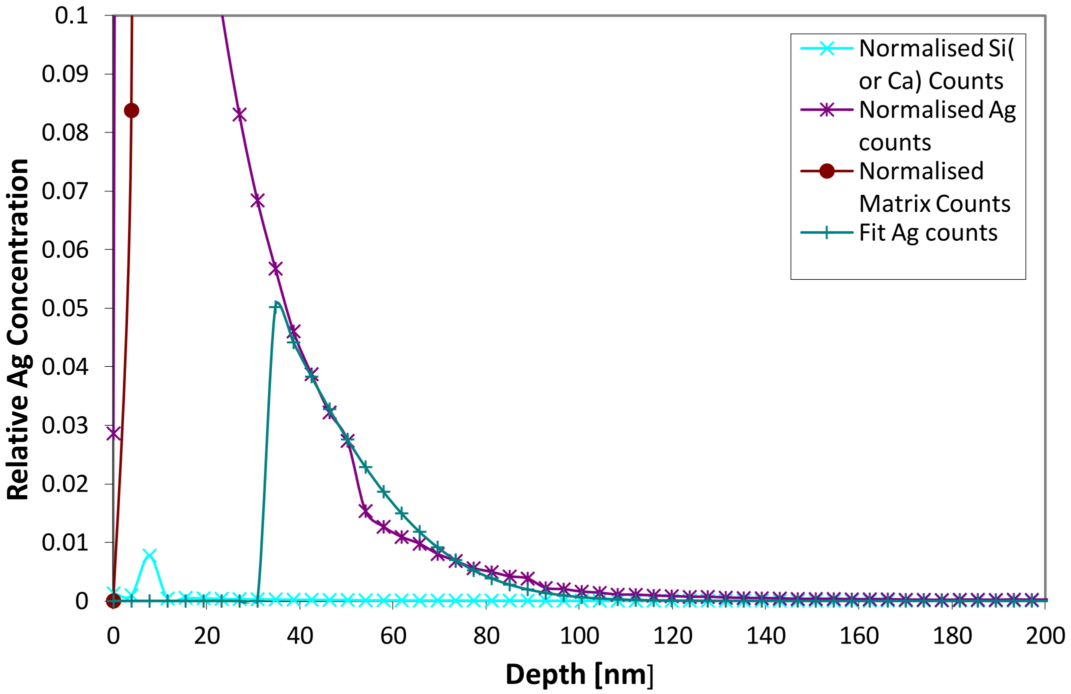

Figure 10.29: Example of analytical solution of Fick's second diffusion law. Graph shows silver fit in sample 4.1. Depth (nm) as a function of relative Ag concentration with a fitted Ag data at concentration between 0-0.1 (see Chapter 9.2.2), which determines the diffusion coefficient value for silver atoms.

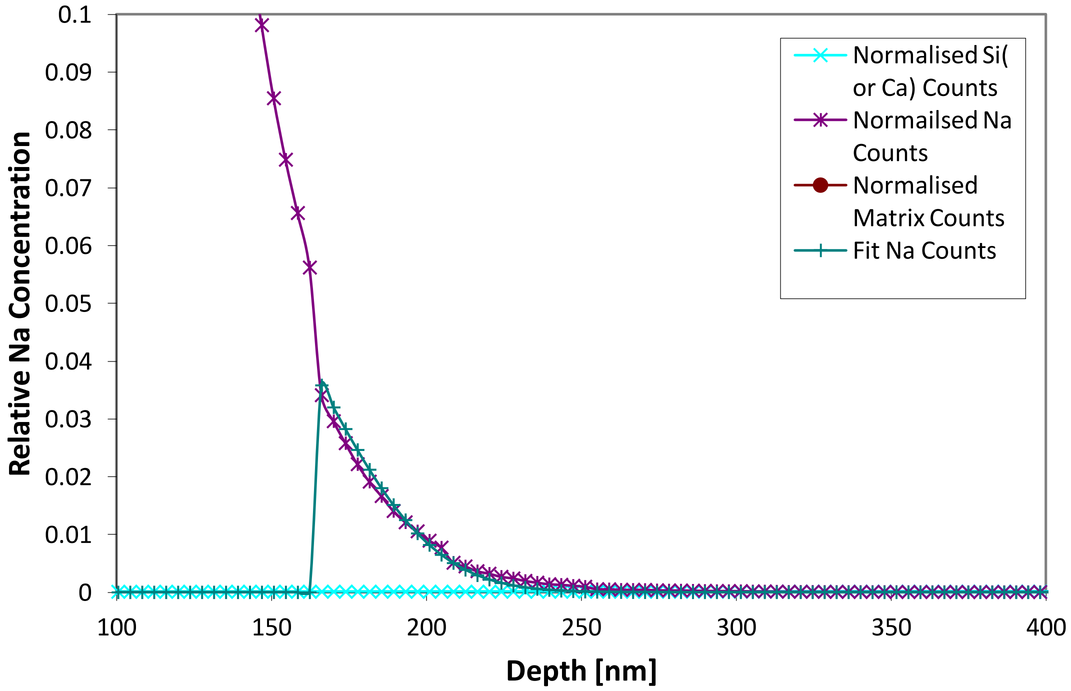

Figure 10.30: Sodium fitting into Fick's second diffusion law (sample 4.1).

10.2.3 TiO_2: XPS Diffusion Studies

SIMS is not a quantitative analytical method, therefore the Ag/TiO_2/glass samples were also investigated by XPS. The analytical procedure is described in Chapter 9.2.

Figures 10.31 and 10.32 show XPS spectra obtained after the first sputtering sequence (i.e. after 4 minutes long sputtering the material off the sample surface) and after reaching the titania/glass interface, respectively. In Figure 10.31 the dominant ion detected at the film surface is silver, whereas while completing further sputtering sequences and penetrating into the film bulk, the silver signal disappears and the level of Ti and O becomes more significant (Figure 10.32). Furthermore, atoms like silicon, calcium and sodium seen in Figure 10.32 come from the glass substrate, which either diffused through the titania layer after heat treatment, or the titania/glass interface has been reached already.

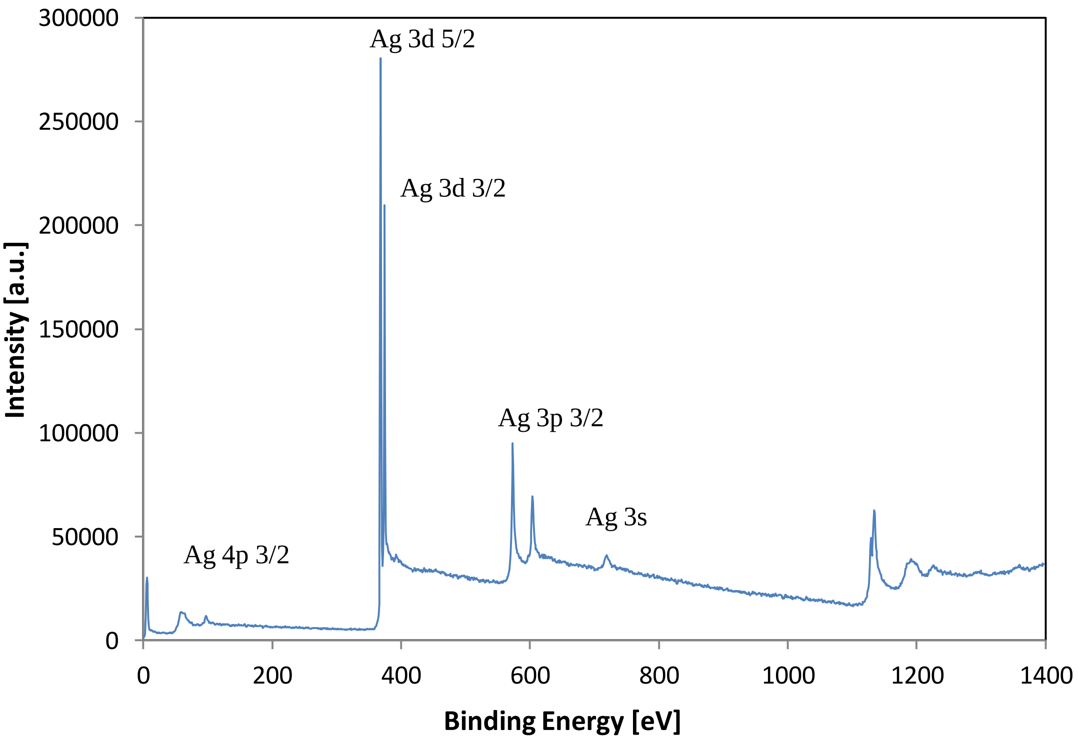

Figure 10.31: XPS spectrum collected for sample 6.1 after first sputter sequence (i.e. after first bombardment of the sample surface with Ar^+ gun to remove the material subjected to XPS depth profiling analysis).

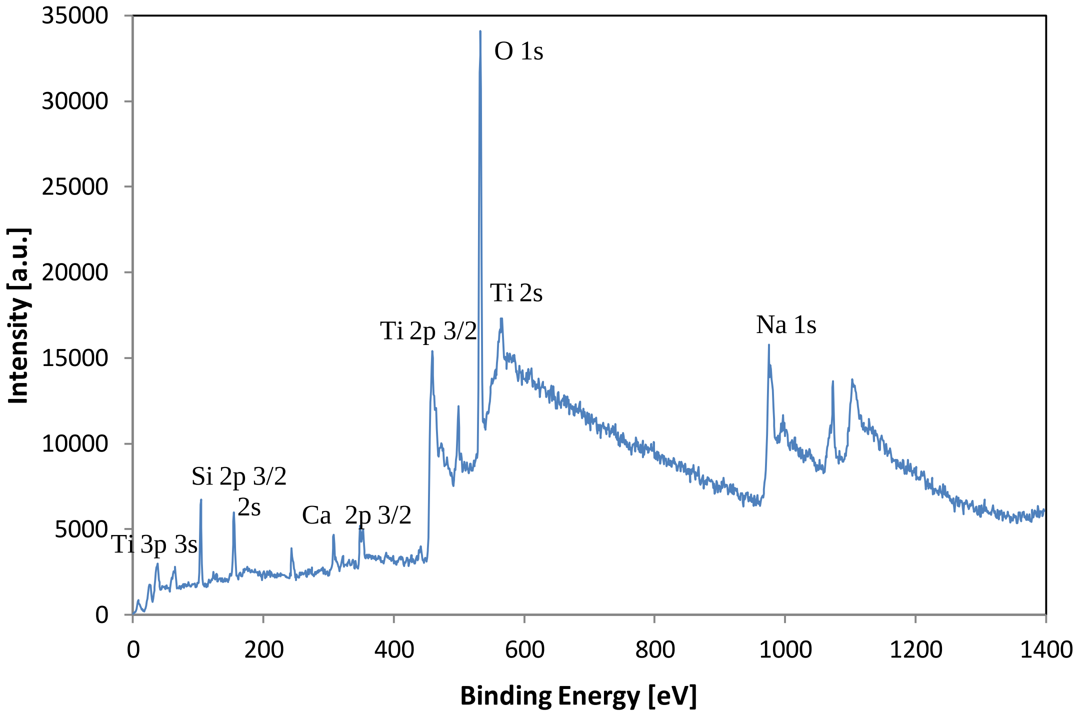

Figure 10.32: XPS spectrum collected for sample 6.1 after reaching the TiO_2/glass layer interface.

XPS depth profiling analysis is shown in Figures 10.33-10.35 and the first two figures present samples 2.1 and 6.1 aligned together. In this case the concentration of silver atoms is similar in both samples, suggesting that silver diffusion rates in these samples will be similar. SIMS depth profiling on the other hand, discussed in the previous chapter, showed a significant difference in silver profiles between samples 2.1 and 6.1. This is caused by the difference in sensitivity between XPS and SIMS. However Na profiles show quite significant differences in the concentration of sodium atoms detected in the selected TiO_2 coatings. In sample 6.1 Na has been picked up by XPS after 12 minutes of sputtering, whereas 16 minutes were required for sample 2.1 (see Figure 10.34). This indicates that sodium has travelled faster (and further) in the sample heated at a higher temperature. The level of Na detected by XPS depth profiling is significantly lower than in SIMS, due to differences in the sensitivity between these methods. XPS in general is much less sensitive that SIMS, but it is a quantitative technique, which describes ion intensities in atomic concentration percentage. On the other hand quantification of SIMS images requires the use of a reference standard of a known mass, since the intensity of the secondary ion current is not solely dependent on the amount of molecule present in the sample. Factors influencing signal intensity include the chemical composition of the sample matrix, topography, matrix-primary ion interactions, instrumental transmission and detector response. [137]

Figure 10.35 shows samples 3.1 and 4.1 aligned together. These samples were annealed at 400°C for different times of 10 and 30 minutes. Once more SIMS depth profiling picked up significant differences in the amount of sodium in the titania coating. However, here, due to the lower sensitivity of XPS analysis this difference in sodium intensity is not significant. There is only a slightly higher concentration of Na detected in sample 3.1, annealed for 30 minutes, than in sample 4.1, annealed at 400°C for 10 minutes.

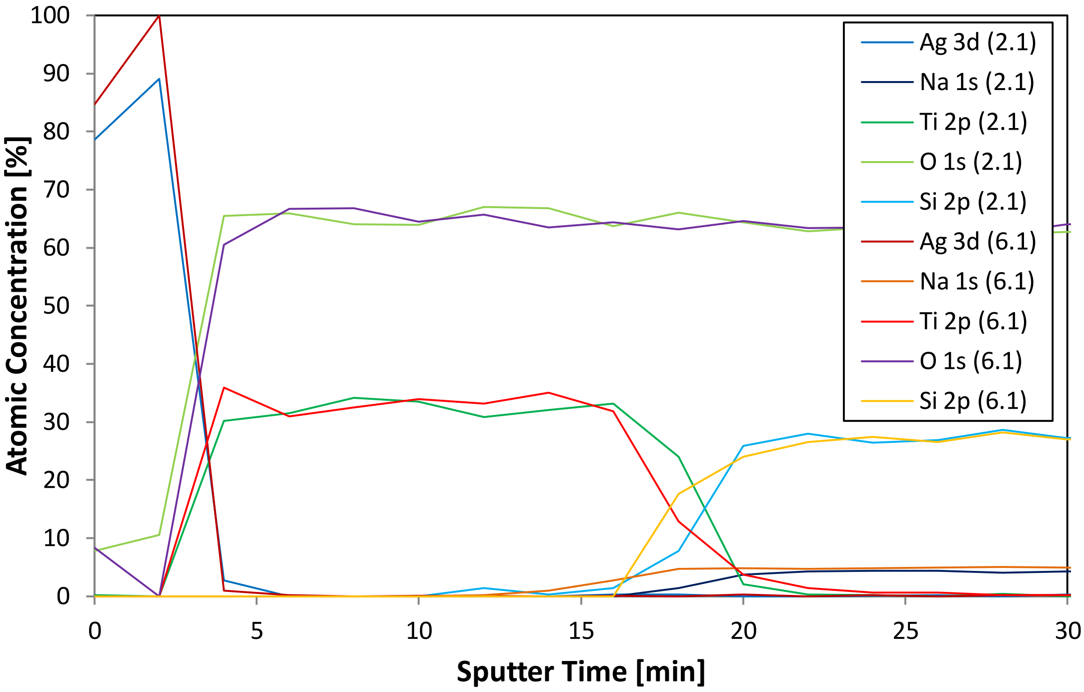

Figure 10.33: Atomic concentration against sputtering time. XPS profile collected from samples 2.1 and 6.1.

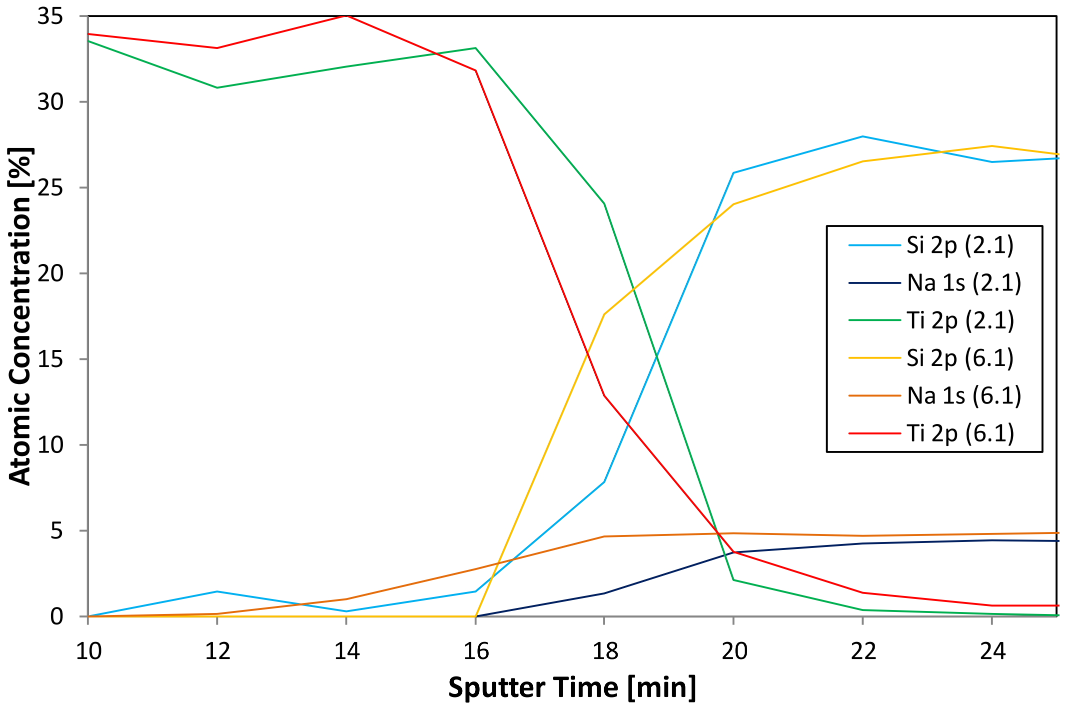

Figure 10.34: Magnification of the titania/glass interface region of Figure 10.33, to emphasise the difference in sodium profiles in samples 2.1 and 6.1.

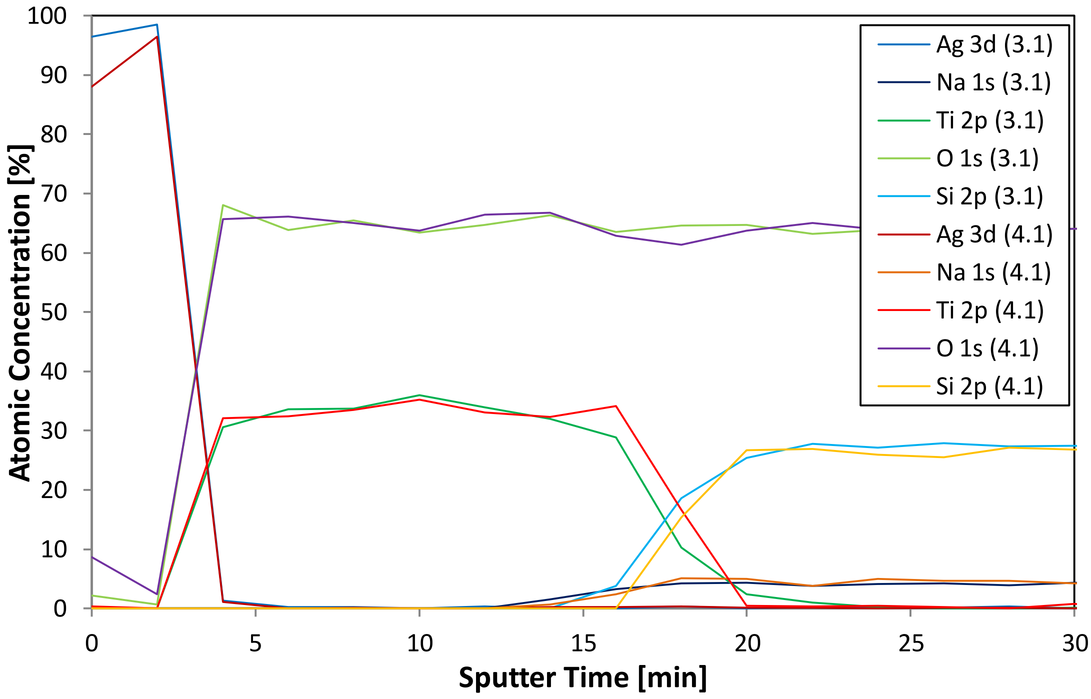

Figure 10.35: Atomic concentration versus sputtering time collected from sample 3.1 and 4.1 by XPS depth profiling analysis.

10.3 TiO_2: Summary

TiO_2 annealing studies showed that the as-deposited magnetron sputtered titania coatings had rather amorphous structures with some predominant semi-crystalline regions with a very small grain sizes. The structure transforms through a mixed crystalline phase into pure anatase when the samples undergo post-deposition heat treatment. Samples annealed at temperatures above 600°C shows mainly rutile structures, which are known to be formed by more energetic processes than anatase. Therefore total anatase-to-rutile transformation should occur after annealing at even higher temperatures than 800°C, and/or longer annealing times, which could not be studied here, due to the limitations of the glass substrate; soda-lime glass starts softening at about 726°C.

SEM micrographs showed smooth and dense film surfaces, with some small defects or crystals existing on the surface. It was shown that coatings undergo re-crystallisation during annealing at 700°C and above. Large grains have been noticed after heat treatment at elevated temperatures. Raman analysis of these grains has not confirmed a specific crystalline phase of titanium dioxide, rather mixed anatase-rutile crystals. However increasing annealing temperature has led to increased rutile phase in the mixed structure, therefore further temperature rise could lead to complete anatase to rutile transformation. EDX analysis showed that the titania coatings deposited in this work has had stoichiometric compositions in most films, which is dependent on Ar/O_2 ratio during film sputtering. AFM analysis showed that the surface roughness of the TiO_2 samples equals about 13 nm Ra, and differs between as-deposited and annealed coatings only by about 0.6 nm, which therefore will not have a significant impact on diffusion.

Annealing time plays an important role in structure formation and also in diffusion processes. Silver diffuses faster through samples which were subjected to the highest annealing temperature and longer annealing time. This may be related to the anatase microstructure and crystal packaging in the lattice. Diffusion of silver in the remaining samples occurs with similar rates; therefore it most likely occurs along similar paths. As volume diffusion occurs from one interstitial site to another and requires high activation energy, resulting in relatively slow diffusion rates. It is more likely that also in these samples silver was travelling along surface defects. [121] Sodium on the other hand diffuses during the first annealing conditions, and the second annealing process has a significant impact on Na migration just in the case of the as-deposited sample and the sample annealed at 200°C. For small and very mobile sodium cathions diffusion through interstitials may occur easily in all samples, as they can readily fit through the interstitial sites of larger atoms. Grain boundary diffusion on the other hand, serves as additional fast tracks for sodium atoms in crystalline samples. Sodium diffusion could not be calculated in samples annealed at higher temperatures due to diffusion calculator limitations. The data was out of the range in which calculator operates.

Both SIMS and XPS analysis showed similar trends in sodium and silver migration through the titania coatings, despite quite significant differences in sensitivity and performance of both techniques. In both cases silver does not show vast differences in diffusivity values, whereas sodium significantly changes its profile. This is related to the first annealing conditions of the titania samples, before the silver layer deposition.

11. Results: Al-doped Zinc Oxide Coatings

Al-doped zinc oxide samples have been deposited at MMU in the Large Area coating rig, as described in Chapter 9.1. Samples were divided into two batches. Batch 1 contained relatively thick ZnO samples (~1 µm) and in Batch 2 samples have had a thickness of around 80 nm. The reason for this approach was the requirement for examination of the Al-doped ZnO coatings by EDX, which requires a thickness of about 1 µm to produce reliable set of results.

11.1 Thick Al-doped ZnO: Coating Characterisation

Table 11.1 shows deposition conditions of five aluminium doped zinc oxide samples and a thickness assigned to these samples obtained by Dektak profilometer after sample deposition.

Table 11.1: Deposition conditions for Al-doped ZnO coatings.

Sample number	Frequency [kHz]	Plasma movement [rpm]	Ar flow [SCCM]	O_2 flow [SCCM]	Pressure [Pa]	Thickness [µm]
1	20	0	10	20	0.35	0.98±0.04
2	100	250	10	15	0.30	1.02±0.04
3	100	250	15	15	0.22	0.96±0.03
4	100	250	11	15	0.76	0.93±0.04
5	100	250	15	15	3.25	1.16±0.04

Samples were analysed by EDX to find their composition. The stoichiometric composition of 2 wt % Al-doped zinc oxide consists of 78.7 wt % of Zn, 19.8 wt % of O, which in atomic composition equates to 48.5 at % of Zn, 48.5 at % of O and 3.0 at % of Al. However while depositing coatings reactively in mixed Ar/O_2 gasses environments it is quite difficult to find the ideal deposition conditions to create coatings having exactly stoichiometric composition. Possible formation of Al_xO_x may occur alongside ZnO, which may be incorporated into the coating structure, and therefore change the coating stoichiometry. Results presented in Table 11.2 show that except for sample 5, there is a slightly higher oxygen content within the samples, which may be due to an excess of reactive gas during film deposition. The zinc content is slightly lowered in favour of the amount of Al. This could be due to the development of a small amount of Al_xO_x alongside the Al-doped ZnO formation.

Table 11.2: Composition of Al-doped ZnO coatings.

	Sample 1	**Sample 2**	**Sample 3**	**Sample 4**	**Sample 5**
Zn at%	42	41	37	44	48
Zn wt%	74	73	70	75	78
O at%	50	50	50	49	46
O wt%	22	22	24	21	18
Al at%	4	4	3	4	4
Al wt%	3	3	3	3	3

SEM micrographs of the as-deposited AZO samples were prepared and examined. Coatings show dense structures with relatively small grains existing on the surface. Most of the samples show relatively rough surfaces, except sample 2. Quite large grains can be distinguished on surface of the film in samples 2 and 4, with fewer, larger grains present in sample 2. Figures 11.1-11.5 show images collected from selected samples.

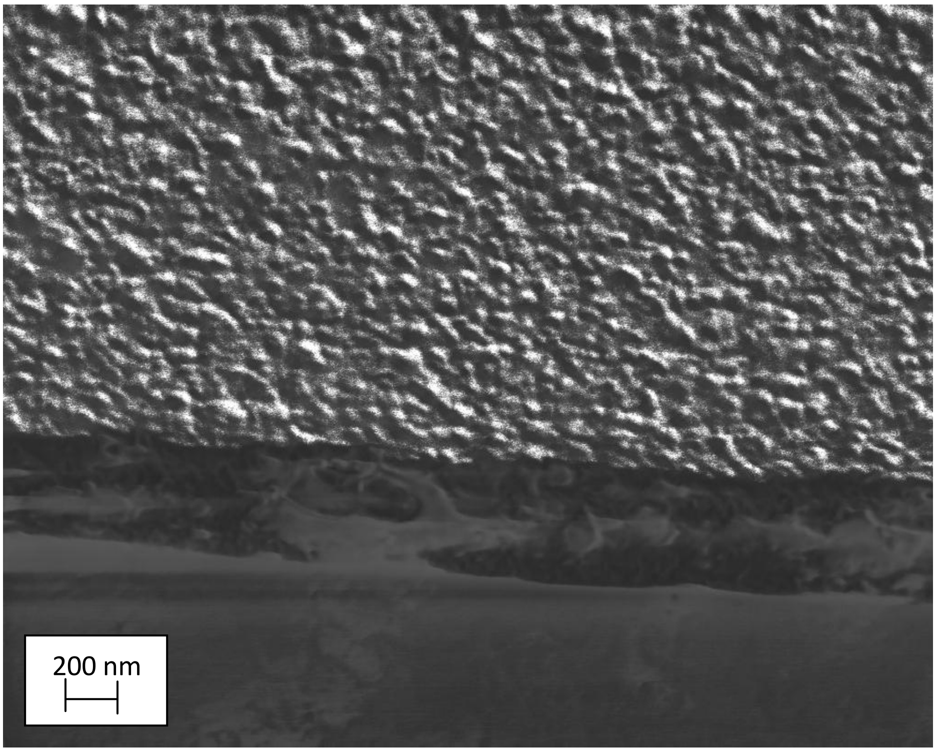

Figure 11.1: SEM micrographs of the fracture section of AZO sample 1 deposited onto float glass substrate.

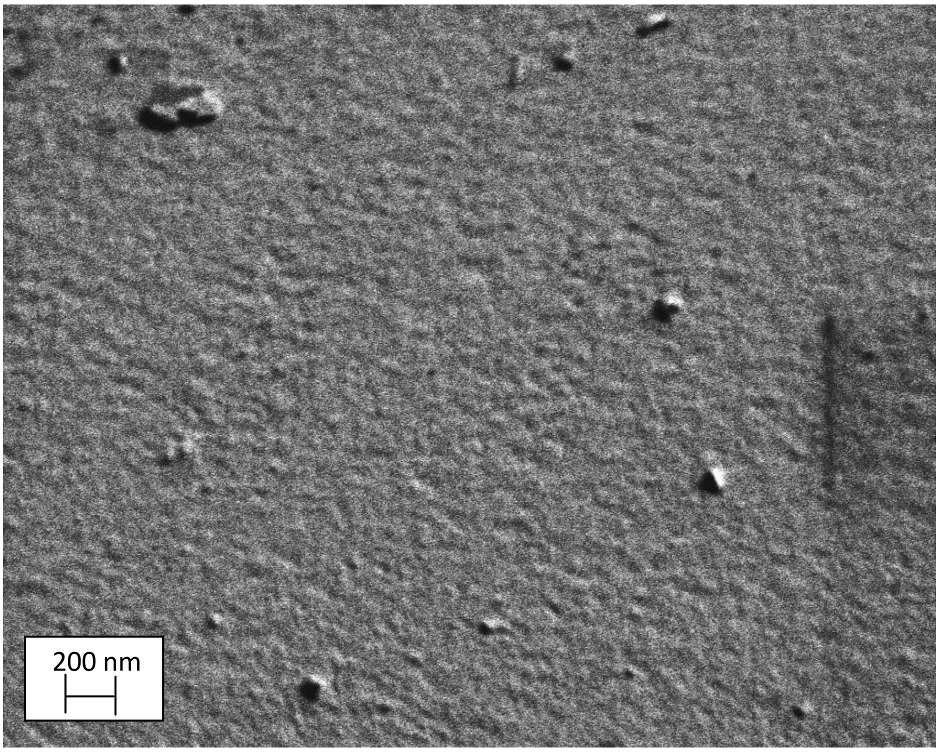

Figure 11.2: SEM image of the top surface of Al-doped ZnO sample 2, deposited onto float glass substrate.

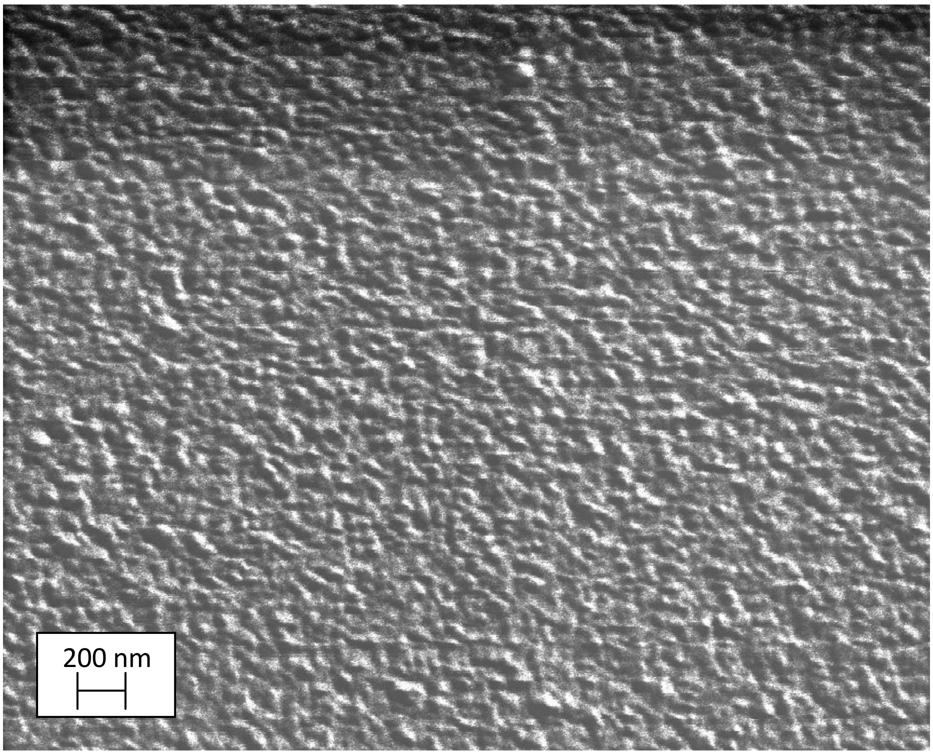

Figure 11.3: SEM micrograph of the top surface of AZO sample 3, deposited on float glass substrate.

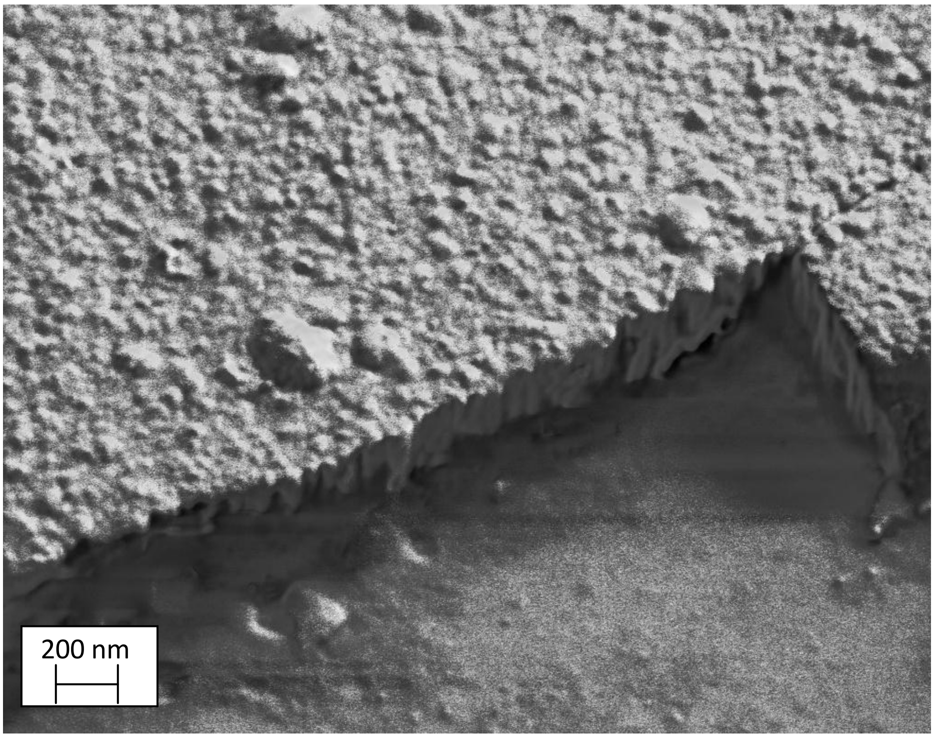

Figure 11.4: SEM micrograph of the fracture section of the sample 4, deposited onto float glass substrate.

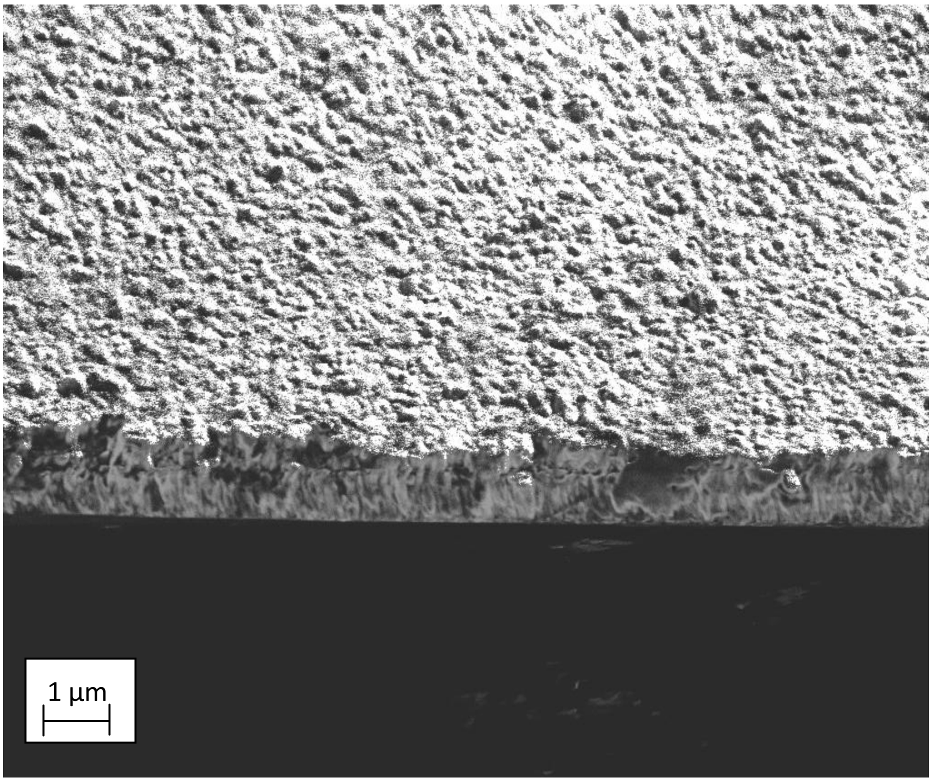

Figure 11.5: SEM image of the fracture section of AZO sample 5 deposited onto float glass substrate.

11.2 Thin Al-doped ZnO: Coating Characterisation

Thin (~80 nm) aluminium doped zinc oxide samples were deposited as described in Chapter 9.1. Table 11.3 presents the deposition conditions used during the production of these films (at a constant argon flow rate of 35 SCCM), as well as oxide annealing conditions and thickness measured by Dektak profilometer assigned to each sample.

Table 11.3: Deposition conditions of thin Al-doped ZnO samples.

Sample number	Power [W]	Pressure [Pa]	O_2 flow [SCCM]	Annealing conditions	Thickness [nm]
1.1	300	0.9	8	650°C/5 min	80±1.0
2.1	300	0.8	8	650°C/5 min	90±5.0
3.1	500	0.3	13	650°C/5 min	76±3.0
4.1	300	0.4	10	650°C/5 min	80±1.0
5.1	300	0.2	12	650°C/5 min	83±2.0
6.1	500	0.3	15	650°C/5 min	78±2.0
7.1	300	0.6	9	650°C/5 min	83±2.0
8.1	300	0.6	9	**-**	83±2.0
9.1	500	0.3	13	-	76±3.0

To characterise the crystal structure of the post-deposition annealed Al-doped ZnO samples XRD analysis was performed (see Chapter 9.2.1). Figure 11.6 shows Al-doped ZnO XRD diffractograms collected from nine selected samples. Samples are assigned to have a typical wurtzite structure of ZnO, which is the most common and thermodynamically stable under ambient conditions. The wurtzite structure has a hexagonal unit cell and belongs to the C_{6v}^{4}space group in the Schoenflies notation. [138-139]

In all cases the (002) ZnO peak was distinguished. Peak broadness is due to grain size and calculated grain size values are presented in Table 11.4. The peak width suggests that the grain sizes are relatively small in each analysed sample. This is due to dependency between peak broadening and grain size; peak broadening indicates a decrease in grain size. In other words, sharp, thin peaks indicate large grains, while short, rounded peaks usually represents small grains in the crystal structure. This assumption agrees with grain sizes calculated using the full width half maximum of the (002) peaks from the Debye-Scherrer equation (see Chapter 8.5), although the effects of micro-strain have not been de-convoluted. [140]

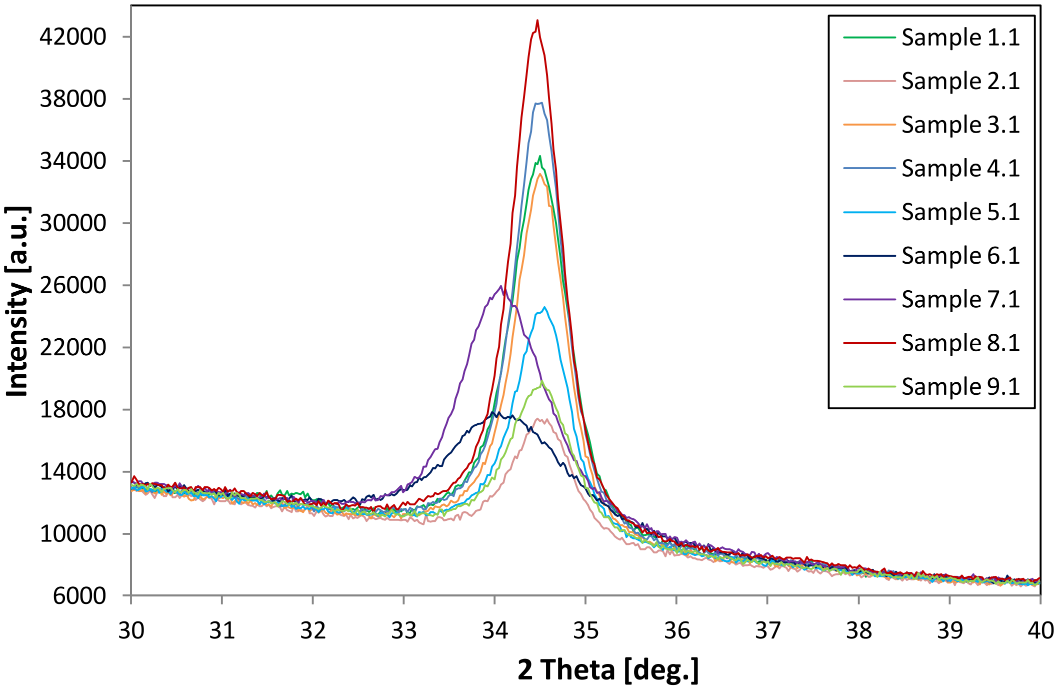

Figure 11.6: Al-doped ZnO samples deposited onto float glass substrate, analyzed by XRD.

It was found that the grain sizes are similar for the most of the samples, except samples 6.1 and 9.1. It these cases, grain sizes are smaller than 10 nm. Both samples were deposited under similar condition (~0.3 Pa operating pressure, 500 W power introduced to the magnetron and with a 35 and 15 SCCM flows of argon and oxygen gas, respectively), but sample 9.1 has not been post-deposition annealed at 650^{o}C. It may suggest that this heat treatment does not have a crucial impact on the crystalline structure of the Al-doped ZnO films. On the other hand, when comparing grain sizes of samples 3.1 and 9.1 the difference in grain size is significant. Samples 3.1 and 9.1 have been deposited under identical conditions, but sample 3.1 was annealed after deposition at 650^{o}C. The grain size increases from 9.3 nm in as-deposited sample 9.1 to 14.5 nm after heat treatment in sample 3.1, which implies that the post-crystallisation occurs due to the heat treatment.

Table 11.4: Grain size and d-spacing estimated from the (002) Al-doped ZnO peak.

Sample number	**1.1**	**2.1**	**3.1**	**4.1**	**5.1**	**6.1**	**7.1**	**8.1**	**9.1**
Grain size [nm]	12.9	14.5	14.5	15.0	12.9	7.2	12.9	12.0	9.3
d-spacing [nm]	0.260	0.260	0.260	0.260	0.259	0.263	0.260	0.260	0.263

The d-spacing values presented in Table 11.4 are in good agreement with the literature value of d=0.2602 nm for zinc oxide. [141] Samples 6.1 and 9.1 show slightly higher values of 0.263 nm, which indicates peak shifts to the lower 2θ angle. This may be due to the intrinsic stress of the coating, as it is known that compressive stress causes peak shifts to lower angles in XRD. It is known that compressive stress within the coating causes an increase in the d-spacing between the planes in the crystal, and it has been already observed by numbers of authors. [142-148] Thornton *et al.* [149] showed that heavy ions or energetic particles striking the film during deposition are responsible for compressive stresses. The energy of the ions bombarding the growing film will be greatest at lower sputtering pressures. Samples 6.1 and 9.1 were deposited under the lowest operating pressure chosen in this work (0.3 Pa) and a higher power of 500 W was introduced to the magnetron. In this case it is possible that shifts to the lower 2θ angles are caused by compressive stress. Sample 3.1, which was deposited under identical conditions to sample 9.1, but was then post-deposition annealed at 650°C for 5 minutes, does not show a peak shift, which may be due to re-crystallisation and stress relaxation as a result of the annealing process. On the other hand, sample 6.1 which has also been post-deposition annealed, showed the lowest grain size values from all of the samples. This sample has been deposited under low operating pressure and high power but also under the highest oxygen flow rate. When increasing oxygen flow rate the number of highly energetic ions increases due to the presence of O^- species in the plasma. Therefore the low grain size in this case may be due to a higher number of high energy particles impinging on the coating surface. However Kappertz and others showed in their study that varying the oxygen/argon ratio did not have a significant impact onto film texture. [150] Further work is required to investigate changes in plasma behaviour with pressure and oxygen ion to depositing atom ratio and its impact on the film structure.

AFM analysis was carried out onto selected Al-doped zinc oxide samples, to compare surface roughness between samples deposited under different conditions. Figure 11.7 shows 1 µm x 1 µm images of selected AZO samples. Table 11.5 shows root-mean-square (RMA) and roughness average (Ra) values for each sample. The RMS value is the biggest for sample 2 and equals 1.1 nm, whereas the remaining samples have RMS values below 1 nm. All of the selected samples show similar grain sizes, therefore we can exclude that the difference in roughness is related to grain size. Sample 2.1 was deposited at the highest operating pressure, whereas the smoothest, sample 3.1, was deposited under higher power. Both pressure and power play an important role in sputter deposition processes and can be used to deliberately change film structure, and both could have played a role in the roughness variation in the analysed coatings. Therefore, at higher operating pressures, i.e. sample 2.1, the mean-free-path decreases, which cause a reduction of ion and neutral energies due to gas phase collisions. Particles incident at the substrate surface may not have enough energy to diffuse and form dense films. When films are deposited under higher power, as in case of sample 3.1, then the voltage which drives the ion current is higher, and therefore the ions energy is high (higher accelerating voltage). Nevertheless roughness values found for AZO samples are quite low in general and the difference in Ra between samples in small, which means that each sample has a relatively smooth surface. This, in turn, means that interface roughness effects will not have an impact on silver diffusion through the AZO films.

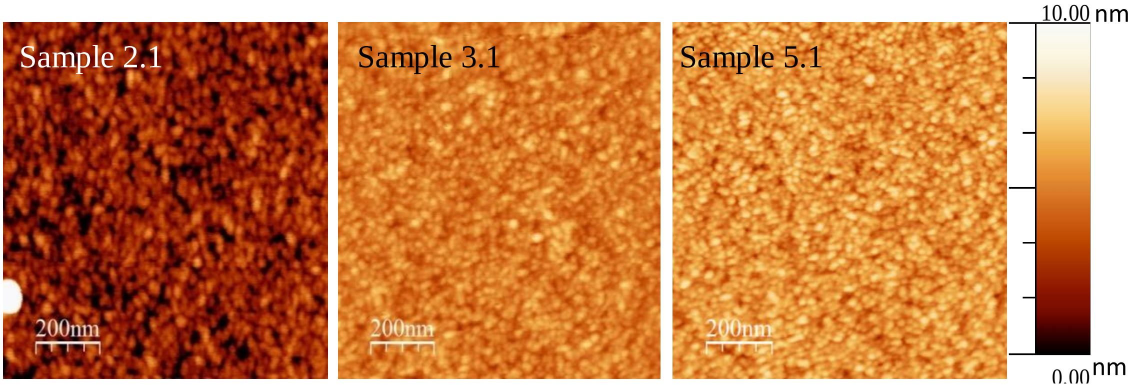

Figure 11.7: AFM images collected from selected Al-doped ZnO samples deposited onto float glass substrate.

Table 11. 5: Ra and RMS values obtained from selected Al-doped ZnO samples.

Sample number	Ra [nm]	RMS [nm]
Sample 2.1	0.9	1.1
Sample 3.1	0.6	0.7
Sample 5.1	0.8	1.0

The optical properties of Al doped ZnO films were measured to find refractive index (n) and extinction coefficient (k) values for the selected coatings. In Table 11.6 the n and k values at 550 nm wavelength are listed. The literature values of the refractive index for zinc oxide are 2.008, 2.029 [151], and values obtained for n from optical analysis are 1.90-1.93 and slightly decreases from 1.93 to 1.90 when the operating pressure was increased for the analysed Al-doped zinc oxide samples. Extinction coefficient values are very low and vary from 4.05×10^{-5} to 1.38×10^{-8}. Such a low values of k~0 indicate that Al-doped ZnO films are highly non-absorbing, and were also found by other authors to be as low as characterised in this work. [152-156]

Table 11.6: Optical constants of Al-doped ZnO selected samples as a function of pressure.

Sample number	Pressure [Pa]	Refractive index (n)	Extinction coefficient (k)
1.1	0.9	1.90	6.69×10^{-8}
3.1	0.3	1.93	1.47×10^{-6}
5.1	0.2	1.93	3.79×10^{-6}
6.1	0.3	1.92	2.46×10^{-6}
8.1	0.8	1.91	4.05×10^{-5}
9.1	0.6	1.91	1.38×10^{-7}

11.2.1 Thin Al-doped ZnO: Diffusion Studies

The Ag/ZnO/glass samples were characterized using TOF-SIMS as described in Chapter 9.2.2. Figure 11.8 presents a standard sample analysed by TOF-SIMS, which as in the titania study, explained in Chapter 10, was a sample that after being over coated with silver was not submitted to post-deposition heat treatment at 250°C for 5 minutes, but instead was measured after spending approximately 24 hours at room temperature. The degree of sodium in the sample is due to the Al-doped ZnO annealing at 650°C. Figures 11.9 and 11.10 show examples of the composition profiles for Ag/ZnO/glass stacks in as-deposited and annealed samples, respectively. The region on the x axis where the sodium profile rises dramatically is the point where the soda-lime glass substrate has been reached.

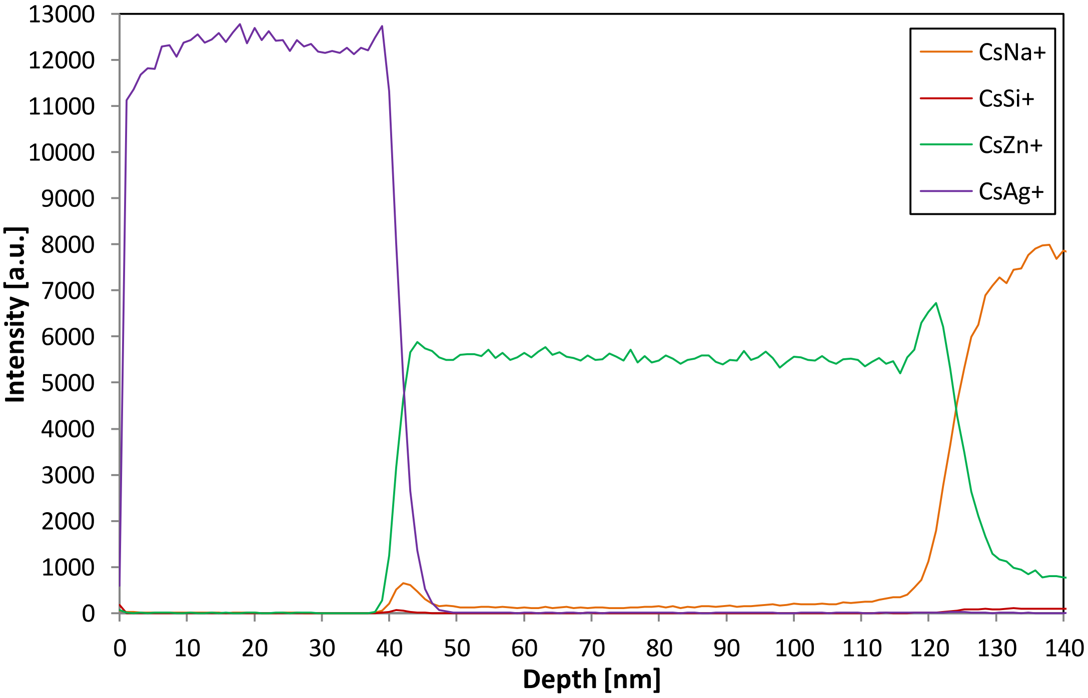

Figure 11.8: TOF-SIMS depth profiling collected from Al-doped ZnO standard sample on float glass substrate. Detected species creates ion clusters with caesium sputter beam, which are less matrix dependent than metal ions (see Chapter 9.2.2).

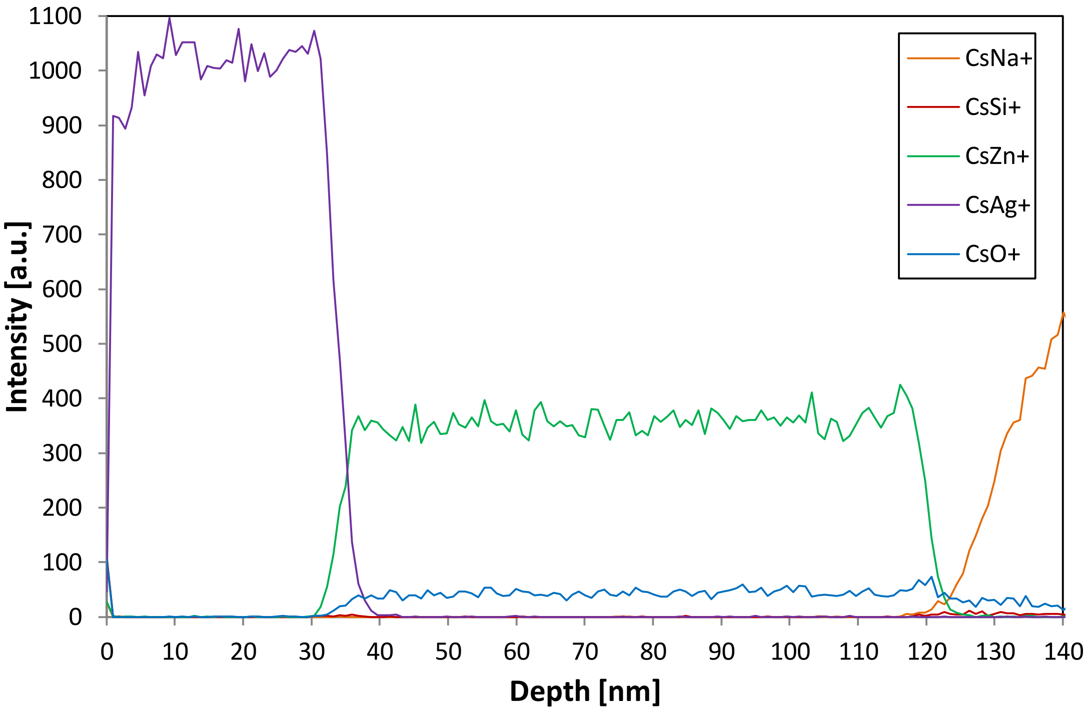

Figure 11.9: Example of TOF-SIMS diffusion profile from as- deposited Al-doped ZnO sample 8.1.

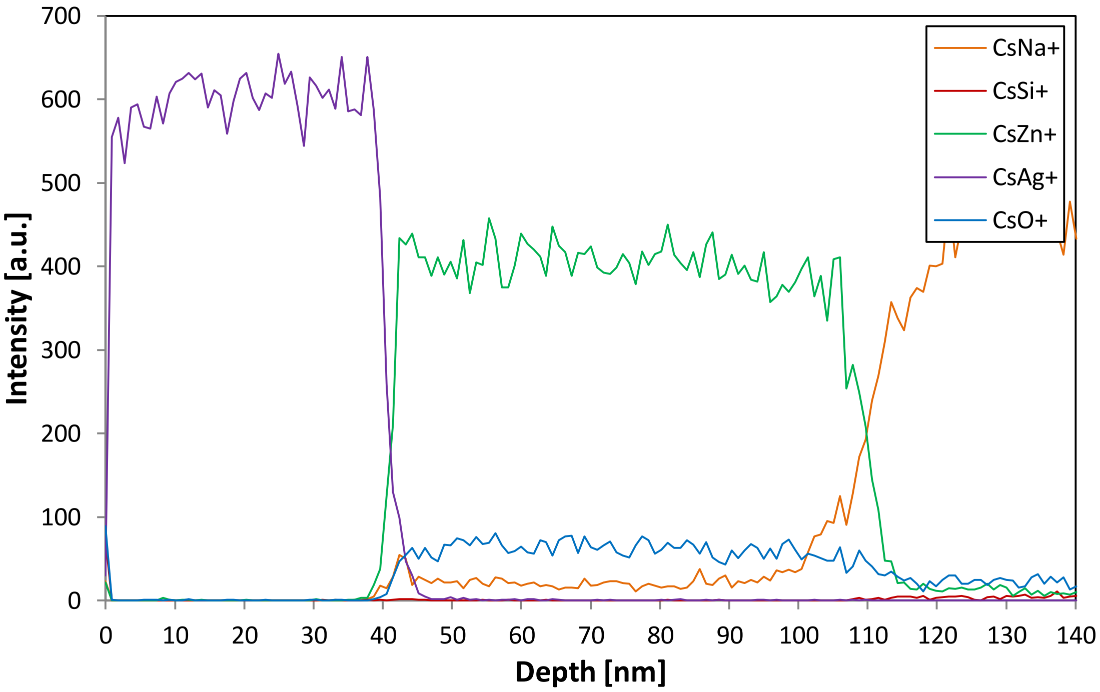

Figure 11.10: Example of TOF-SIMS profile collected from annealed Al-doped ZnO sample 3.1.

The results obtained from TOF-SIMS analysis show almost no difference in silver diffusion profiles between all nine aluminium doped zinc oxide samples (see Table 11.7). Silver diffusion coefficient values varied between 1.8 and 7.5×10^{-21} m^2/s in selected samples. There is no obvious trend between operating pressure and oxygen flow and diffusivity of silver atoms. Figure 11.11 shows scattered data points suggesting that, over the range tested, operating conditions have no impact on silver diffusivity. This is related to the Al-doped zinc oxide structure, which proved to be similar for all the coatings deposited for the purpose of this study. Relatively small diffusivity values suggest that Al-doped zinc oxide is rather difficult material to diffuse through for silver atoms. In comparison with titanium dioxide samples studied in Chapter 10, where diffusivity values as high as 10^{-19} m^2/s were obtained for most of the samples, silver migration rates through Al-doped ZnO are two orders of magnitude lower. This implies that Al-doped ZnO will provide a more efficient Ag diffusion barrier layer when deposited adjacent to silver in low emissivity stacks. The diffusivity of silver atoms through the AZO standard sample at room temperature was found to be 1.55×10^{-23} m^2/s.

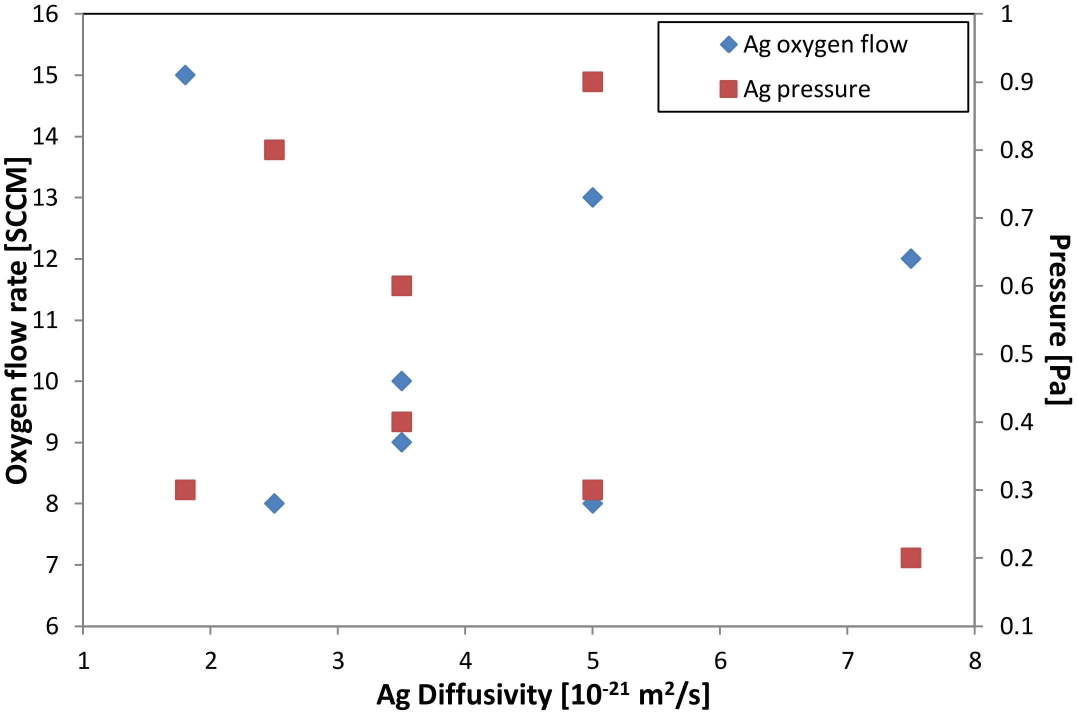

Figure 11.11: The dependency of silver diffusion values on operating pressure and oxygen flow during AZO samples deposition. Samples were post-deposition annealed at 650°C.

The intensity of sodium on the other hand, which migrates from the glass substrate through dielectric films, differs significantly in as-deposited and annealed AZO samples. Sodium in the as-deposited sample (Figure 11.9) has only been detected near the zinc oxide/glass interface region (at the depth of about 120 nm), whereas in the annealed sample (Figure 11.10) it can be still seen at the depth of about 40 nm, within the zinc oxide layer. This behaviour is caused by the first annealing conditions, and therefore sodium diffuses faster in toughened samples. The second annealing at 250°C may not cause any more differences in the diffusion profiles. The diffusivity of sodium in samples annealed at 650°C show almost no difference, as the values stay between 1 and 2×10^{-18} m^2/s, and sample 6 shows an even lower sodium diffusion value of 8×10^{-19} m^2/s. The diffusivity for the as-deposited samples was 2 orders of magnitude lower than in the annealed samples. Moreover sodium is a much smaller element than silver, which makes it even easier to travel through host lattices. Figure 11.12 shows the dependency of AZO films deposition conditions against sodium diffusivity. As in the case of silver, there is no obvious trend detected. The graph contains only heat treated samples, as in the as-deposited ones the difference in sodium diffusion is due to annealing not operating conditions.

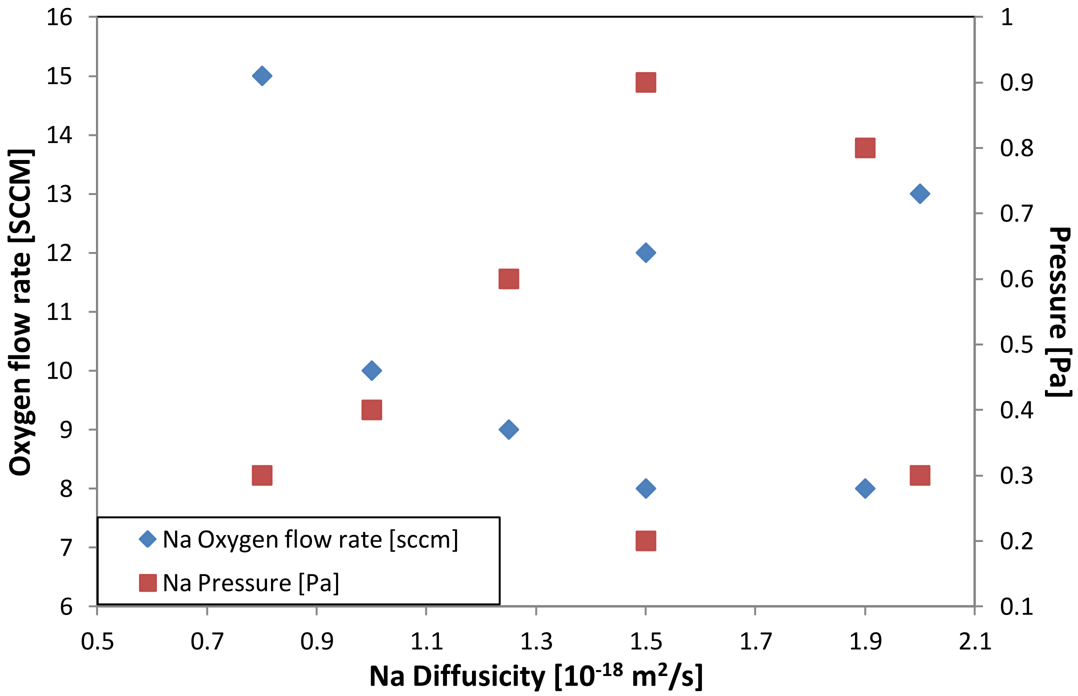

Figure 11.12: Sodium diffusion dependency on operating pressure and oxygen flow during coatings deposition. No trend obtained.

Figures 11.13 and 11.14 show examples of the analytical solution to Fick's second law of diffusion in zinc oxide samples for silver and sodium, respectively. Calculated values of diffusion coefficient can be seen in Table 11.7 for both silver and sodium atoms.

Table 11.7: Diffusion coefficient values obtained by fitting TOF-SIMS data to Fick's second diffusion law analytical solution. D_{Ag} and D_{Na} show diffusion coefficients for silver and sodium atoms, respectively.

ZnO	D_{Ag} [m^2/s]	D_{Na} [m^2/s]
Standard	1.55×10^{-23}	-
1.1	5.00×10^{-21}	1.50×10^{-18}
2.1	2.50×10^{-21}	1.90×10^{-18}
3.1	5.00×10^{-21}	2.00×10^{-18}
4.1	3.50×10^{-21}	1.00×10^{-18}
5.1	7.50×10^{-21}	1.50×10^{-18}
6.1	1.80×10^{-21}	8.00×10^{-19}
7.1	3.50×10^{-21}	1.25×10^{-18}
8.1	5.00×10^{-21}	3.20×10^{-20}
9.1	2.50×10^{-21}	2.75×10^{-20}

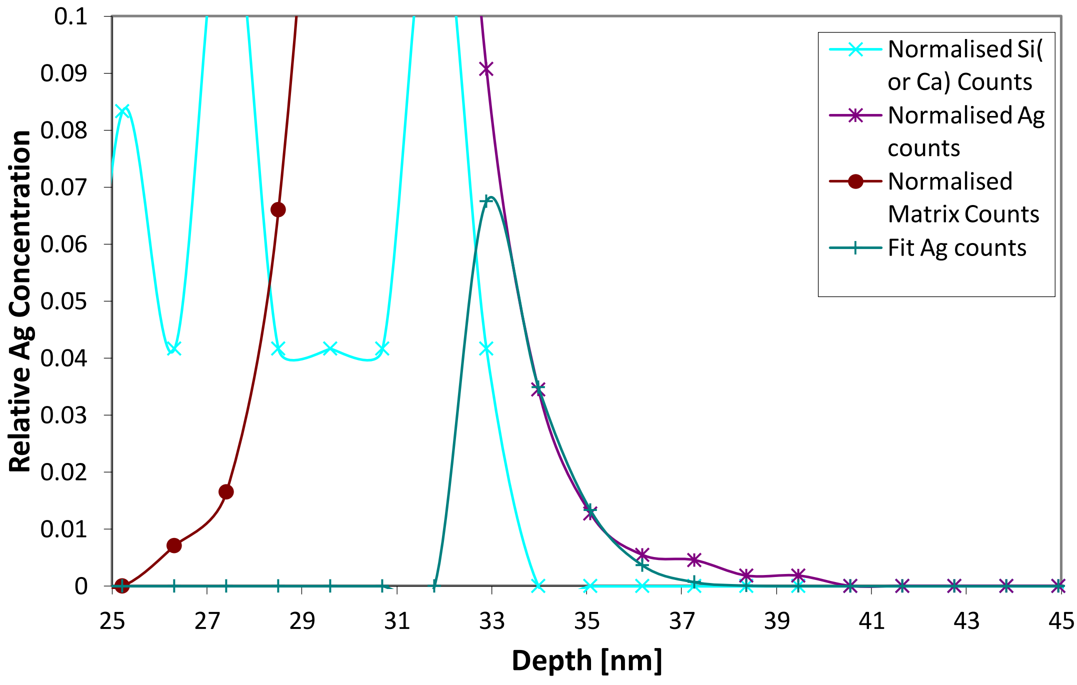

Figure 11.13: An example of an analytical solution to Fick's second law for silver atoms in the Al-doped ZnO sample 1.1.

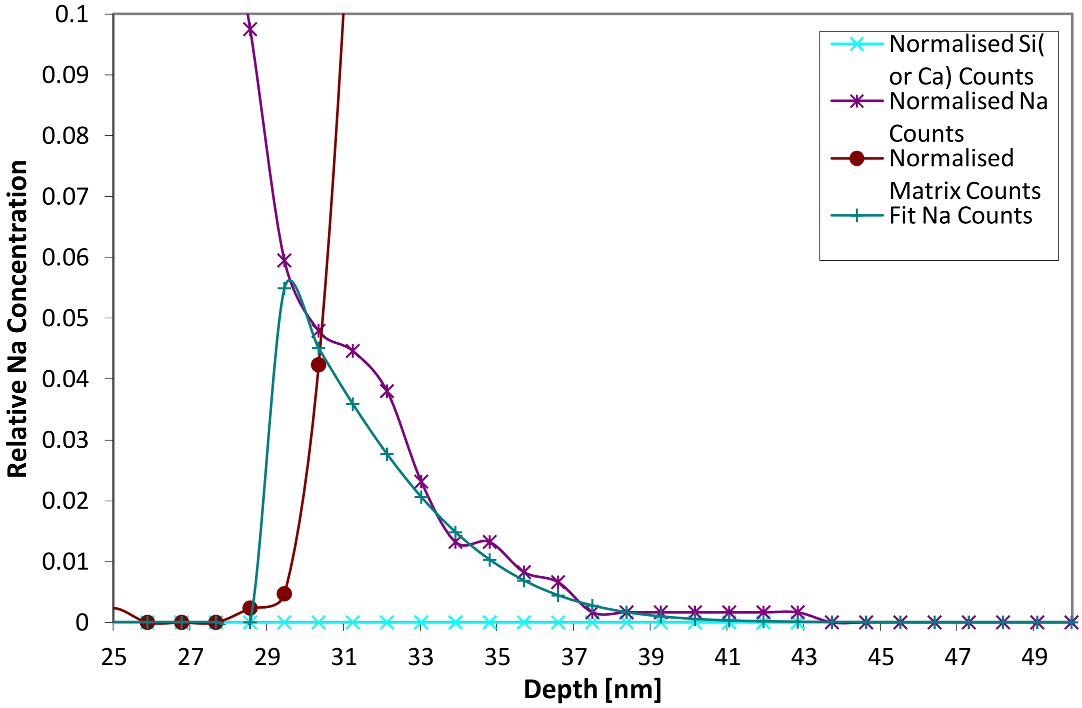

Figure 11.14: An example of an analytical solution to Fick's second law for sodium atoms in the Al-doped ZnO sample 8.1.

11.3 Al-doped ZnO: Summary

Al-doped zinc oxide samples have been deposited in two batches for coating characterisation. The first batch contained samples of about 1 µm thickness, which were characterised by EDX and SEM. The second batch which contained Al-doped ZnO films of about 80 nm thickness was analysed by XRD, AFM and optical spectroscopy. Samples were over-coated with silver and analysed by TOF-SIMS to determine the diffusion rates of silver and sodium atoms.

EDX analysis showed that the samples have atomic compositions very close to stoichiometric, with slightly heightened oxygen content, which was most likely due to flooding the chamber with O_2 during deposition. Also as the aluminium content in the samples is higher, the formation of Al_xO_x might have occurred.

SEM images showed that each sample has a fully dense structure with some texture existing on the surface.

XRD analysis distinguished one characteristic peak for ZnO crystals at 34.44°, which represents the (002) peak of a typical wurtzite ZnO crystalline structure. Samples consist of relatively small grains and show some peak shifts to lower 2θ values, which are most likely due to the intrinsic stress of the coating.

AFM analysis performed on selected Al-doped ZnO samples showed that samples had rather smooth surfaces, as in each case RMS values were determined to be close to 1 nm. Optical analysis was performed on selected AZO samples to find refractive indices and extinction coefficient values. It was found that refractive indices tend to decrease with increasing operating pressure while depositing the samples.

Diffusion studies revealed that silver diffusion coefficient values are very similar in all analysed samples and their values are very low and stays between $1.8\text{-}7.5\times10^{-21}$ m^2/s. Sodium on the other hand diffuses significantly faster in annealed samples, which is directly connected to the first annealing temperature of 650^oC. The diffusion coefficient values obtained for sodium in as-deposited samples are two orders of magnitude smaller that in annealed ones at around 3×10^{-20} m^2/s. Therefore the Al-doped ZnO coatings acts as excellent barrier coatings for silver atoms and show very good results for sodium diffusion, when not annealed at relatively high temperatures.

12. Results: Zinc Stannate Coatings

Zinc stannate coatings were deposited in the Pilkington Technology Management Ltd. in Lathom, as described in the experimental procedures section (Chapter 9.1). Coatings were subjected to annealing and then analysed by XRD, AFM, SEM and optical spectroscopy to characterise the structure of the deposited zinc stannate films. After over-coatings the Zn_2SnO_4 layers with silver the samples were re-annealed at 250^{o}C for 5 minutes and analysed by TOF-SIMS.

12.1 Zn_2SnO_4: Coating Characterisation

Table 12.1 presents deposition conditions assigned to 20 zinc stannate samples deposited in this study. Run conditions and the magnetron types used to deposit the zinc stannate films are assigned to each sample, as well as the post-deposition annealing conditions. Thickness of deposited samples was estimated to be 80 nm (with ±1.0 nm variations).

Table 12.1: Deposition conditions for zinc stannate coatings.

Sample number	**Magnetron type**	**Power [kW]**	**Pressure [Pa]**	**O_2 flow [SCCM]**	**Annealing conditions [^oC]**
1	DC	1	0.3	70	650
2	DC	3	0.3	120	650
3	DC	3	0.3	170	650
4	DC	3	0.8	120	650
5	DC	3	1.2	120	650
6	DC	5	0.3	150	650
7	Dual AC	3	0.3	120	650
8	Dual AC	3	0.3	170	650
9	Dual AC	3	0.8	100	650
10	Dual AC	3	1.2	100	650
11	Dual AC	5	0.3	140	650
12	Dual AC	5	0.3	160	650
13	Rot. AC	3	0.3	100	650
14	Rot. AC	3	0.3	170	650
15	Rot. AC	5	0.8	80	650
16	Rot. AC	5	1.2	80	650
17	DC	3	0.3	120	-
18	Dual AC	3	1.2	100	-
19	Dual AC	5	0.3	160	-
20	Rot. AC	3	0.3	100	-

XRD analysis was carried out on selected zinc stannate samples. Samples were scanned for 5 hours using the X'Celerator detector at Lathom. Figure 12.1 shows an overlay of the nine diffractograms collected from selected zinc stannate samples. No crystallographic reflections were obtained from any of the coatings indicating that there was either no crystallinity or any present crystallinity was below the detection sensitivity of the measurements. The background shapes detected are typical of amorphous materials indicating that some short-range order is present. However it was reported in the literature that RF deposited zinc stannate films sputtered from ceramic targets show crystallographic reflections after annealing at 650°C and above. [51, 57] Nevertheless in most cases the annealing time was much longer and equalled 1 hour in contrast to the 5 minutes applied in this work. Therefore annealing time may not be sufficient for amorphous zinc stannate to convert into inversed spinel Zn_2SnO_4 crystals. Moreover it was pointed out that the optimal conditions of formation of a crystalline ZTO structure is post-deposition annealing at 800°C, which could not be performed here due to glass substrate limitations. [157-158]

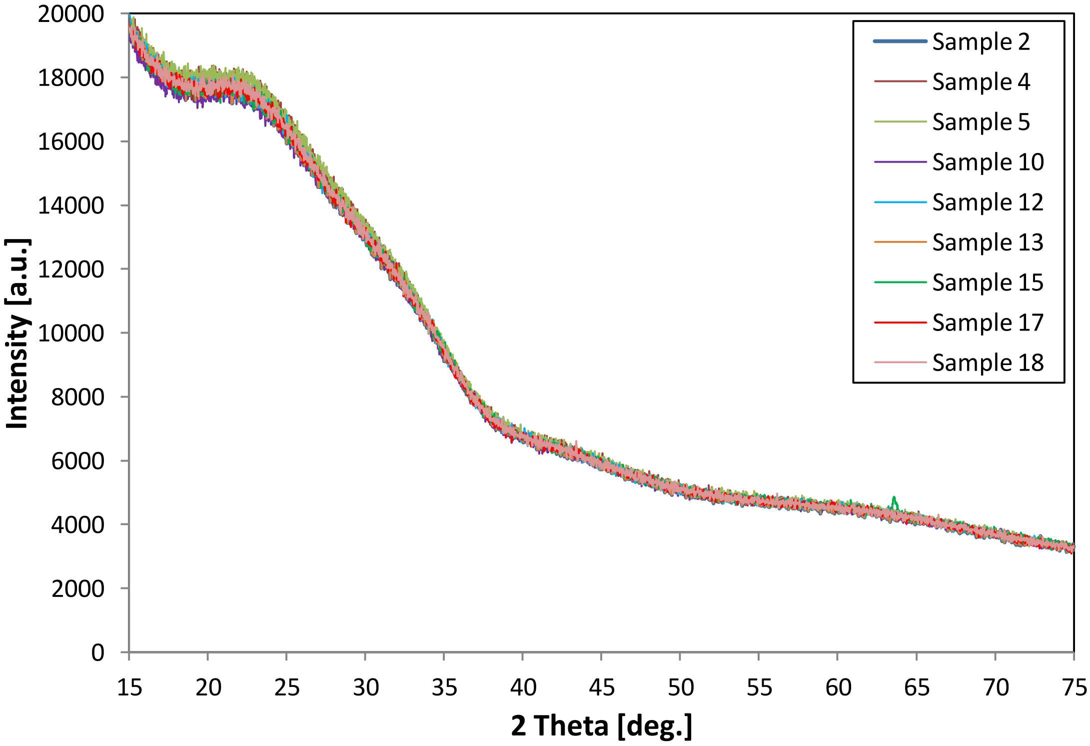

Figure 12.1: XRD results collected from selected zinc stannate samples post-deposition annealed at 650°C.

SEM analysis showed that the zinc stannate films consisted of very smooth and dense, glassy like structures, with small defects existing on the surfaces. This is a characteristic of amorphous structures, which has been already determined by XRD. Examples of the structures are shown in Figures 12.2-12.3.

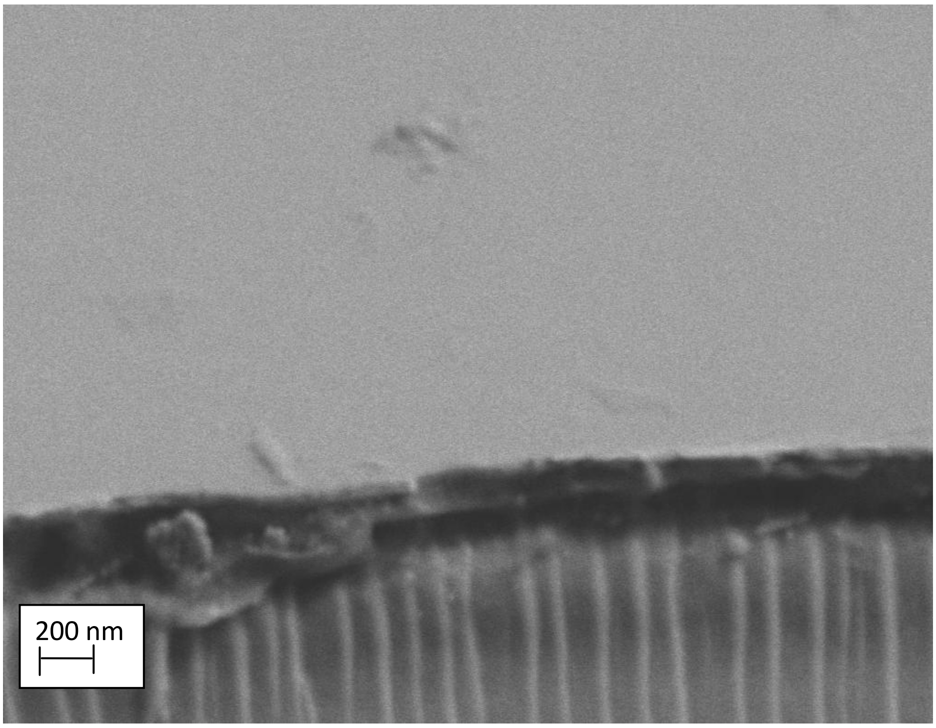

Figure 12.2: SEM micrographs of the fracture section of the zinc stannate sample 2 deposited onto float glass substrate.

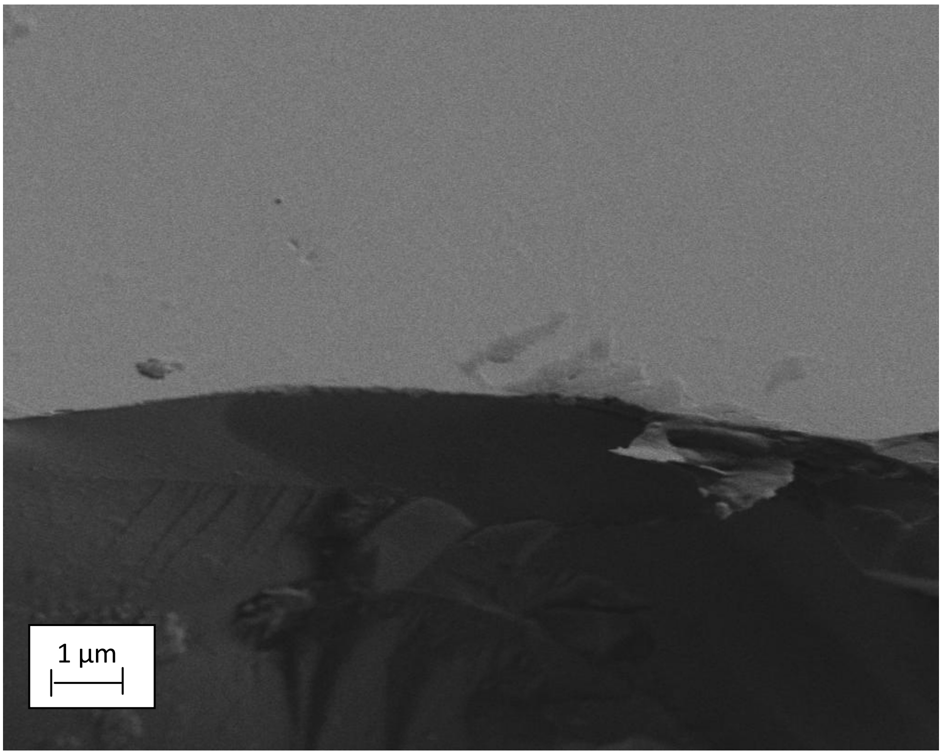

Figure 12.3: SEM micrograph of the fracture section of zinc stannate samples 10 deposited onto float glass.

Figure 12.4 shows 500 nm x 500 nm AFM images of selected ZTO samples. Table 12.2 shows root-mean-square (RMS) and roughness average (Ra) values for each sample. Sample 12 showed the lowest values for root mean square and roughness average from the six selected samples, which suggests that sample 12 has the smoothest surface. Sample 2 on the other hand shows the highest RMS and Ra values, and so shows the roughest surface. This sample was deposited under a working pressure of 0.3 Pa by DC sputtering, whereas sample 12 was deposited under a similar pressure in dual AC mode. There are no significant differences in surface roughness observed between the other samples.

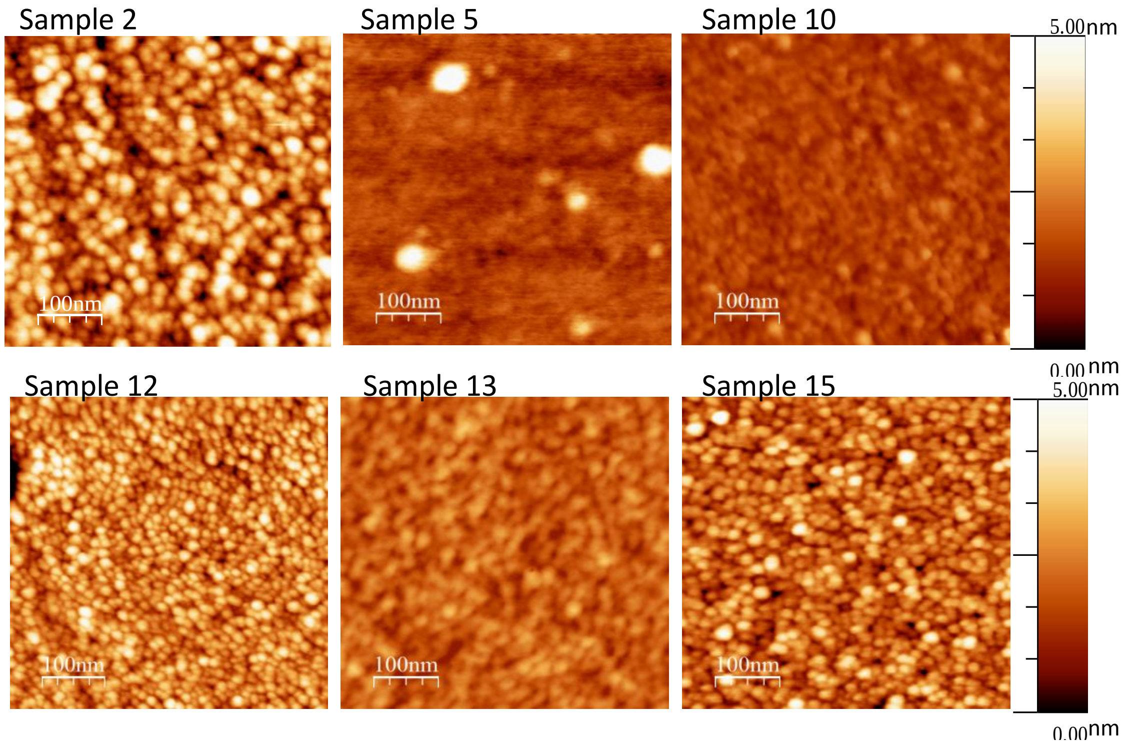

Figure 12.4: AFM images of six selected zinc stannate samples deposited onto float glass substrate.

Table 12.2: ZTO samples RMS and Ra values obtained from AFM analysis.

Sample number	**RMS [nm]**		**Ra [nm]**	
	1 µm × 1µm	**500nm ×500nm**	**1 µm × 1µm**	**500nm ×500nm**
2	1.092	0.835	0.834	0.618
5	0.732	0.723	0.582	0.576
10	0.711	0.765	0.558	0.602
12	0.310	0.284	0.225	0.216
13	0.467	0.569	0.307	0.335
15	0.502	0.435	0.352	0.347

The optical proprieties of the Zn_2SnO_4 films were measured to find refractive index (n) and extinction coefficient (k) values of the selected coatings. In Table 12.3 the n and k values at 550 nm wavelength are listed. The literature values of the refractive index for zinc stannate are 2.12-2.15 [159] and values obtained from optical analysis for n and k are 2.00-2.07 and 0.00615-0.00195 respectively. The values of refractive index slightly decreased from 2.05 to 2.00 when the operating pressure increased for the zinc stannate films deposited by AC power. Samples sputtered under DC conditions did not follow the same trend.

Table 12.3: Optical constants of Zn_2SnO_4 selected samples as a function of pressure.

Sample number	**Pressure [Pa]**	**Refractive index (n)**	**Extinction coefficient (k)**
2	0.3	2.00	6.32×10^{-3}
10	1.2	2.00	3.10×10^{-3}
12	0.3	2.07	1.25×10^{-3}
13	0.3	2.05	1.95×10^{-3}
15	0.8	2.05	1.25×10^{-3}
17	0.3	2.05	6.22×10^{-3}

12.2 Zn_2SnO_4: Diffusion Studies

Silver diffusion occurs significantly faster in zinc stannate than in the other oxide films, so far investigated. Figure 12.5 shows a standard sample analysed by TOF-SIMS and the silver diffusion coefficient calculated for this sample is 7×10^{-23} m^2/s. High sodium level in this sample is related to first annealing of oxide coating at 650^oC for 5 minutes.

In most cases there is an insignificant difference in the Ag diffusivity values between the annealed and as-deposited ZTO samples as values varies between 1 and 2×10^{-18} m^2/s. The only exception is sample 19, which was determined to have a silver diffusion coefficient of 1×10^{-19} m^2/s. Sodium diffusion on the other hand is impossible to measure using the diffusion calculator, probably due to the path of the diffusing atoms. It is possible that sodium has found a fast path through zinc stannate films, which enables it to diffuse through these coatings fairly easily. From the TOF-SIMS depth profiling obtained from the annealed sample presented in Figure 12.7 it can be seen that Na diffuses through the entire thickness of the zinc stannate coating and its concentration decreases when it has reached the silver layer.

Figures 12.6-12.7 show examples of depth profiles collected from as-deposited and annealed Ag/Zn_2SnO_4/glass samples respectively.

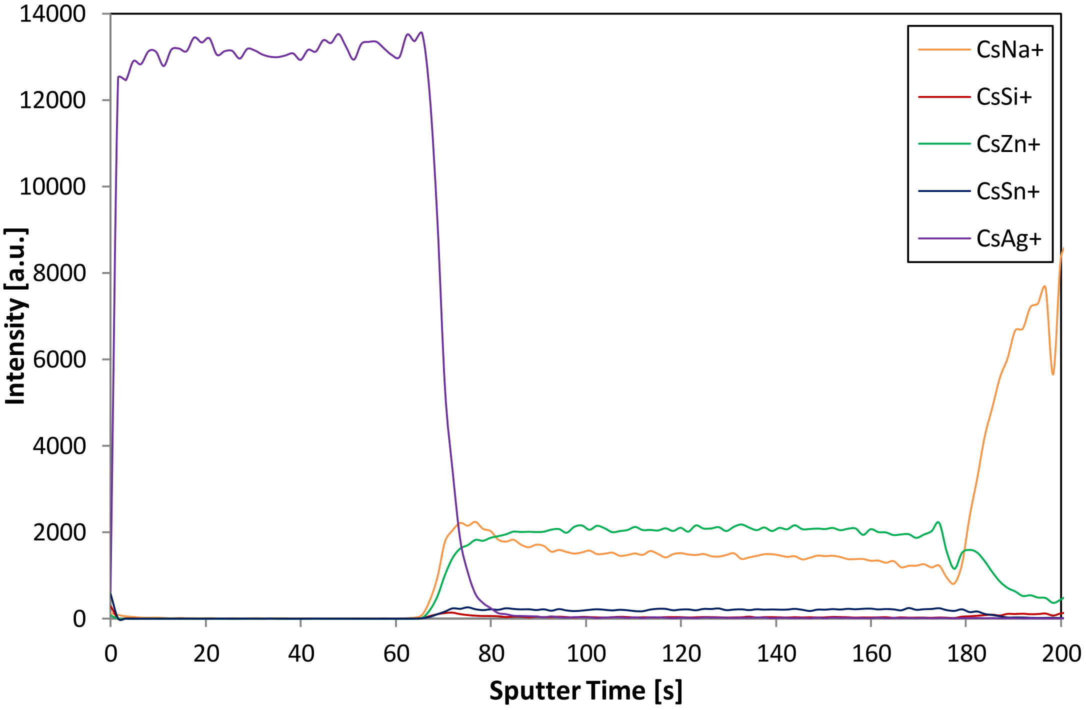

Figure 12.5: TOF-SIMS depth profiling collected from zinc stannate standard sample deposited onto float glass substrate.

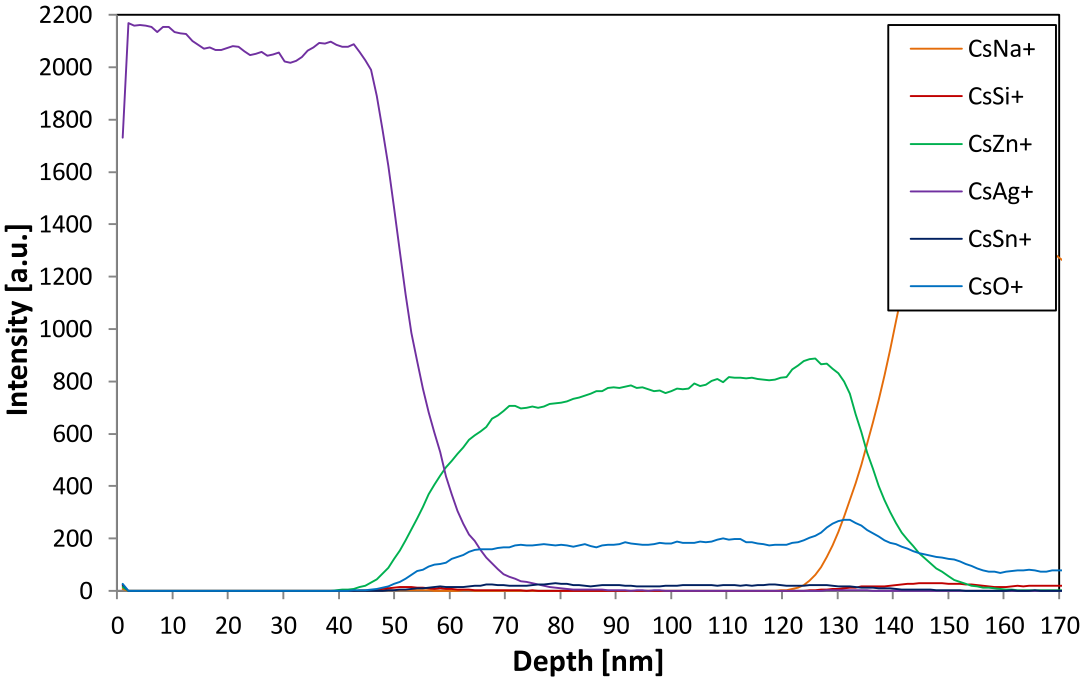

Figure 12.6: An example of TOF-SIMS depth profiling in as-deposited zinc stannate sample 17.

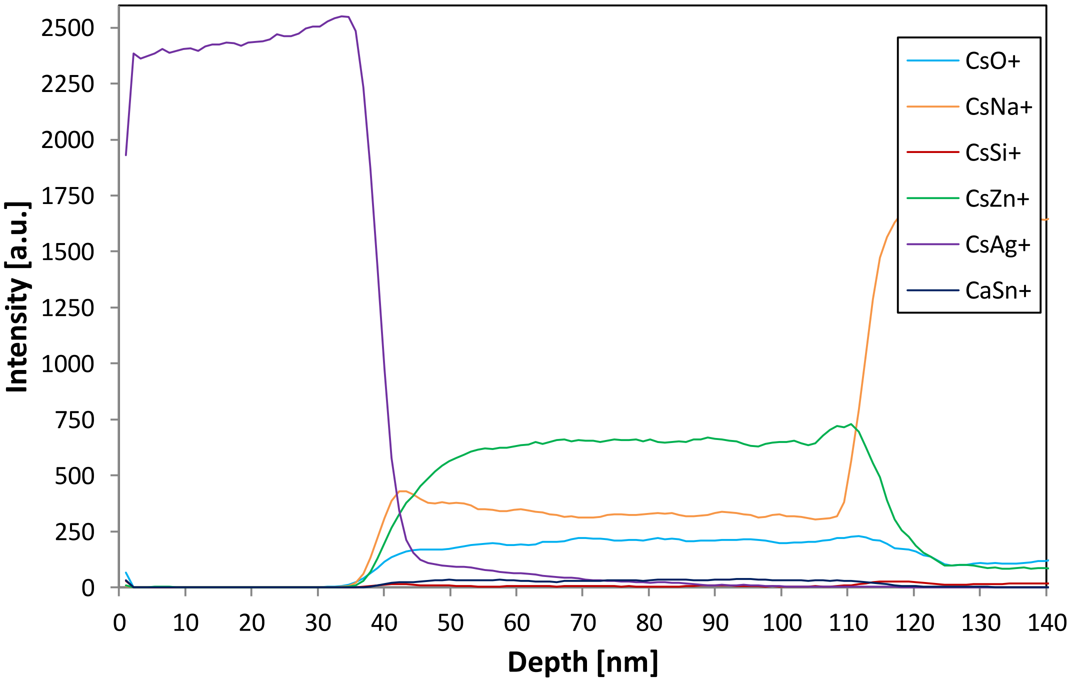

Figure 12.7: TOF-SIMS profile for zinc stannate sample 7 annealed at 650°C.

Table 12.4 shows the diffusion coefficient values calculated for silver in 20 zinc stannate samples. As mentioned earlier there is almost no difference in Ag diffusivity in the analysed samples, however sample 19, which has been deposited using the dual AC magnetron type, which was driven at 5 kW power at an operating pressure of 0.3 Pa and oxygen flow rate of 160 SCCMs shows a significantly lower diffusion rate than the remaining samples. This sample was not post-deposition annealed at 650^{o}C for 5 minutes, but only at 250^{o}C after silver deposition. Sample 12 on the other hand, which was deposited under the same conditions as sample 19, but was annealed at 650^{o}C, presents silver diffusion in a similar range to that obtained for the other zinc stannate samples. Figure 12.8 magnifies the silver profiles of the TOF-SIMS curves at the knee-like region where the silver intensity heads towards zero, to see more clearly the difference in the diffusion distance in these two samples. There is a clear difference in silver distribution between these two samples. The curve obtained from sample 19 shows a smaller $\sqrt{Dt}$ length (see Chapter 6.5), which generally represents lower diffusion flux, whereas in the profile obtained from sample 12, the length is longer suggesting a higher diffusion rate. In general, it is expected that for a diffusion free system the profile of the diffusing species rapidly drops to zero when the interface between two species (films) is reached. The diffusion of silver occurs in these samples during annealing. The annealing temperature and time are equal for both samples, and under these conditions silver atoms travel through the interface into the adjacent film to a distance $\sqrt{Dt}$. When the diffusion rate is higher $\sqrt{Dt}$ becomes longer, and therefore the profile of sample 12 shows a larger slope than the profile of sample 19. However the reason for higher Ag diffusivity in this sample is not clear as there is no correlation between deposition conditions and diffusion coefficient values (more repeats needed). Figures 12.9-12.11 show diffusion values as a function of pressure, power and oxygen flow in samples deposited from three different magnetron configurations. In each case data are scattered showing no trend in diffusion coefficient values. Therefore silver diffusion in zinc stannate coatings appears to be independent of deposition conditions, which is due to the fact that zinc stannate coatings deposited under different deposition conditions show similar amorphous structures, which do not change after annealing at 650^{o}C for 5 minutes, as was described in the previous chapter.

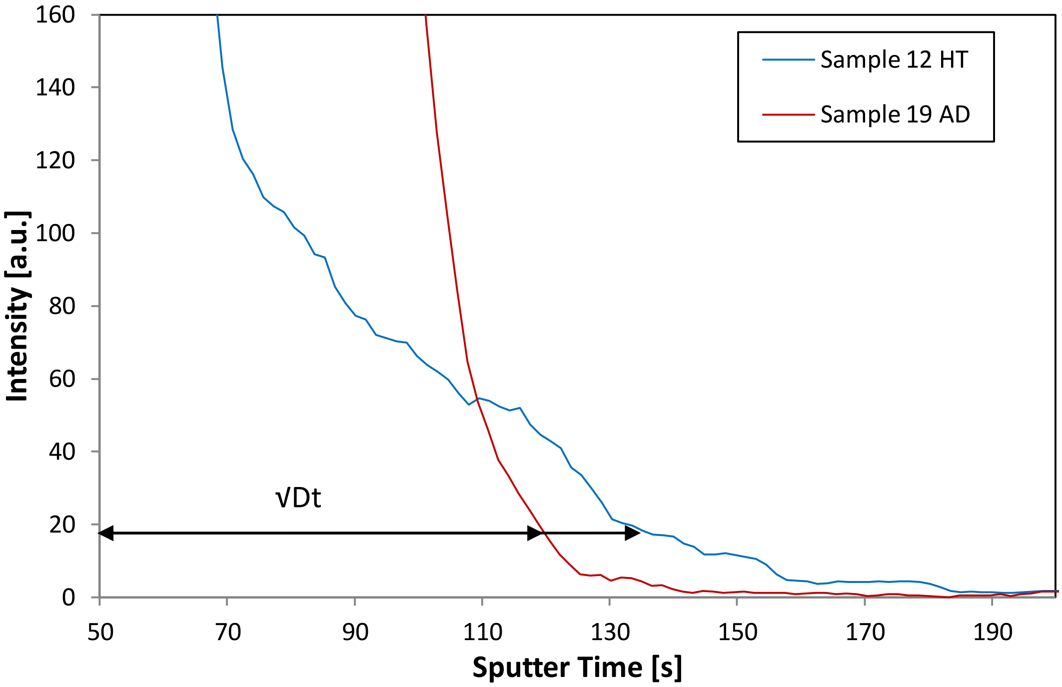

Figure 12.8: Magnifies profile of silver curves collected by TOF-SIMS depth profiling from samples 12 and 19. Quite a significant difference in the diffusion distance has been distinguished.

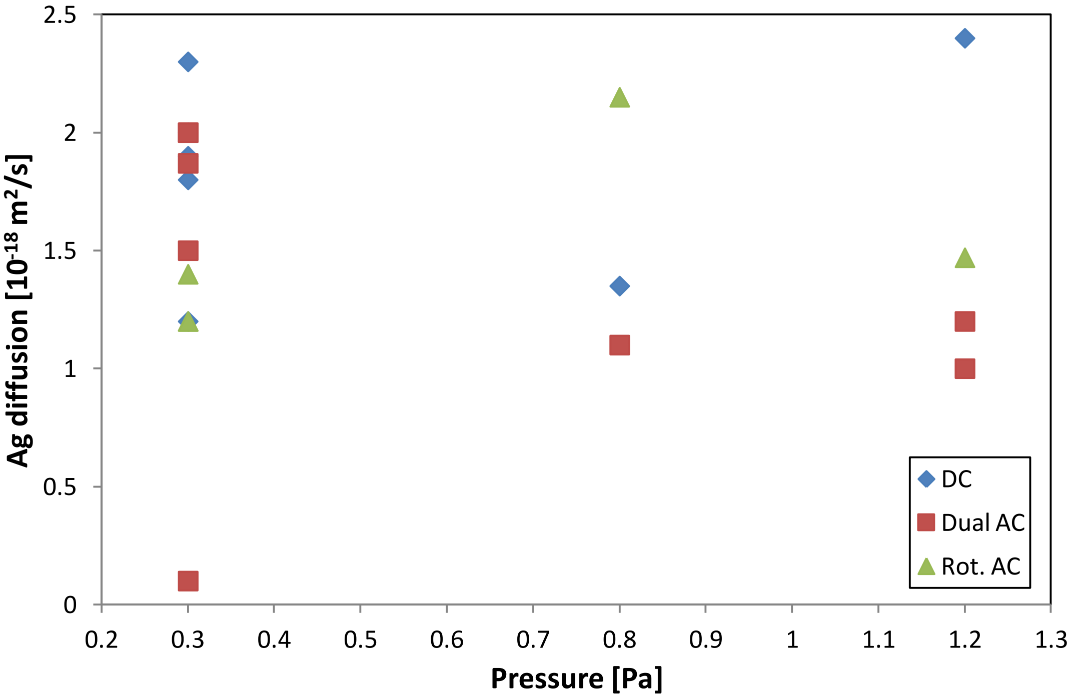

Figure 12.9: Silver diffusion dependency on operating pressure. Samples deposited from single planar magnetron in DC mode, from dual planar magnetrons in AC mode and from rotatable cylindrical in AC mode.

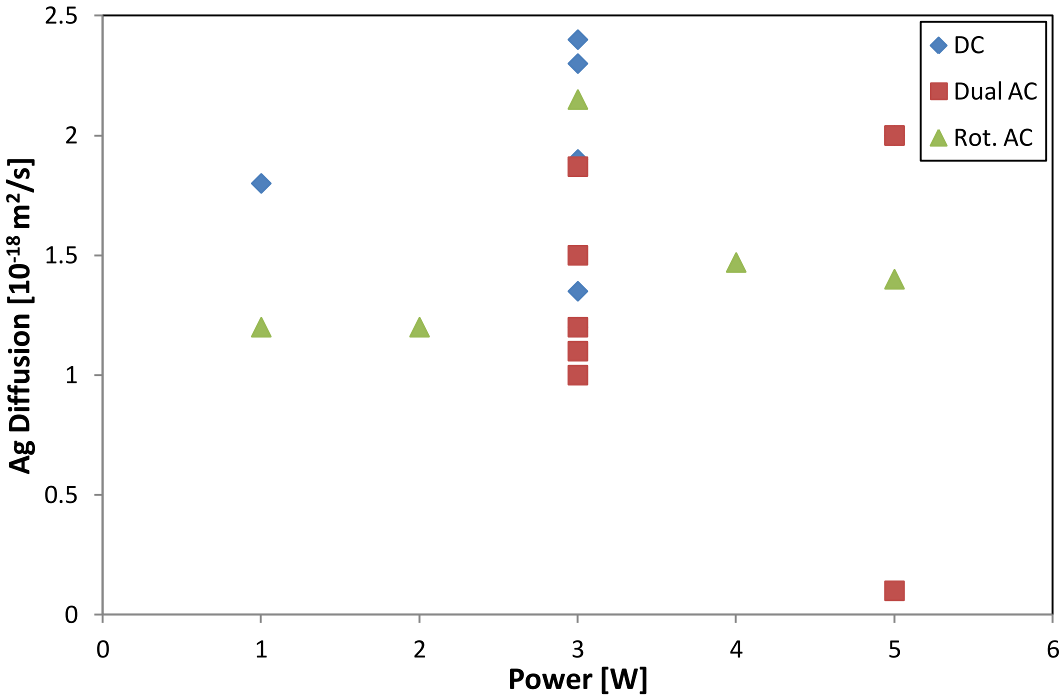

Figure 12.10: Silver diffusion dependency on power used during sample deposition. Samples sputtered from dual planar and rotatable cylindrical magnetrons in AC mode and from single planar magnetron in DC mode.

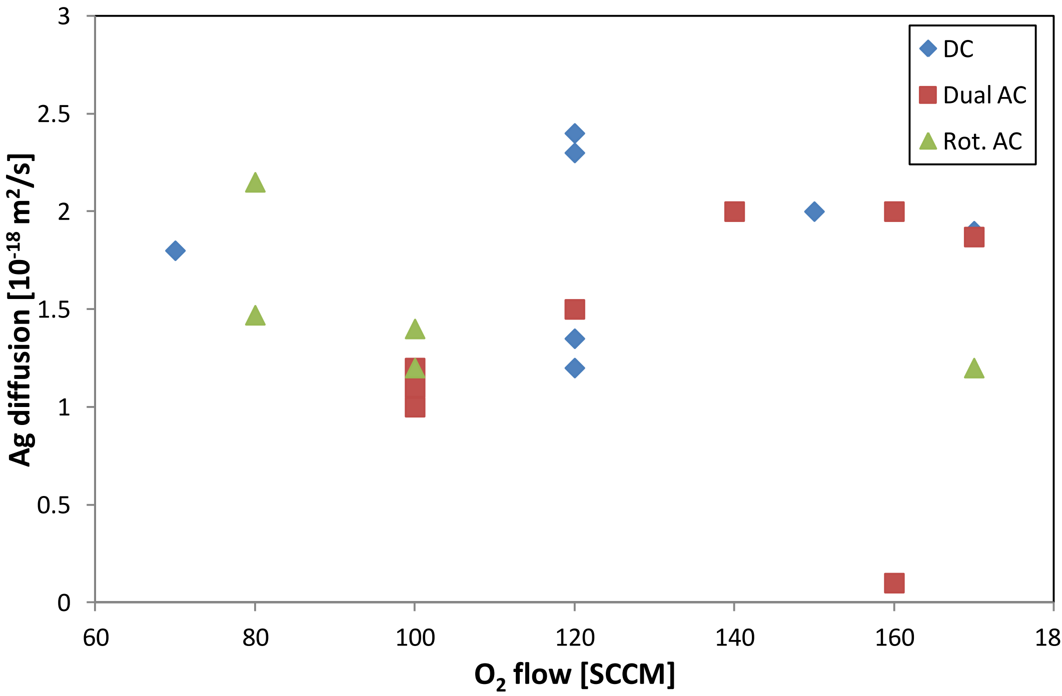

Figure 12.11: Silver diffusion coefficient dependency on oxygen flow rate during samples deposition in three magnetron configuration systems: DC and AC sputtered from planar targets and rotatable AC from cylindrical targets.

It was not possible to determine the diffusion coefficient values from the sodium profiles using the diffusion calculator. This anomaly is probably caused by the nature of migration of sodium atoms in annealed zinc stannate samples. Figure 12.12 shows an example of modelled sodium data obtained using a diffusion calculator programme. The fitting of the complementary error function (analytical solution to Fick's second law) is not satisfactory, as the shape of the Na curve is nothing like that expected according to the Fickian diffusion mechanism (see Chapter 6.5.2). It seems like sodium rapidly diffuses through the entire thickness of the zinc stannate coatings and starts to slow down at the zinc stannate/silver interface. This suggests that the silver layer serves as a more difficult medium to travel through than the ZTO coatings. The major difference between those coatings is the crystal structure. As discussed earlier, zinc stannate coatings remain amorphous even after annealing, whereas metallic silver layers present typical face-centred cubic arrangements in the lattice. Amorphous materials have lower densities than crystalline materials due to random arrangements in the lattice and, as in the case of glassy silica, they can have dangling bonds, which promote diffusion. It is known that rapid diffusion occurs through interstitial sites (open spaces between atoms in the matrix) and this is the path which is usually ideal for small atoms, like Na. However if the structure of the hosting coating was rather open then also larger metal atoms could find their way to diffuse through these interstitial sites. [95] This may be the case here, as sodium diffuses very easily through zinc stannate coatings, whereas silver, which has an atomic size much larger than sodium, also has found a quick way through Zn_2SnO_4 compared with the previously studied materials in this work. Moreover when sodium reaches the silver/zinc stannate interface the diffusion rate decreases rapidly, which is caused by the structure of the silver layer. In crystalline close packed arrangements the diffusion occurs by different mechanisms than in amorphous materials (see Chapter 6.6). The structure is now closed and it is more challenging to diffuse through the lattice. The only fast tracks are grain boundaries and dislocations, which in the case of sodium migration are not faster to travel along than the zinc stannate lattice.

In as-deposited ZTO samples sodium diffusion coefficient values are low and were determined to be about 1×10^{-20} m^2/s. Sample 20 shows the lowest diffusion coefficient value of 4×10^{-21} m^2/s and it was deposited in AC mode from a dual cylindrical rotatable magnetron configuration at an operating pressure of 0.3 Pa, oxygen flow of 100 SCCM and an applied power of 3 kW. The remaining as-deposited samples were deposited under the broad range of conditions (see Table 12.1), but there is no correlation between deposition conditions and sodium diffusivity. Sample 17 was sputtered under similar conditions to sample 20, but in DC mode from a planar magnetron. However, the sodium diffusion coefficient value established for this sample is 1.13×10^{-20} m^2/s. The main difference between these samples was the mode and magnetron type used to deposit the coatings. Since there is no other as-deposited sample sputtered from rotatable magnetrons and analysed by TOF-SIMS, it cannot be confirmed that operating conditions have had an impact on film structure and hence on sodium diffusion.

Table 12.4: Diffusion coefficient values obtained from zinc stannate samples by fitting TOF-SIMS data to Fick's second diffusion law. D_{Ag} and D_{Na} describes diffusion coefficient values calculated for silver and sodium atoms respectively.

Sample number	**D_{Ag} [m^2/s]**	**D_{Na} [m^2/s]**
Standard	7.00×10^{-23}	-
1	1.80×10^{-18}	-
2	2.30×10^{-18}	-
3	1.90×10^{-18}	-
4	1.35×10^{-18}	-
5	2.40×10^{-18}	-
6	2.00×10^{-18}	-
7	1.50×10^{-18}	-
8	1.87×10^{-18}	-
9	1.10×10^{-18}	-
10	1.00×10^{-18}	-
11	2.00×10^{-18}	-
12	2.00×10^{-18}	-
13	1.20×10^{-18}	-
14	1.20×10^{-18}	-
15	2.15×10^{-18}	-
16	1.47×10^{-18}	-
17	1.20×10^{-18}	1.13×10^{-20}
18	1.20×10^{-18}	1.00×10^{-20}
19	1.00×10^{-19}	1.50×10^{-20}
20	1.40×10^{-18}	4.00×10^{-21}

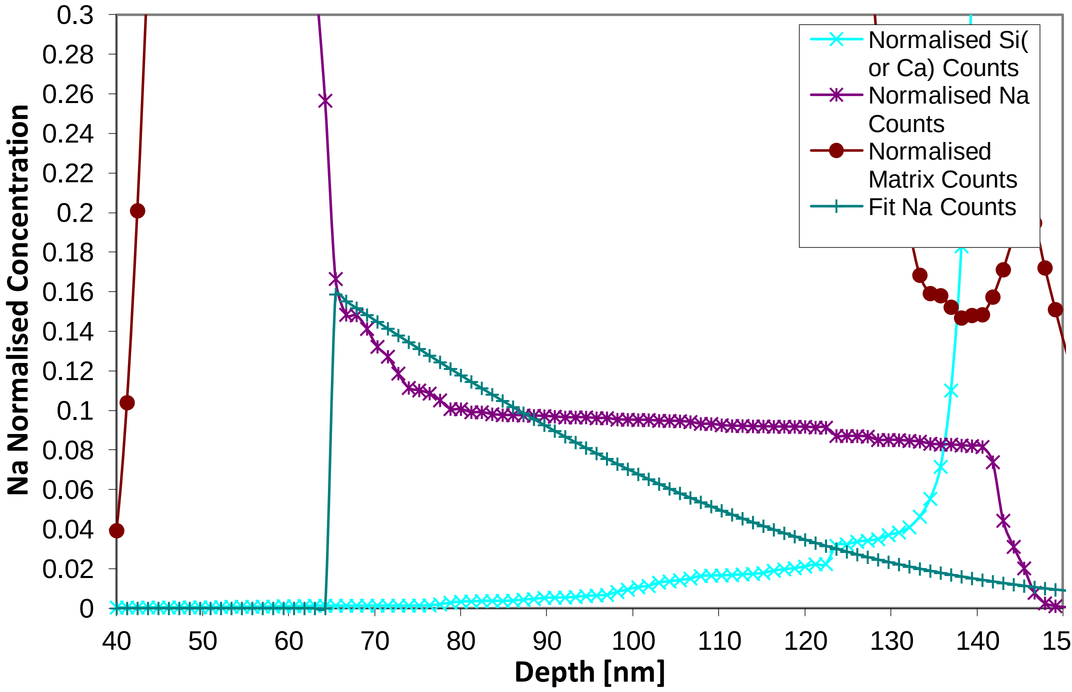

Figure 12.12: An example of Na counts fitting into diffusion calculator of the annealed zinc stannate sample 6.

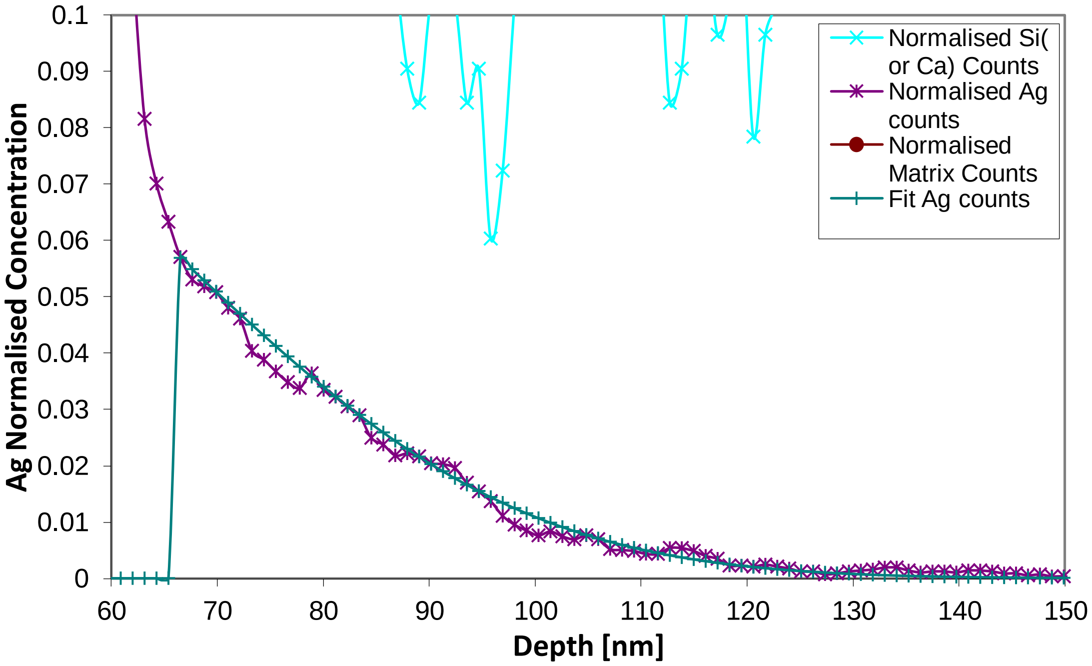

Figure 12.13: An example ZTO sample 9 silver data fitted into diffusion calculator to find the analytical solution to Fick's diffusion law.

12.3 Zn_2SnO_4: Summary

ZTO coatings were deposited in Pilkington Technology Management Ltd. laboratories in Lathom. Overall 20 samples were prepared under a wide range of operating conditions. Samples were sputtered from three different magnetron configuration systems: planar magnetrons in DC and AC mode, and from cylindrical rotatable magnetrons in AC mode.

XRD analysis showed no difference in crystal structures between the samples, even after annealing. All of the samples analysed in this studies remained amorphous. SEM micrographs showed that ZTO films have dense and smooth surfaces with a glassy finish characteristic of amorphous materials. Selected samples were analysed by AFM to find surface roughness. Analysed samples showed smooth surfaces with RMS vales below 1 nm, except for sample 2, deposited in DC mode at 0.3 Pa operating pressure. Optical spectroscopy analysis determined refractive indices and extinction coefficient values for selected samples at 550 nm wavelength. Refractive index seems to decrease when operating pressure increases in samples deposited in AC power.

Diffusion measurements determined that the silver diffusion coefficient values for all of the samples were in the range of $1\text{-}2.5\times10^{-18}$ m^2/s, and that the lowest diffusion coefficient value was obtained for as-deposited sample 19. No trend was observed in diffusion coefficient values against deposition conditions used during sample preparation or after heat treatment. Therefore it can be assumed that in general annealing at $250^{o}C$ and/or deposition conditions (over the range tested) does not influence the silver diffusion rates through ZTO films. Sodium diffuses very quickly through entire ZTO layers, and its profile suddenly drops down when the silver/ZTO interface is reached. This may be related to the differences in the crystalline structure of these films, as in general diffusion occurs more rapidly in amorphous materials. The sodium diffusion rates in as-deposited samples stayed in the range of 10^{-20} m^2/s for most of the samples, except sample 20, which was found to have the diffusion coefficient equal to 4×10^{-21} m^2/s.

13. Results: Silicon Nitride Coatings

Silicon nitride thin films were deposited at MMU in the Large Area coating chamber. The methodology has been described in Chapter 9. Coatings were reactively sputtered from a silicon target in the presence of nitrogen gas. Table 13.1 lists the samples with the deposition conditions assigned to them.

Table 13.1: Silicon nitride samples deposition conditions.

Sample number	Power [W]	Pressure [Pa]	N_2 flow [SCCM]	Annealing conditions
1	300	0.3	11	650°C
2	300	0.3	10	650°C
3	300	0.5	9	650°C
4	300	0.5	11	650°C
5	300	0.9	9	650°C
6	300	0.9	9	650°C
7	150	0.3	9	650°C
8	150	0.5	11	650°C
9	300	0.9	9	-
10	150	0.5	11	-

13.1 Si_3N_4: Coating Characterisation

XRD analysis was carried out onto selected, post-deposition annealed silicon nitride coatings, scanning samples from 5 to 75 degrees 2θ for 30 minutes using a X'Celerator detector. No crystallographic reflections were obtained from any of the coatings, indicating that there was either no crystallinity or any present crystallinity was below the detection sensitivity of the measurements. Therefore a more surface sensitive analysis technique was used; glancing angle XRD (GA-XRD), which also failed to identify crystallinity within the selected sample (see Figure 13.3). Consequently the Si_3N_4 coatings have been characterised as being amorphous. The background features detected are typical of amorphous materials indicating that some short-range order is present. Löbl *et al.* have investigated silicon nitride coatings deposited by magnetron sputtering and determined that silicon nitride films become crystalline after annealing at 825°C. Below this temperature coatings remained amorphous. Moreover he pointed out that as-deposited silicon nitride has so called dangling bonds, which are responsible for electrical conductivity. Annealing reduces the number of dangling bonds leading to fewer states in the band gap, therefore reducing its conductivity. [160]

The results from XRD collected from all the samples are presented in Figures 13.1. Figure 13.2 compares diffractograms collected from two samples deposited under the same conditions, but where one sample was post-deposition annealed at 650°C and the other was not, to emphasise that the crystal structure does not change after high temperature treatment.

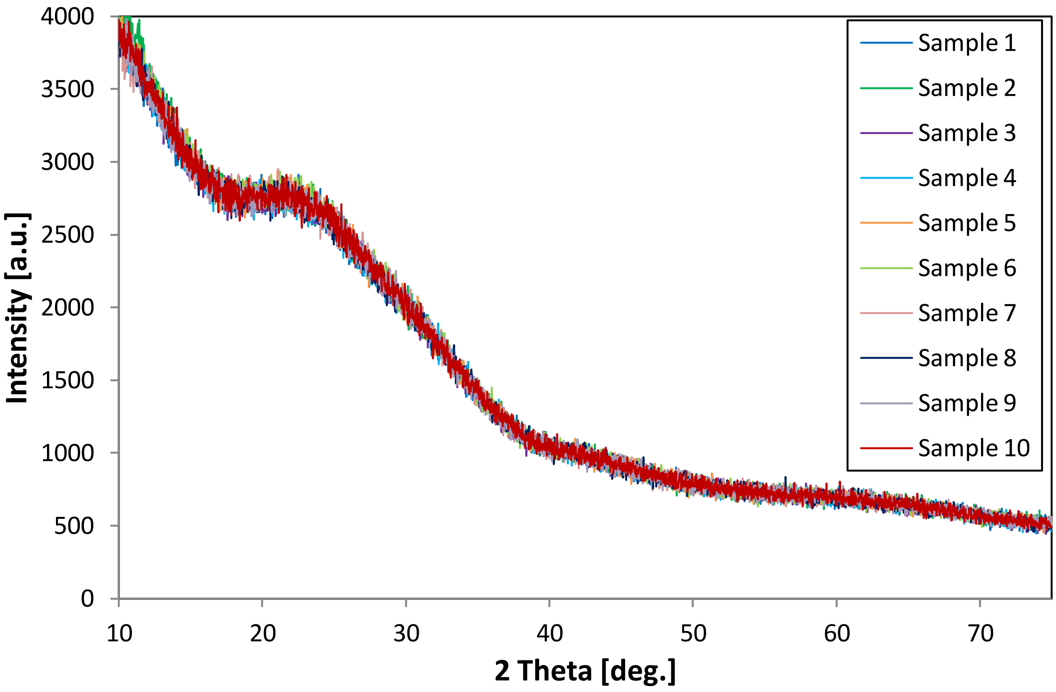

Figure 13.1: XRD spectra collected from ten Si_3N_4 samples investigated in this work.

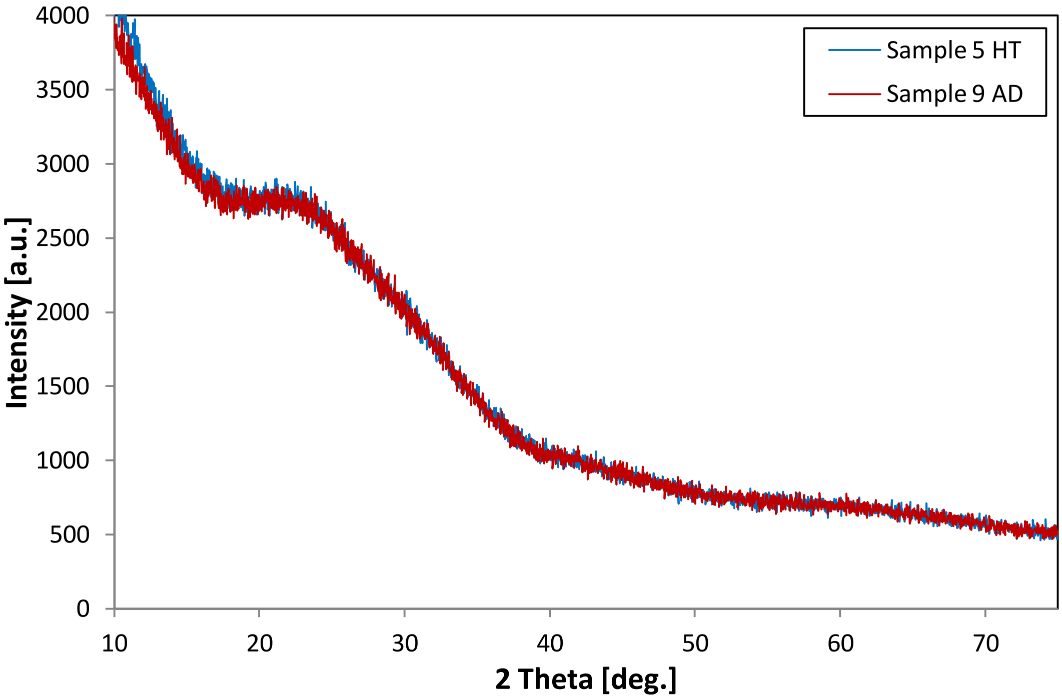

Figure 13.2: XRD spectra collected from samples deposited under the same condition, but sample 5 was post-deposition annealed at 650°C, whereas sample 9 was not.

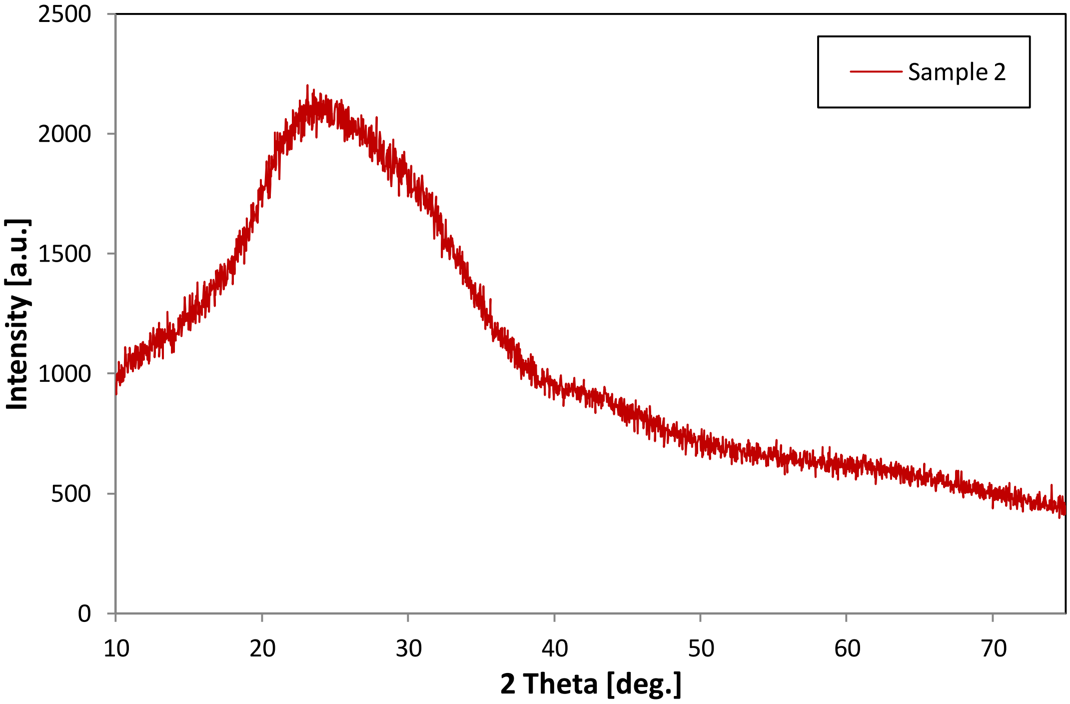

Figure 13.3: Silicon nitride sample 2 deposited onto float glass substrate, analyzed by glancing angle X-ray diffraction.

X-Ray reflectometry (XRR) was performed on silicon nitride samples to model thickness, roughness and density of the coatings. Reflectograms were obtained by scanning each sample for 2 hours using the phase detector.

Samples 1, 2, 3 and 4 provided good fits; whereas the remaining samples (5-10) provided satisfactory fits. Figures 13.4 and 13.5 show spectra collected from good and satisfactory XRR fits respectively. The good fit represents the modelled data, which largely corresponds to the measured data line, with some discrepancies, and therefore presents a low level of uncertainty of the modelled data. Thickness, roughness or density of some layers is different than expected. The satisfactory fit shows average level of uncertainty, as the model fit roughly corresponds to the measured data line. Thickness, roughness or density of most layers in this case varied from the expected. The modelled thicknesses, density and roughness values are shown in Table 13.2. There is a low level of uncertainty for the model data sets with good fits and an average level of uncertainty for the model data sets with satisfactory fits. The theoretical density of silicon nitride films is 3.4 g/cm^3, whereas measured values for silicon nitride films varied from 2.6 g/cm^3 for samples 10 to 3.2 g/cm^3 for sample 7. However for most of the samples the density is around 3 g/cm^3 and post deposition annealing at 650^{o}C for 5 minutes does not cause a significant difference in film density. Sample 8 shows the lowest density, which may be related to the deposition conditions used. The relatively low power of 150 W used for sample deposition might have a significant impact on the structure of the silicon nitride films. Operating a magnetron at low power usually means the discharge voltage is also low, leading to a lower ion current and lower ion energies. Consequently when particles arrive on the substrate surface they may not have enough energy to create dense films. As densification occurs by surface diffusion processes it is reasonable to assume that molecules having relatively low energy will not be as mobile as highly energetic ones in film densification. Sample 7 was also deposited at 150 W and its density is comparable with the remaining samples. However samples 7 and 8 were also deposited under different pressures of 0.3 and 0.5 Pa, respectively. It is known that during sputtering process the mean free path of incident ions decreases when operating pressure increases, therefore ion energy is reduced. This means that sample 8, deposited under higher pressure had a shorter mean free path than sample 7, and therefore ions incident at the substrate surface had lower energy on average than those in sample 7. This means that both low power and higher operating pressure could have been responsible for creation of more open film structures due to the delivery of lower energy ions to the substrate surface.

Film roughness was measured against standard roughness values obtained for float glass which is equal to 0.6 nm. Surface roughness varied from 0.8 nm obtained for sample 1, to 3.1 nm for sample 6. Comparing as-deposited and annealed samples, which were deposited under the same conditions, it can be seen that in each case the difference in surface roughness before and after annealing is insignificant. In the case of sample 5 (annealed) and 9 (as-deposited) the change in roughness equals 0.3 nm and is higher in the as-deposited sample, whereas samples 8 (annealed) and 10 (as-deposited) shows identical values of roughness average values of 2.1 nm. Therefore it can be assumed that annealing conditions do not affect the surface roughness of the silicon nitride films investigated in this study. However the highest Ra values have been obtained for samples deposited under the highest operating pressure of 0.9 Pa. Figure 13.6 shows the gradual increase of surface roughness values with operating pressure. Li *et al.* reported that in RF magnetron sputtered Si_3N_4 films, coating density increased with increasing nitrogen/argon flow ratio from 2.4 to 3.17 g/cm^3, but no correlation was observed between roughness and gas flow, as on average Ra value were around 0.6 nm. [161] Xu *et al.* on the other hand showed that there is no correlation between substrate temperatures during film deposition and surface roughness or coatings density. Values varied from 3.06 to 3.12 g/cm^3 for film density and from 0.44 to 0.5 nm for roughness obtained by XRR. Moreover he reported that surface roughness obtained from AFM analysis is around one half of the values detected by XRR and equalled around 0.24 nm. [162]

The coating thickness variation overall is close to the +/-5% expected for good model fits in XRR. Moreover the difference between thickness values measured physically by Dektak profilometry and those measured by XRR varies from 0 to 7.9 nm, which gives a maximum percent of difference of about 9%.

Table 13.2: Table shows thickness values, roughness average and density modelled by XRR. Samples 1-8 were post-deposition annealed at 650°C for 5 minutes, whereas samples 9 and 10 were not. Thickness compared with physically measured values by Dektak profilometry.

Sample number	XRR Thickness [nm]	Dektak Thickness [nm]	Ra [nm]	Density [g/cm^3]
1	80.7	86±2.0	0.8	3.0
2	75.7	80±1.0	1.0	3.0
3	86.0	80±2.0	1.2	3.0
4	81.5	80±2.0	1.4	3.1
5	89.4	81±1.0	2.5	3.1
6	86.7	93±2.0	3.1	2.9
7	76.8	81±1.0	1.9	3.0
8	70.8	73±3.0	2.1	2.7
9	85.6	80±1.0	2.8	2.9
10	73.0	73±3.0	2.1	2.6

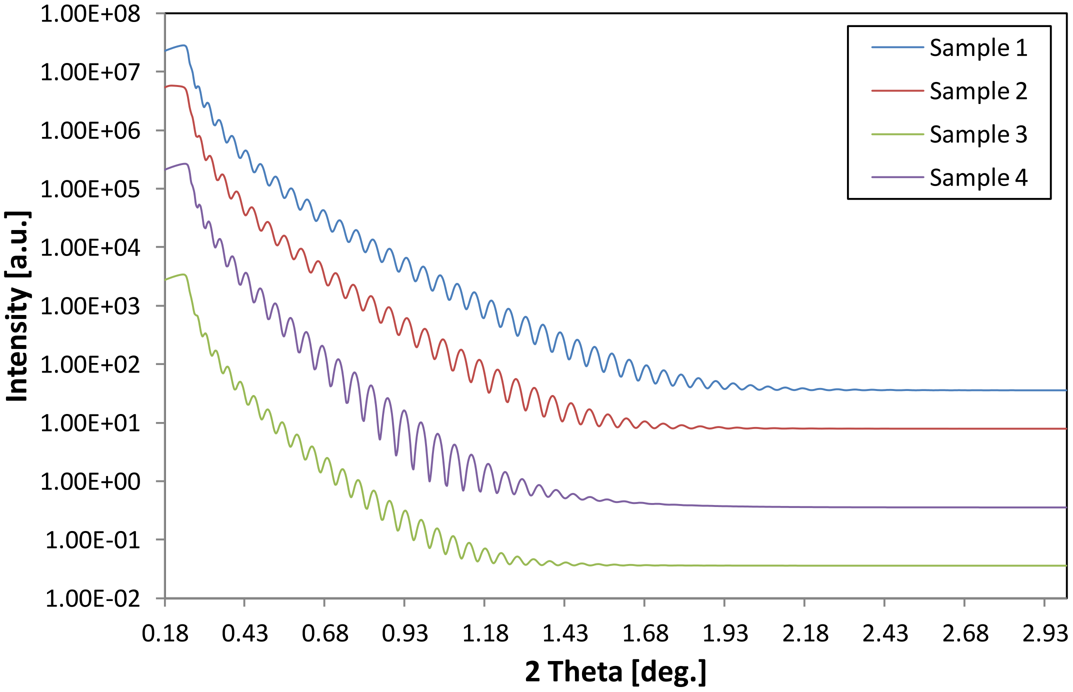

Figure 13.4: X-ray reflectometry spectra showing good data fit in silicon nitride samples 1-4 deposited onto float glass substrate and annealed at 650°C for 5 minutes.

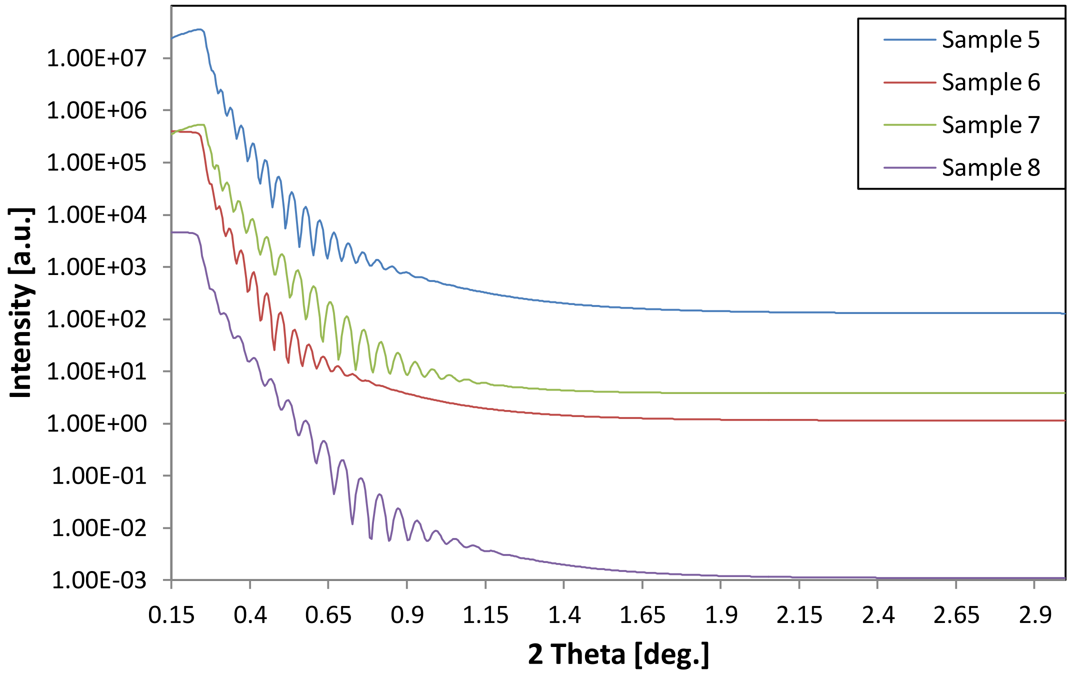

Figure 13.5: XRR plot of silicon nitride samples 5-8 deposited onto float glass substrate, post-deposition annealed at 650°C for 5 minutes. Samples show satisfactory fit.

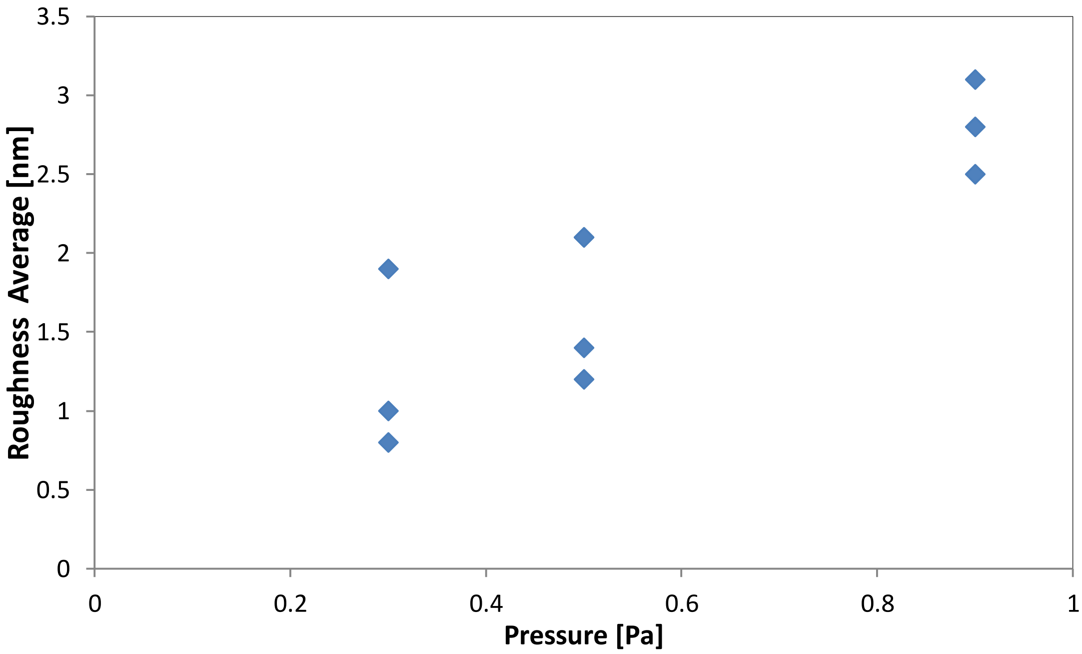

Figure 13.6: Ra values as a function of operating pressure obtained for silicon nitride samples. Roughness gradually increases when operating pressure increases.

Stoichiometric silicon nitride-Si_3N_4 consists of 60.1 wt % of Si (42.9 at %) and 39.9 wt % of N (57.2 at %), and according to EDX results all of the deposited samples show similar composition. The amount of nitrogen in all samples is about 1-2% less than in stoichiometric silicon nitride, which may be due to sample contamination. There is a small amount of oxygen detected in the samples, which probably comes from the sample surface, due to sample oxidation in the atmosphere after deposition. If there was oxygen present in the silicon nitride coating, its amount would have been significantly higher. Silicon tends to bond more easily with oxygen than with nitrogen, so the SiO_2 would have been formed, and therefore a higher oxygen content would have been detected. Table 13.3 shows EDX results collected from selected Si_3N_4 samples. The operating conditions during sample deposition as well as thickness are described in the table.

Table 13.3: EDX results collected from selected silicon nitride samples.

	Sample 1	**Sample 2**	**Sample 7**
Si at %	43	43	43
Si wt%	61	61	60
N at %	56	56	55
N wt%	39	39	39
O at %	1	1	2
O wt%	1	1	1
Operating Pressure [Pa]	0.3	0.3	0.5
N_2 flow rate [SCCM]	11	10	11
Power [W]	300	300	150
Thickness [µm]	1.00±0.03	1.09±0.01	0.97±0.02

SEM images have been collected from three selected samples. All micrographs show fully dense and rather smooth surfaces. As-deposited samples have glassy like structures with some grains or defects existing on the sample surface. Annealed samples on the other hand show more texture on the surface. This is caused by heat treatment, as it is known that the grain growth and re-crystallisation is a thermally activated process. Nevertheless XRD data did not show crystalline diffraction in annealed or as-deposited silicon nitride samples. Figures 13.7-13.12 show micrographs collected from selected Si_3N_4 samples.

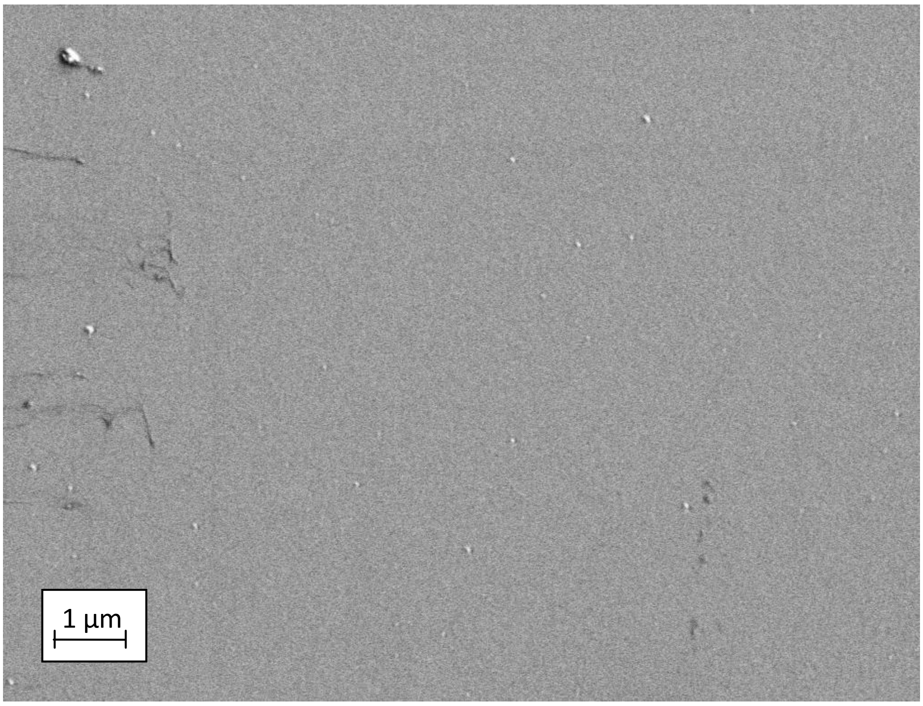

Figure 13.7: SEM micrograph of the top surface of the as-deposited silicon nitride sample 1, deposited onto float glass substrate.

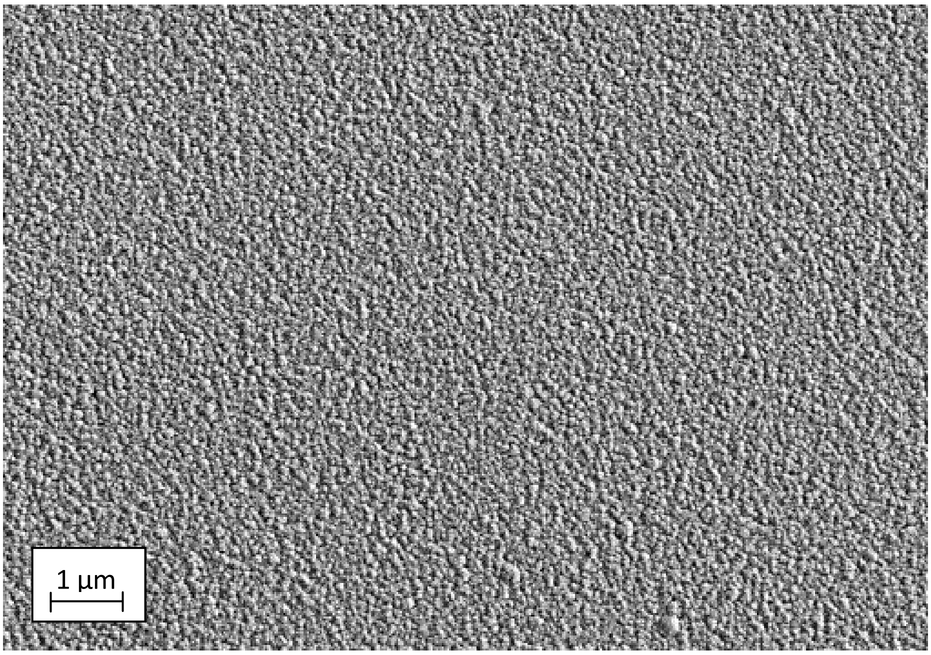

Figure 13.8: SEM micrograph of the silicon nitride surface collected from sample 1 deposited onto float glass, post-deposition annealed at 650°C for 5 min.

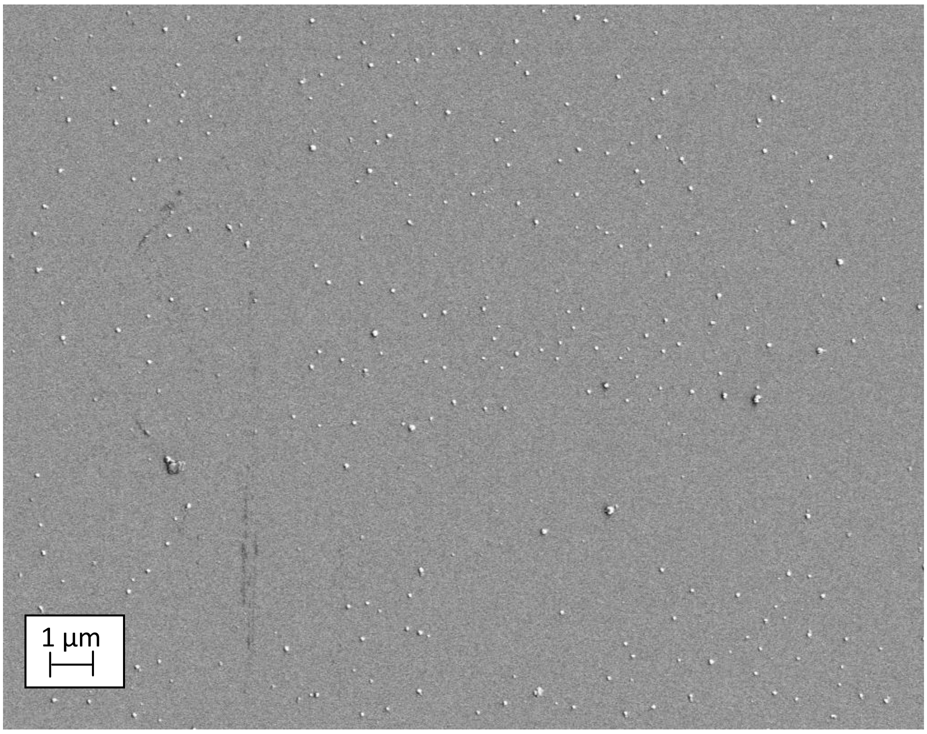

Figure 13.9: SEM image of the top surface of the as-deposited silicon nitride sample 2, deposited onto float glass.

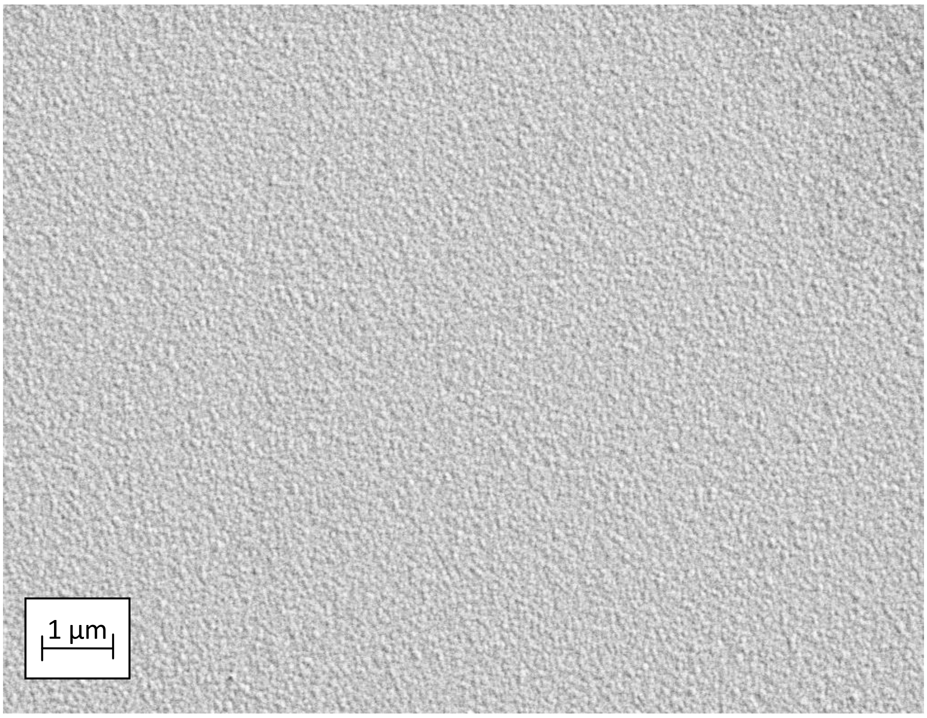

Figure 13.10: SEM image collected from the top surface of the Si_3N_4 sample 2 deposited onto float glass, post-deposition heat treated at 650°C for 5 minutes.

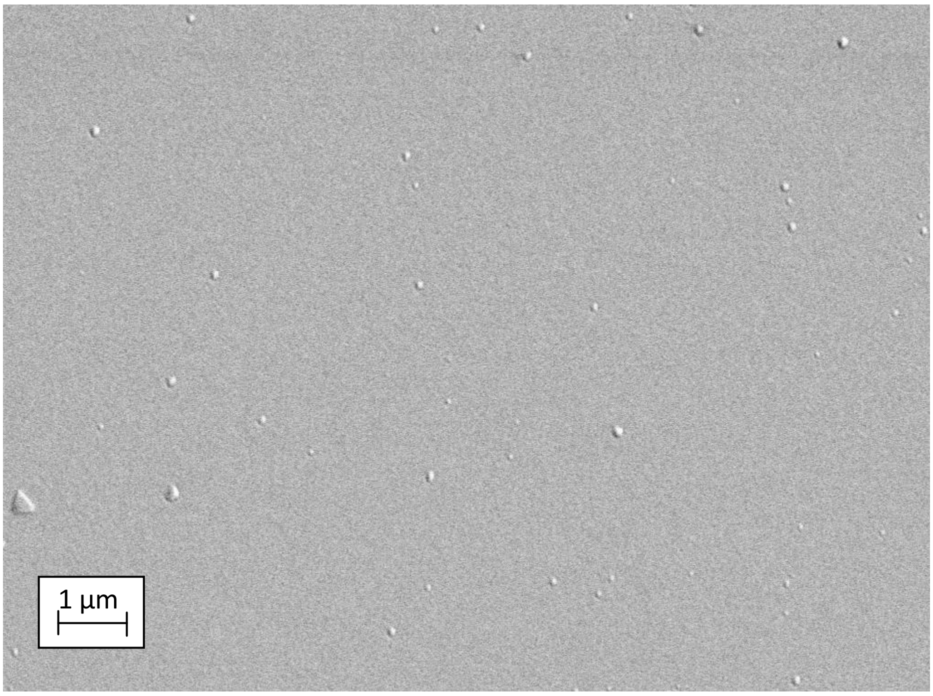

Figure 13.11: SEM micrograph of the as-deposited silicon nitride sample 7, deposited onto float glass substrate.

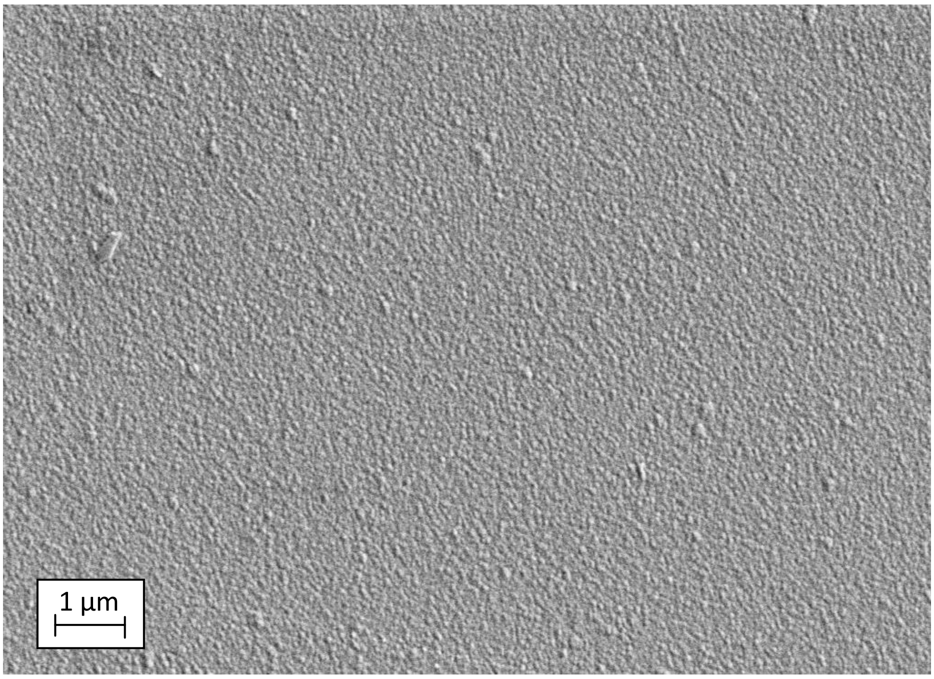

Figure 13.12: SEM micrograph of the top surface of silicon nitride sample 7 deposited onto float glass, post-deposition annealed at 650°C for 5 minutes.

AFM analysis was used to estimate surface roughness and morphology of silicon nitride films. Selected, post-deposition annealed silicon nitride samples deposited under different conditions were subjected to surface roughness analysis to investigate the dependency between deposition conditions and the surface roughness of these films.

Figure 13.13 represents 1 µm x 1 µm images collected from selected silicon nitride samples. Table 13.4 shows Ra and RMS values obtained for each analysed sample. All of the samples present rather smooth surfaces, with root-mean-square values below 0.5 nm. Samples 1 and 4 show the smoothest surfaces, whereas sample 6 presents the most texture. However the difference in RMS values obtained from AFM analysis between analysed samples is very small, therefore insignificant for diffusion studies. Moreover roughness obtained by AFM is much smaller than characterised by XRR. However from both analyses sample 1 shows the smoothest surface, whereas sample 6 presents the highest surface roughness value. Nevertheless, comparing AFM results with images obtained from SEM, quite significant difference in texture between as-deposited and annealed samples has been obtained. AFM suggest that the surface is very smooth after annealing at 650^{o}C for 5 min, however some defects (or grains) have been detected and are presented as light-orange spots in the Figure 13.13 (Sample 1 and 4), which suggest that the height of these grains is significantly larger than the surrounding surface. As the surrounding film area is very smooth the RMS and Ra values obtained from AFM are very small, and therefore the texture obtained from SEM could be related to these defects, which arose during heat treatment and falsely seemed to represent rather rough film surface.

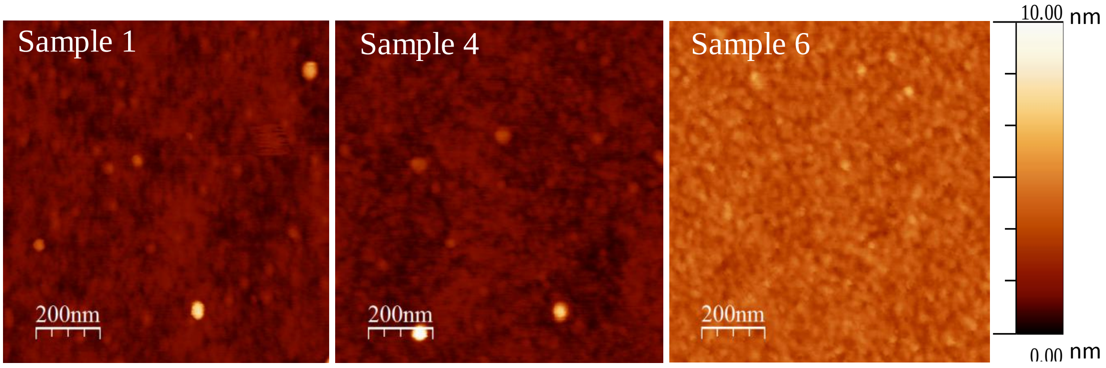

Figure 13.13: AFM images collected from selected silicon nitride samples post-deposition annealed at 650^{o}C for 5 minutes.

Table 13.4: Ra and RMS values obtained from silicon nitride samples.

Sample number	Ra [nm]	RMS [nm]
Sample 1	0.2	0.2
Sample 4	0.2	0.3
Sample 6	0.4	0.4

13.2 Si_3N_4: Diffusion Studies

Silicon nitride samples have been analysed by TOF-SIMS to measure the diffusion coefficient of silver and sodium atoms. Figure 13.14 presents a standard sample, measured without applying second annealing at 250°C after silver deposition. The silver diffusion coefficient in the standard sample was calculated to be 1×10^{-24} m^2/s. Figure 13.15 and 13.16 show schematic representations of TOF-SIMS depth profiling in annealed and as-deposited samples, respectively. The main and very evident difference between these two spectra is the sodium profile. The level of Na in the annealed sample is significantly higher than in the heat treated samples. This suggests that during the first annealing at 650°C sodium diffuses through almost the entire thickness of the silicon nitride coating. Whereas, the as-deposited sample shows sodium atoms only close to the glass/silicon nitride coating interface.

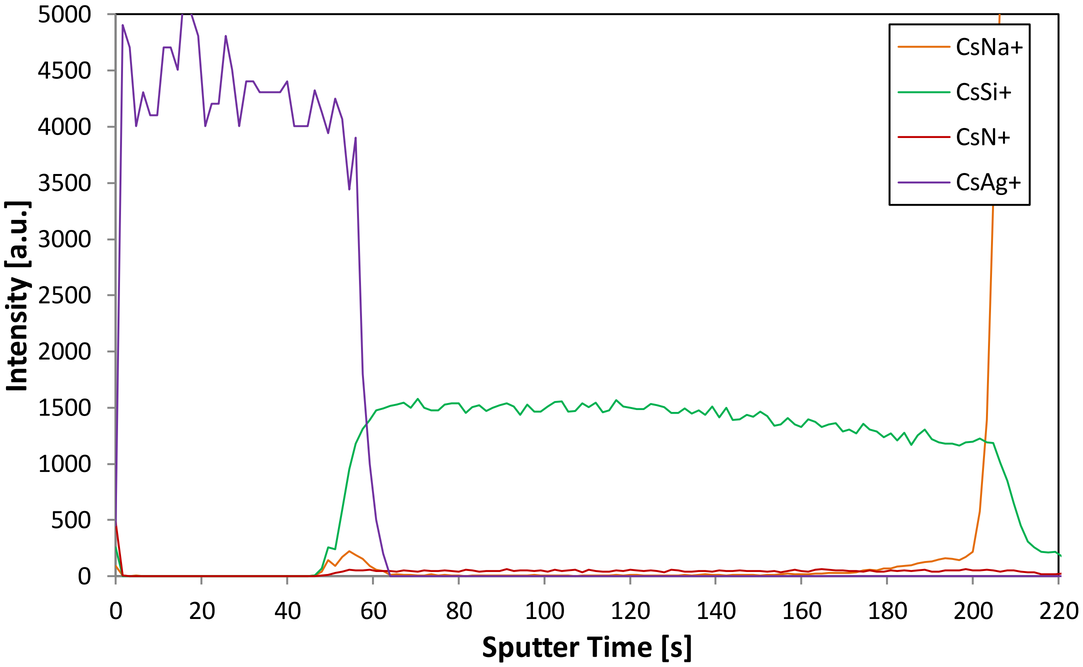

Figure 13.14: TOF-SIMS depth profile of a standard silicon nitride sample deposited onto float glass substrate.

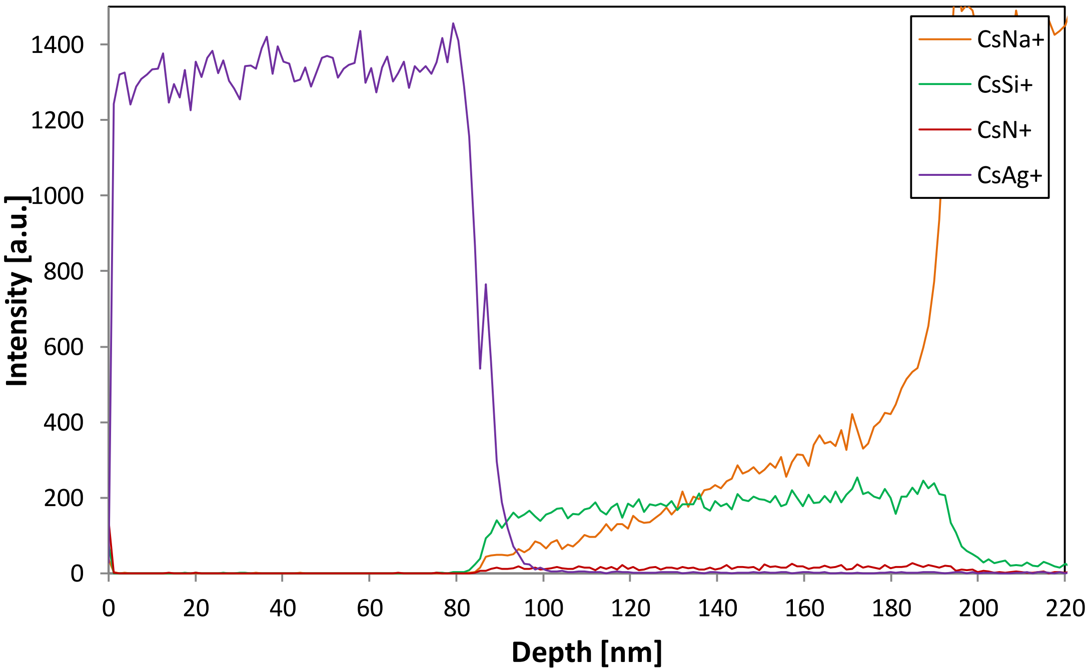

Figure 13.15: TOF-SIMS depth profiling collected from silicon nitride/Ag sample 5 deposited onto float glass, post-deposition annealed at 650°C for 5 minutes.

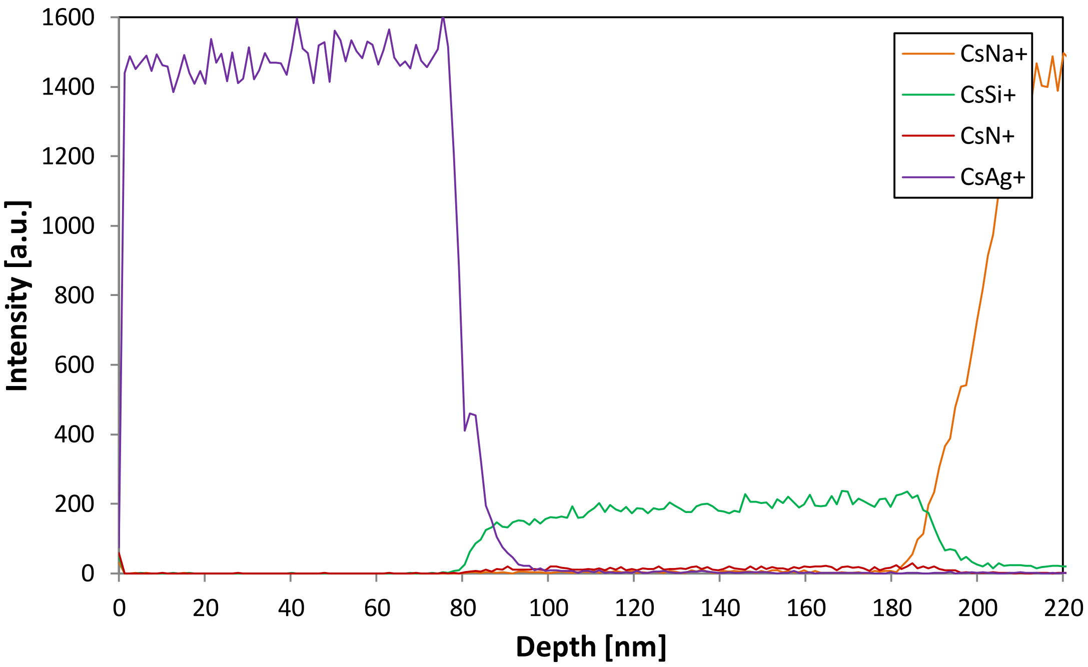

Figure 13.16: TOF-SIMS depth profiling of as-deposited silicon nitride/Ag sample 9 deposited onto float glass substrate.

Table 13.5 shows diffusion coefficient values calculated for silver and sodium in silicon nitride samples. Diffusion modelling showed that silver diffuses at similar rates in all Si_3N_4 samples prepared in this work. The diffusion rates are relatively low and stay in the range of 1-5.5×10^{-20} m^2/s for all of the samples. Sample 6 and 7 shows the highest diffusion rate of 5.5×10^{-20} m^2/s, whereas in samples 2-4 diffusion coefficient values are the lowest. However there is no correlation obtained between depositions conditions plotted against diffusion coefficient values presented in Figures 13.17 and 13.18. Therefore silver diffuses through silicon nitrite coatings at an average rate of 2×10^{-20} m^2/s independently of the operating conditions selected in this work.

Furthermore no difference in silver diffusion coefficient values was obtained between the annealed and as-deposited Si_3N_4 samples. XRD analysis showed that silicon nitride samples stay amorphous after annealing at 650°C, and even though SEM micrographs showed differences in the texture between as-deposited and annealed samples roughness values provided by AFM analysis showed very small RMS values.

Sodium on the other hand diffuses with different rates through the silicon nitride samples. Diffusion coefficient values vary from 1×10^{-20} to 1.1×10^{-18} m^2/s. However the majority of samples show sodium diffusion rates to be around 2×10^{-19} m^2/s, except the as-deposited samples, in which diffusivity is in the range of 10^{-20} m^2/s. Moreover samples 1 and 8 have sodium diffusion coefficient values of 1×10^{-20} and 1.1×10^{-18} m^2/s, respectively. Sample 1 has a diffusivity value as low as those obtained for the as-deposited samples, even though this sample was annealed at 650°C and then after silver layer deposition, re-annealed at 250°C for 5 minutes. This sample was deposited at a pressure of 0.3 Pa, 11 SCCM of nitrogen flow and power delivered to the magnetron of 300 W, and as mentioned earlier in this chapter, it was characterised by AFM to have the smoothest surface. Sample 2 was deposited under similar conditions; however sodium diffusion in this sample is greater by one order of magnitude. Comparing SEM images collected from samples 1 and 2 before and after annealing at 650°C, sample 1 seemed to develop more texture. This may suggest that the glassy-like, more open amorphous structure presented in as-deposited film has created more closely packed grains in the lattice, and possibly reduced the number of dangling bonds making the silicon nitride lattice more difficult for sodium atoms to diffuse through.

Sample 8 shows the highest diffusion coefficient value obtained for sodium in silicon nitride samples equal to 1.1×10^{-18} m^2/s. Silicon nitride in general has a dense structure and unlike silica does not provide open channels, therefore it effectively blocks even small ions, such as Na^+. However as it was discussed earlier, sample 8 was sputtered at 0.5 Pa operating pressure and 11 SCCM of nitrogen introduced into the chamber during sputtering, with the magnetron driven at 150 W. X-ray reflectivity measurements showed that sample 8 has the lowest density from all the silicon nitride samples analysed in this work, equal to 2.7 g/cm^3. This was assigned to relatively low ion energy and therefore the creation of a more open structure in the film compared to the remaining samples. As a result, sodium could find it easier to diffuse though the free spaces in this coating than in remaining silicon nitride films.

Table 13.5: Diffusivity values calculated for silver (D_{Ag}) and sodium (D_{Na}) in silicon nitride samples.

Sample number	**D_{Ag} [m^2/s]**	**D_{Na} [m^2/s]**
Standard	1.00×10^{-24}	-
1	1.20×10^{-20}	1.00×10^{-20}
2	1.00×10^{-20}	2.00×10^{-19}
3	1.00×10^{-20}	1.50×10^{-19}
4	1.00×10^{-20}	3.00×10^{-19}
5	2.50×10^{-20}	1.00×10^{-19}
6	5.50×10^{-20}	2.00×10^{-19}
7	5.50×10^{-20}	1.50×10^{-19}
8	1.30×10^{-20}	1.10×10^{-18}
9	2.50×10^{-20}	2.50×10^{-20}
10	1.30×10^{-20}	4.00×10^{-20}

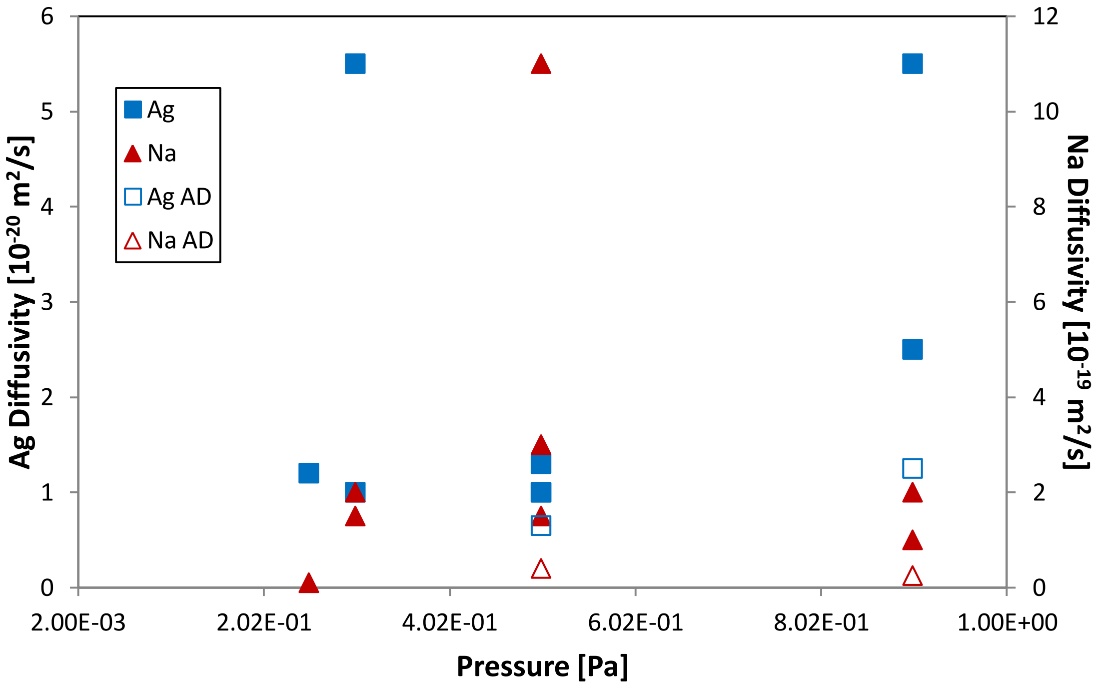

Figure 13.17: Silver and sodium diffusivity as a function of operating pressure in silicon nitride samples. No clear trends obtained.

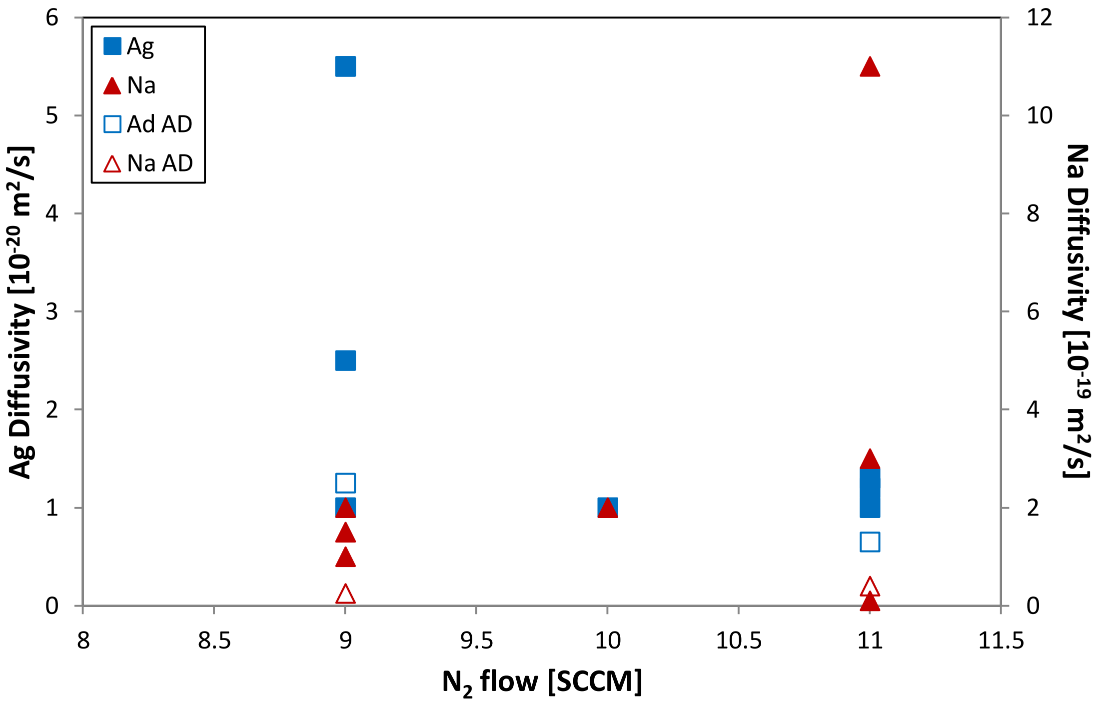

Figure 13.18: Silver and sodium diffusivity values as a function of nitrogen flow rate during coatings deposition. No correlation was found.

13.3 Si_3N_4: Temperature Dependence of Silver Diffusion

The temperature dependency of silver diffusion was investigated using the Arrhenius diffusion principle, described in Chapter 6.6. Sample 7 was chosen to investigate the changes in silver diffusion after annealing at four different temperatures. Sample 7, in which diffusion was already investigated after annealing at 250°C, was additionally annealed at 100, 400 and 600°C for 5 minutes, and the silver diffusion was also investigated by TOF-SIMS analysis. Table 13.6 shows silver diffusion coefficient values found for the different temperature treatments.

Table 13.6: Diffusion coefficient values obtained for Si_3N_4/Ag samples annealed at 100, 250, 400 and 600°C for 5 minutes.

Annealing Temperature [°C]	**D_{Ag} [m^2/s]**
100	2.00×10^{-20}
250	5.50×10^{-20}
400	6.00×10^{-18}
600	1.35×10^{-17}

Figure 13.19 shows an Arrhenius plot of the logarithms of diffusion coefficients, lnD, as a function of the reciprocal temperature, $^1/_T$ [K^{-1}]. Plotting the Arrhenius equation should give a linear dependency between temperature and diffusivity, where the gradient equals $-^Q/_R$, where Q is the activation energy for diffusion and R is the gas constant (8.314 J/mol K) and the intercept allows calculation of the frequency factor value (D_0). Hence, from the plot showed in Figure 13.19 the activation energy was found to be approximately 38.1±1.9 kJ/mol (~0.3945 eV) and the frequency factor equals 2.13×10^{-15} m^2/s.

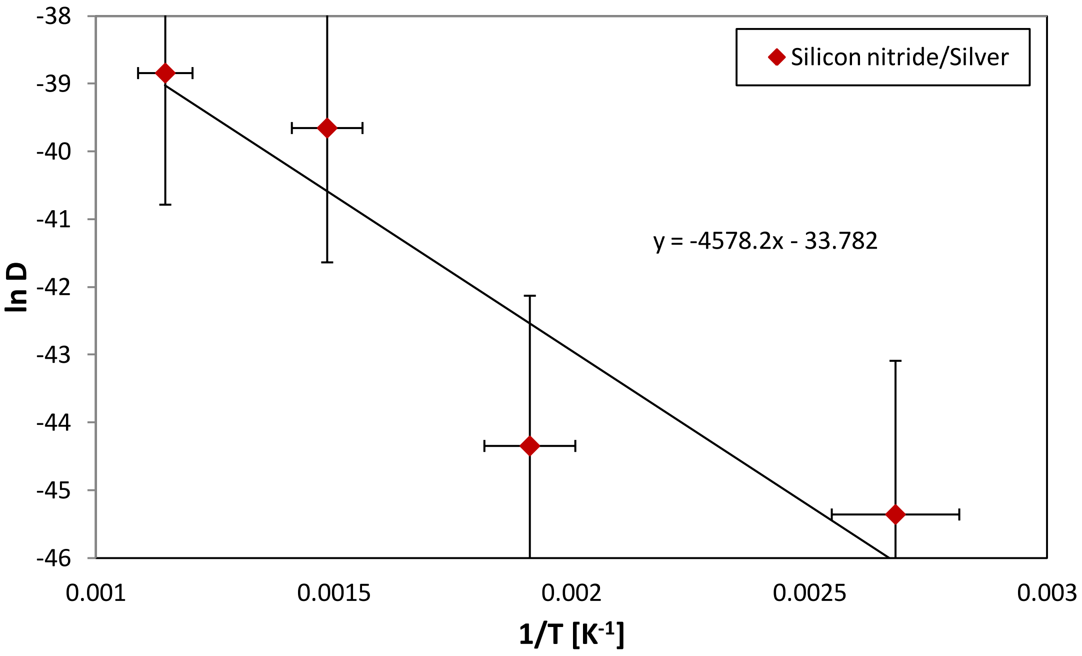

Figure 13.19: Arrhenius dependency between diffusion and annealing temperature obtained from selected silicon nitride/silver sample annealed at the temperature range of 100-600°C.

A satisfactory trend was obtained from plotting the natural logarithm of diffusion coefficient against inverse temperature. As expected, diffusion coefficient values increase with increasing annealing temperature. Values calculated for activation energy and the frequency factor are much lower than reported in the literature, i.e. for silver self-diffusion in the lattice, an activation energy of 170 kJ/mol (~1.77 eV) and a frequency factor of 4×10^{-6} m^2/s were obtained. [84] Many authors have used the Arrhenius plot to determine the dependency between silver diffusion and annealing temperature in thin films or bulk materials. For example Lee *et al.* investigated the diffusion of silver in copper films and found the activation energy and frequency factor to be 0.46±0.06 eV and ~1×10^{-12} m^2/s respectively [163]; Chen *et al.* found that the Ag activation energy to diffuse through Si (111) is 2.46±0.26 eV. [164] Moreover Xiangyang *et al.* found that Ag diffusing through Ni-B alloys requires an activation energy of 0.58 eV and D_0 is 3.9×10^{-10} m^2/s [165], and Bacaksiz *et al.* reported that the activation energy and frequency factor of silver diffusing in ZnS are 0.1 eV and 8×10^{-13} m^2/s respectively. [166] Activation energy, which describes the minimum energy required for diffusion to occur, varies and depends on the temperature and on the matrix or system through which silver is diffusing. Q values obtained here are rather average compared with silver activation energy values found in other materials. The frequency factor on the other hand is between 2 to 5 orders of magnitude lower compared to those from the literature.

13.4 Si_3N_4: Summary

Silicon nitride samples were deposited onto float glass samples, post-deposition annealed at 650^{o}C for 5 minutes and over-coated with silver. Samples were characterised by XRD, XRR, EDX, SEM and AFM analysis to learn about coatings structures, morphology and composition. X-ray diffraction was carried out on annealed and as-deposited samples, but in either case crystal diffraction was not detected. Glancing angle XRD also failed to detect crystallinity, therefore the silicon nitride samples have been characterised as amorphous.

X-ray reflectometry was used to estimate density and surface roughness values for the coatings. The lowest density was obtained in samples deposited at a power of 150 W, which was the lowest power used in this work to deposit Si_3N_4 films. Surface roughness analysis established that the highest roughness values were obtained for the samples deposited at the highest operating pressure of 0.9 Pa. Roughness values obtained from AFM, which was performed on 3 selected samples, showed much lower values of Ra compared to the XRR analysis. Nevertheless results from both analyses suggest that surface roughness increases with operating pressure.

SEM micrographs showed that silicon nitride coatings had smooth, glassy like structures characteristic of amorphous materials in the as-deposited samples. Images collected from annealed films indicate that during the heat treatment process grain growth occurred in silicon nitride films, which could be seen on the coating surfaces. However possible grain growth did not change the density of these coatings, as from XRR analysis no correlation was obtained between annealing and film density. AFM analysis, which was performed on heat treated samples only, suggests that the roughness has not changed after annealing, as values obtained from selected samples showed very low roughness, even for sample 1, which showed the most texture in SEM imaging. This could be related to defects on films surfaces, which were obtained in as-deposited samples and could have arisen during heat treatment, and as a result created an impression of relatively rough surface in SEM images.

EDX analysis showed that film composition was very close to stoichiometry, as each characterised sample showed only about 1% nitrogen deficiency. Moreover small amounts of oxygen were detected, which probably came from the sample surface, as only a trace of oxygen was detected.

Ag/Si_3N_4/glass samples were re-annealed at 250^{o}C for 5 minutes and analysed by TOF-SIMS. Data from depth profiling analysis were then fitted into the diffusion calculator to find diffusion coefficient values for silver and sodium atoms. It was found that silver diffuses at similar rates in annealed and as-deposited samples, whereas sodium diffusion rates varied in the range of 10^{-20} to 10^{-18} m^2/s. The diffusivity value for sample 1 was as low as the as-deposited samples, which is about one order of magnitude lower than the average value obtained for most of the samples of 2×10^{-19} m^2/s. Sample 8 on the other hand, presents the highest diffusion rate obtained for sodium atoms in silicon nitride samples, and equals 1.1×10^{-18} m^2/s. This was assigned to deposition conditions and the low energy of ions bombarding the substrate during film deposition. Hence, a more open film structure was created, which was confirmed by the density measurements by XRR. More open silicon nitride structures created an easier medium for sodium to travel through.

One sample was selected to investigate the dependency of silver diffusion on temperature using the Arrhenius relationship. The sample was annealed at 100, 400 and 600^{o}C in addition to 250^{o}C used for silver diffusion studies in the previous work. A satisfactory trend was obtained between diffusion coefficient values and temperature, as diffusion rate increased with annealing temperature. The activation energy and frequency factor values were found from the plot, and equal 38.1 kJ/mol and 2.13×10^{-15} m^2/s respectively.

14. Results: Dielectric/Ag/Dielectric Stacks

In this chapter silver diffusion in dielectric/Ag/dielectric ‘sandwich’ coatings is described. The dielectric coatings selected for this study were titanium dioxide, Al-doped zinc oxide and silicon nitride. Zinc stannate coatings were not prepared due to the lack of facilities at MMU, where the sandwich coatings were deposited. Each dielectric film was about 80 nm thick and they were deposited before and after a 10 nm layer of silver. These three layer stacks were deposited in the UPD450 coating chamber (see Chapter 10.2), without breaking the vacuum, by using a rotatable cylindrical drum as the substrate holder. This allowed the substrate to be held in front of each target in turn for the production of the stack. Deposition conditions were selected from previous investigations of coatings structures, and the deposition conditions and procedure is explained in Chapter 9.1.

Samples were post deposition annealed over the range of temperatures of 100-600^{o}C and at an additional temperature of 250^{o}C, which was used for the investigation of silver diffusion in dielectric/Ag layers in the previous chapters. Samples were annealed in air for 5 minutes and subjected to TOF-SIMS depth profiling analysis.

TiO_2/Ag/TiO_2 was also deposited onto silicon wafer substrates to compare the behaviour of silver on a ‘sodium free’ substrate. Samples deposited on Si wafer and glass substrates, were annealed at 250 and 600^{o}C for 5 minutes and analysed by XPS in order to produce quantitative results. XPS measures the amount of material in atomic concentration percentage, which enables comparison of the areas under the silver curves. In theory the silver curve after annealing should have a Gaussian distribution, which broadens and lowers in intensity with time as silver diffusion progresses. Nevertheless the area under the curve should stay the same at all times.

14.1 $TiO_2/Ag/TiO_2$

Figure 14.1 shows silver distribution in titania/silver/titania stacks as measured by TOF-SIMS depth profiling analysis in samples annealed over the range of temperatures between 100-600^{o}C. Since TOF-SIMS analysis is not quantifiable, the intensity is described in arbitrary units and the values do not represent real atomic concentration of silver in these samples. Therefore the areas under the silver curves between samples do not represent the real change in the silver diffusion profile at different annealing temperatures, but gives an indication of how silver profiles develop with temperature.

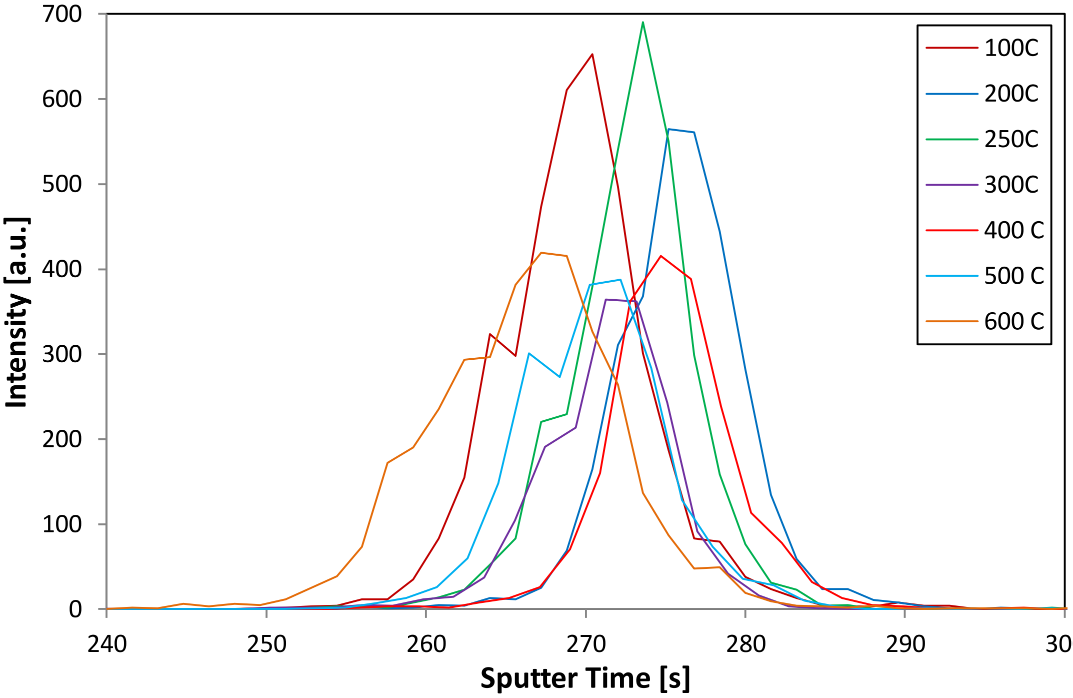

Figure 14.1: Silver profiles obtained by TOF-SIMS analysis in $TiO_2/Ag/TiO_2$ stacks, annealed at the range of temperatures of 100-600^{o}C.

Diffusion coefficient values for silver atoms have been calculated for each sample by fitting both sides of the curve to the diffusion calculator, assuming that due to the different surroundings at the boundaries of each titania layer in the deposited stack, silver may diffuse with slightly different rates (i.e. the upper dielectric layer has an open surface and the lower dielectric layer has an interface with the substrate, which may change the diffusion thermodynamics quite significantly). Diffusivity values have been then added together and the overall values are presented in Table 14.1. To find the dependency between the annealing temperature and the diffusion coefficient values an

Arrhenius plot was used. Figure 14.2 shows that the data points are rather scattered. This is due to very similar diffusion rates between samples annealed at 100-500°C. These samples show silver diffusivity values in the range of $3\text{-}7\times10^{-21}$ m^2/s, whereas the sample annealed at 600°C shows the diffusion rate to be one order of magnitude higher than in the other samples. With that exception, the silver diffusion coefficients values are very similar in these samples, which suggests that there are very few if any changes in films thermodynamics due to increasing the annealing temperature, at least up to 500°C. It is important to remember, that each coating was only submitted to an annealing time of 5 minutes (then removed from the oven and cooled in air), and this time remained constant throughout the study of silver diffusion through dielectric/Ag/dielectric coatings. Many authors decreased the annealing time at higher temperature to provide similar thermodynamic conditions, as diffusion occurs faster at higher temperatures. Therefore decreasing the time of annealing allows balancing the rapid diffusion at higher temperatures with a slower process at relatively low temperatures. Thus, plotting the diffusivity values against temperature should give a linear relationship between D and temperature. [9, 167-169] However in this study different annealing times were not investigated as this is not relevant to the project aims. Therefore it was shown here that annealing at temperatures up to 500°C will not change silver diffusion rates dramatically. Nevertheless Mallard *et al.* pointed out that for diffusion coefficient values below 4×10^{-15} m^2/s the data tend to be scattered, therefore it is not considered as the best fit to the Arrhenius equation. [170] This also may be the case here as silver diffusion is in the range of $10^{-20}\text{-}10^{-21}$ m^2/s.

Another possible explanation for data scattering is uncertainty resulting from the thermocouple in the oven used for the annealing process, which may not have been positioned correctly. However, this is unlikely to have introduced a large error in the data.

Table 14.1: Diffusion coefficient values calculated for titania/Ag/titania stack.

Annealing Temperature [^oC]	**D_{Ag} [m^2/s]**
100	3.50×10^{-21}
200	6.75×10^{-21}
250	4.25×10^{-21}
300	5.80×10^{-21}
400	3.75×10^{-21}
500	5.00×10^{-21}
600	5.93×10^{-20}

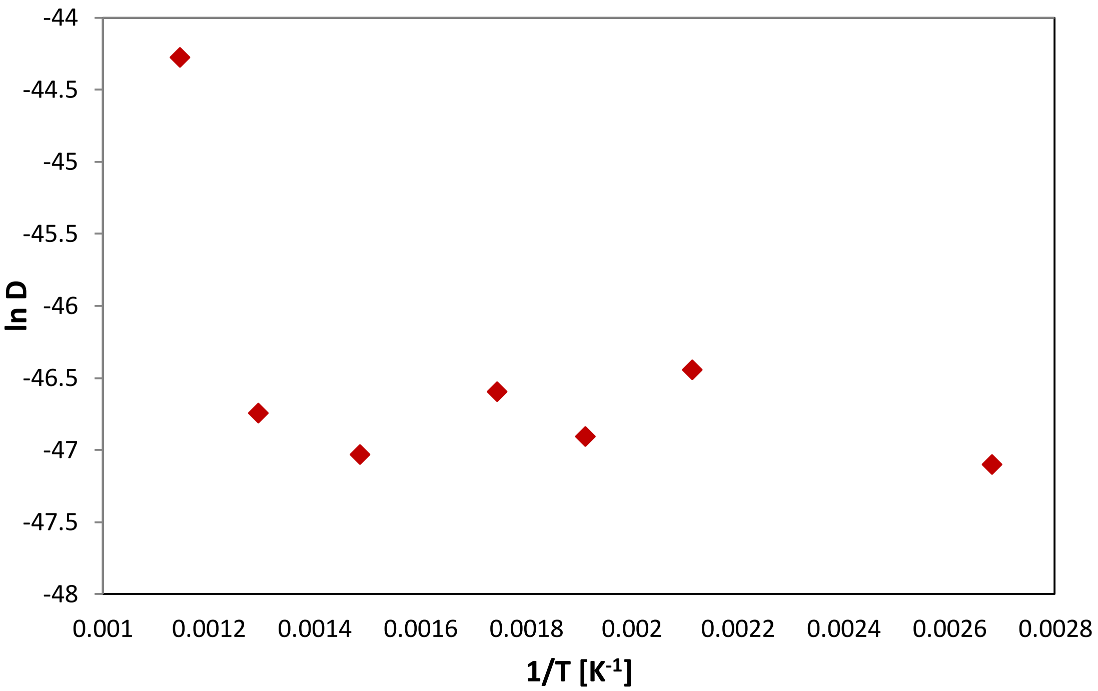

Figure 14.2: Arrhenius dependency between temperature and diffusion coefficient values obtained from $TiO_2/Ag/TiO_2$ samples annealed at temperature range of 100-600°C.

To investigate if the entire silver amount deposited between the oxide layers would diffuse when the annealing time was increased, a titania/silver/titania sample was annealed at 600°C for one hour. The annealing time was selected to be long enough to make sure that silver will diffuse completely through the titania, taking into account the silver layer thickness and the modelled diffusion distances in samples annealed at the same temperature for 5 minutes. Figure 14.3 shows TOF-SIMS depth profiling analysis obtained from this sample. There is no silver peak detected here, which agrees with the theoretical assumptions that silver spreads throughout the titania layers. However, the silver intensity should be much higher than that shown in Figure 14.3. TOF-SIMS has an excellent sensitivity therefore, such a low signal picked up from the silver suggests that there is only a trace amount of silver remaining in the coating. This suggests that either the silver layer is evenly distributed across the sample giving only a few counts in every layer which has been sputtered off and analysed by TOF-SIMS or silver has diffused into the glass and TOF-SIMS is picking up traces of silver remaining in the coating. Moreover it is interesting to find that sodium has filled in the free space left between the titania coatings after silver has diffused. This suggests that perhaps a similar process to ion-exchanged diffusion has developed between Na and Ag. Silver-doped glass has applications in optoelectronics, colour changing in decorative glasses and in hybrid microelectronics, as interconnections or electrodes for dielectric layers. [171-173] It was reported that for thermal treatments at temperatures above 320°C and an annealing time of 1 hour the ion exchange process took place. Sheng *et al.* showed that during thermal annealing the ion-exchange process occurs and silver diffuses into the glass matrix replacing alkaline ions present on the glass surface. [172]

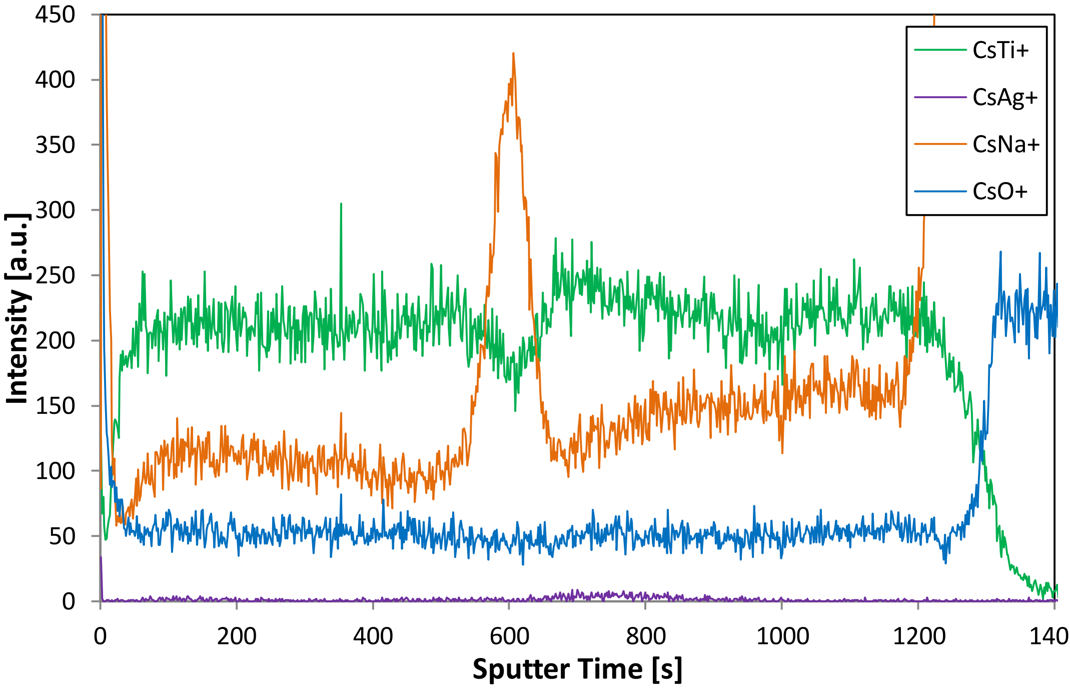

Figure 14.3: TOF-SIMS depth profiling collected from titania/silver/titania coating annealed at 600°C for 1 hour.

To measure the diffusion phenomena in titania/silver/titania coatings quantitatively, samples annealed at 250^{o}C for 5 minutes and at 600^{o}C for 5 minutes and 1 hour were investigated by XPS. Since it was observed that sodium diffuses from the glass through the entire thickness of the coating stack after annealing, additional sample were also deposited on silicon wafer substrates and annealed for 1 hour at 600^{o}C for comparison purposes.

Figures 14.4-14.5 show silver representation in samples annealed at 250 and 600^{o}C for 5 minutes and 600^{o}C for 1 hour, deposited on glass and silicon wafer, respectively. Depth profiles are very different between the samples deposited on glass and silicon wafer. Samples were deposited during the same run therefore, any potential run-to-run variations can be excluded here. This suggests that the differences in coatings structure and silver behaviour are related to the substrate. In samples deposited on glass only the one annealed at 250^{o}C shows a silver peak, whereas the remaining samples have almost no silver present in the coatings. Comparing samples deposited onto silicon wafer, there is visible layer of silver in each sample. The peak has a Gaussian shape only in the sample annealed at 250^{o}C, however differences in silver distribution across samples annealed at 600^{o}C are directly related to diffusion processes. Areas under the silver curve in samples deposited on Si wafer show less than 5% difference between samples annealed at 600^{o}C and the one annealed at 250^{o}C and equals 332 and 347.5 at %×s, respectively. Therefore silver is diffusing into the adjacent layers, but its presence can be still detected, unlike in the glass substrate, where XPS hardly picked up any signal from Ag atoms. A similar silver profile was detected by TOF-SIMS depth profiling in the sample deposited onto glass substrate and annealed at 600^{o}C for one hour. This confirms that silver diffuses through the glass substrate during introducing longer annealing times at a relatively high temperature. On the other hand there is a relatively strong signal picked up from the sample annealed at 600^{o}C for 5 minutes in TOF-SIMS analysis, whereas XPS failed to detect silver. This may be related to the higher sensitivity of the TOF-SIMS technique.

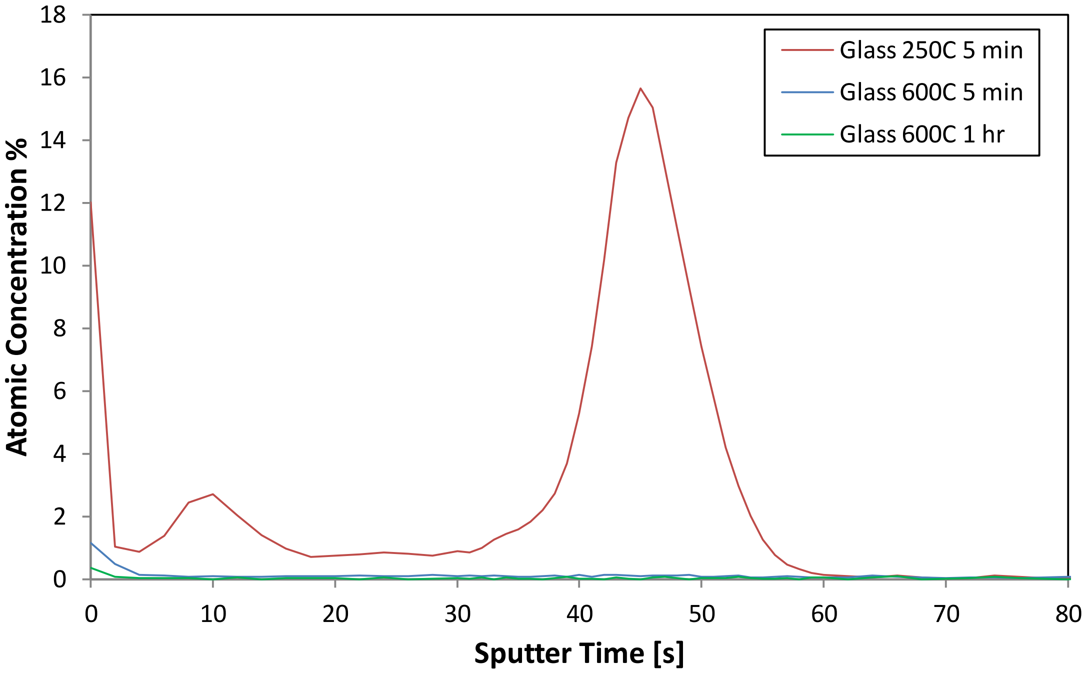

Figure 14.4: Silver distribution in samples deposited onto glass substrate annealed at 250, 600°C for 5 minutes and 600°C for 1 hour, analysed by XPS.

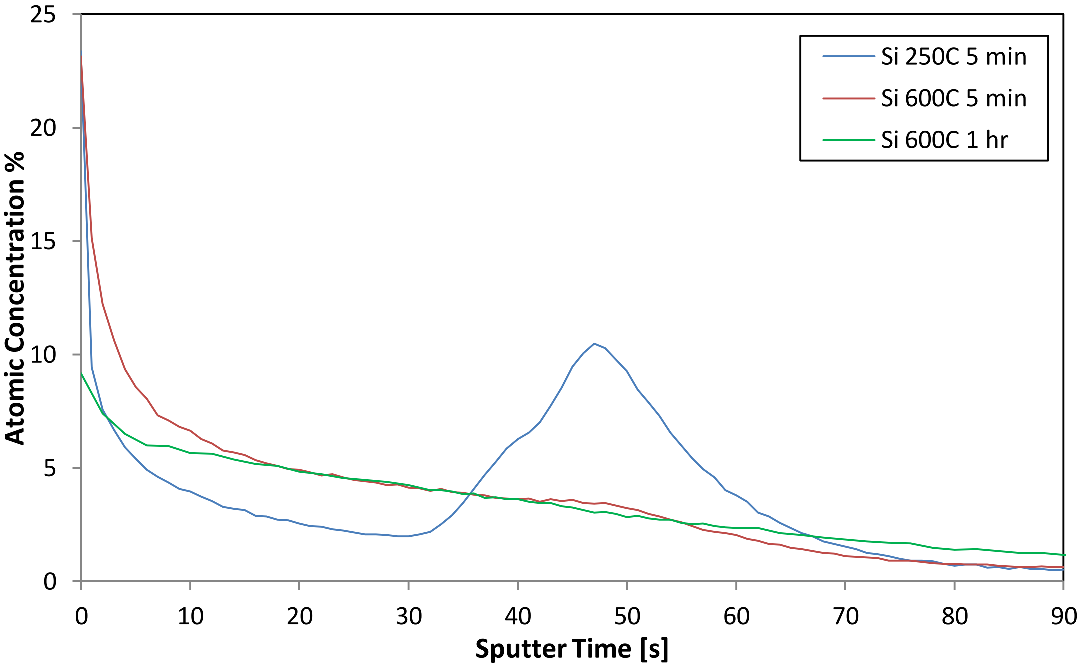

Figure 14.5: Silver profiles collected from titania/silver/titania samples deposited onto silicon wafer substrate and annealed at 250, 600°C for 5 minutes and at 600°C for 1 hour analysed by XPS.

The surface morphology of the TiO_2/Ag/TiO_2 samples deposited on glass and Si wafer annealed at 250°C and 600°C was investigated by SEM. It can be seen in most of the samples that due to the diffusion process, silver atoms have agglomerated on the film surface, creating clusters. The compositional contrast given by the backscatter detector gives a clear distribution of grains on the sample surface. Silver particles are brighter as they have the highest atomic number in the analysed titania/silver/titania stack. However the sample deposited onto a glass substrate and annealed at 600°C shows much less silver on the surface than the remaining samples. There are still white spots present, which are probably Ag atoms, but the characteristic clusters cannot be seen. This may be related to silver diffusion into the glass substrate. Figures 14.6-14.9 show SEM images collected from selected samples.

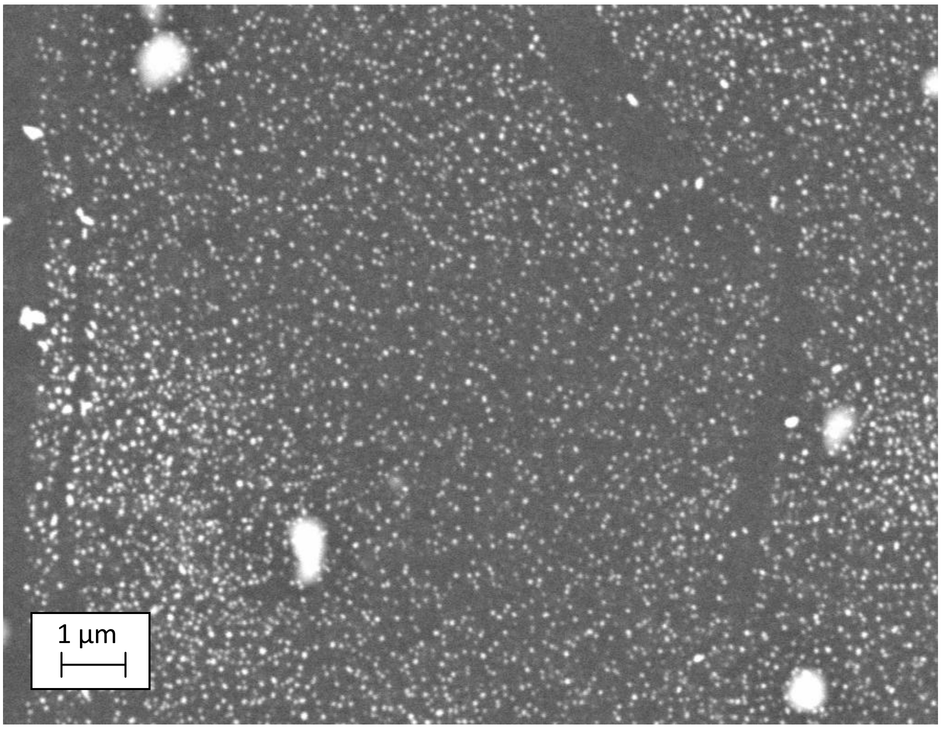

Figure 14.6: SEM image collected from titania/silver/titania sample deposited on glass, annealed at 250°C for 5 minutes.

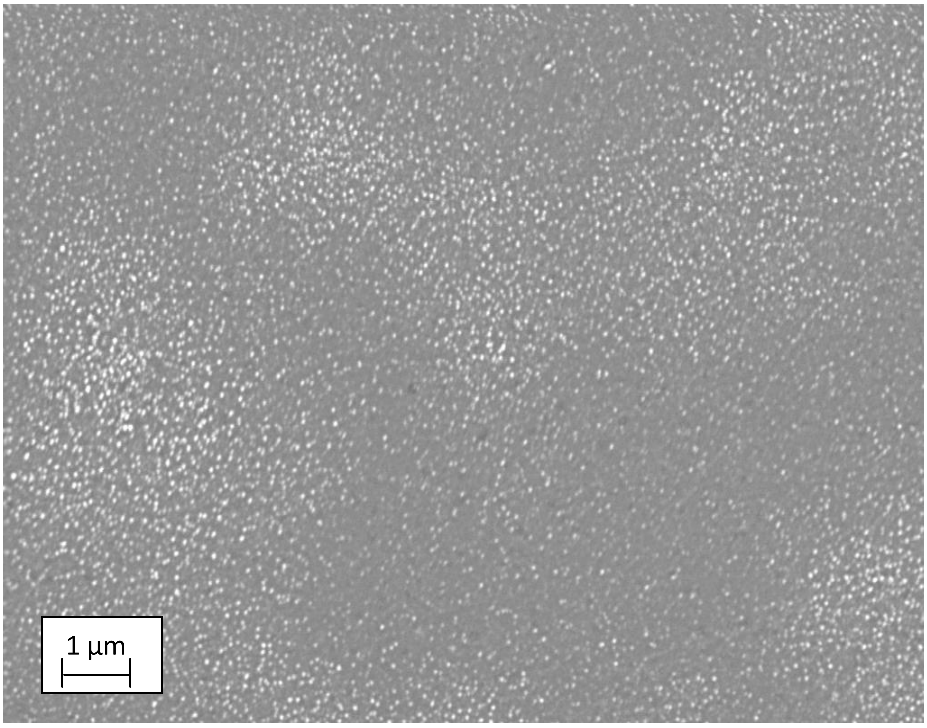

Figure 14.7: SEM micrograph of $TiO_2/Ag/TiO_2$ sample deposited onto glass substrate, post-deposition annealed at 600^oC for 1 hour.

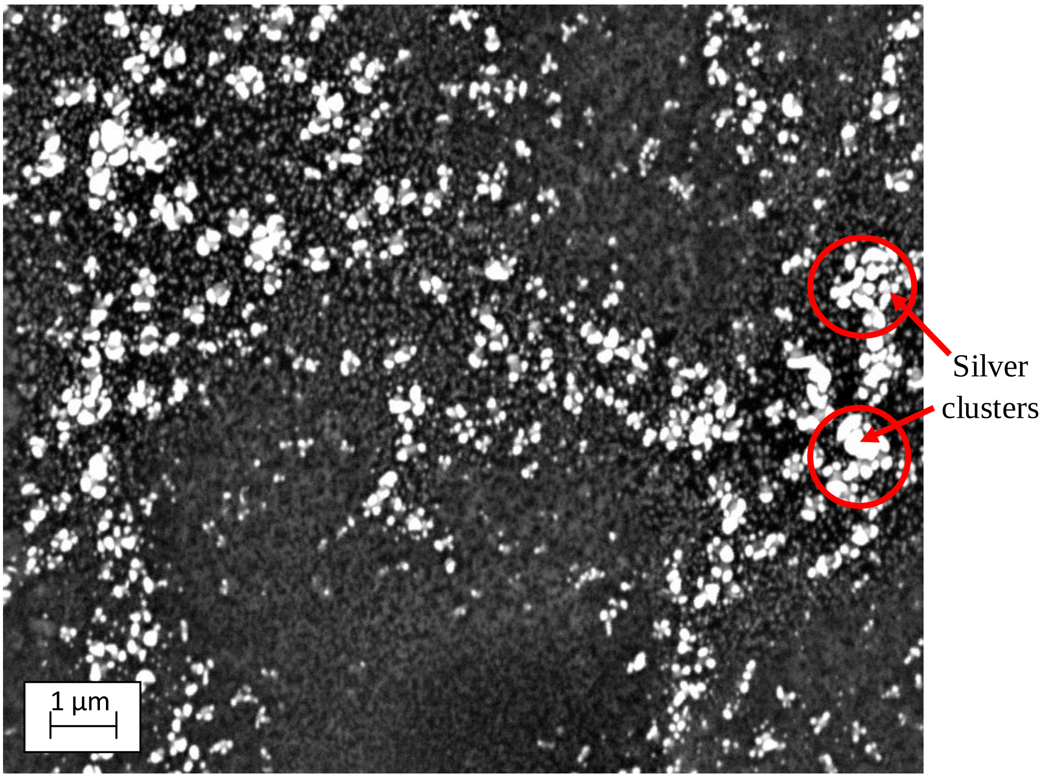

Figure 14.8: SEM image collected from $TiO_2/Ag/TiO_2$ sample deposited on Si wafer substrate, annealed at 250^oC for 5 minutes.

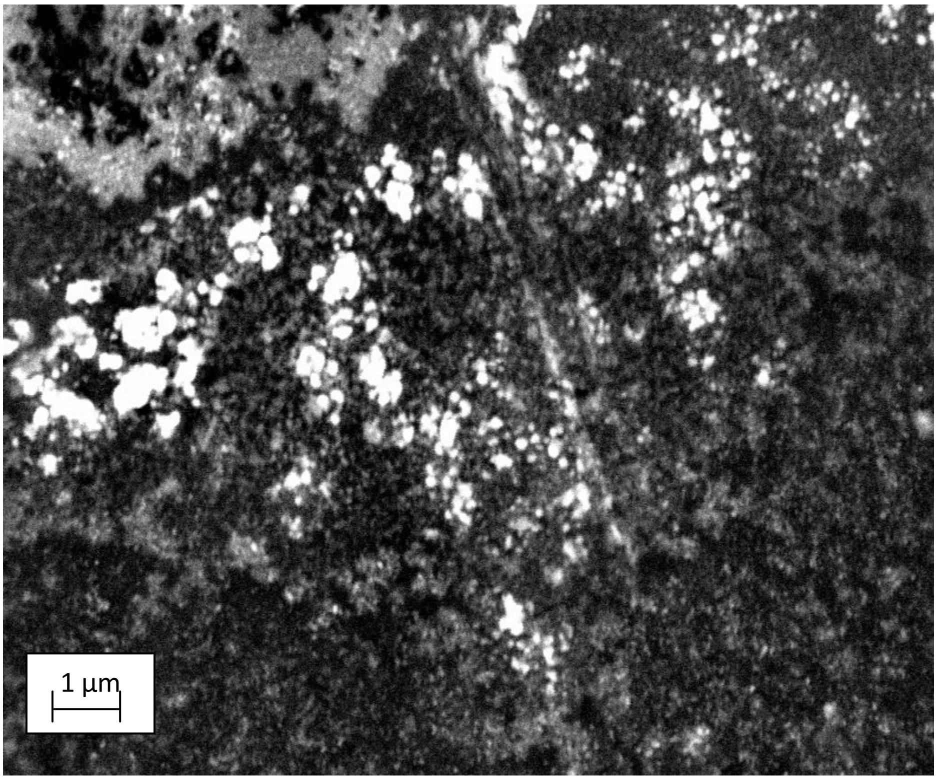

Figure 14.9: SEM micrograph of the top view of titania/Ag/titania sample deposited on Si wafer, annealed at 600°C for 1 hour.

To prove that the white areas detected by SEM analysis are really silver clusters EDX mapping was performed. Figure 14.10 shows atomic arrangements in the sample deposited onto silicon wafer and annealed at 600°C. Comparing the silver map with the SEM image it is clearly seen that the bright areas are silver agglomerations on the coating surface. However the mapping analysis could not be produced from the sample deposited onto the glass substrate and annealed at 600°C, due to the sensitivity limitation of the instrument used. Silver concentration is too low at the sample surface to distinguish it from other elements.

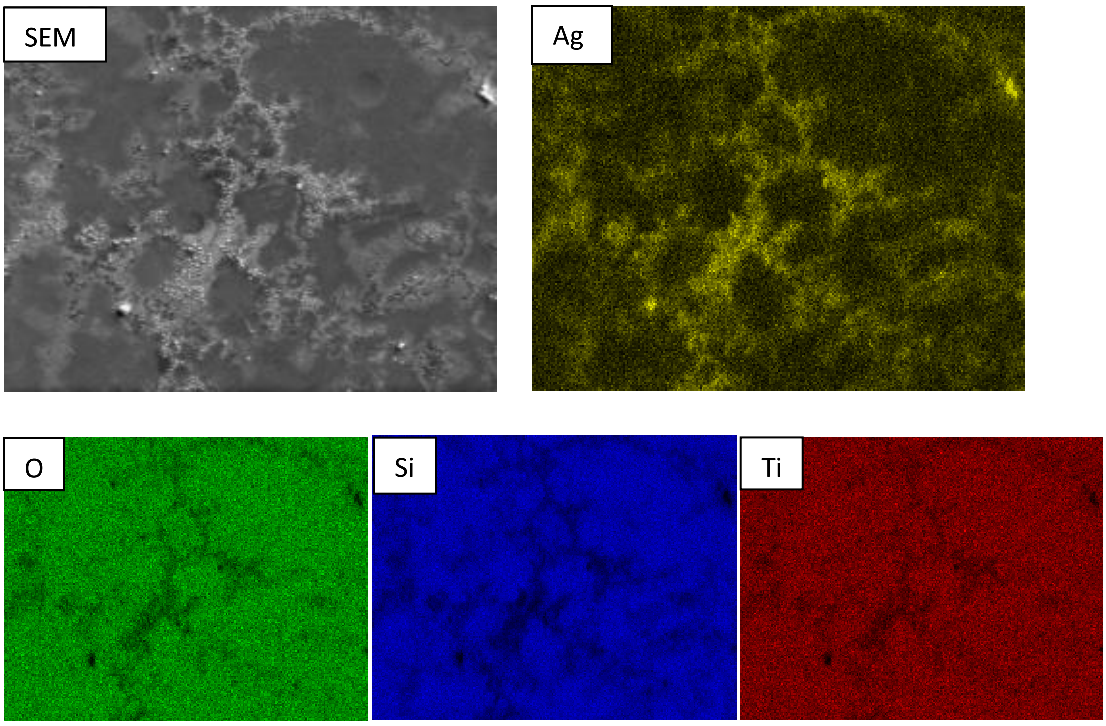

Figure 14.10: EDX mapping performed onto $TiO_2/Ag/TiO_2$ sample deposited onto Si wafer substrate. Comparing EDX results with the surface image (SEM), it can be seen that the white clusters agglomerated onto the surface are silver atoms.

EDX compositional analysis was also performed to find the atomic composition of elements present in the titania/silver/titania samples, after the preliminary theory that silver migrates into the glass matrix. Tables 14.2 and 14.3 below show the composition of titania/silver/titania stacks deposited onto silicon wafer and glass substrates, respectively, and annealed at 600^{o}C for 1 hour. The atomic concentration of silver in the sample deposited onto glass is about 3% less than in the sample deposited onto silicon wafer. This confirms that instead of creating cluster agglomerations on the film surface, silver probably diffuses into the glass substrate. Considering that the EDX ion beam penetrates the samples at about 1 µm deep, there is only about 170 nm of data picked up from coatings, whereas the remaining signal comes from glass substrate. The composition of silver is still extremely low in samples deposited on glass in comparison to those deposited on silicon wafer. This suggests that silver atoms have penetrated the glass deeper than 1 µm. It was reported elsewhere that after annealing at 600^{o}C for 45 hours the depth reached by silver was more than 200 µm [172], therefore it might be expected that silver could have reached a greater depth than 1 µm in the glass matrix.

Table 14.2: Elemental composition obtained from TiO_2/Ag/TiO_2 deposited onto glass, annealed at 600°C.

Element	Wt %	At %
O	38	54
Na	11	11
Mg	2	2
Al	3	3
Si	27	21
Ag	1	0.2
Ca	6	3
Ti	11	5

Table 14.3: EDX results calculated from titania/silver/titania deposited onto Si wafer, annealed at 600°C.

Element	Wt %	At %
O	15	27
Na	0.1	0.1
Si	60	62
Ag	12	3
Ti	13	8

14.2 Al-doped ZnO/Ag/Al-doped ZnO

AZO/Ag/AZO stacks were deposited onto glass substrates as described in Chapter 9.1. Samples were then annealed in the temperature range of 100-650^{o}C for 5 minutes to investigate the diffusion of Ag through the adjacent layers. Figure 14.11 shows silver peak distributions in selected samples, and silver diffusion coefficient values calculated on both sides of the Gaussian curve and added together are presented in Table 14.4.

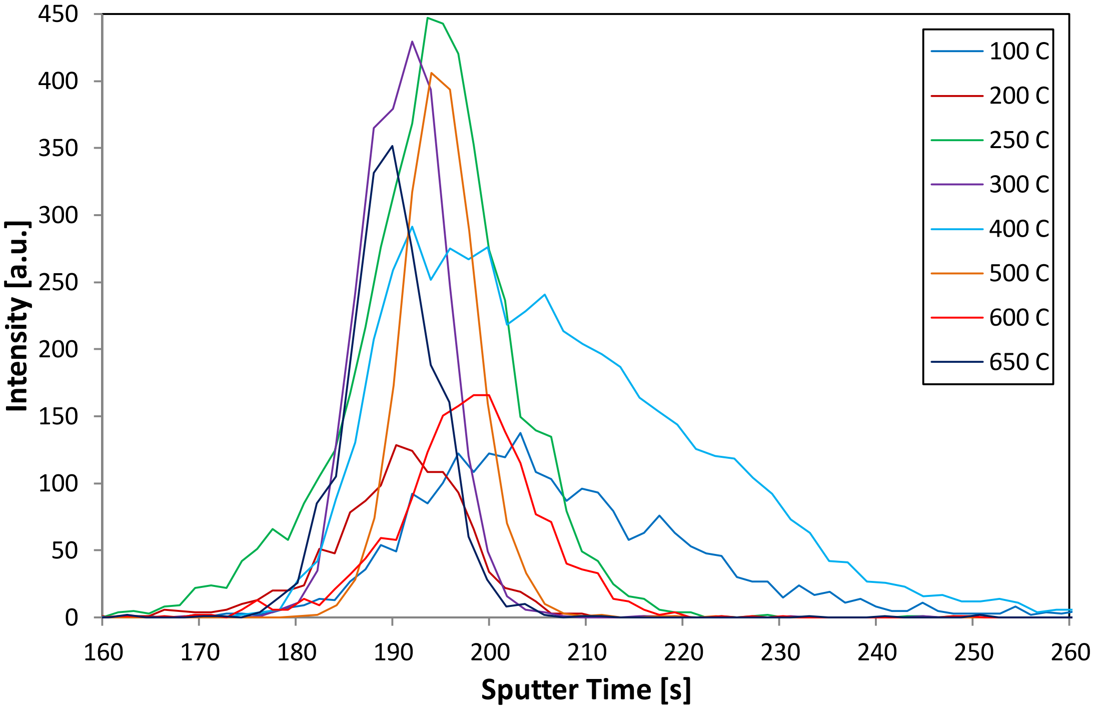

Figure 14.11: Silver distribution in AZO/Ag/AZO samples deposited onto float glass substrate, annealed at the range of temperature of 100-650^{o}C.

Table 14.4: Silver diffusion coefficient values calculated from AZO/Ag/AZO samples annealed at different temperatures.

Annealing conditions [^{o}C]	**D_{Ag} [m^2/s]**
100	6.00×10^{-20}
200	1.50×10^{-20}
250	2.73×10^{-20}
300	8.00×10^{-20}
400	4.55×10^{-20}
500	1.74×10^{-20}
600	1.95×10^{-20}
650	1.10×10^{-20}

The Ag diffusivity values calculated for samples annealed at different temperatures are in the same order of magnitude for most of the samples, suggesting that annealing temperature does not cause significant changes in silver diffusion through AZO layers. Moreover even within this range, there is no clear trend obtained in the diffusion coefficient values, as they seem to be scattered independently of temperature. Hence the lowest diffusion coefficient was obtained from the sample annealed at the highest temperature, whereas the sample annealed at 300^{o}C shows the highest diffusion rate. Figure 14.12 shows the Arrhenius plot, which represents scattered data from AZO/Ag/AZO stacks. This suggests that silver diffusion in Al-doped zinc oxide films occurs independently of temperature. The diffusion coefficient values are relatively low of the order of 10^{-20} m^2/s. Increasing annealing time, especially while heat treating at lower temperatures, could have increased the diffusion of silver. As mentioned in the previous chapter, in the literature there are studies that show a linear dependency between diffusion and temperature when the annealing time was altered with temperature. Nevertheless the study showed that in the case of AZO/Ag/AZO stacks, silver diffusion is low even at elevated temperatures for constant, relatively short annealing times.

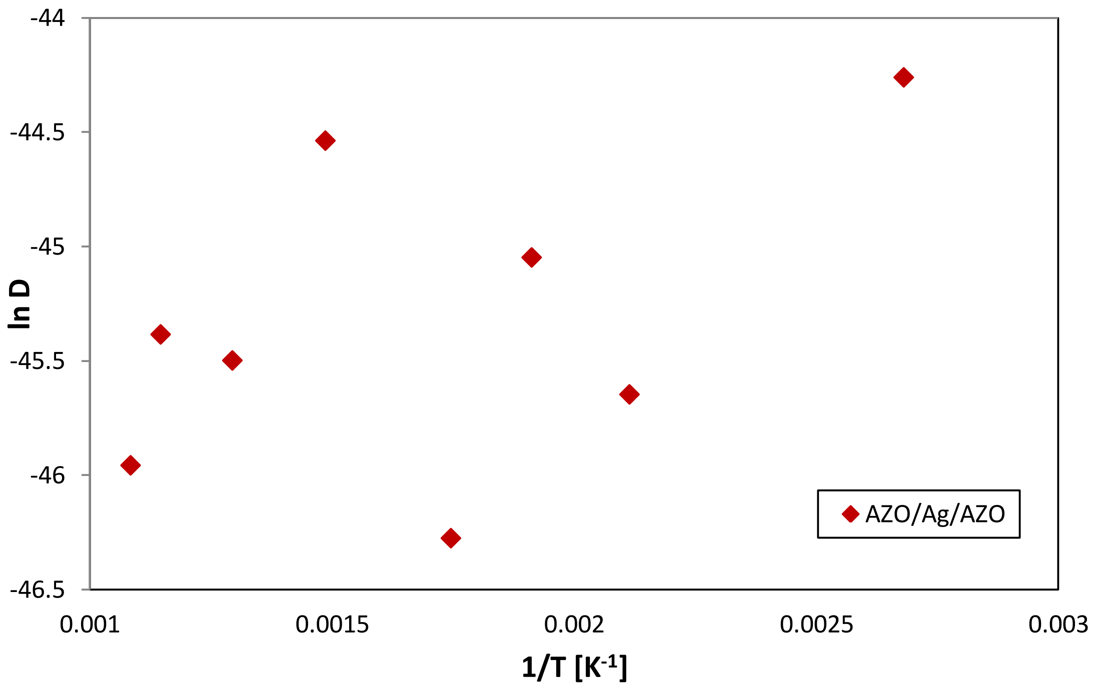

Figure 14.12: Arrhenius plot of Al-doped ZnO/Ag/Al-doped ZnO coating stack annealed at different temperatures.

14.3 $Si_3N_4/Ag/Si_3N_4$

Table 14.5 shows the diffusion coefficient values calculated for silver atoms travelling through adjacent silicon nitride films in $Si_3N_4/Ag/Si_3N_4$ coating stacks. It was discovered that silver follows the Arrhenius dependency of diffusion coefficient values with temperature. Silver diffusivity increases with rising annealing temperatures quite significantly, showing differences of three orders of magnitude between samples annealed at the lowest and the highest temperatures selected for this study. Figure 14.13 presents the Arrhenius plot, which shows good linear fit, which enables calculations of the activation energy and frequency factor. The activation energy was found to be 34.3±1.7 kJ/mol (~0.3554 eV) and the frequency factor equals 3.10×10^{-17} m^2/s.

Silver profiles from silicon nitride/Ag/silicon nitride samples annealed at the range of temperatures of 100-600^{o}C are shown in Figure 14.14.

Table 14.5: Silver diffusion through silicon nitride coatings at different temperatures.

Annealing Temperatures [°C]	**D_{Ag} [m^2/s]**
100	1.00×10^{-21}
200	4.25×10^{-21}
250	4.75×10^{-21}
300	1.75×10^{-20}
400	6.65×10^{-20}
500	1.05×10^{-19}
600	7.65×10^{-19}

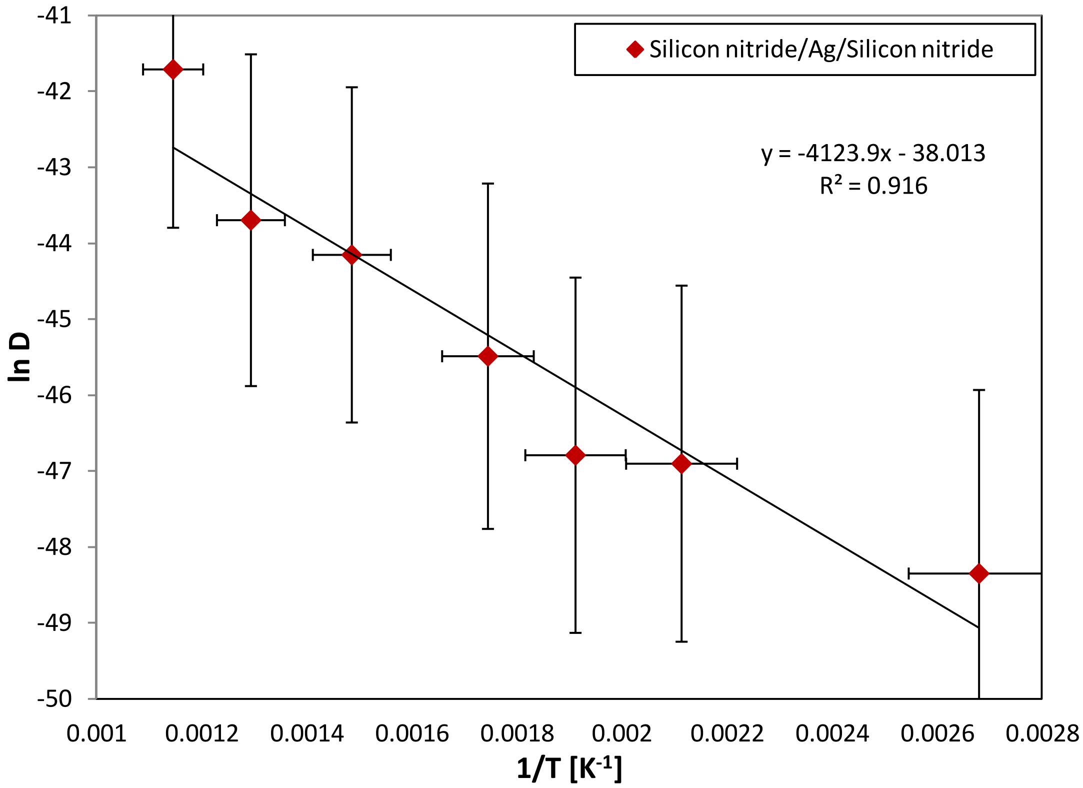

Figure 14.13: Arrhenius plot for silicon nitride/silver/silicon nitride stack deposited on float glass substrates.

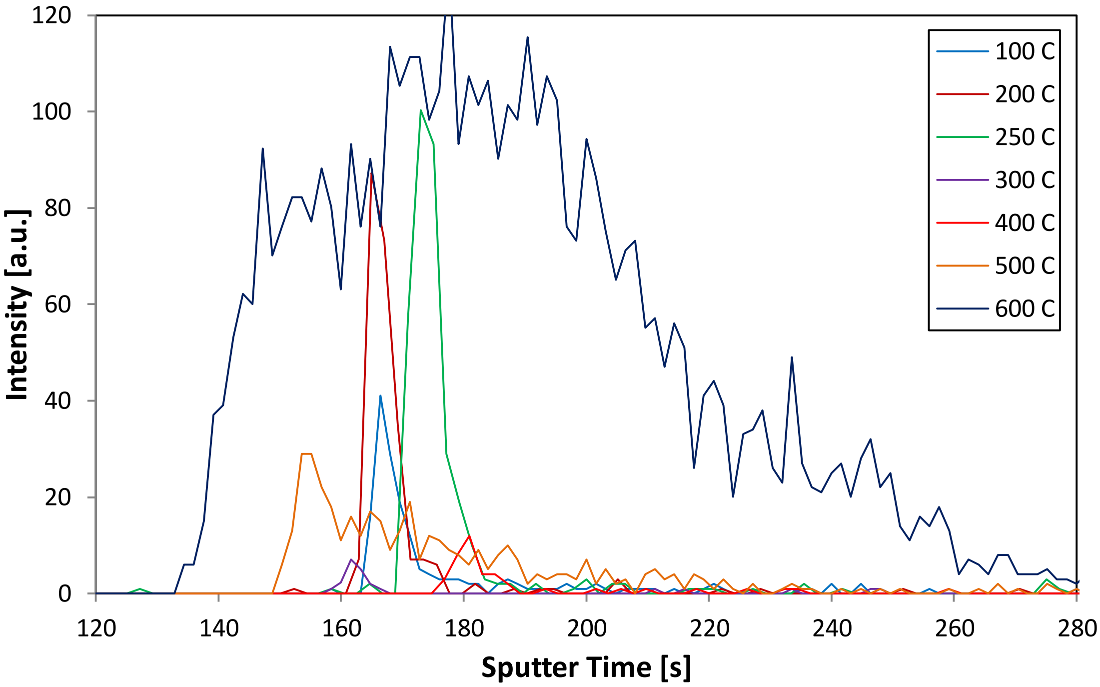

Figure 14.14: Silver distribution in Si_3N_4/Ag/Si_3N_4 coatings deposited on glass and annealed at the range of temperatures of 100-600^oC for 5 minutes.

14.4 Dielectric/Ag/Dielectric: Summary

Dielectric/Ag/dielectric stacks have been deposited onto glass substrates and subjected to annealing over the range of temperature of 100-600^oC for 5 minutes to investigate silver diffusion and its dependency on annealing temperature using an Arrhenius plot. Dielectric coatings deposited in this study were TiO_2, Al-doped ZnO and Si_3N_4.

In TiO_2/Ag/TiO_2 stacks, silver diffused at similar rates in the samples annealed at temperatures in the range of 100-500^oC, whereas a significant increase in diffusion coefficient was detected in the sample annealed at 600^oC for 5 minutes. This may be related to the structure of titania, as it was established in the previous study that as-deposited amorphous TiO_2 becomes anatase after annealing at relatively high temperatures and becomes easier to diffuse through for silver atoms. On the other hand, lack of significant differences in the diffusion coefficient values in samples annealed at temperatures below 600^oC may just mean that relatively small changes in annealing conditions have no significant impact on silver diffusion in titania/silver/titania stacks.

Further investigations of silver diffusion in titania stacks showed that increasing the annealing time to 1 hour at 600^oC leads to complete diffusion of the silver atoms, most likely into the glass substrate due to an ion-exchange mechanism. Sodium diffusion from the glass fills in the free spaces in the coatings created by silver diffusion. Samples analysed by XPS have confirmed these results, as there was no silver detected in the stack after annealing at 600°C for 1 hour. However in the sample deposited onto a silicon wafer substrate silver diffused to the surface creating large clusters on the film surface. EDX mapping analysis confirmed that clusters, which appeared at the surface of the films deposited on Si wafers, are silver agglomerations due to diffusion mechanism.

Silver diffuses in Al-doped ZnO stacks with similar rates, independently of annealing temperature. This suggests that the annealing process does not cause changes in the AZO film structure, therefore keeping the silver diffusion low. This makes Al-doped ZnO a very attractive material in Low-E coatings technology, as glass toughening processes at elevated temperature will not encourage silver diffusion, and therefore decomposition of the stack structure.

Silver follows the Arrhenius dependency only in Si_3N_4 coatings, significantly increasing its diffusion rates with increasing annealing temperatures. The activation energy and frequency factor values obtained from the data are 34.3 kJ/mol (0.3554 eV) and 3.1×10^{-17} m^2/s respectively. Values are lower than those obtained from the Arrhenius plot for the Ag/Si_3N_4/glass system, which may be related to differences in the silver thickness.

15. Conclusions

In this work, the diffusion of silver and sodium through dielectric coatings was investigated. The coating operating conditions, annealing temperature and time, and film structure was studied to find correlation between these parameters and diffusion rates, since these factors are known to have an impact on diffusion processes in solids. The main findings during this project are as follows:

Coating characterisation revealed that the structure of some of the dielectric films deposited in this study can be modified by the operating parameters selected during coating deposition and also by the post-deposition annealing. Studies of the titania films showed that the as-deposited coatings had rather amorphous structures with some predominant semi-crystalline regions with very small grain sizes. The structure transformed through a mixed crystalline phase into pure anatase when samples underwent post-deposition heat treatment and re-crystallisation. As-deposited and annealed Al-doped ZnO coatings show a typical wurtzite ZnO crystalline structure with crystals of relatively small grains, which may increase during annealing at relatively high temperatures. Zinc stannate and silicon nitride samples remained amorphous at various deposition conditions investigated in this work and after a relatively short time annealing at 650^{o}C.

Coatings deposited in this project are dense and present rather smooth surfaces, with some defects (or grain) located on the surface after annealing. This could be related to re-crystallisation process occurring under high temperature treatments. Films sputtered in reactive modes from metal targets, in the mixed Ar/reactive gas ambients, show mostly stoichiometric compositions.

Diffusion studies revealed that silver travels with similar diffusion rates through as-deposited and annealed samples of ZTO, AZO and Si_3N_4 coatings, which could be related to relatively insignificant changes (if any) in the film morphology after heat treatment. The only exception is titanium dioxide, when the structure changes dramatically from amorphous to fully crystalline after long time heat treatment times at relatively high temperatures. In this case silver diffuses faster probably through so called short circuit paths in grain boundaries.

Differences in sodium diffusion are related to the first annealing at relatively high temperatures. In the titania samples, which were annealed at various temperatures and times, sodium showed higher diffusion rates in samples annealed at higher temperature ranges and for longer times. In the remaining dielectric samples sodium diffuses at significantly lower rates in as-deposited samples than in post-deposition annealed samples. The difference in diffusivity varies between one and two orders of magnitudes in AZO and Si_3N_4 samples and in ZTO the diffusion coefficient values could not been found for sodium in heat treated samples due to the limitation of the diffusion calculator programme and possibly due to the diffusion path, which is not fully understood by the author.

Moreover the deposition conditions of silicon nitride samples may have an impact on sodium diffusion. It was found that one of the samples, which was post-deposition annealed at 650^{o}C showed Na diffusion rates as low as in the as-deposited samples, whereas the other samples showed a significant increase in Na diffusivity after comparing to the as-deposited samples. This was attributed to the deposition conditions and low energy of ions incident at the substrate during film deposition, resulting in the formation of a more open film structure creation.

The dependency of silver diffusion on temperature was investigated in Ag/Si_3N_4/glass samples using the Arrhenius relationship. A selected sample was annealed at 100, 400 and 600^{o}C in addition to 250^{o}C used for the silver diffusion studies in the previous work. A satisfactory trend was obtained between diffusion coefficient values and temperature, as diffusion rate increased with annealing temperature. The activation energy and frequency factor values were found from the plot to equal 38.1 kJ/mol (0.3945 eV) and 2.13×10^{-15} m^2/s respectively.

Finally, from dielectric/Ag/dielectric stacks studies it was found that the Arrhenius plot was only followed by silver sandwiched between silicon nitride films. The activation energy and frequency factor values obtained from the plot were 34.3 kJ/mol (0.3554 eV) and 3.1×10^{-17} m^2/s, respectively. In the case of silver diffusion in titania/Ag/titania stacks, no trend was obtained while increasing annealing temperature. In titania films, the diffusion coefficient value increased quite significantly after annealing at 600^{o}C, which is related to structural changes of these coatings, as previously found for the Ag/TiO_2/glass stacks. Further investigations of silver diffusion in titania/Ag/titania stacks showed that increasing the annealing time to 1 hour at 600^{o}C leads to complete diffusion of the silver atoms, most likely into the glass substrate due to an ion-exchange mechanism. Sodium diffusion from the glass fills in the free spaces in the coatings created by silver diffusion. Similar results were obtained also from XPS in sample deposited onto glass substrate, whereas in the sample deposited onto a silicon wafer substrate, silver diffused to the surface creating large clusters on the film surface. EDX mapping analysis confirmed that clusters, which appeared at the surface of the films deposited on Si wafer, are silver agglomerations due to diffusion mechanism.

Overall diffusion studies showed that Al-doped ZnO coatings can act as excellent barrier coatings for silver atoms and show very good results for sodium diffusion, when samples were not annealed at relatively high temperatures. Zinc stannate, on the other hand, was found to be the material through which atoms in general seem to diffuse fairly easily. Results obtained for both silver and sodium atoms had the highest diffusion rates comparing to diffusion measurements from the remaining coatings investigated in this work.

16. Future Work Suggestions

Diffusion due to its complex nature and relatively low number of studies in thin films, still needs further work in certain areas to develop a better understanding of the process. Therefore the possible future work could be continued in the following areas:

1. The TiO_2 structural changes could be additionally investigated by TEM to get more information about crystalline lattices created due to the re-crystallisation process during annealing.
2. Titania could be deposited under operating conditions which creates as-deposited fully crystalline forms of the film, by for example heating the substrate up during deposition. This would reveal if further post-deposition annealing changes the titania structure and if the process has an impact on diffusion.
3. To gain more understanding of diffusion in ZTO coatings, more in-depth diffusion investigations could be performed, which would involve creating a better model of diffusion in amorphous materials. This could solve the problem of having very high concentrations of sodium diffusing through ZTO and possibly allow diffusion coefficient values to be determined.
4. Moreover ZTO could be annealed at higher temperatures and for longer times to try to achieve crystalline structures. Then silver diffusion could be measured and its rates could be compared with those obtained for amorphous ZTO films.
5. The Arrhenius temperature dependency could be investigated at different (maybe higher) annealing times and temperatures, to obtain the Arrhenius plot and therefore solve the equation by finding Q and D_0 values for silver diffusion through the dielectric coatings investigated in this work.
6. Overall, to gain more understanding about diffusion processes in thin films, a more specific diffusion profile could be created, which would distinguish different diffusion paths, such as GBs or lattice diffusion, in thin films.

Appendix 1: Hysteresis Behaviour

During reactive sputtering the introduction of a reactive gas can lead to changes in operational parameters, such as cathode potential (see Chapter 4.5.2.1). In this work dielectric coatings were deposited in mixed argon/oxygen (or argon/nitrogen in case of silicon nitride films) atmosphere and parameters such as pressure, target voltage and current were monitored. In case of titanium dioxide the OEM signal was also monitored, whereas in remaining coatings a feedback system was not used during coating deposition. This is due to difficulties of finding stable operating conditions using the OEM system. Hence dielectric coatings, except titania, were deposited in mixed argon/reactive gas environment controlling the partial pressures of the introduced gasses. In general the amount of reactive gas introduced into the chamber during sputtering was equivalent to the volume of reactive gas at the first transition region in the hysteresis curve.

The hysteresis curves will be presented here as an output voltage under constant power delivered to the system. The output voltage is a very good indicator of the hysteresis behaviour as its value is related to secondary electron emission at the target surface and the degree of target poisoning. [174] The voltage may either increase or decrease when the reactive gas partial pressure in the chamber is increased. This depends on the target material and the choice of reactive gas. [175]

A. TiO_2 Hysteresis Studies

The hysteresis behaviour of titanium dioxide coatings sputtered from FFE magnetrons was investigated. The power supply was operated in DC mode introducing a constant power of 1 kW to the magnetron The magnetron was operated in stationary mode and at three various rotating speeds of 50, 150 and 300 rpm. Oxygen was gradually increased from zero to a maximum flow of 6 SCCM using a MKS mass flow controller. Prior to the introduction of reactive gas the chamber was filled with 18 SCCM of argon gas, giving a pressure of 0.18 Pa. Figures A.1-A.4 show the variation in cathode voltage and current with oxygen flow rate changes.

In Figure A.1 both parameters voltage and current shows rapid changes between oxygen flow rates of 3.0 and 3.2 SCCM. The cathode potential increases in magnitude from

-433 to -523 V and the target current drops from 2.31 to 1.91 A. These changes are associated with the transition from metallic to poisoned mode, described in Chapter 4.5.2.1. The second transition point occurs when oxygen flow is decreased from 1.5 to 1.0 SCCM and represents the system coming back to the metallic mode. Introducing oxygen gas into the chamber while sputtering titanium in argon gas atmosphere can lead to the formation of titania on the target surface and chamber walls. A transition represents the point at which the amount of oxygen in the chamber is higher than the pumping speed of the pump and therefore gas removal. Hence titania is being formed and deposited in this conditions.

The increase in the cathode potential (in this work found between 3.0 and 3.2 SCCM of introduced oxygen) has been assigned to the difference in the secondary electrons coefficient, which is lower in titania than in Ti. [175]

In the remaining data sets sputtered at different rotation speeds of the magnets in the FFE magnetron design (see Figures A.2-A.4) the hysteresis loop has also been seen. However the loops differ in shapes and the transition mode occurs between 1.8 and 2.0 SCCM for speeds of 50 and 150 rpm, and between 2.0 and 2.2 SCCM for the speed of 300 rpm. Moreover the increase in the cathode potential is lower than in the case of the data acquired from the stationary mode studies. This is probably related to the constant changes in the target voltage during magnets rotation. The power supply displays an average voltage, which may not be indicative to the full variation in voltage during a full cycle.

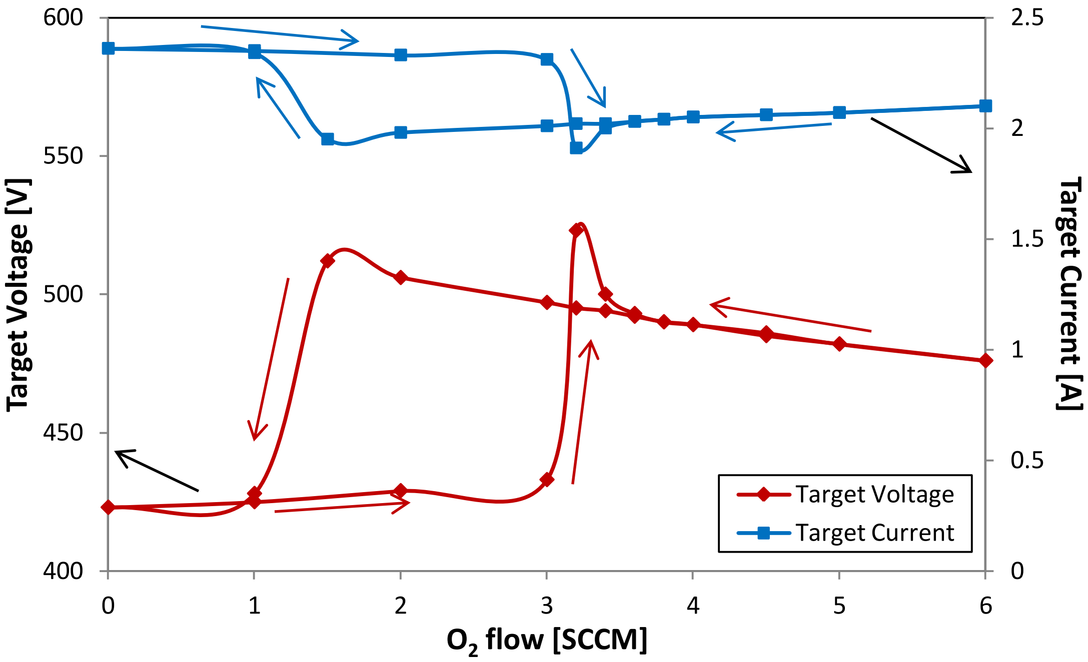

Figure A.1: The effect of the oxygen flow on cathode voltage and current in TiO_2 operated under stationary mode using FFE magnetron design. The arrows show the way in which the data was acquire.

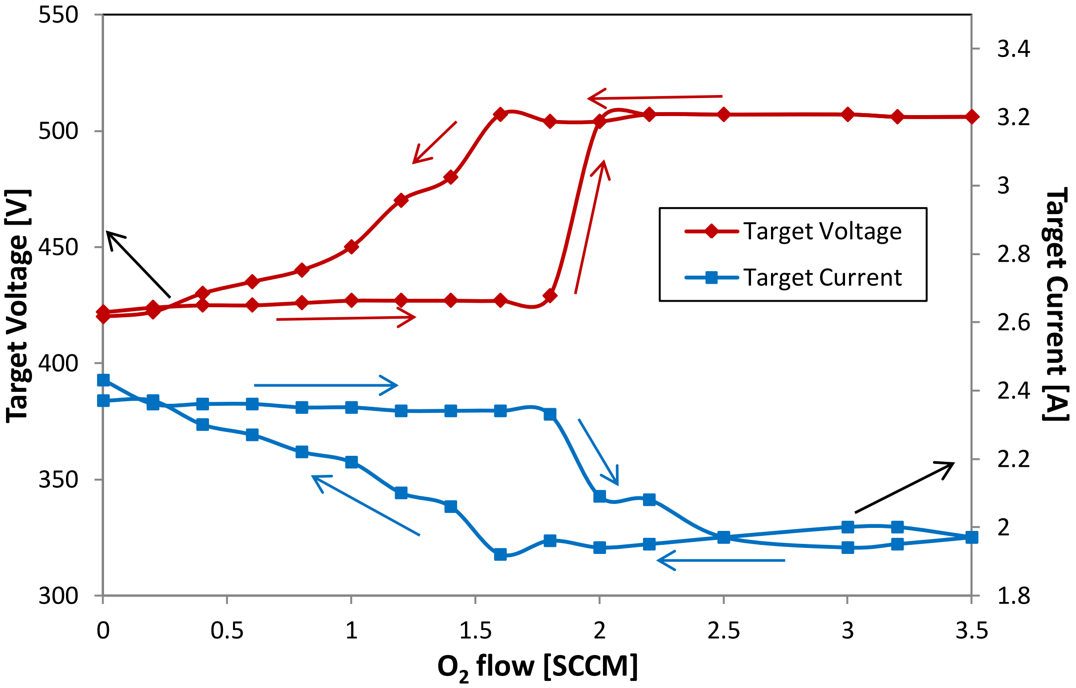

Figure A.2: The effect of the oxygen flow rate on cathode voltage and current in TiO_2 operated under 50 rpm magnetron speed. The arrows show the way in which the data was acquire.

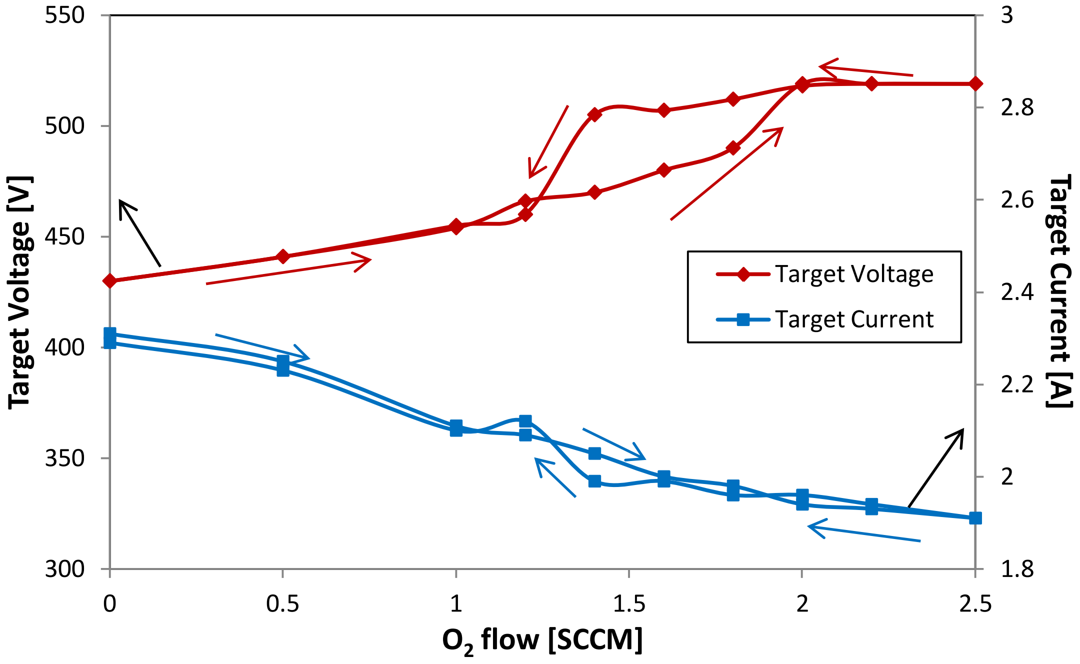

Figure A.3: The effect of the oxygen flow on cathode voltage and current in TiO_2 sputtered under the magnet rotation of 150 rpm. The arrows show the way in which the data was acquire.

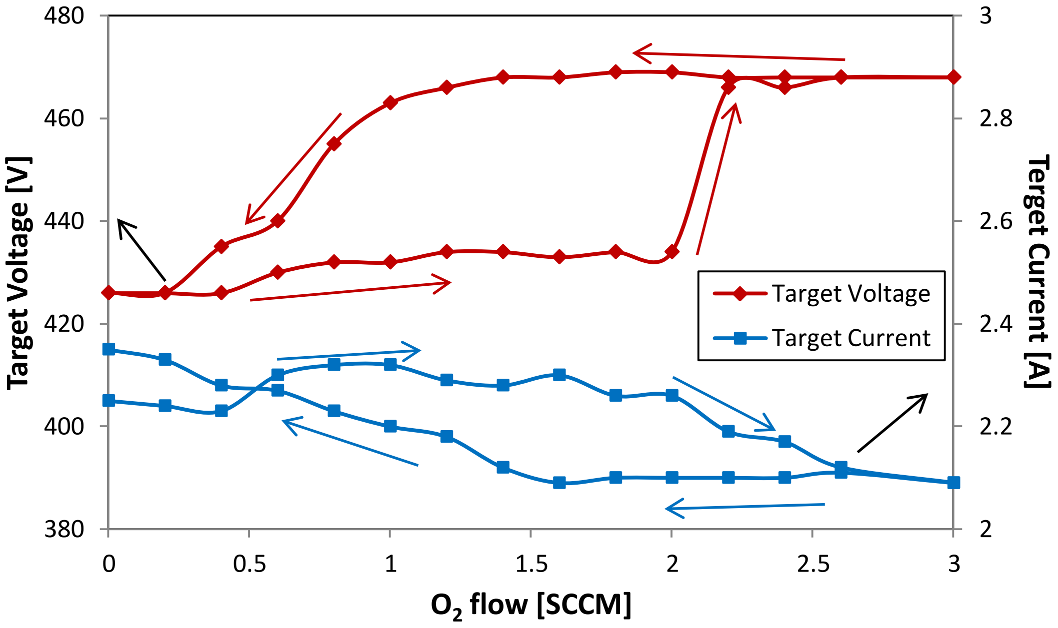

Figure A.4: The effect of oxygen flow rate on cathode voltage and current in TiO_2 sputtered from FFE magnetron rotating at 300 rpm speed. The arrows show the way in which the data was acquire.

The OEM signal was also monitored and it showed a rapid decrease from 64 to 4% of the full metal signal, when the oxygen flow was increased from 3.0 to 3.2 SCCM (see Figure A.5). This large drop in the signal is related to the reduction in the amount of sputtered titanium in the plasma, due to changes in the composition of the target surface. Hence significant differences in the OEM signal between the metallic and poisoned modes makes the system suitable to use as a feedback signal from the plasma to control oxygen flow during sputtering.

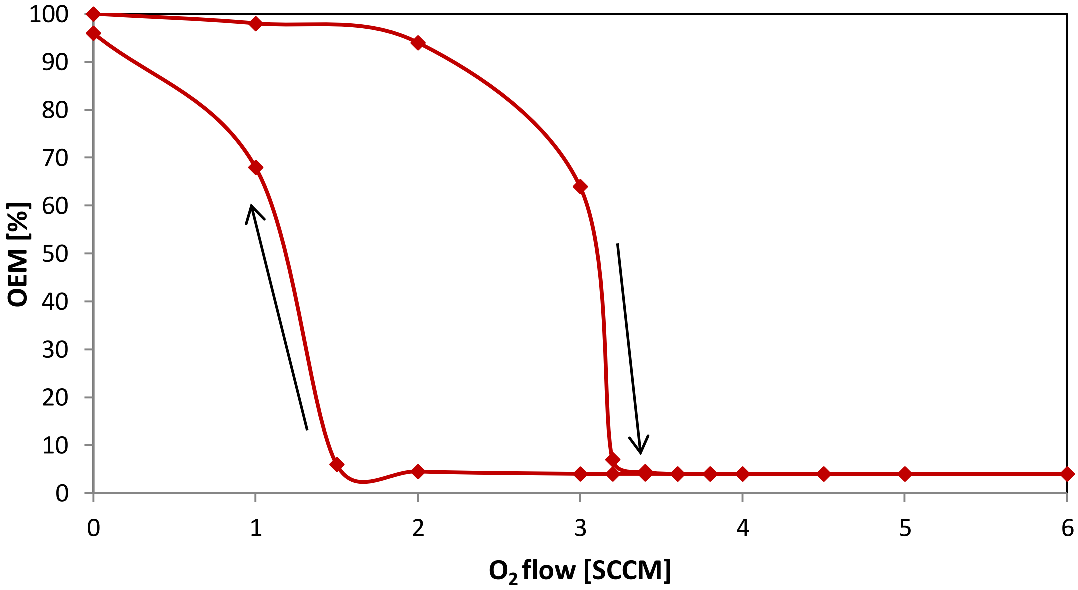

Figure A.5: The effect of the oxygen flow on the OEM signal in titania sputtered at stationary mode from FFE magnetron. The arrows show the way in which data was acquire.

B. Al-doped ZnO Hysteresis Studies

The hysteresis behaviour was investigated during sputtering AZO in the stationary mode of the FFE magnetron. The magnetron was driven in pulsed DC mode with a pulse frequency of 100 kHz and 4.0 µs off time and a constant power introduced to the system of 200 W. The chamber was filled with 32 SCCM of argon giving an operating pressure of 0.4 Pa. The oxygen was gradually increased from 0 to 10 SCCM in total. Figure B.1 shows the effect of oxygen flow rate on cathode voltage and current.

The first transition point has been detected between the oxygen flow rates of 4 and 4.2 SCCM, indicated by a drop in target voltage from -452 to -280 V and increase in target current from 0.44 to 0.71 A. The second transition point, when the oxygen flow was decreased, was found between 0.4 and 0.3 SCCM of oxygen and between these points cathode voltage and current changes from -380 to -780 V and 0.53 to 0.26 A, respectively.

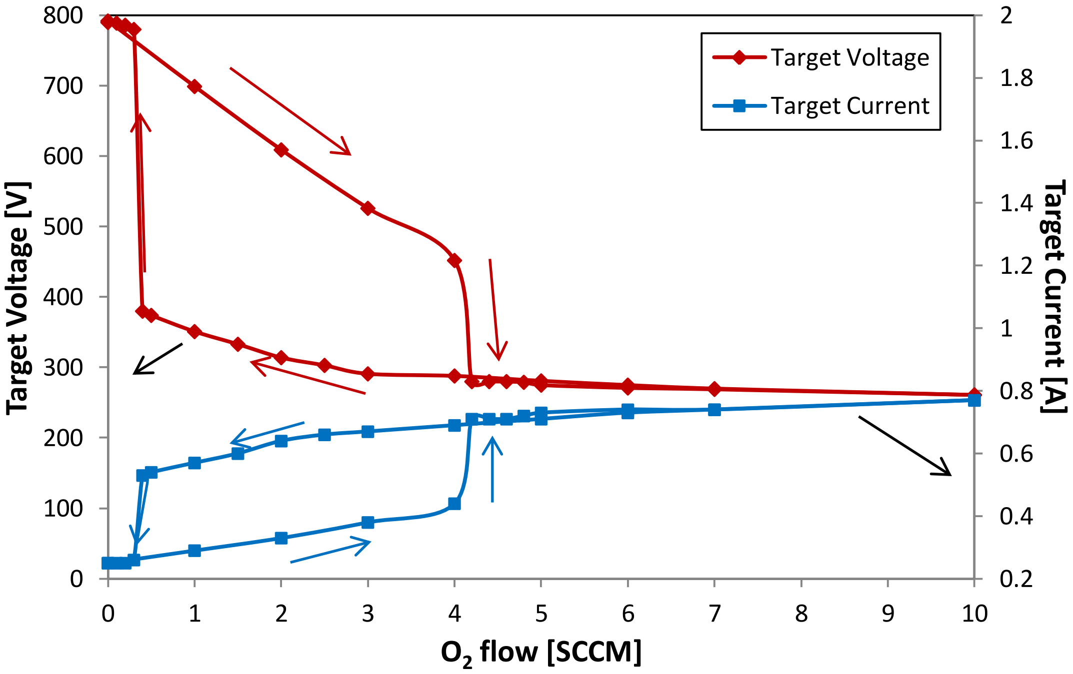

Figure B.1: The effect of the oxygen flow on the cathode voltage and current in AZO sputtered from FFE magnetron at stationary mode. The arrows show the way in which the data was acquired.

Changes in the total metal signal were also investigated (see Figure B.2). However the results obtained from the study are rather difficult to explain. When the oxygen flow rates increases from 0 to 3 SCCM the OEM signal increases from 100 to 118%, and then drops back down to 100% after 4 SCCM of oxygen was introduced to the system. From this point a rapid decrease in OEM signal is noticed as it drops from 100 to 51% between 4.0 and 4.2 SCCM of oxygen. Finally, when the oxygen flow is decreased the OEM signal starts rising from 55 to 65% between 4 and 2 SCCM of oxygen, and then drops between 2 and 0.4 SCCMs of oxygen to 47%. From 0.4 to 0.2 SCCM of oxygen a rapid increase in OEM signal occurs from 47 to 100%. These instabilities in the OEM system and relatively low decrease in the full metal signal between metallic and poisoned modes makes the OEM not suitable as a feedback control device in controlling oxygen flow during sputtering. Therefore in this work AZO coatings were deposited without the use of OEM feedback controlling system, but were sputtered in mixed Ar/O$_2$ atmosphere, where the amount of introduced gasses was controlled by MKS mass flow controllers. The non-systematic behaviour of the OEM system may indicate that the wrong line in the AZO emission spectra was selected at the control point. However, several candidate lines were tested and none showed reliable control of the process.

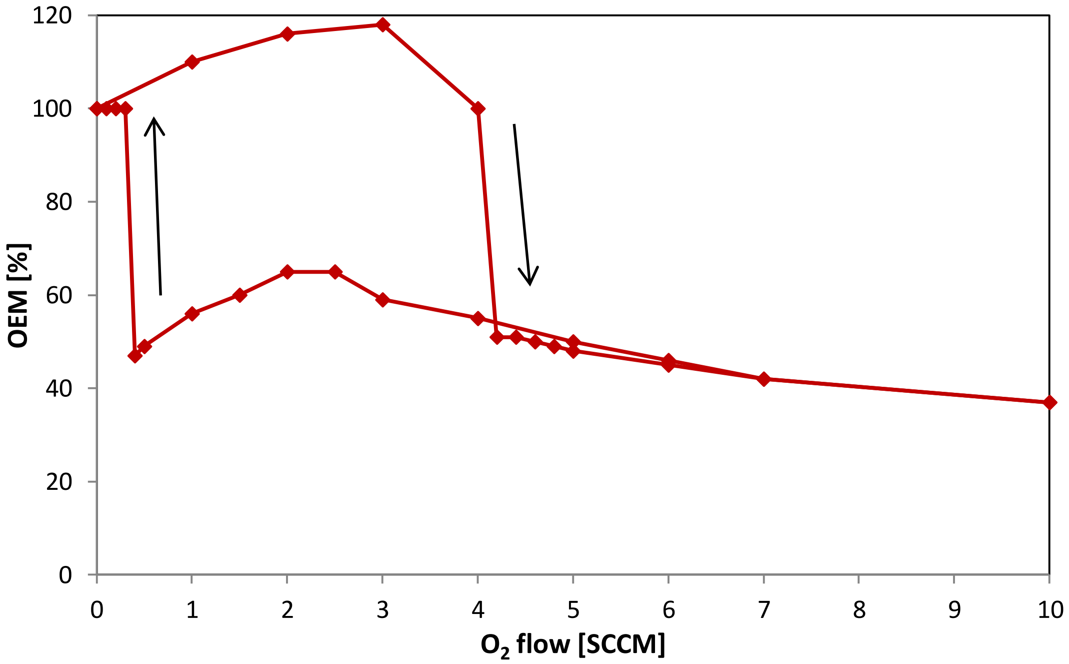

Figure B.2The effect of the oxygen flow on the OEM signals in AZO. The arrows show the way in which the data was acquired.

C. Zn_2SnO_4 Hysteresis Studies

Hysteresis behaviour was investigated in ZTO coating sputtered from single planar, dual planar and dual cylindrical rotatable magnetron designs. The conditions selected for these studies were as follows: constant power delivered to magnetrons of 1, 3 and 5 kW, at a constant argon flow rate of 120 SCCM. Moreover in case of single planar magnetron design operating pressure varied from 0.2 to 1.3 Pa, and in case of the rotatable magnetron configuration tubes was set at 5, 6 and 7.5 rpm rotation speed. The total amount of oxygen introduced into the chamber varied from 0 to 190 SCCMs. Figures C.1-C.5 show the effect of oxygen flow on the cathode voltage in ZTO films sputtered under different conditions from three magnetron configurations.

There is no significant drop in the target voltage at any point when the oxygen flow was increased. In general, the voltage is gradually decreased in most of the measurements obtained, whereas in dual planar design, at a power of 5 kW, a more significant decrease in target voltage was detected from -540 to -422 V between oxygen flows from 150 to

170 SCCM. Similarly the second transition point is the most obvious in hysteresis data performed under these conditions, where between the oxygen flows from 150 to 120 SCCM, the target voltage increased from -425 to -584 V. In the remaining studies the voltage gradually increases when the oxygen flow rate decreases, therefore showing relatively little hysteresis.

Moreover there is only insignificant difference in the hysteresis curve shapes between the data obtained for chosen magnetron designs at different powers and also no difference between the data acquire at different pressures (see Figure C.5) and at different rotating speeds in the rotatable magnetron design (see Figure C.4). Therefore it can be assumed that magnetron design and operating parameters do not change significantly the hysteresis behaviour of zinc stannate. As during sample deposition, the system was operated in partial pressures mode, with the oxygen flow rates were chosen from the hysteresis curve at the tail of the metallic to poisoned mode transition curve, where the increasing flow rate did not caused further changes in the target voltage. Therefore for single planar magnetron sputtered at 5 kW power the oxygen partial pressure was 160 SCCM (see Figure C.1).

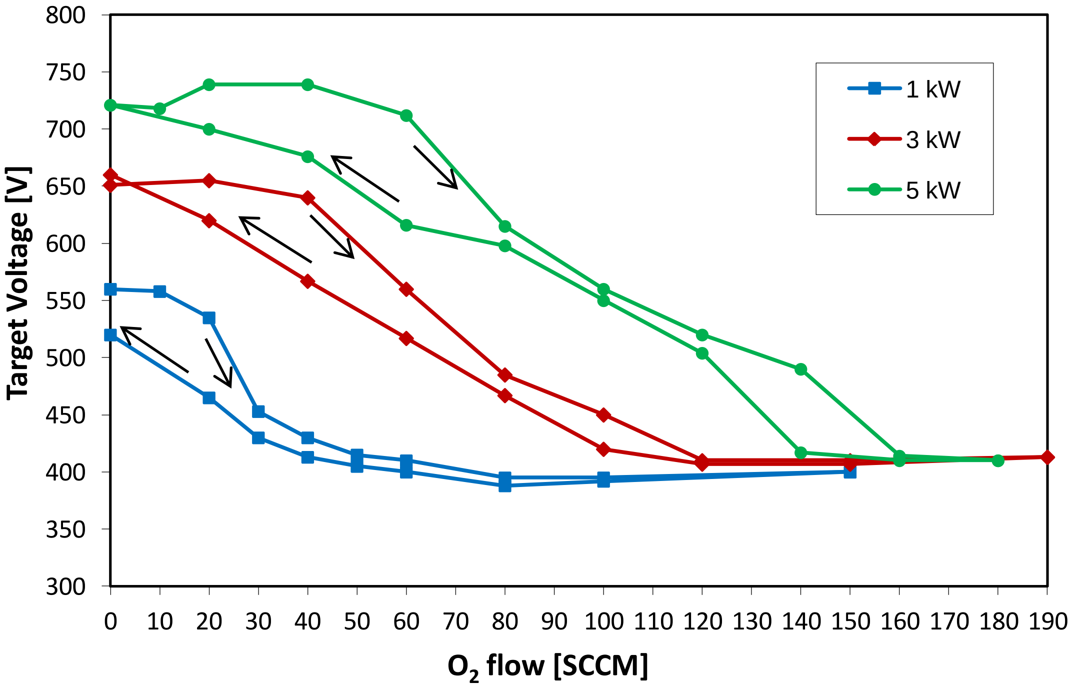

Figure C.1: The effect of the oxygen flow on the cathode potential in zinc stannate films sputtered from single planar magnetron in DC mode at power of 1, 3 and 5 kW respectively. The arrows show the way in which the data was acquired.

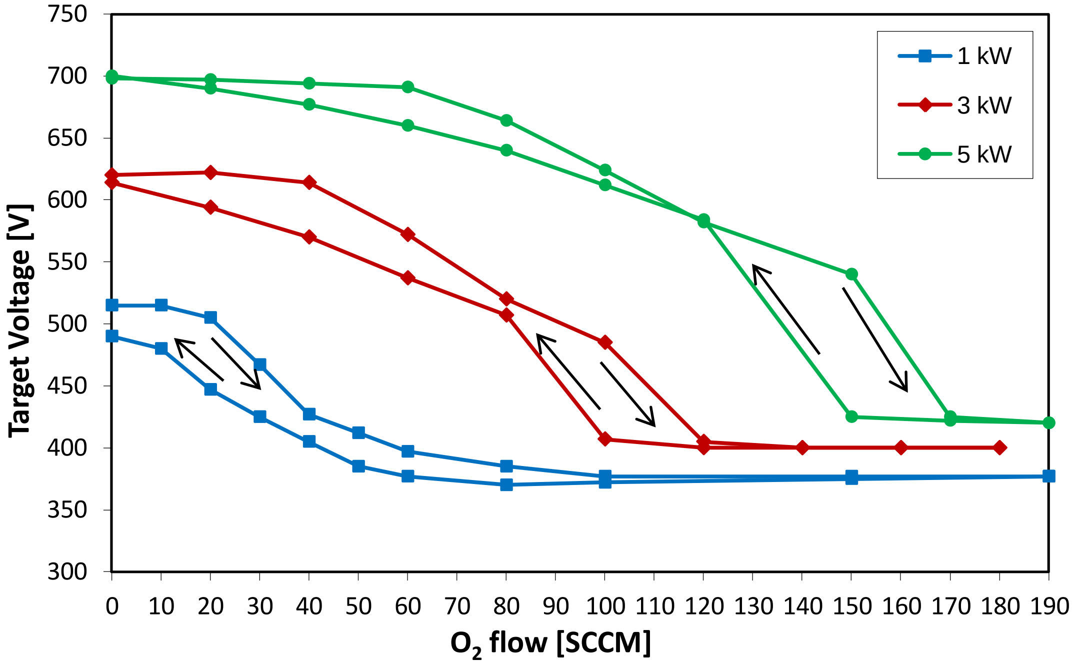

Figure C.2: The effect of the oxygen flow on the target voltage in zinc stannate sputtered from dual planar magnetron design in AC mode and constant powers of 1, 3 and 5 kW, respectively. The arrows show the way in which data was acquired.

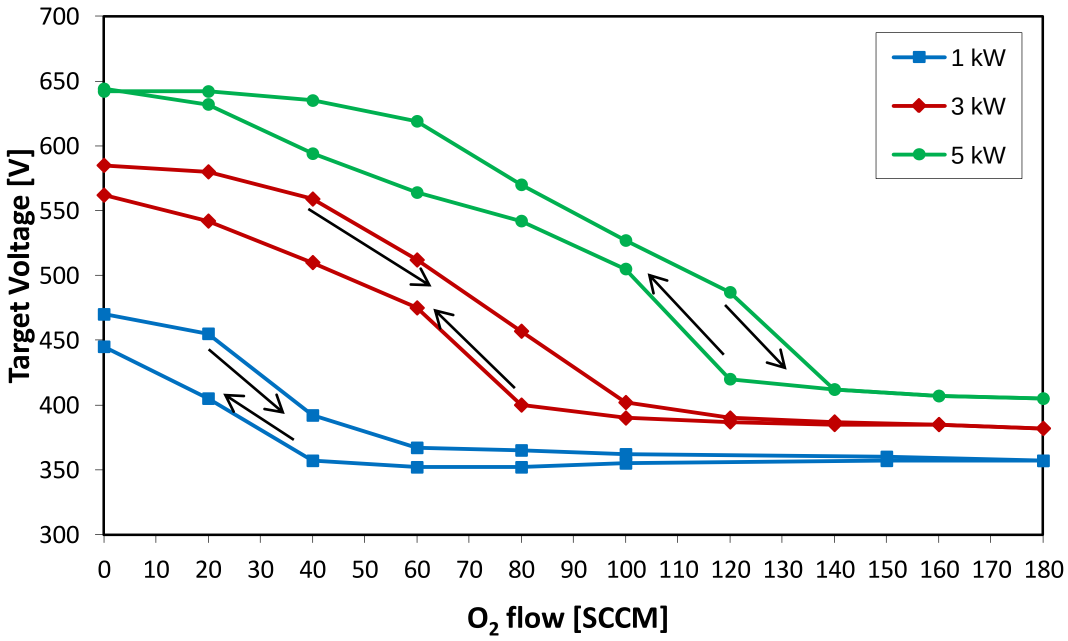

Figure C.3: The effect of the oxygen flow on target voltage in zinc stannate sputtered from dual cylindrical rotatable magnetrons in AC mode and constant powers of 1, 3 and 5 kW. The arrows show the way in which the data was acquired.

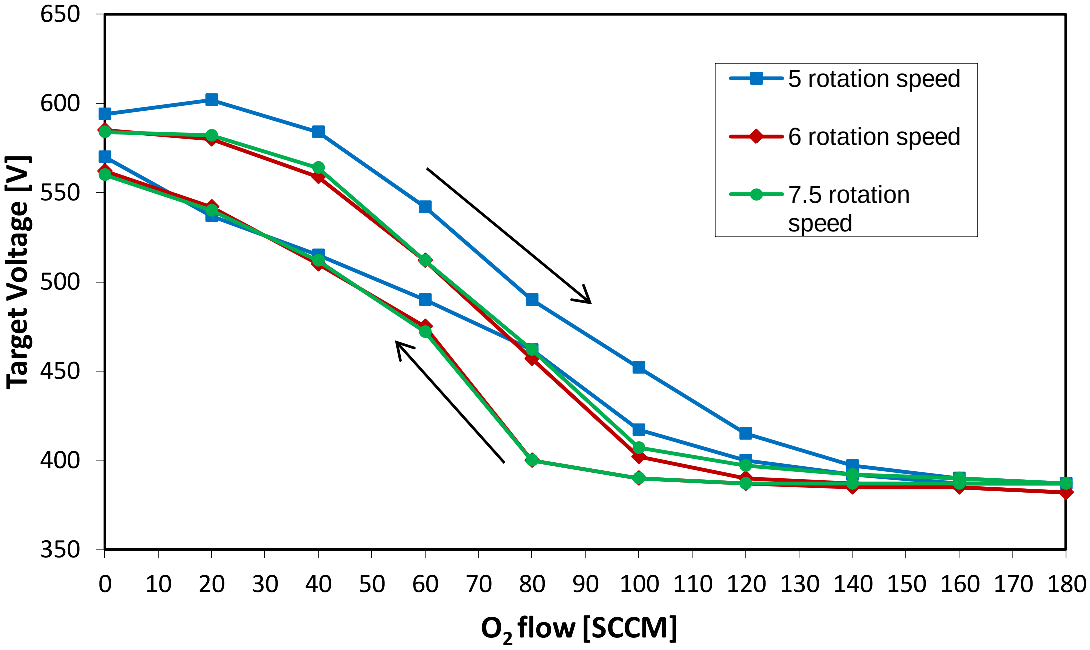

Figure C.4: The effect of the oxygen flow on the target voltage in rotatable magnetron design driven in AC mode at constant power of 3 kW and different rotation speed of 5, 6 and 7.5. The arrows show the way in which the data was acquired.

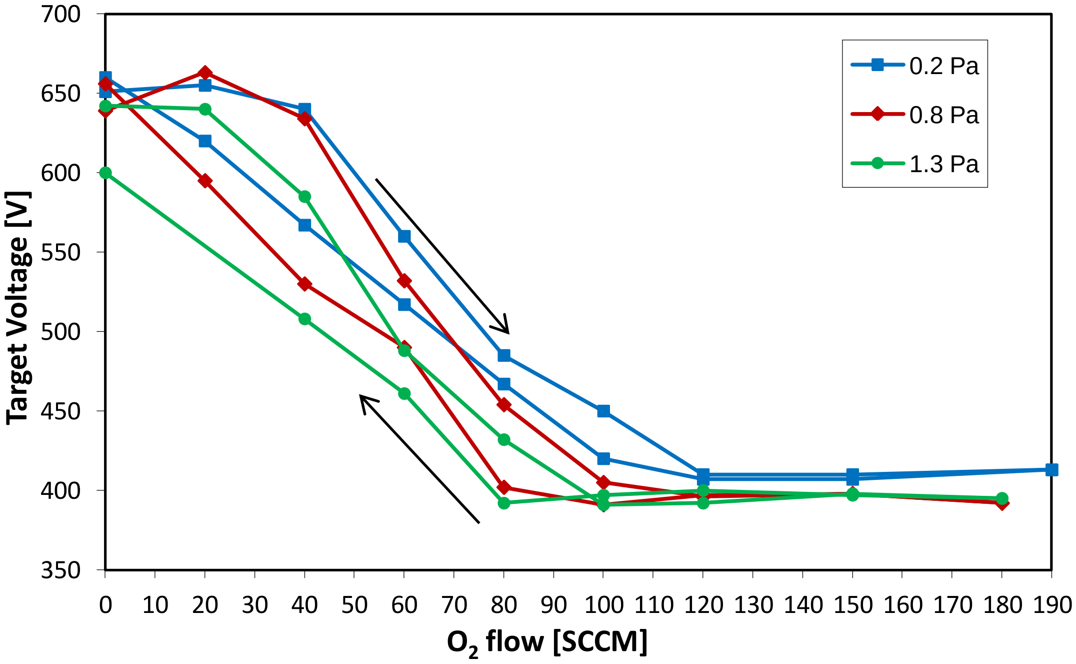

Figure C.5: The effect of the oxygen flow on the target voltage in zinc stannate sputtered in DC more from single planar magnetron at constant power of 3 kW and operating pressure of 0.2, 0.8 and 1.3 Pa, respectively.

D. Si_3N_4 Hysteresis Studies

The hysteresis behaviour of silicon nitride was investigated. The silicon target at stationary mode was sputtered by pulsed DC mode at 100 kHz frequency and 5 µs off time, and at a constant power of 300 W. The amount of argon gas introduced into the chamber was 35 SCCM, which gave an operating pressure of 0.25 Pa. Nitrogen was gradually introduced into the chamber from 0 to 22 SCCM in 0.5 SCCM intervals. Figure D.1 shows the effect of nitrogen flow on target voltage. It has been shown that silicon nitride does not follow hysteresis behaviour when the amount of the reactive gas is increased gradually. Similar results have been found by Smith *et al.* who reported that there is a very little hysteresis behaviour in silicon nitride studies for stationary magnetron mode and negligible hysteresis at rotating targets. [174]

The absence of hysteresis means that the deposition process can be controlled by simply controlling the flow of reactive gas, without the need for the feedback system. Therefore in this work nitrogen gas was controlled by MKS mass flow controller during silicon nitride coatings deposition.

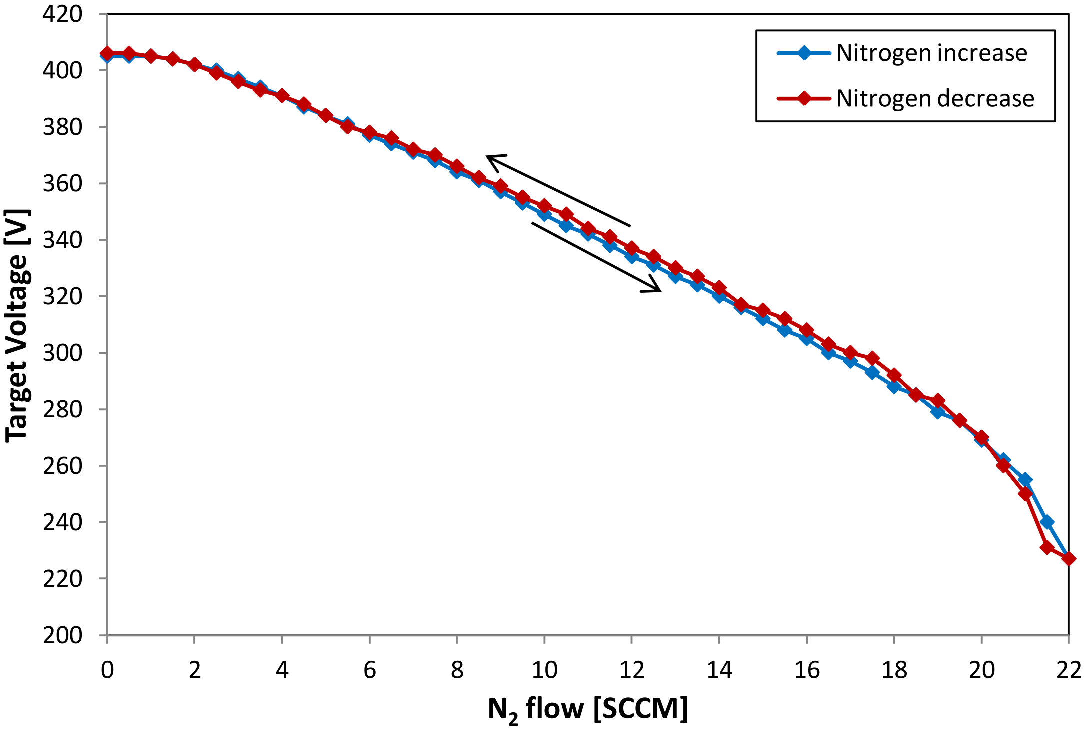

Figure D.1The effect of nitrogen flow on target voltage in silicon nitride. The arrows show the way in which the data was acquired.

Appendix 2: Laplace Transform

The Laplace transform is a mathematical device, which found its applications in diffusion equations removing the time variable, and therefore leaving an ordinary differential equation the solution of which yields the transform of the concentration as a function of the space variables x, y, z. This is then interpreted to give an expression of the concentration in terms of x, y, z and time t, satisfying the initial and boundary conditions. [83]

If $f(t)$ is known as a function of t, where t>0, then the Laplace transform $\bar{f}(t)$ of $f(t)$ is defined as:

$$\bar{\boldsymbol{f}}(\boldsymbol{p}) = \int_{\boldsymbol{0}}^{\infty} \boldsymbol{e}^{-\boldsymbol{pt}} \boldsymbol{f}(\boldsymbol{t}) \boldsymbol{dt} \qquad \text{Equation 67}$$

where p is a real positive number to make integral converge, i.e. if f(t)= e^{2t}, p must exceed 2. Equation 68 shows an example of Laplace transform, whereas extensive tables of Laplace transforms can be found in Crank’s book. [83]

$$\boldsymbol{f}(\boldsymbol{t}) = \boldsymbol{e}^{\boldsymbol{at}}, \bar{\boldsymbol{f}}(\boldsymbol{p}) = \int_{\boldsymbol{0}}^{\infty} \boldsymbol{e}^{-\boldsymbol{pt}} \boldsymbol{e}^{\boldsymbol{at}} \boldsymbol{dt} = \int_{\boldsymbol{0}}^{\infty} \boldsymbol{e}^{-(\boldsymbol{p}-\boldsymbol{a})\boldsymbol{t}} \boldsymbol{dt} = \frac{\boldsymbol{1}}{\boldsymbol{p}-\boldsymbol{a}} \qquad \text{Equation 68}$$

Appendix 3: Rutherford Backscattering Spectrometry (RBS)

To back up the ion-exchange diffusion theory for the titania/silver/titania samples (see Chapter 14) annealed at 600^{o}C for 1 hour RBS analysis was performed by the Danish Technological Institute on a float glass reference sample and titania/Ag/titania samples in the as-deposited and annealed at 600^{o}C for 1 hr conditions, respectively. Figures E.1-E.3 show the finding from this analysis and the report received is as follow:

The upper x-axis refers to the energy of the backscattered He ions. Since the energy of the backscattered He ions depends on the mass of the atom they collide with (higher sample atom mass gives higher backscattered energy) and in what depth in the sample the scattering took place (the deeper the lower backscattered energy). It is possible to extract a depth concentration profile for the various elements; however, it is necessary to know the approximate structure of a layered coating and the nature of the substrate for example. Figure E.1 shows a measurement of the float glass reference sample with the fitted, simulated curve and the chemical composition included in the spectrum.

The y-axis, counts, refers to the concentration of an element weighted with the scattering cross section. For heavier elements the scattering cross section are higher.

Comparing the measurement of the glass substrate (Figure E.1) with the ones with the TiO_2/Ag/TiO_2 coatings (Figures E.2 and E.3), extra features that corresponds to the spectra from the coating can be seen. The coating spectra has just been added to the reference spectrum, with the minor detail that all the energies belonging to the glass substrate has now been reduced since He ion backscattered from the substrate now has to traverse the coating (which gives the energy loss). The peak at about 1400 keV in Figure E.2 refers to Ti from TiO_2. If the TiO_2 layer has a homogeneous concentration profile the height of the measured signal from TiO_2 should be almost flat. The 'dip' in the peak reveals the fact that the Ag layer is sandwiched in between two TiO_2 layers. In Figure E.3 the 'dip' is not as pronounced as in previous one showing that the two TiO_2 layers have merged together after annealing at 600^{o}C for 1 hour.

On the other hand, if Ag was present on the surface its signal should rise at channel number ~480 (1730 keV). This actually seems to be the case on both spectra (Figure E.2 and E.3). However, the main Ag signal in the TiO_2/Ag/TiO_2 samples rise at a lower energy, which means it is present in some depth below the film surface. Ag in as-deposited sample shows one peak meaning one layer. Shoulder on the right side may suggest a little Ag tail towards the substrate surface. Whereas Ag in sample annealed at 600^{o}C for 1 hr shows two broad peaks of relatively low intensity. The Ag is no longer present as a single layer but has diffused to the surface and towards the substrate/film interface. Therefore, the ion-exchange diffusion (as it was discussed in Chapter 14.1) could have occurred after annealing at 600^{o}C for 1 hr, and hence the intensity of diffused silver is significantly lower than in as-deposited titania/Ag/titania sample.

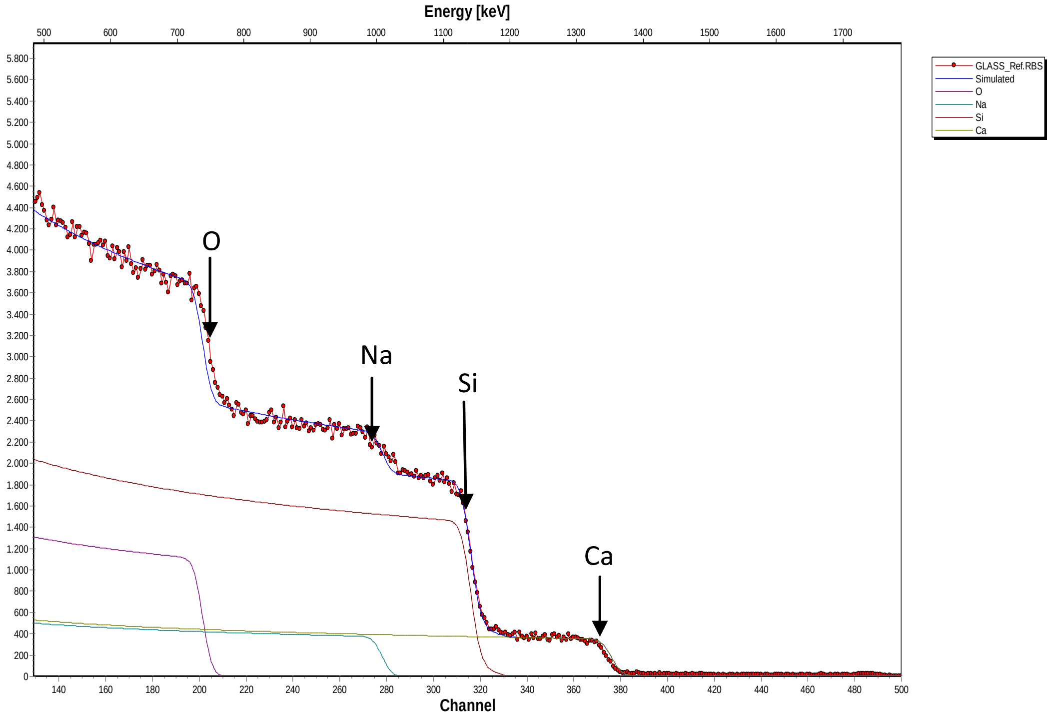

Figure E.1: The reference RBS spectrum of the float glass. The red points are the measured spectra. The blue curve is a theoretical simulation of a sample with chemical composition: O equals 61 at %, Na 11 at %, Si 26 at % and Ca 3 at %.

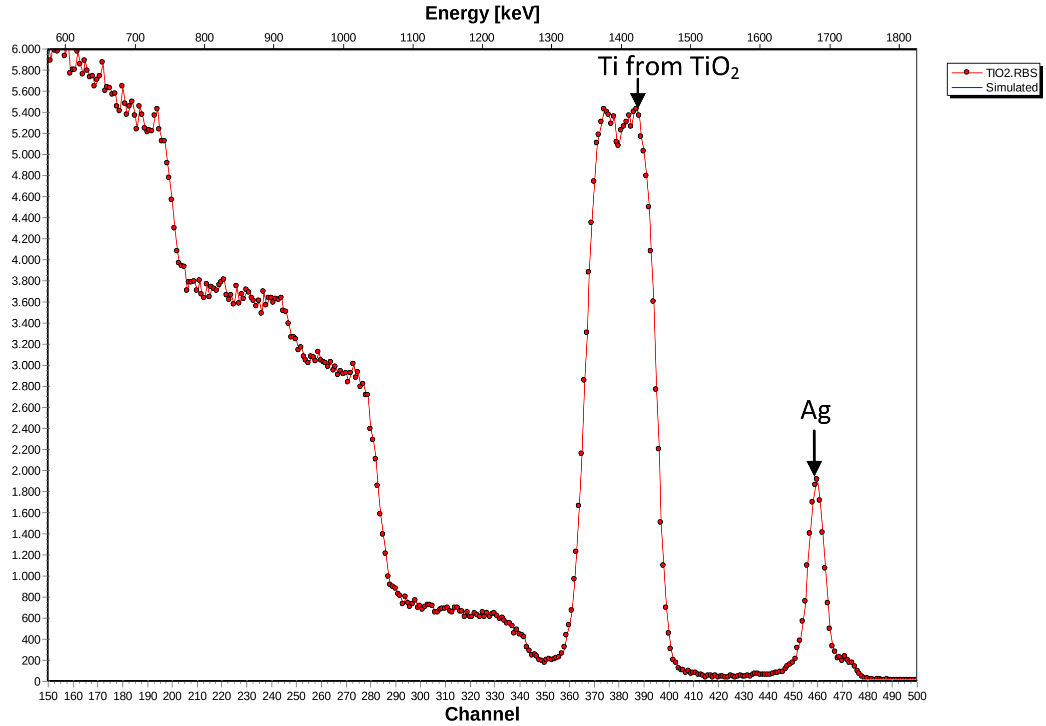

Figure E.2: RBS spectrum collected from as-deposited titania/silver/titania sample deposited onto float glass substrate.

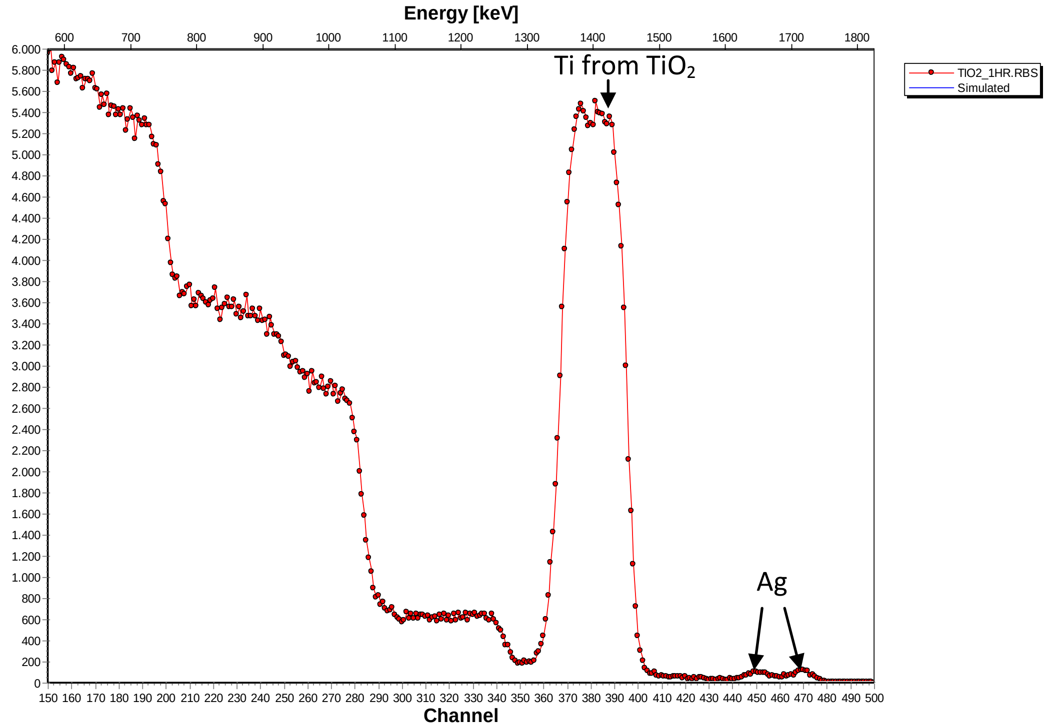

Figure E.3: RBS spectrum collected from titania/silver/titania sample annealed at 600°C for 1 hr, deposited onto float glass substrate.

References

1. E. Ando, S. Suzuki, N. Aomine, M. Miyazaki, M. Tada, *Vacuum*, 59 (2000) 792-99.
2. K. Chiba, T. Takahashi, T. Kageyama, H. Oda, *App. Surf. Sci*., 246 (2005) 48-51.
3. E. Hammarberg, A. Roos, *Thin Solid Films*, 442 (2003) 222-226.
4. A.M. Abdul-Lettif, *Physica B*, 388 (2007) 107-111.
5. C.Y. Chen, H.L. Huang, *J. Vac. Sci. Technol*., 18 (1981) 398-400.
6. A. L. Greer, *App. Surf. Sci*., 86 (1995) 329-337.
7. Y.S. Lee, K.Y. Lim, D. Chung, C.N. Whang, J.J. Woo, Y.P. Lee, *J. Vac. Sci. Technol. A*., 15 (1997) 2013-2016.
8. A. Bukaluk, M. Rozwadowski, *Vacuum*, 46 (1995) 579-582.
9. A. Bukaluk, *App. Surf. Sci*., 144-145 (1999) 395-398.
10. C.-B. Ene, G. Schmitz, T. Al-Kassab, R. Kirchheim, *Ultramicroscopy*, 107 (2007) 802-807.
11. A. Celik, U. Cevik, E. Bacaksiz, N. Celik, *Thin Solid Films*, 517 (2008) 2851-2854.
12. M. Mitkova, M.N. Kozicki, H.C. Kim, T.L. Alford, *Thin Solid Films*, 449 (2004) 248-253.
13. W. Losch, P.M. Jardin, *Scripta Materialia*, 38 (1998) 1857-1861.
14. W.E. Martinez, G. Gregori, T. Mates, *Thin Solid Films*, 218 (2010) 2585-2591.
15. D.L. Beke, Z. Erdélyi, G.A. Langer, A. Csik, G.L. Katona, *Vacuum*, 80 (2005) 87-91.
16. H. Weis, T. Müggenburg, P. Grosse, L. Herlitze, I. Friedrich, M. Wutting, *Thin Solid Films*, 351 (1999) 184-189.
17. J.J. Finley, *Thin Solid Films*, 351 (1999) 264-273.
18. M.M. Hasan, A.S.M.A. Haseeb, H.H. Masjuki, *Surface Engineering*, 27 (2011) 382-388.
19. S.J. Nadel, *J. Vac. Sci. Technol. A*, 5 (1987) 2709-2713.
20. E. Ando, M. Miyazaki, *Thin Solid Films*, 392 (2001) 289-293.
21. H. Ohsaki, Y. Kokubu, *Thin Solid Films*, 351 (1999) 1-7.
22. E. Ando, M. Miyazaki, *Thin Solid Films*, 351 (1999) 308-312.
23. http://www.pilkington.com/ , 29th Aug 2011, 13:20.
24. D.M. Mattox, *"Handbook of Physical Vacuum Deposition (PVD) Processing."* Noyes Publications, Westwood, New Jersey, USA (1998).
25. P.I. Gouma, P.K. Dutta and M.J. Mills, *NanoStructured Materials*, 11 (1999) 1231-1237.
26. P. Löbl, M. Huppertz, D. Mergel, *Thin Solid Films*, 251 (1994) 72-79.
27. J.C. Yu, J. Yu, J. Zhao, *App. Cat. B: Environmental*, 36 (2002) 31–43.
28. K.A. Vorotilov, E.V. Orlova, V.I. Petrovsky, *Thin Solid Films*, 207 (1992) 180-184.
29. T. Yoko, L. Hu, H. Kozuka, S. Sakka, *Thin Solid Films*, 283 (1996) 188-195.
30. H.M. Yates, M.G. Nolan, D.W. Sheel, M.E. Pemble, *J. Photochemistry and Photobiology A: Chemistry*, 179 (2006) 213–223.
31. J.-P. Lu, J. Wang, R. Raj, *Thin Solid Films*, 204 (1991) L13-L17.
32. K.S. Yeung, Y.W. Lam, *Thin Solid Films, 109 (1983) 169-178.*
33. V.G. Bessergenev, I.V. Khmelinskii, R.J.F. Pereira, V.V. Krisuk, A.E. Turgambaeva, I.K. Igumenov, *Vacuum*, 64 (2002) 275–279.
34. W.G. Lee, S.I. Woo, J.C. Kim, S.H. Choi, K.H. Oh, *Thin Solid Films*, 237 (1994) 105-111.

35. F. Zhang, S. Jin, Y. Mao, Z. Zheng, Y. Chen, X. Liu, *Thin Solid Films,* 310 (1997) 29-33.
36. D. Mardare, P. Hones, *Mat. Sci. Eng. B*, 68 (1999) 42–47.
37. M. Gratzel, *Renewable Energy,* 5 (1994) 118-133.
38. L.-J. Meng, M.P. dos Santos, *Thin Solid Films*, 226 (1993) 22-29.
39. S. Schiller, G. Beister, W. Sieber, G. Schirmer, E. Hacker, *Thin Solid Films*, 83 (1981) 239-245.
40. B. O'Regan,M. Grätzel, *Nature*, 353 (1991) 737-740.
41. V. Stengl, S. Bakardjieva, N. Murafa, J. Subrt, H. Měšt'ánková, J. Jirkovský, *Materials Chemistry and Physics*, 105 (2007) 38–46.
42. D. Song, *App. Surf. Sci.*, 254 (2008) 4171-4178.
43. M.L Glasser, *Journal of Physics and Chemistry of Solids*, 10 (1959) 229-241.
44. A. Tanuševski, V. Georgieva, *App. Surf. Sci.*, 256 (2010) 5056-5060.
45. K.-H. Lee, N.-I. Cho, E.-J. Yun, H.G. Nam, *App. Surf. Sci.,* 256 (2010) 4241-4245.
46. Q.-B. Ma, Z.-Z. Ye, H.-P. He, L.-P. Zhu, J.-R. Wang, B.-H. Zhao, *Materials Letters*, 61 (2007) 2460-2463.
47. R.J. Hong, X. Jiang, G. Heide, B. Szyszka, V. Sittinger, W. Werner, *J. Crystal Growth*, 249 (2003) 461-469.
48. S. Flickyngerova, K. Shtereva, V. Stenova, D. Hasko, I. Novotny, V. Tvarozek, P. Sutta, E. Vavrinsky, *App. Surf. Sci*., 254 (2008) 3643-3647.
49. E. Ando, M. Miyazaki, *Thin Solid Films*, 516 (2008) 4574–4577.
50. J.H. Ko. I.H. Kim, D. Kim, K.S. lee, J.-H. Jeong, B. Cheong, Y.J. Baik, W.M. Kim, *Thin Solid Films,* 494 (2006) 42-46.
51. J.H. Ko, I.H. Kim, D. Kim, K.S. Lee, T.S.Lee, B. Cheong, W.M. Kim, *App. Surf. Sci.*, 253 (2007) 7398-7403.
52. K. Satoh, Y. Kakehi, A. Okamoto, S. Murakami, K. Moriwaki, T. Yotsuya, *Thin Solid Films*, 516 (2008) 5814–5817.
53. A.R. Babar, S.B. Kumbhar, S.S. Shinde, A.V. Moholkar, J.H. Kim, K.Y. Rajpure, *J. Alloys and Compounds*, 509 (2011) 7508–7514.
54. K. Satoh, Y. Kakehi, A. Okamoto, S. Murakami, F. Uratani, T. Yotsuya, *Jpn. J. Appl. Phys*., 44 (2005) L34-L37.
55. H. Wang, H. Huang, B. Wang, *Solid State Communications*, 149 (2009) 1849-1852.
56. J. Xu, X. Jia, X. Lou, J. Shen, Solid-State Electronics, 50 (2006) 504–507.
57. M.V. Nikolić, K. Satoh, T. Ivetić, K.M. Paraskevopoulos, T.T. Zorba, V. Blagojević, L. Mančić, P.M. Nikolić, *Thin Solid Films*, 516 (2008) 6293–6299.
58. I.A. Afanasyev-Charkin (on laptop)
59. S. Guruvenket, J. Ghatak, P.V. Satyam, G. Mohan Rao, *Thin Solid Films*, 478 (2005) 256– 260.
60. S.P Muraka, *"Encyclopaedia of materials science and technology"*, 2nd edition, Rensselaer Polytechnic Institute, Troy, New York (2003).
61. I. Sugimoto, K. Yanagisawa, H. Kuwano, S. Nakano, A. Tago, *J. Vac. Sci. Technol. A*, 12 (1994) 2859-2866.
62. E. Kusano, J. Kawaguchi, K. Enjouji, *J. Vac. Sci. Technol. A*, 4 (1986) 2907-2910.
63. S.M. Rossnagel, J.J. Cuomo, W.D. Westwood, *"Handbook of Plasma Processing Technology. Fundamentals, Etching, Deposition, and Surface Interactions"*, Noyes Publications, New Jersey, USA (1990)
64. R.N. Franklin, *"Plasma Phenomena in Gas Discharge",* Clarendon Press, Oxford (1976)

65. J.L. Vossen, W. Kern, *"Thin Film Processes II",* Academic Press Inc., San Diego (1991)
66. M. Ohring, *"Materials science of Thin Films. Deposition and Structure",* Academic Press, San Diego (2002)
67. K. Wasa, M. Kitabatake, H. Adachi, *"Thin Film Materials Technology. Sputtering of Compound Materials"*, William Andrew Inc., Norwich, USA (2004)
68. R.L. Boxman, D.M. Sanders, P.J. Martin, J.M. Lafferty, "Handbook of Vacuum Arc Science and Technology. Fundamentals and Applications", Noyes publications, New Jersey, USA (1995)
69. K. Seshan, *"Handbook of Thin Film Deposition, Processes and Techniques-Principles, Methods, Equipment and Applications",* Noyes Publications/ William Andrew Publishing, Norwich, USA (2002)
70. P.J. Kelly, R.D. Arnell, Vacuum, 56 (2000) 159-172.
71. P.J. Kelly, "Multi-Layer Pyrotechnic Coatings by Ion Plating", Department of Aeronautical and Mechanical Engineering, University of Salford, Manchester (1994)
72. B. Window, F. Sharples, N. Savvides, *J. Vac. Sci. Technol. A*, 3 (1985) 2368-2372.
73. B. Window, N. Savvides, *J. Vac. Sci. Technol. A*, 4 (1986) 196-202.
74. B. Window, N. Savvides, *J. Vac. Sci. Technol. A*, 4 (1986) 453-456.
75. N. Savvides, B. Window, *J. Vac. Sci. Technol. A*, 4 (1986) 504-508.
76. I. Safi, *Surface and Coatings Technology*, 127 (2000) 203-219.
77. P. J. Kelly, J.W. Bradley, *J. Optoelectronics and Advanced Materials*, 11 (2009) 1101-1107.
78. C.A. Bishop, *"Vacuum Deposition onto Webs, Films and Foils"*, William Andrew Inc., New York (2007)
79. B.A. Movchan, A.V. Demchishin, *Fiz. Metal. Metalloved.*, 28 (1969) 653-660.
80. A. Anders, *Thin Solid Films*, 518 (2010) 4087-4090.
81. J.A. Thornton, *J. Vac. Sci. Technol.*, 11 (1974) 666-670.
82. A. Anders, *Surface & Coatings Technology*, 205 (2011) S1–S9,
83. J. Crank, *"The Mathematics of Diffusion",* 2nd edition, Clarendon Press, Oxford (1975)
84. D. Gupta, *"Diffusion Processes in Advanced Technological Materials",* William Andrew Inc., Norwich, USA (2005)
85. A. Einstein, "Investigations of the Theory of the Brownian Movement", Dover Publications Inc., New York (1956)
86. G. Antczak, G. Ehrlich, *Surface Science*, 589 (2005) 52–66.
87. Zs. Tôkei, J. Bernardini, G. Erdélyi, I. Gôdény, D.L. Beke, *Acta Materialia*, 46 (1998) 4821-4825.
88. D. Gupta, *Canadian Metallurgical Quarterly*, 34 (1995) 175-183.
89. A.L. Greer, *Current Opinion in Solid State and Materials Science &Metallurgy*, 2 (1997) 300-304.
90. M.E. Glicksman, K.-G. Wang, S.P. March, *J. Crystal Growth*, 230 (2001) 318-327.
91. P.G. Shewmon, *"Diffusion in solids",* 2nd edition, TMS AIME, Warrendale, PA, USA (1989)
92. V.B. Sapozhnikov, M.G. Goldiner, *Thin Solid Films*, 111 (1984) 183-187.
93. D. Gupta, P.S. Ho, *Thin Solid Films*, 72 (1980) 399-418.
94. R.D. Thompson, D. Gupta, K.N. Tu, *Phys. Rev. B*, 33 (1986) 2636-2641.

95. K.A. Jackson, *"Kinetic Processes. Crystal Growth, Diffusion, and Phase Transition in Materials",* WILEY-VCH Verlag GmbH & Co. KGaA, Weinheim (2004)
96. R.W. Balluffi, J.M. Blakely, *Thin Solid Films*, 25 (1975) 363-392.
97. D. Udler, D.N. Seidman, *Physical Review B,* 54 (1996) 133-136.
98. H. Gleiter, P. Pumphrey, *Materials Science and Engineering*, 25 (1976) 159-164.
99. H. Gleiger, *Scripta Metallurgica*, 11 (1977) 305-309.
100. M. Kaspar, H. Gleiter, *Acta Metallurgica*, 32 (1984) 1903-1906.
101. R.S. Barnes, *Nature*, 166 (1950) 1032-1033.
102. Y. Mishin, Chr. Herzig, *Materials Science and Engineering A*, 260 (1999) 55–71.
103. Y. Mishin, *Defect Diffusion Forum*, 194-199 (2001) 1113-1126.
104. J. Cermak, I. Stloukal, J. Ruzickova, A. Pokorna, *Intermetallics*, 6 (1998) 21-28.
105. J. Cermak, J. Ruzickova, I. Stloukal, A. Pokorna, *Scripta Materialia*, 37 (1997) 31-35.
106. N.P. Zulina, E.V. Bolberova, I.M. Razumovskii, *Acta Materialia*, 44 (1996) 3625-3631.
107. St. Frank, Chr. Herzig, *Materials Science and Engineering A*, 239–240 (1997) 882–888.
108. Chr. Herzig, T. Wilger, T. Przeorski, F. Hisker, S. Divinski, *Intermetallics*, 9 (2001) 431–442.
109. Zs. Tôakei, J. Bernardini, D.L. Beke, *Acta Materialia*, 47 (1999) 1371-1378.
110. L.G. Harrison, *Trans. Faraday Soc.*, 57 (1961) 1191-1199.
111. http://gencoa.com, 20th Sept 2011, 16:15.
112. E. Smith, G. Dent, "*Modern Raman Spectroscopy. A practical Approach",* John Wiley & Sons Ltd., Chichester, UK (2005)
113. J.J. Goldstein, D.E. Newbury, P. Echlin, D.C. Joy, A.D. Roming, Jr, C.E. Lyman, C. Fiori, E. Lifshin, "*Scanning electron Microscopy and X-ray Microanalysis",* Plenum Press, New York (1992)
114. V.S. Ramachandran, J.J. Beaudoin (2001), "*Handbook of Analytical Techniques in Concrete Science and Technology",*(William Andrew Publishing/Noyes, Ottava, Canada (2001)
115. C.R. Brundle, C.A. Evans, Jr., S. Wilson, "*Encyclopaedia of Materials Characterisation",* Butterworth-Heinemenn, Boston (1992)
116. P.E.J. Flewitt, R.K. Wild (2003), "*Physical methods for Material Characterisation",* IOP Publishing Ltd., Bristol, UK (2003)
117. C. Hammond, "*The Basics of Crystallography and Diffraction",* Oxford University Press Inc., New York (2001)
118. http://ia.physik.rwth-aachen.de/methods.xray.www-xray-eng.pdf?menu_id=80&language=german. 13th Jul 2012, 22:50.
119. I. Kojima, B. Li, *The Rigaku Journal*, 16 (1999) 31-41.
120. R.W. Bowen, N. Hilal, "*Atomic Force Microscopy in Process Engineering. Introduction to AFM for Improved Processes and productions",* Butterworth-heinemann/Elsevier Ltd., Oxford, UK (2009)
121. D.R. Askeland, P.P. Phule, "*The Science and Engineering of Materials",* 5th edition, Nelson, Thomson Canada Ltd., USA (2006)
122. G.E. McGuire, *"Characterisation of Semiconductor Materials. Principles and Methods Volume I",* Noyes Publications, New Jersey, USA (1989)

123. J.F. Watts, J. Wolstenholme, "*An Introduction to Surface Analysis by XPS and AES",* John Willey & Sons Ltd, Chichester, UK (2003)
124. I. Horcas, R. Fernández, J.M. Gómez-Rodriguez, J. Colchero, J. Gómez-Herrero, A.M. Baro, *Review of Scientific Instruments*, 78 (2001) 1-8.
125. J.C. Vickerman, D. Briggs, "*ToF-SIMS: Surface Analysis by Mass Spectrometry",* IMPublications/SurfaceSpectra Ltd., Chichester/Manchester, UK (2001)
126. A. Li Bassi, D. Cattaneo, V. Russo, C.E. Bottani, E. Barborini, T. Mazza, P. Piseri, P. Milani, F.O. Ernst, K. Wegner, S.E. Pratsinis, *J. Applied Physics*, 98 (2005) 1-9.
127. C. Giolli, F. Borgioli, A. Credi, A. Di Fabio, A. Fossati, M.M. Miranda, S. Parmeggiani, G. Rizzi, A. Scrivani, S. Troglio, A. Tolstoguzov, A. Zoppi, U. Bardi, *Surface & Coatings Technology*, 202 (2007) 13–22.
128. T. Sekiya, S. Ohta, S. Kamei, M. Hanakawa, S. Kurita, J. *Physics and Chemistry of Solids*, 62 (2001) 717-721.
129. A.F. Khan, M. Mehmood, M. Aslam, S.I. Shah, *J. Colloid and Interface Science,* 343 (2010) 271–280.
130. B. Karunagaran, K. Kim, D. Mangalaraj, J. Yi, S. Velumani, *Solar Energy Materials & Solar Cells*, 88 (2005) 199–208.
131. S. Balaji, Y. Djaoued, J. Robichaud, *J. Raman Spectroscopy*, 37 (2006) 1416-1422.
132. Y. Xie, X. Zhao, H. Tao, Q. Zhao, B. Liu, Q. Yuan, *Chemical Physics Letters*, 457 (2008) 148–153.
133. P.J. Kelly, G. West, Y.N. Kok, J.W. Bradley, I. Swindells, G.C.B. Clarke, *Surface & Coatings Technology*, 202 (2007) 952–956.
134. P.S. Henderson, P.J. Kelly, R.D. Arnell H. Bäcker J.W. Bradley, *Surface and Coatings Technology*, 174 –175 (2003) 779–783.
135. R.D. Arnell, P.J. Kelly, J.W. Bradley, *Surface & Coatings Technology*, 188–189 (2004) 158–163.
136. www.uio.no/studier/emner/matnat/kjemi/KJM5120/v05/undervisringsmateriale/KJM5120-Ch5-Diffusion.pdf , 21st Sept 2011, 14:30.
137. S.G. Ostrowski, M.E. Kurczy, T.P. Roddy, N. Winograd, A.G. Ewing, *Analitycal Chemistry*, 79 (2007) 3554-3560.
138. H. Morkoç, Ü. Özgür, *"Zinc Oxide: Fundamentals, Materials and Device Technology"*, WILEY-VCH Verlag GmbH &Co. KGaA, Weinheim (2009)
139. Z.L. Wang, *J. Physics: Condensed Matter*, 16 (2004) R829-R858.
140. Y. Qu, T.A. Gessert, T.J. Coutts, R. Noufi, J. Vac. Sci. Technol. A, 12 (1994) 1507-1512.
141. *"Powder Diffraction File"*, Vol. Inorganic Volume, No. PD1S-5iRB, Join Committee on Powder Diffraction Standards, Pennsylvania, USA (1974)
142. E.M. Bachari, G. Baud, S. Ben Amor, M. Jacquet, *Thin Solid Films*, 348 (1999) 165-172.
143. K. Ellmer, R. Cebulla, R. Wendt, *Thin Solid Films*, 317 (1998) 413–416.
144. K. Ellrner, R. Cebulla, R. Wendt, *Surface and Coatings Technology*, 98 (1998) 1251-1256.
145. M.K. Puchert, P.Y. Timbrell, R.N. Lamb, *J. Vac. Si. Technol. A*, 14 (1996) 2220-2230.
146. T. Tsuji, M. Hirohashi, *Applied Surface Science*, 157 (2000) 47–51.
147. L. Li, L. Fang, X.M. Chen, J. Liu, F.F. Yang, Q.L. Li, G.B. Liu, S.J. Feng, *Physica E*, 41 (2008) 169-177.

148. S. Rahmane, M.A. Djouadi, M.S. Aida, N. Barreau, B. Abdallah, N. Hadj Zoubir, *Thin Solid Films*, 519 (2010) 5-10.
149. J.A. Thornton, D.W. Hoffman, *J. Vac. Sci. Technol.*, 14 (1977) 164-168.
150. O. Kappertz, R. Drese, M. Wutting, *J. Vac. Sci. Technol. A*, 20 (2002) 2084-2095.
151. R.C. Weast, *"Handbook of Chemistry and Physics",* CRC Press Inc., Cleveland, Ohio, USA (1974)
152. A.C. Galca, G. Socol, V. Craciun, *Thin Solid Films*, 520 (2012) 4722–4725.
153. A.C. Gâlcă, M. Secu, A. Vlad, J.D. Pedarnig, *Thin Solid Films*, 518 (2010) 4603–4606.
154. C. Besleaga, G.E. Stan, A.C. Galca, L. Ion, S. Antohe, *Applied Surface Science*, 258 (2012) 8819– 8824.
155. J. Clatot, G. Campet, A. Zeinert, C. Labrugere, A. Rougier, *Applied Surface Science*, 257 (2011) 5181–5184.
156. M.F. Al-Kuhaili, S.M.A. Durrani, I.A. Bakhtiari, A.M. Al-Shukri, *Optics Communications*, 283 (2010) 2857–2862.
157. M.K. Jayaraj, K.J. Saji, K. Nomura, T. Kamiya, H. Hosono, *J. Vac. Sci. Technol. B*, 26 (2008) 495-501.
158. Y. Sato, J. Kiyohara, A. Hasegawa, T. Hattori, M. Ishida, N. Hamada, N. Oka, Y. Shigesato, *Thin Solid Films*, 518 (2009) 1304–1308.
159. E. Çetinörgü, *Optics Communications*, 280 (2007) 114–119.
160. H.P. Löbl, M. Huppertz, *Thin Solid Films*, 317 (1998) 153–156.
161. B. Li, T. Fujimoto, N. Fukumoto, K. Honda, I. Kojima, *Thin Solid Films*, 334 (1998) 140-144.
162. W. Xu, T. Fujimoto, I. Kojima, *Thin Solid Films*, 394 (2001) 109-114.
163. Y.S. Lee, K.Y. Lim, Y.D. Chung, C.N. Whang, J.J. Woo, Y.P. Lee, *J. Vac. Sci. Technol. A*, 15 (1997) 2013-2016.
164. L. Chen, Y. Zeng, P. Nyugen, T.L. Alford, *Materials Chemistry and Physics*, 76 (2002) 224–227.
165. L. Xiangyang, C. Huansheng, H. Wenquan, Y. Fujia, *Chin. Phys. Lett.*, 11 (1994) 577-580.
166. E. Bacaksiz, O. Görür, M. Tomakin, E. Yanmaz, M. Altunbaş, *Materials Letters*, 61 (2007) 5239–5242.
167. A. Lakatos , G. Erdelyi, G.A. Langer, L. Daroczi, K. Vad, A. Csik, A. Dudas, D.L. Beke, *Vacuum*, 85 (2010) 493-497.
168. J. Breuer, T. Wilger, M. Friesel, Chr. Herzig, *Intermetallics,* 7 (1999) 381-388.
169. St. Frank, U. Södervall, Chr. Herzig, *Intermetallics,* 5 (1997) 221-227.
170. W.C. Mallard, A.B. Gardner, R.F. Bass, L.M. Slifkin, *Physical Review*, 129 (1963) 617-625.
171. A.Y. Zhang, T. Suetsugu, K. Kadono, *J. Non-Crystalline Solids*, 353 (2007) 44–50.
172. J. Sheng, J. Li, J.Yu, *International Journal of Hydrogen Energy*, 32 (2007) 2598 – 2601.
173. M. Prudenziati, B. Morten, A.F. Gualtieri, M. Leoni, *J. Materials Science: Materials in Electronics*, 15 (2004) 447-453.
174. A.W. Smith, N.G. Butcher, D. Walker, *Society of Vacuum Coaters*, ISSN 0737-5921 (2002) 113-118.
175. S. Berg, T. Nyberg, *Thin Solid Films*, 476 (2005) 215– 230.